



**University of
Nottingham**

UK | CHINA | MALAYSIA

Understanding the double diaphragm forming process: Moving towards multi-component forming

By

Ángela Lendínez Torres

MSc.

Thesis submitted to the University of Nottingham
for the degree of Doctor of Philosophy

September 2024

Abstract

Composite materials, formed by combining two or more distinct constituents, offer superior mechanical properties compared to traditional materials, making them essential in industries such as automotive, aerospace, and renewable energy. In advanced manufacturing processes, double diaphragm forming enables the transformation of 2D dry fabric blanks into 3D structures. However, this process presents challenges, including defect formation such as wrinkling and bridging, which can compromise the structural integrity of the final component. As sustainability and process efficiency become increasingly critical, optimising forming techniques is essential. This research focusses on non-crimp fabrics due to their superior mechanical properties and structural performance, investigating key factors influencing defect formation and exploring strategies to enhance the efficiency and sustainability of the double diaphragm forming process.

This thesis aims to enhance the understanding of the double diaphragm forming process and to assess the feasibility of multi-component forming. Established numerical and experimental methodologies were used to explore the effect of key parameters on defect formation. Multi-component forming was evaluated to investigate the effect of fabric and diaphragm interactions, with the goal of improving the sustainability and efficiency of the process.

An experimental and numerical methodology were established, defining mesh configuration, mass scaling and material parameters for the numerical model. The numerical predictions were validated against experimental results, with the model providing valuable insights, but further refinement is required to improve defect prediction accuracy.

The influence of process parameters, including diaphragm size, breather configuration, two-step preforming, stacking sequence and modelling of the breather were explored. Diaphragm size significantly influences wrinkling patterns, with optimal dimensions ranging between 500 mm and 1000 mm or 1300 mm, depending on the fabric orientation. Breather positioning affects material draping, with placement in non-draping areas reducing wrinkling.

Two-step preforming reduced wrinkling severity but did not decrease the number of wrinkles, making it less cost-effective due to increased labour and material use. Stacking sequence also played a key role, with a 0° relative fibre angle minimising the severity of wrinkles, whereas a 45° angle was more likely to induce severe wrinkling. Including the breather in the numerical model improved defect predictions, aligning wrinkling patterns more closely with experimental observations, though conformity to tool remained underpredicted.

The last chapter of the thesis explored fabric and diaphragm interactions to assess the feasibility of simultaneous multi-component forming. Studies were conducted using two and three hemispherical tools of different size.

Results indicated that forming two preforms simultaneously reduced draping and required precise in-plane spacing. A horizontal spacing of 200 mm to 600 mm between the fabric edges was optimal, while a vertical spacing below 100 mm between the edge of one fabric and the centre of another improved forming due to proximity to the diaphragm edge. Additionally, specific orientations and forming two hemispheres of different radii was found to be beneficial to the forming process.

For three tool forming, fabric positioning critically influenced defect patterns. Increasing spacing in the x-direction generally improved conformity of fabrics 1 and 2, while increasing spacing in the y-direction was more beneficial for fabric 3.

Acknowledgements

This thesis would not have been possible without the support and guidance of many people. I would like to express my deepest gratitude to Professor Nicholas Warrior for your expertise and guidance throughout this work. I would also like to express my appreciation to Dr Shuai Chen for sharing your modelling knowledge and for those valuable discussion. I am grateful for the support provided by Dr Lee Harper during our forming discussion.

I would like to thank Liam Sprake, not only for your technical knowledge and assistance but also for your emotional support. I gratefully acknowledge the financial support of the EPSRC Future Composite Manufacturing Research Hub, without which this research would not have been possible.

Many thanks to my colleagues Guy, George, Monika, Joe, Adam, Phoebe, Jesus, Jimi, Mikhail, Albert and Matt for those valuable conversations in and outside of work. Thank you to the UTC team: Erik, Mariam, Mohamed, Bea, and Pachi, for sharing lunches and many amazing moments outside of work. Without you all, this journey would not have been the same.

I would like to thank my best friend, Jolene; it was great to share our university years together. To my partner, Tom, for your patience and understanding, especially during moments when I doubted my abilities, thank you for always being there for me. I am also grateful to the Bermingham family and my family, especially Iñigo and Carlos, for believing in me and for your constant encouragement.

Lastly, I would like to thank my mum, Manuela. Mami, you are such an inspiration. Thank you for showing me that with hard work and perseverance, anything is possible. I would not be here without your lifelong support.

Acknowledgements

Contents

Abstract.....	I
Acknowledgements	III
Contents.....	V
List of figures.....	IX
List of tables.....	XVII
Acronyms	XX
Chapter 1 Introduction.....	1
1.1 Background and motivation	1
1.2 Scope of thesis.....	3
1.3 Outline of the thesis.....	4
Chapter 2 Literature Review	7
2.1 Composite reinforcements.....	7
2.2 Fabric forming and pre-forming processes.....	13
2.2.1 Hand layup	14
2.2.2 Matched tool forming.....	15
2.2.3 Diaphragm forming process	16
2.3 Forming mechanisms	20
2.3.1 In-plane shear.....	21
2.3.2 In-plane tension.....	22
2.3.3 Out-of-plane bending.....	23
2.3.4 Friction	24
2.4 Forming related defects.....	26

Contents

2.4.1	Defects specific to DDF	30
2.5	Material characterisation	30
2.5.1	In-plane shear tests	31
2.5.2	In-plane tension tests	36
2.5.3	Out-of-plane bending tests	38
2.5.4	Friction tests.....	39
2.6	Forming simulations	40
2.6.1	Simulation approaches	40
2.6.2	Fabric forming modelling.....	46
2.6.3	DDF forming simulation.....	55
Chapter 3	Methodology	59
3.1	Experimental.....	59
3.1.1	Rig.....	59
3.1.2	Tooling	62
3.1.3	Equipment	63
3.1.4	Materials.....	65
3.2	Modelling	74
3.2.1	Modelling approach	74
3.2.2	Model set-up/ Parameters of simulations.....	76
3.2.3	Mesh configuration.....	78
3.2.4	Effect of mass scaling.....	84
3.2.5	Fabric parameters.....	86
3.3	Chapter summary	91
Chapter 4	Validating the numerical model	93

4.1	Characterisation/Evaluation of forming	93
4.1.1	Shear angle.....	93
4.1.2	Deformed shape	94
4.1.3	Preform-tool distance (Dist2Tool)	95
4.1.4	Evaluation of methods.....	98
4.1.5	Defect distribution chart	99
4.2	Validation results.....	100
4.2.1	Experimental data	101
4.2.2	Numerical data.....	107
4.3	Comparison and validation of results	112
4.3.1	One-ply results.....	112
4.3.2	Two-ply results	113
4.3.3	Evaluation of results.....	113
4.4	Chapter summary	114
Chapter 5	Process studies.....	117
5.1	Effect of diaphragm size	117
5.2	Effect of breather arrangement	124
5.2.1	[90 ⁰ /0 ⁰] orientation	125
5.2.2	[-45 ⁰ /+45 ⁰] orientation.....	128
5.2.3	Strain distribution on the diaphragm	131
5.2.4	Evaluation of results.....	135
5.3	Effect of two-step preforming	136
5.4	Effect of stacking sequence	138
5.5	Effect of modelling breather.....	142

Contents

5.6	Chapter summary	147
Chapter 6	Investigating multi-component forming	149
6.1	Numerical considerations and benchmark results	149
6.2	Horizontal separation	150
6.2.1	Numerical study.....	150
6.2.2	Experimental study	155
6.2.3	Evaluation of results	163
6.3	Vertical separation	164
6.4	Three tool forming	168
6.5	Chapter summary	177
Chapter 7	Conclusions and outlook.....	179
7.1	Contributions and reflections	179
7.2	Key outcomes.....	181
7.3	Limitations	181
7.4	Outlook and future work.....	182
References	XXI

List of figures

Figure 2.1 Constituents of a composite material.....	7
Figure 2.2. Examples of fibre forms.....	8
Figure 2.3. Different textile fabric structures: woven, non-crimp fabric, braided, knitted. Adapted from [23]......	9
Figure 2.4. Schematic of the hierarchical nature of fabric structures [24].	9
Figure 2.5. Typical yarn architectures of woven fabrics.....	10
Figure 2.6. a) Architecture of a multi-axial non-crimp fabric [14]. Several plies are stack and then knitted together. b) Stitch types: pillar (up), tricot (middle) and plain (down) [30]......	11
Figure 2.7. Schematic of the fibre directions of a biaxial ($+45^0/-45^0$) NCF reinforcement.	12
Figure 2.8. Schematic presenting the difference between positive and negative shear for a $0^0/90^0$ biaxial non-crimp fabric with pillar stitch at 45^0 [33].	12
Figure 2.9. Example of prepreg layup draping techniques [47]......	14
Figure 2.10. Matched tooling forming process.....	15
Figure 2.11. Schematic of the single diaphragm forming vs double diaphragm forming.....	16
Figure 2.12. Schematic of the different stages of the double diaphragm forming process [51]......	17
Figure 2.13. Shear force vs shear angle of a NCF with chain/pillar stitch [40].	22
Figure 2.14. Tensile behaviour of two non-crimp fabrics with different stitch patterns [66]......	23
Figure 2.15. Bending moment per specimen width vs curvature along the sample profiles [70]......	24

Figure 2.16. Static and dynamic coefficients of friction when varying the slip direction [72].....	25
Figure 2.17. Out-of-plane and in-plane defects commonly affecting textile structures [77].....	26
Figure 2.18. Schematic diagram of a) out-of-plane waviness and b) in-plane waviness [83].....	27
Figure 2.19. Example of bridging and wrinkling during the DDF process.....	30
Figure 2.20. Schematic of the bias extension test and the different shear zones.....	32
Figure 2.21. Picture frame test for a NCF sample with the stitches in tension and compression.....	34
Figure 2.22. Biaxial tensile test for a NCF sample [63].....	37
Figure 2.23. Schematic of a standard cantilever test [106].	39
Figure 2.24. Schematic of the a) tool/fabric friction and b) fabric/fabric friction test setup [110].....	40
Figure 2.25. Draping algorithm with the initial constrained yarns and an example of draping on a hemispherical surface [111].....	42
Figure 2.26 Schematic of the yarn directions before and after deformation [120].....	47
Figure 2.27. Draping on a cylinder considering a) tensile stiffness, b) tensile and in-plane shear stiffness, and c) tensile, in-plane shear and bending stiffness [42].....	48
Figure 2.28. Compression in the fibre direction of a woven ply for a bending stiffness of a) 1 N/mm, b) 5 N/mm and c) 10 N/mm [129].....	49
Figure 2.29. Decoupling the bending and tensile behaviour using the laminate technique [117].....	50
Figure 2.30. Shear resistance curve for FCIM359 biaxial non-crimp fabric [33].....	52

Figure 2.31. a) Bending moment vs. curvature and b) non-linear bending stiffness vs. curvature for the FCIM359 NCF [107].	54
Figure 2.32. Characterisation of the diaphragm material using Marlow's hyperelastic model for a) uniaxial tension, b) equibiaxial tension and c) planar shear [131].	57
Figure 3.1. Schematic of the double diaphragm forming process.	60
Figure 3.2. Laboratory-scale Double diaphragm forming machine.	61
Figure 3.3. Fabric material a) before and b) after vacuum is applied between the lower diaphragm and the tool.	61
Figure 3.4. Schematic of a) the hemisphere with a 50 mm radius mounted on a platform, b) the hemisphere with a 50 mm radius and, c) the hemisphere with a 100 mm radius.	62
Figure 3.5. Automated cutting machine, X-CUT-TT, cutting the NCF samples to the required size.	63
Figure 3.6. In-situ scanning of the preform with the HandySCAN 3D™.	64
Figure 3.7. Relevant NCF ply orientations for the thesis.	66
Figure 3.8. Double diaphragm hemispherical preform a) with breather and b) without breather.	68
Figure 3.9. Breather tensile test a) set-up, b) sample size and c) samples before and after the test.	69
Figure 3.10. Force (N) vs crosshead displacement (mm) for samples cut in the a) perpendicular, b) 45° and c) parallel direction.	71
Figure 3.11. Schematic of the double diaphragm forming process with a hemispherical tool.	74
Figure 3.12. Pressure variation for the upper and lower diaphragms as a function of time.	76
Figure 3.13. Integration points for S4 and S4R elements for the first order-interpolation.	80

List of figures

Figure 3.14. Mesh size vs mesh density for a mesh size of 2 mm, 4 mm and 6 mm.....	81
Figure 3.15. Shear angle ($^{\circ}$) contour for the fabric for S4R elements for the different mesh sizes.....	81
Figure 3.16. CPU time (h) and maximum in-plane principal stress on the fabric (MPa) for the different mesh sizes.....	82
Figure 3.17. Shear angle ($^{\circ}$) contour for the fabric when using membrane and shell elements to mesh the diaphragm.....	83
Figure 3.18. CPU time (h) and ratio of all kinetic energy versus all internal energy (%ALLKE/ALLIE) for the different mass scaling factor values ranging from 10-1000.	85
Figure 3.19. Shear angle ($^{\circ}$) contour for the fabric for a mass scaling of 10, 200 and 400.....	86
Figure 3.20. Schematic of the distribution of the plies per part.	87
Figure 3.21. Shear angle ($^{\circ}$) contour for the fabric for the different cases in the fabric parameter study.	88
Figure 3.22. von Mises stress distribution in the upper diaphragm for case B and C in the fabric parameter study.	90
Figure 4.1. Deformed outline examples for the a) $[0^{\circ}/90^{\circ}]$ and b) $[+45^{\circ}/-45^{\circ}]$ NCF plies.....	94
Figure 4.2. Outline and diagonal nomenclature for future assessment of the forming.....	95
Figure 4.3. Preform points with a Dist2Tool above the threshold of a) 1 mm, b) 1.5 mm, c) 1.75 mm and 2.5 mm.....	97
Figure 4.4. Grid measurement of the undeformed and deform fabric using a coordinate measuring machine [33].	98
Figure 4.5. Shear deformable areas for the a) $[0^{\circ}/90^{\circ}]$ and b) $[+45^{\circ}/-45^{\circ}]$ NCF plies.....	99

Figure 4.6. Preform areas more susceptible to defects for a) $[0^0/90^0]$ and b) $[+45^0/-45^0]$ NCF.....	100
Figure 4.7. Preform-tool distance contour plot for the six experimental one ply scenarios.....	102
Figure 4.8. Preform-tool distance contour plot for the five experimental two ply scenarios.....	104
Figure 4.9. Preform-tool distance contour plot of the two repetitions for the three different stacking sequences to evaluate the repeatability of the experimental results.....	106
Figure 4.10. Preform-tool distance contour plot for the three numerical one ply scenarios.....	108
Figure 4.11. Preform-tool distance contour plot for the five numerical two ply scenarios.....	110
Figure 5.1. Preform-tool distance contour plot for the $[0^0/90^0]$ and $[+45/-45^0]$ orientations and 412 mm, 700 mm, 1100 mm and 1300 mm diaphragm sizes.....	119
Figure 5.2. Maximum preform-tool distance for the $[0^0/90^0]$ and $[+45/-45^0]$ orientations and all the diaphragm sizes.....	120
Figure 5.3. %0-1.75 conformity values for the $[0^0/90^0]$ and $[+45/-45^0]$ orientations and all the diaphragm sizes.....	121
Figure 5.4. Diagonal and edge length for the $[0^0/90^0]$ and $[+45/-45^0]$ orientations and all diaphragm sizes.....	122
Figure 5.5. von Mises stress distribution in the upper diaphragm for the $[0^0/90^0]$ and $[+45/-45^0]$ orientations and 700 mm, 1100 mm and 1300 mm diaphragm sizes.....	123
Figure 5.6. Schematic representation of the six breather arrangements: a) cross, b) X shape, c) cross and X shape, d) square 250x250, e) parallel 8, and f) full breather. The fabric is shown in black, and the breather in grey.....	125

Figure 5.7. Picture of the forming for the six $[90^0/0^0]$ breather arrangement scenarios.....	126
Figure 5.8. Preform-tool distance contour plot for the six $[90^0/0^0]$ breather arrangement scenarios.....	127
Figure 5.9. Picture of the forming for the six $[-45^0/+45^0]$ breather arrangement scenarios.....	129
Figure 5.10. Preform-tool distance contour plot for the six $[-45^0/+45^0]$ scenarios.....	130
Figure 5.11. Distortion of regular grid around the tool for the different breather arrangements.....	133
Figure 5.12. Strain pattern on the edge of the upper diaphragm for the parallel 8 and cross breather arrangements.....	135
Figure 5.13. Preform-tool distance contour plot for a conventional one-step forming and a two-step forming for a stack sequence of $[90^0/0^0, -45^0/+45^0]$.	137
Figure 5.14. Preform-tool distance contour plot for the different stacking sequence cases by relative fibre angle.	140
Figure 5.15. Schematic of the breather positioning for the parallel 8 configuration. The breather strips are highlighted in red.....	143
Figure 5.16. Preform-tool distance contour plot for the numerical cases with breather for the $[90^0/0^0, 0^0/90^0]$ stacking sequence.....	144
Figure 5.17. Preform-tool distance contour plot for the numerical cases with breather for the $[90^0/0^0]$ and $[-45^0/+45^0, +45^0/-45^0]$ stacking sequences.....	146
Figure 6.1. Schematic of the fabric positions for the numerical two tool study.	151
Figure 6.2. Diagonals and edge length for fabric 1 and 2 and all the <i>dxfabrics</i> distances for the numerical two tool study.	152
Figure 6.3. Preform-tool distance contour plot for both fabrics and a distance between fabrics of 12, 400 and 100 mm for the numerical two tool study.	154

Figure 6.4. Schematic of the fabric positions for the experimental lateral study for the two tool arrangements. The <i>dxfabrics</i> is the x-distance between fabrics for the experimental two tool study.....	155
Figure 6.5. Diagonals and edge length for fabric 1 and 2, for the 2x100r configuration and all the <i>dxfabrics</i> distances for the experimental two tool study.....	157
Figure 6.6. Diagonals and edge length for fabric 1 and 2, for the 1x100r 1x50r configuration and all the <i>dxfabrics</i> distances for the experimental two tool study.....	159
Figure 6.7. Preform-tool distance contour plot for both fabrics, 2x100r configuration and a x-distance between fabrics of 100 mm and 400 mm for the experimental two tool study.....	161
Figure 6.8. Preform-tool distance contour plot for both fabrics, 1x100r 1x50r configuration and a x-distance between fabrics of 100 mm and 400 mm for the experimental two tool study.....	162
Figure 6.9. Schematic of the fabric positions for the numerical two tool vertical separation study. The <i>dxfabrics</i> is the x-distance between fabrics, and the <i>dyfabrics</i> is the y-distance between fabrics.....	164
Figure 6.10. Diagonals and edge length for fabric 1 and 2 and all the <i>dyfabrics</i> distances the numerical two tool vertical separation study.	165
Figure 6.11. Preform-tool distance contour plot for both fabrics and the different y-distances for the numerical two tool vertical separation study.....	167
Figure 6.12. Maximum Dist2Tool and %0-1.75 value for both fabrics and the different y-distances for the numerical two tool vertical separation study.....	168
Figure 6.13. Schematic of the fabric positions for the experimental three tool study.....	169
Figure 6.14. Pictures of the experimental distribution for the three tool study.	170

List of figures

Figure 6.15. Diagonals and edge length for fabric 1 for the experimental three tool study.....	171
Figure 6.16. Diagonals and edge length for fabric 2 for the experimental three tool study.....	172
Figure 6.17. Diagonals and edge length for fabric 3 for the experimental three tool study.....	173
Figure 6.18. Location of the shear areas for the three tool experiments.	174
Figure 6.19. Preform-tool distance contour plot for both fabrics for the experimental three tool study.....	174

List of tables

Table 3.1. Material parameters for the biaxial NCF, Hexcel FMIC359, under study.....	66
Table 3.2. Material parameters for the breather material VACB4.	68
Table 3.3. Breather dimensions, weight and density calculations.	69
Table 3.4. Young's modulus and Poisson's ratio calculations for the different displacements.....	73
Table 3.5. Model parameters for all the numerical studies.	77
Table 3.6. Process parameters for all the numerical studies.....	78
Table 3.7. Maximum and minimum shear angle values and computational time when using the membrane and shell elements to mesh the diaphragm.....	84
Table 3.8. Parameters for each case in the fabric parameter study.	87
Table 3.9. Maximum and minimum shear, and energy balance for both plies for the different cases in the fabric parameter study.....	89
Table 4.1. Percentage of points above the threshold values of 1 mm, 1.5 mm, 1.75 mm and 2.5 mm.....	97
Table 4.2. Parameters for the one and two ply studies to validate the numerical model.....	100
Table 4.3. Maximum Dist2tool and %0-1.75 values for the six experimental one ply scenarios.....	101
Table 4.4. Maximum Dist2tool and %0-1.75 values for the five experimental two ply scenarios.	105
Table 4.5. Parameters used to evaluate the repeatability of the experimental results.....	107
Table 4.6. Maximum Dist2tool and %0-1.75 values for the three numerical one ply scenarios.....	109
Table 4.7. Maximum Dist2tool and %0-1.75 values for the five numerical two ply scenarios.....	111

List of tables

Table 4.8. Parameters used to evaluate the repeatability of the numerical predictions.....	112
Table 5.1. Description of the studies in chapter 5.....	117
Table 5.2. Parameters for the breather arrangement study.....	125
Table 5.3. Maximum Dist2Tool and %0-1.75 values for the six $[90^0/0^0]$ scenarios.....	128
Table 5.4. Maximum Dist2Tool and %0-1.75 values for the six $[-45^0/+45^0]$ scenarios.....	131
Table 5.5. Parameters for the strain tracking study.....	132
Table 5.6. Parameters for the two-step preforming study.....	136
Table 5.7. Maximum Dist2Tool and %0-1.75 values for a conventional one-step forming and a two-step forming for a stacking sequence of $[90^0/0^0, -45^0/+45^0]$	137
Table 5.8. Parameters for the stacking study.	138
Table 5.9. Maximum Dist2Tool and %0-1.75 value for different stacking sequence cases by relative fibre angle between plies.....	141
Table 5.10. Summary of the experimental and numerical no breather results previously presented for the $[90^0/0^0, 0^0/90^0]$ stacking sequence.....	144
Table 5.11. Maximum Dist2Tool value for different breather modelling cases.....	145
Table 5.12. Summary of the experimental and numerical no breather results previously presented for the $[90^0/0^0]$ and $[-45^0/+45^0, +45^0/-45^0]$ stacking sequences.....	146
Table 5.13. Maximum Dist2Tool value for different breather modelling cases.	147
Table 6.1. Description of the studies presented in this chapter.	149
Table 6.2. Distances between fabrics evaluated for the numerical two tool study, and their fabric-diaphragm edge distances. All the distances are in millimetres.....	151

List of tables

Table 6.3. Parameters for the experimental two tool study.....	156
Table 6.4. Stacking sequence for both fabrics for the experimental two tool study, where A is $[0^0/90^0, 0^0/90^0]$ and B is $[90^0/0^0, 90^0/0^0]$	156
Table 6.5. Maximum Dist2Tool and %0-1.75 value for both fabrics, both tool configurations and a x-distance between fabrics of 100 mm and 400 mm for the experimental two tool study.....	163
Table 6.6. Coordinates of the fabric centres in mm for the experimental three tool study.	169
Table 6.7. Maximum Dist2Tool and %0-1.75 value for both fabrics for the experimental three tool study.....	176

Acronyms

Acronym	Meaning
%ALLKE/ALLIE	Ratio of all kinetic energy to all internal energy
BET	Bias Extension Test
DDF	Double Diaphragm Forming
FE	Finite element
GFRP	Glass fibre reinforced polymer
LBM	Linear bending model
MTF	Matched tool forming
NCF	Non-crimp fabric
NLBM	Non-linear bending model
PFT	Picture frame test
RTM	Resin transfer moulding
SDF	Single diaphragm forming

Chapter 1 Introduction

1.1 Background and motivation

Composite materials, formed by combining two or more distinct materials, offer superior performance compared to traditional materials such as metals [1]. Their key advantages include light weight, leading to high specific strength and stiffness, and their ability to form into complex geometries, making them critical in numerous industries.

In the automotive sector, composites were first introduced in high-performance racing, due to their weight-driven performance benefits, and in luxury vehicles, due to their aesthetic appeal [2]. As the industry shifts towards electric vehicles, composite adoption is expected to grow significantly, particularly to offset the added weight of large battery packs. The global automotive composite market is projected to double in revenue by 2032 [3].

The energy sector is another major consumer of composites, spanning both fossil fuel and renewable energy applications [4]. Glass fibre reinforced polymers (GFRPs) are widely used for wind turbine blades, where their lightweight and high-strength properties contribute to improved efficiency and durability.

In the sports and recreation industry, composites are valued for their vibration damping, corrosion resistance, and ability to be tailored for specific performance requirements [5]. The market for composites in sporting goods is estimated to reach \$1.5 billion by 2030 [6].

Another important example is the aerospace industry, which has undergone a major transformation, with composites becoming a material of choice for modern aircraft [7]. The Boeing 787 Dreamliner and Airbus 350 are composed of approximately 50% carbon fibre composites by weight, leading to significant fuel savings and improved structural performance. Technological advancements

driven by the market such as out-of-autoclave processing techniques, like resin transfer moulding (RTM), are reducing production costs and energy consumption while enabling the production of large and complex structures.

RTM involves transforming a 2D blank into a 3D complex shape, which can be achieved using double diaphragm forming (DDF) or matched tool forming. However, preforming dry fabrics is a complex process, and parts manufactured using the double diaphragm forming process often experience defects such as wrinkling or bridging. This stage is crucial for resin injection, as defects introduced during manufacturing can compromise the performance of the final component [8], [9]. Therefore, understanding the process and identifying the key factors influencing defect occurrence are critical to ensure the quality of the final component.

Forming composite materials is a complex task and due to the high cost of composite materials, the traditional “trial and error” approach is impractical [10]. Numerical methods allow for detailed modelling of intricate interactions to predict the material behaviour under different conditions or configurations without the need for costly experiments. This facilitates the optimisation of the process parameters. However, developing high fidelity simulations requires a deep understanding of the forming mechanics, material behaviour, and careful consideration of model parameters to ensure accuracy [11].

In parallel, there is an increased drive for sustainable manufacturing processes [12]. This includes adopting low-energy processes or using simulation and modelling techniques to optimise the manufacturing process. One key challenge in the double diaphragm forming process is its limited production efficiency, as typically only one preform is manufactured at a time. Improving process efficiency, such as enabling the simultaneous production of multiple preforms, could significantly enhance productivity, reduce material waste and

lower operational costs, ultimately improving the sustainability of the forming process.

Among the different composite reinforcements, textiles offer unique properties, such as their handleability or their ability to form into complex shapes [13]. This research focusses specifically on non-crimp fabrics, as when compared to other textiles like woven fabrics, they offer superior mechanical properties [14], such as increased tensile strength, due to their highly aligned and straight fibres, and their multidirectional configuration. Additionally, the stitches provide some out-of-plane reinforcement, which translates into better through-thickness properties and impact resistance [15], [16].

1.2 Scope of thesis

This research aims to enhance the understanding of the double diaphragm forming process and assess the feasibility of multi-component forming. Using established experimental and numerical methodologies, it examines key process parameters influencing defect formation, applying this knowledge to evaluate the feasibility of multi-component forming. Multi-component forming has the potential to reduce material waste, operation time and to increase the sustainability of the process, as multiple preforms are produced simultaneously in the same machine bed and using the same consumables (diaphragm, breather, etc.). The main aims of this work are:

1. **To validate the numerical predictions against the experimental results:** ensuring that the predictions are accurate and reliable, identifying any discrepancies that could help refining the model to better reflect the forming conditions.
2. **To understand the influence of key parameters on the DDF process:** exploring how variables such as the mesh settings (how parts are divided into smaller elements for calculation), mass scaling (artificially modifying mass to enhanced computational efficiency),

and breather configuration, among others, affect defect occurrence and their prediction.

3. **To assess the feasibility of multi-component forming:** investigating fabric interactions and their effects on material conformity and defect formation.

In order to address these aims, five objectives are proposed:

1. **Establish an experimental methodology**, detailing equipment and materials.
2. **Establish a numerical methodology**, understanding the effect of mesh configuration, mass scaling, and other parameters on the numerical predictions.
3. **Validate the numerical model** by establishing approaches to evaluate the forming and comparing predictions with experimental results.
4. **Analyse process parameters**, evaluating the impact of the diaphragm size, the breather arrangement and fabric stacking sequence on defect occurrence and conformity; and evaluating the feasibility of a two-step preforming compared to conventional preforming.
5. **Explore multi-component forming**, examining the effect of fabric-fabric and diaphragm-fabric spacing on the draping and defect occurrence.

1.3 Outline of the thesis

This thesis is divided in seven chapters that address these aims and objectives:

- **Chapter 2 – Literature Review:** This chapter presents a detailed literature review on the characterisation and forming of composite

textile materials, as well as forming simulations. It identifies key limitations and gaps in the existing literature, providing a foundation for the research focus of the thesis.

- **Chapter 3 – Methodology:** This chapter introduces the experimental and numerical methods for the double diaphragm forming process used in this thesis, addressing objectives 1 and 2. It details the equipment and materials used, and outlines the modelling approach, establishing the mesh, mass scaling and fabric parameters, providing the foundation for the research framework.
- **Chapter 4 – Validating the numerical model:** This chapter compares numerical predictions against experimental results to validate the model, addressing objective 3. It outlines several evaluation approaches for the forming process, including shear angle, deformed shape, and the distance between the preform and the tool. A defect distribution chart is also provided for subsequent data analysis. Validating the model enhances the reliability of the findings in later chapters.
- **Chapter 5 – Process studies:** This chapter explores the effect of parameters such as diaphragm size, breather arrangement, two-step preforming and stacking sequence on the double diaphragm forming process, addressing objective 4. Adjustments on the modelling approach, including modelling the breather, are introduced to improve the accuracy of the predictions. Understanding these factors and advancing the modelling capabilities is essential to improve the overall quality and predictability of the process.
- **Chapter 6 – Investigating multi-component forming:** This chapter explores the feasibility of multi-component forming by investigating the effects of fabric-fabric and fabric-diaphragm spacing on the forming process, addressing objective 5. Studies are conducted

using two and three hemispherical tools of different size. Understanding these parameters is crucial, as multi-component forming could significantly enhance the productivity and sustainability of the double diaphragm forming process.

- **Chapter 7 – Conclusions and outlook:** This chapter presents the conclusions of the work, summarising the key contributions, discussing any limitations and providing an outlook for future research.

Chapter 2 Literature Review

This chapter presents the different textile materials and processes involved in fabric forming and preforming, with a particular focus on double diaphragm forming. It also addresses the key forming mechanisms, related defects, material characterisation techniques, and simulation approaches to model these processes. This section outlines any limitations or gaps in the existing literature, providing the foundation for the research framework.

2.1 Composite reinforcements

A composite material, also known as composite, is a combination of two or more components with a distinguishable interface between them, where superior properties are achieved compared to those of the individual constituents (see Figure 2.1) [1]. Typically, composite materials are composed of three components (Figure 2): (i) matrix, the continuous phase; (ii) the reinforcement, a dispersed phase; and (iii) an interface [17]. The reinforcement provides the mechanical strength, whilst the matrix holds the reinforcement in place, transferring the loads between fibres.

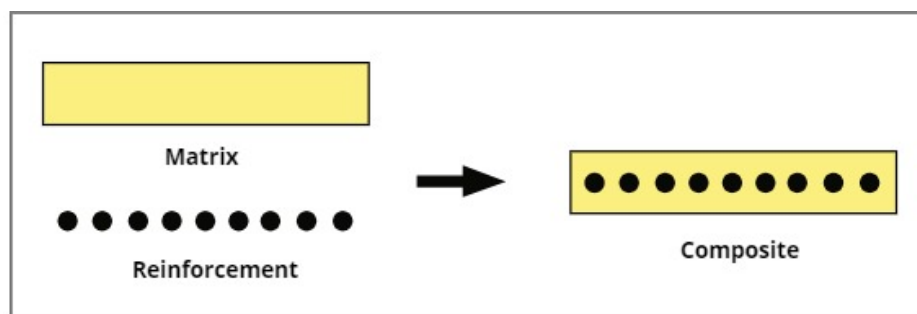


Figure 2.1 Constituents of a composite material.

Composites are used in industries such as aerospace or automotive, as they present relative low density compared to conventional materials such as metals (e.g., 7850 kg/m^3 for quenched and tempered low alloy steel vs. 1620 kg/m^3 for carbon fibre-epoxy unidirectional laminae with 60% volume fibre) [1]. Due to

their lower density, the specific properties of composites are superior, so that the weight of components can be reduced without affecting their performance.

Additionally, by a proper selection of the matrix, reinforcement and manufacturing process, the properties can be further tailored to meet the load requirements [18]. For example, when a continuous reinforcement is used, the properties can be optimised by varying the fibre orientation, as these structures present a high strength and stiffness but only along the fibre direction [19], [20]. Therefore, an effective use of the fibres depends on the correct alignment of the fibres with regards to the stress/strain direction [20].

Whilst different reinforcements can be used, only carbon fibre reinforcements are of interest in the current research. Different fibre forms can be selected such as chopped strands, tape, mat, or textiles such as braid, woven or non-crimp fabrics (Figure 2.2). The fibre forms present different properties, influencing the mechanical performance of the final component.

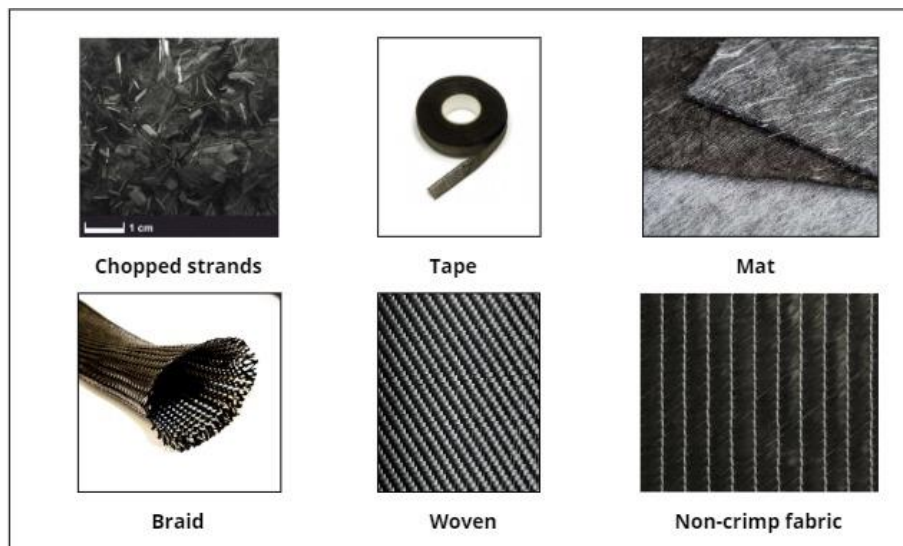


Figure 2.2. Examples of fibre forms.

Among composite reinforcements, textiles structures have gained popularity as they present unique properties such as easy handling and ability to form into complex shapes [13]. Additionally, by using modern, automated manufacturing techniques it is possible to manufacture large quantities at a reasonable cost [21].

The term 'textile' was originally reserved for woven fabrics, but now it has a broader meaning, applying to fibres, filaments and yarns [22]. Textiles could refer to threads, cords, ropes and braids: woven, knitted and non-woven fabrics, among others (see Figure 2.3).

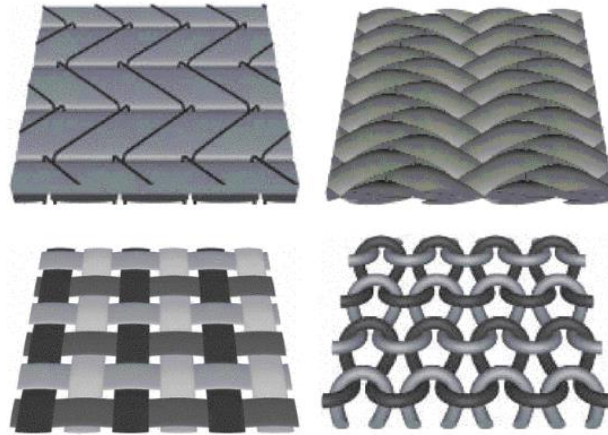


Figure 2.3. Different textile fabric structures: woven, non-crimp fabric, braided, knitted. Adapted from [23].

Textiles are fibrous materials, presenting fibre diameters from 5 μm to 50 μm . The fibres are gathered into yarns and fibrous plies, and then into textiles. An important feature of fabric structures is their hierarchical nature, also known as multi-scale. Three hierarchical levels can be distinguished (Figure 2.4) [22], [24], [25]. The scale of the woven unit, macroscopic scale (mm); the scale of the yarn, mesoscopic scale (10^{-1} mm); and the scale of the fibres, microscopic scale (μm).

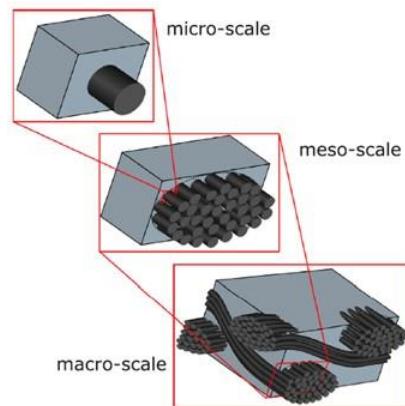


Figure 2.4. Schematic of the hierarchical nature of fabric structures [24].

Whilst there are various types of textile composite structures [22], woven and non-crimp fabrics (NCFs) are commonly used. A woven fabric consists of interlacing warp and weft yarns in a regular pattern and therefore exhibits crimp [26]. These small periodical misalignments are known as fibre undulations, which create variations in the local stress distribution [27], decreasing the in-plane mechanical performance of woven fabrics [14]. Different 2D weaving patterns can be used such as plain, twill or satin weave [22], which influence the drapability, handleability and structural properties of the woven fabric (see Figure 2.5). In the figure, the warp fibre runs top to bottom (red yarn), whilst the weft or fill runs right to left (blue yarn). The crimp effect can be observed on the thickness of the fabrics, plain weave has high level of crimp, whilst satin weave has low level.

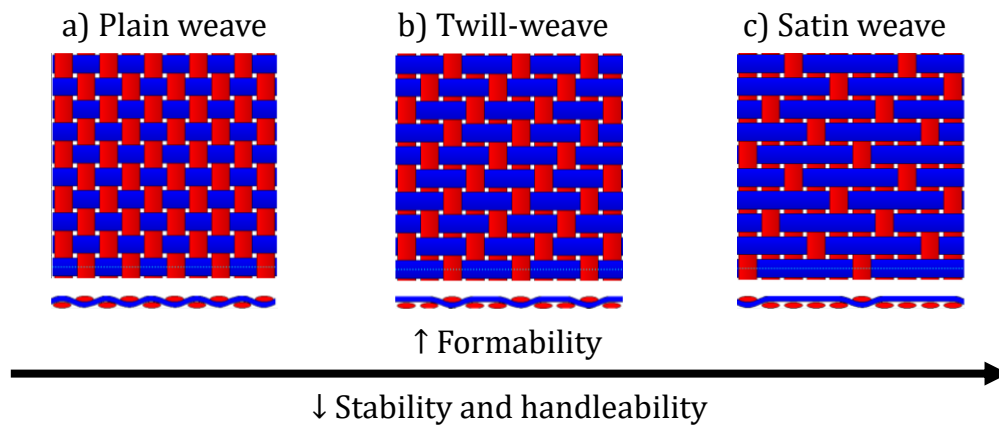


Figure 2.5. Typical yarn architectures of woven fabrics.

Compared to unidirectional reinforcements, woven composites present a higher damage tolerance, dimensional stability and are easier to manufacture due to their structural and handling properties [27]. Another advantage of woven fabrics compared to other textile structures, is that they can mimic double curved shapes due to their low shear resistance [26]. This is due to the angle variations between the warp and weft yarns which accommodate the fabric to the tool surface [28].

On the other hand, non-crimp fabrics, also known as stitched fabrics, consist of a stack of several differently oriented unidirectional plies that are stitched together, by sewing or knitting and/or bonding by chemical agents (Figure 2.6a) [22], [29]. This arrangement provides highly directed, straight fibres, aligned with the directions of interest. There are different stitch types such as pillar, tricot and plain (see Figure 2.6b) [30]. The stitching type affects various properties of the reinforcement, such as the handleability and drapability. The stitching improves the handleability of the layup, but it can influence the deformation behaviour, particularly with stitches outside the shear area having a greater impact than those within it [31].

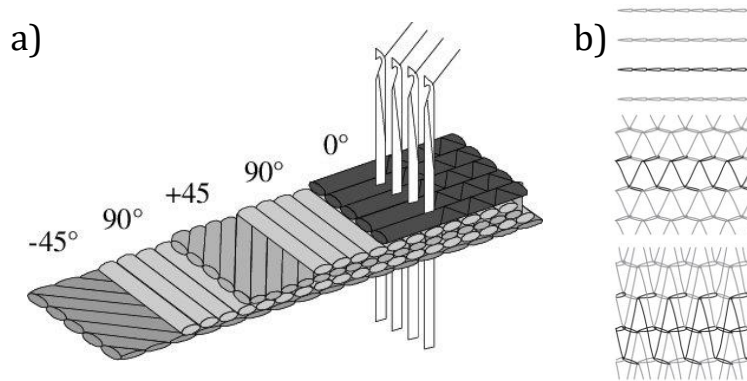


Figure 2.6. a) Architecture of a multi-axial non-crimp fabric [14]. Several plies are stack and then knitted together. b) Stitch types: pillar (up), tricot (middle) and plain (down) [30].

NCFs present several advantages when compared to woven fabrics. Firstly, as they present no crimp, NCFs provide enhanced mechanical properties, such as increased tensile strength [14], [16]. It is important to note that the stitches distort and crimp the fibres [32], however, this is to a lesser extent than the effect crimp produces on woven structures. Secondly, the stitches provide out-of-plane reinforcement [15], which means a better through-thickness properties and impact resistance. However, as a drawback, they are more difficult to form into 3D shapes [33]. The through-thickness stitching hinders the relative movements of the tows, affecting the shear performance and formability of the fabric [15]. This leads to a high resistance to positive shear when the material is sheared parallel to the stitches [34], [35], [36].

NCFs are relatively new to the field, which means that the use of woven fabrics is generally more extended, as more studies have been performed on them. Whilst there are different NCF architectures, biaxial NCFs are the focus in the current work. A biaxial NCF reinforcement consists of layers with parallel fibres at two orientations, typically at $0^\circ/90^\circ$ or $\pm 45^\circ$ (see Figure 2.7).

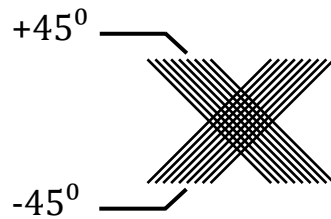


Figure 2.7. Schematic of the fibre directions of a biaxial ($+45^\circ/-45^\circ$) NCF reinforcement.

The main forming mechanism of a biaxial NCF when forming into 3D geometries is in-plane shear deformation [37]. For biaxial NCFs with pillar stitch, the shear behaviour is asymmetric, depending on the position and orientation of the stitches [38], [39]. This results in an asymmetrical draped shape, even when the NCF is formed into a symmetric geometry, such as a hemisphere [40]. The stitches experience positive or negative shear, which corresponds to the stitches being under tension or compression, respectively, as presented in Figure 2.8.

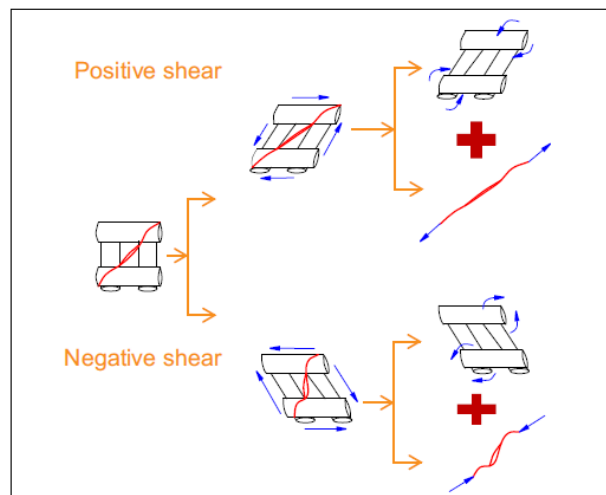


Figure 2.8. Schematic presenting the difference between positive and negative shear for a $0^\circ/90^\circ$ biaxial non-crimp fabric with pillar stitch at 45° [33].

Chen et al. [33], [41] explained that the stitches significantly influence shear resistance, particularly under positive shear, where the shear resistance is dominated by the tensile properties of the stitch. However, the stitches can fail at high strains induced by large shear angles, causing irreversible damage and a significant reduction in shear resistance. When the stitches are under negative shear, the NCF exhibits similar behaviour to a woven fabric, where friction between the yarns becomes the primary source of in-plane shear resistance.

2.2 Fabric forming and pre-forming processes

The previous section introduced composites textiles and their hierarchical nature, focussing on the description of textile structures, in particular woven and non-crimp fabrics. Textile structures are of interest since they exhibit a specific mechanical behaviour due to the relative motions that are possible between yarns and fibres [42]. Preforming takes advantage of these motions to mimic the desired shape. This section focusses on describing different forming and preforming techniques that can be used to produce composite structures.

Prepreg materials were generally used, which require autoclave processing, due to their need for high temperature and pressure to cure the final component. Currently, there is a shifting towards lower energy processes such as liquid composite moulding, which uses dry composite materials [43]. This type of process requires several steps such as preforming, impregnation, consolidation and curing to obtain the final component. Separating the manufacturing process in several steps can help reducing the complexity of the process, increasing the quality of the final product [29].

The preforming step consists of transforming a 2D blank into a 3D complex shape. The fibre orientations and geometry obtained from this stage significantly impact the resin injection, and mechanical properties of the final component [9]. Therefore, choosing the right forming process is important, since it influences production costs and the quality of the final component [44]. A variety of

processes can be used to form composite structures such as hand layup, matched tool forming, or diaphragm forming, among others.

2.2.1 Hand layup

Hand layup is the most common forming method. It is divided into two methods: wet layup and prepreg layup. In the case of wet layup, the resin is applied to the mould, using rollers or brushes to impregnate the reinforcement, while the prepregs are already saturated [45]. The reinforcement is cut using a template, and individual layers are draped manually over the contour of the tool to achieve the desired thickness [46]. Different grips and manipulations are used to adapt the material to the tool (see Figure 2.9) [47]. Figure 2.9a) shows how both hands are used to shear the prepreg, applying tension in opposing directions, whilst Figure 2.9b) shows how the prepreg is pushed into a recess on the tool [47]. Therefore, the quality of the component highly depends on the skills of the operator, and the process is time consuming, taking several hours to lay up complex forms [48].

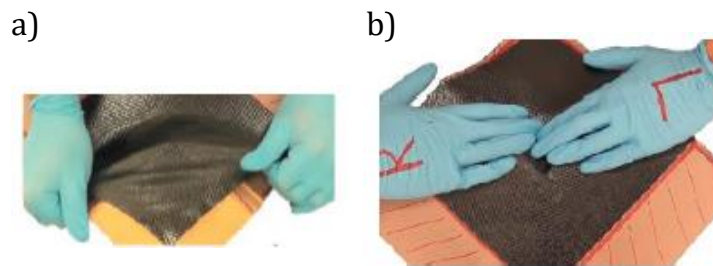


Figure 2.9. Example of prepreg layup draping techniques [47].

The parts can be cured using several methods [43]. The simpler method is to cure them at room temperature, the curing can be accelerated using temperature and vacuum with an oven. However, for high-performance components, temperature and high consolidation pressure is required, these conditions are achieved using an autoclave. When pressure and temperature is needed, the tool is more expensive, due to the material requirements. The final component presents only one finished surface, which is the one in contact with the tool [49].

Even though this process requires highly skilled operators, and the costs can be high, the ability of producing high-performance and complex shapes makes this process popular for low-volume applications [8].

2.2.2 Matched tool forming

The matched tool forming (MTF) process, also known as press forming or hot drape, consist of forming a heated and pre-consolidated laminate using a male and female mould (see Figure 2.10) [50]. Heat would be required for binder activation when dry performed are used. This process allows the use of high pressure, reducing any local changes in thickness preventing bridging [51]. Additionally, a high surface finished on both surfaces can be achieved [52].

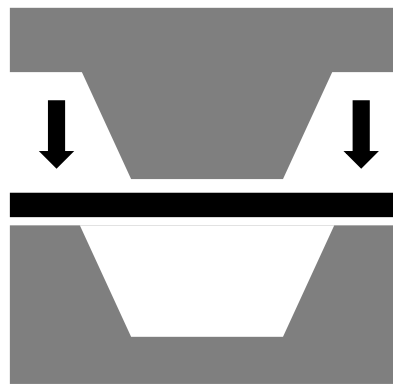


Figure 2.10. Matched tooling forming process.

To produce high-quality parts, the spacing between the two moulds must be of close tolerance [50]. This close tolerance makes the mould production expensive. Different materials can be used for the moulds; however, steel offers better control over the dimensions of the part and improved surface finish and durability [52], making the process suitable for mass production [50].

This process allows for high-rate manufacturing and high consistency. However, the size of the component is limited by the dimensions of the equipment and the process is limited to simple parts [45].

2.2.3 Diaphragm forming process

The diaphragm forming process has the potential for automating the production of low cost preforms for high-volume applications, such as automotive or aerospace components, as it requires lower capital investment than matched tool forming [53]. Compared to other forming process, better control of fibre placement is provided, although at expenses of longer cycle times when heating is used to melt the binder [54].

The diaphragm material controls the forming process, with its stiffness being critical to obtain a good quality part. Additionally, the deformation modes and defects also depend on the material type [55]. For simple shapes, compliant materials are preferred, while for complex shapes, stiffer diaphragms are used [45]. Polymer materials are usually used, but the material selection is usually limited by the commercial availability of the desired properties [55].

The diaphragm forming processes are divided in two methods, depending on the number of diaphragms encapsulating the composite reinforcement (see Figure 2.11) [53]:

- Single diaphragm forming (SDF).
- Double diaphragm forming (DDF).

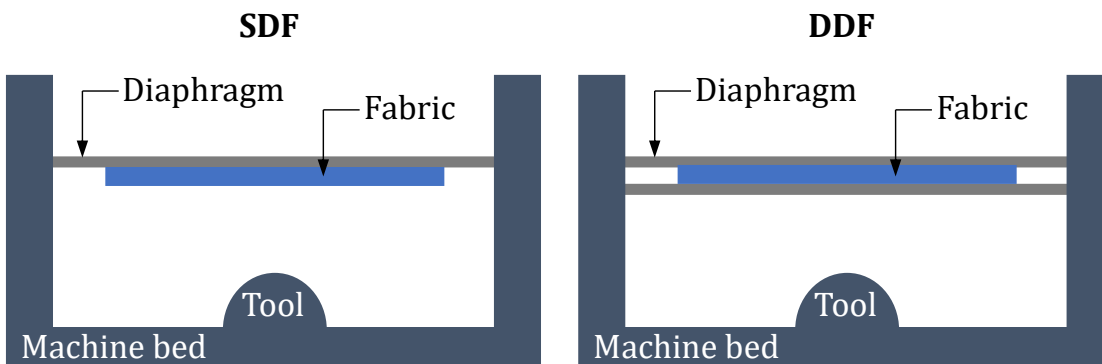


Figure 2.11. Schematic of the single diaphragm forming vs double diaphragm forming.

When comparing both processes, the DDF process provides membrane tension to the laminate, reducing wrinkling and allowing multiple plies to be

formed [56]. On the other hand, the SDF process provides more flexibility, since there is no lower diaphragm contacting the tool to constrain the stack, which can increase variability, especially for complex geometries [53].

The number of diaphragms also affects the surface quality of the forming component. DDF provides a good quality surface for both sides in contact with the diaphragm, whilst SDF provides only a one-side quality surface, the one in contact with the diaphragm [44].

The DDF process is the focus of this research work, this process is compatible with both dry and prepreg materials [56]. Figure 2.12 presents a schematic of the process, which can be divided in four stages:

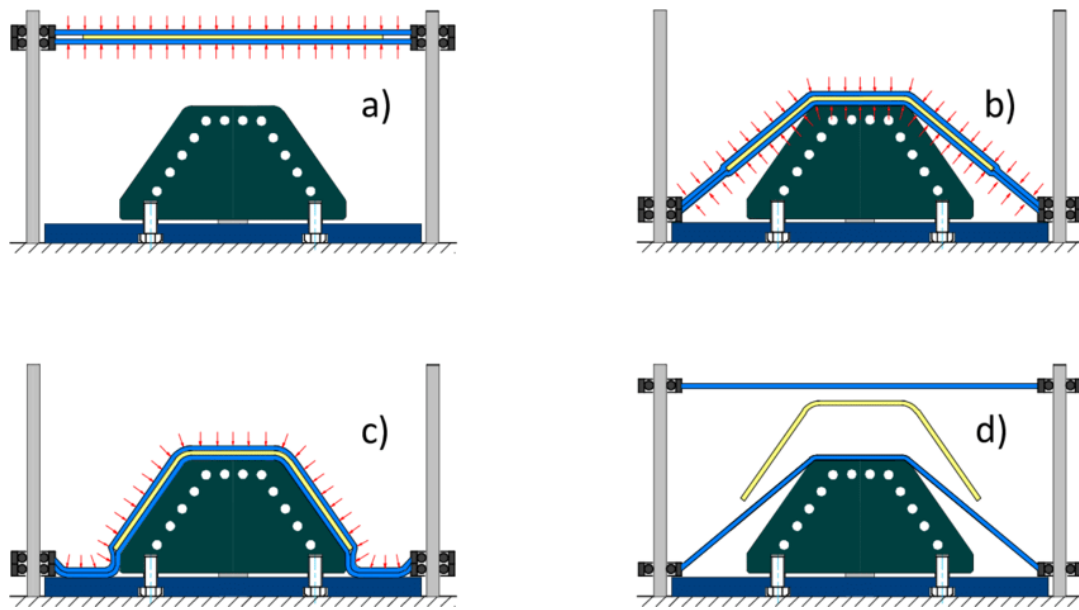


Figure 2.12. Schematic of the different stages of the double diaphragm forming process [51].

- a) The laminate, with or without binder, is placed between the upper and lower diaphragms. Vacuum is applied between the diaphragms to clamp the material. Since only the edges of the diaphragms are clamped, the laminate can slip creating interfacial tensile stress that reduces the wrinkling on the part [50].

- b) If using a binder, the diaphragm arrangement is raised towards the infrared heaters to melt the binder [56]. The frame is moved against the tool surface.
- c) A second vacuum is applied between the lower diaphragm and the tool surface to evacuate any air between them, causing the laminate to adapt to the desired shape.
- d) Lastly, once forming is completed, both vacuums are released, allowing the retrieval of the preform.

Extensive research has been conducted on the diaphragm forming processes using NCFs. Martin et al. [57] focussed on the internal evolution of wrinkling occurring in SDF. The experiments were performed using six NCF plies. The results indicate that the majority of the diaphragm movement and changes in wrinkle size, shape, and location occur during the initial application of vacuum. As vacuum continues to be applied, consolidation takes place, leading to a reduction in wrinkle size while their shape and location remain unchanged.

Chen et al. [51] focussed on characterising a biaxial NCF and the diaphragm material to simulate the DDF process. The experiments were performed using two plies of FCIM359 biaxial NCF. The focus of the work was on predicting and characterising defects using local shear angle, axial compressive strain and axial tensile stress. The results show that bridging, the dominant defect in DDF, can occur in large curvature regions. Wrinkling is generally reduced when compared to MTF due to the relatively low forming pressures.

Viisainen et al. [58] characterised the variability in the wrinkling behaviour during the DDF process. The experiments were performed using one and two plies of different NCF. The results showed that the fabric architecture and lay-up significantly influence both wrinkling amplitude and location. Forming single biaxial NCF is shown to be statistically less variable than forming two layers.

Codolini et al. [59] focussed on determining the critical process variables affecting the DDF process. The experiments were performed using two plies of FCIM359 biaxial NCF. The focus of the work was on evaluating the effect of vacuum pressure, diaphragm tension, ply-tool alignment and geometrical features on wrinkling formation. The results show that pre-tensioning the diaphragm before forming has the most effect on variability in the wrinkling amplitude. Variability in the friction coefficient between fabric plies also has a significant contribution to the amplitude. With regards to tool geometry, geometries with higher asymmetry or Gaussian curve are less susceptible to changes in the process variables when compared to those with larger angularity or conicity.

Most experimental studies to date have focussed on forming NCF multi-ply layups, while the forming behaviour of individual plies has received little attention. This gap in the literature presents an opportunity for innovation by preforming plies separately before stacking and forming them as a layup. This approach has not yet been explored, but it could lead to new strategies for optimising the forming process and improving the quality of the preforms. This thesis addresses this gap by examining the forming behaviour of single plies and evaluating the potential benefits of this two-step forming approach.

Another unexplored approach in DDF is the simultaneous forming of multiple preforms at the same time. Investigating this concept could offer valuable insights into improving the efficiency and sustainability of the process. Despite its potential advantages, this strategy has not been discussed in the literature. This thesis addresses this gap by examining the interactions between fabrics during the process and assessing the potential benefits of this approach.

In experimental forming, a breather material is essential for releasing trapped air. However, existing studies do not report the use of breather or specify its arrangement. This gap in the literature highlights the need for focussed

research to understand the role of the breather in the forming process. This thesis addresses this gap by investigating different breather arrangements and evaluating its impact on forming behaviour and defect formation.

Lastly, the influence of the diaphragm on the forming process has not been thoroughly studied, particularly regarding the effects of diaphragm size and strain distribution on the forming. This lack of detailed investigation presents an opportunity for further research into optimising diaphragm parameters. This thesis addresses this gap by examining the impact of diaphragm size and strain distribution on forming behaviour and defect formation.

2.3 Forming mechanisms

The previous section described different forming and preforming techniques that can be used to produce composite components. Different deformation mechanisms affect the mechanical properties and behaviour of the material during the forming process, which are critical to achieve the desired shape [60]. This section focusses on describing the different deformation mechanisms affecting textile composite structures, particularly biaxial non-crimp fabrics.

For textiles, the mechanical properties are defined by their fibrous structures. Due to the absence of matrix material, textiles lack internal cohesion, allowing for relative slippage between the fibres [61]. Additionally, since textiles present a relatively low compaction, bending and shear rigidities are lower compared to their tensile stiffness, which makes forming textiles easier compared to other composite forms [9].

The main deformation mechanisms affecting textiles are in-plane shear, also known as intra-ply, in-plane tension, and out-of-plane-bending [34], [37]. While friction is not a deformation mechanism in itself, it significantly influences these deformation mechanisms during forming. Additionally, inter-ply sliding is

relevant to non-crimp fabrics, where the stitches act as weak bonds between the fibres, affecting the deformation behaviour [29], [62].

2.3.1 In-plane shear

During in-plane shear, there is a rotation and slipping of the yarns, followed by a compaction of the intersecting yarns [34]. In-plane shear is the most important deformation mode for a preform, as the fibres in the NCFs are quasi-inextensible [36]. As a result, forming over double curved shapes can only be achieved by in-plane shear [42], [63], which allows the fibres to reorient without stretching.

Figure 2.13 presents the characteristic shear behaviour for a biaxial NCF. The shear behaviour is asymmetric, as it depends on the position and orientation of the stitches [38], [39]. The shear resistance is generally higher as the stitches are loaded in tension, which corresponds to positive shear. When the stitches are loaded in compression, which corresponds to negative shear, the tows can rotate, so that the material presents a lower shear resistance [36]. Therefore, the shear behaviour should be characterised in both directions to account for both behaviours.

Figure 2.13 shows that when the stitches are loaded in tension, the shear force increases linearly until the stitches start to fail. The shear then drops significantly as the failure progresses but increases again due to lateral yarn compaction at larger shear angles. When the stitches are loaded in compression, the curve is similar to that of a woven material, and the shear resistance is primarily caused by inter-yarn friction and compaction.

As the fabric shears, a critical shear angle is reached, known as the locking angle. This parameter represents the maximum level of shear deformation that can be achieved before a fabric wrinkles [37], [64]. This parameter is explored in greater depth in the following sections.

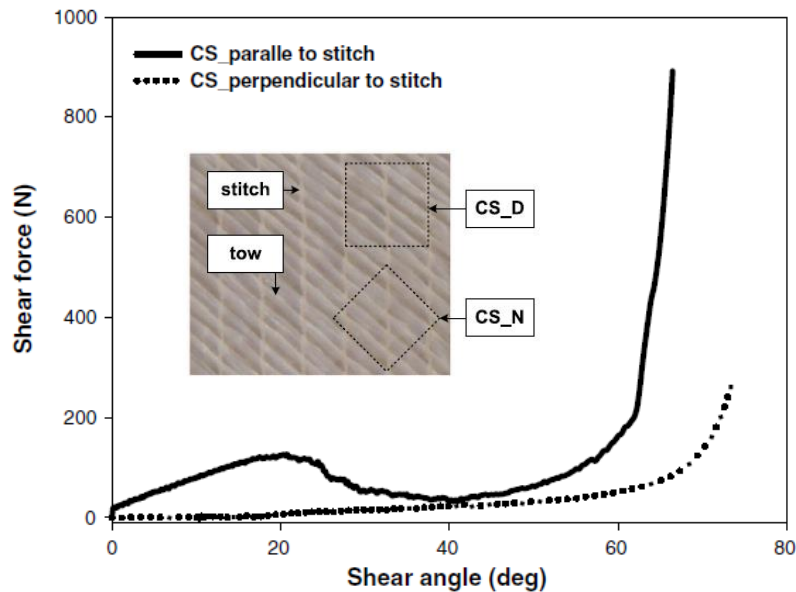


Figure 2.13. Shear force vs shear angle of a NCF with chain/pillar stitch [40].

2.3.2 In-plane tension

In-plane tension is an extension parallel to the direction of the tows [34], leading to a redistribution and elongation of the yarns. NCFs exhibit a relatively linear behaviour, since the fibres remain parallel to the plane of the fabric [37]. Dry reinforcements present a very low resistance to compressive stress, therefore, when a compressive load is applied in the fibre direction, the fibres buckle [47].

The tensile stiffness in the fibre direction is higher than the stiffness associated with other deformation modes. This behaviour accounts for the majority of energy dissipation during forming and should not be neglected [65]. Additionally, areas of high tensile stress are often associated with fabric bridging, particularly in complex tool geometries [51].

For NCFs the fibres are almost straight and not interlaced, they are linked by the stitching [66]. Figure 2.14 presents the characteristic tensile behaviour for two NCFs with different stitch pattern. The tensile behaviour was found to be non-linear at the beginning of the tensile test, likely due to the initial waviness or misalignment, which requires pre-straightening before the fibres can take the full

tensile load. This non-linearity occurs only in the initial phase of the test, after which the material behaviour becomes linear. In forming simulations, to improve computational efficiency, the axial modulus is assumed to be linear. Since the non-linearity is limited to the initial settlement, this assumption does not compromise the accuracy of the results [65].

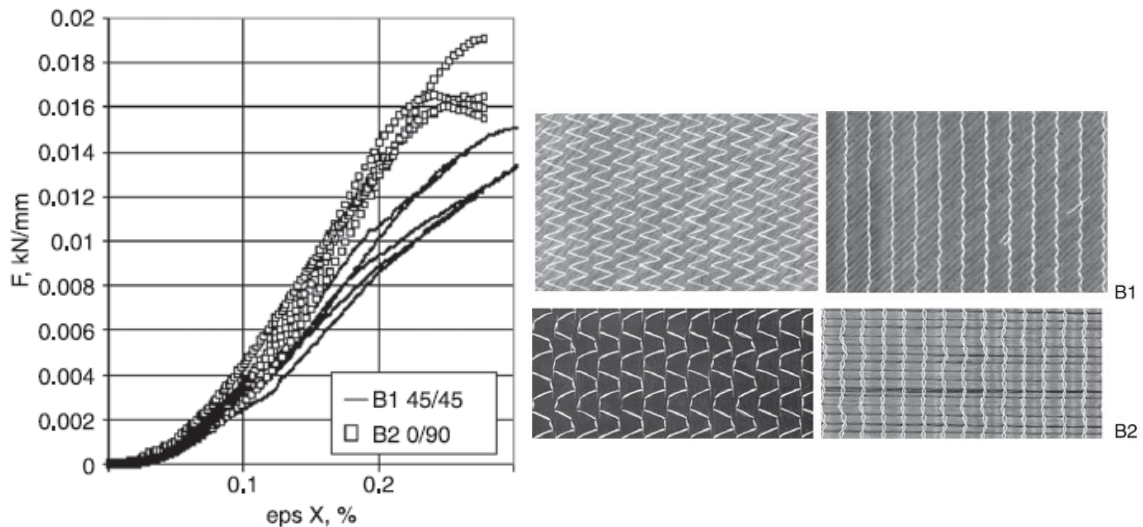


Figure 2.14. Tensile behaviour of two non-crimp fabrics with different stitch patterns [66].

2.3.3 Out-of-plane bending

Out-of-plane bending is the ability of a fabric to bend out of plane [34]. This deformation is another crucial phenomenon for the forming, as it allows forming over double curved shapes without damaging the fibres [61].

The bending stiffness of fabrics is relatively low, as the fibres can slide relative to each other [67], for that reason it was initially overlooked [34], [37]. However, it has been proved that bending is important to obtain accurate wrinkling predictions [42], [68], as the number and size of wrinkles depend on the bending stiffness [61].

The bending behaviour for biaxial NCFs depends on the material orientation [68], and it also depends on the bending direction due to the asymmetric fibre architecture in the thickness direction [69]. Figure 2.15 presents the

characteristic bending behaviour for NCFs. The material presents a linear bending behaviour where the fabrics tend to show a larger bending stiffness under small bending deformation, with the behaviour turning non-linear and the bending stiffness decreasing as the curvature increases, due to slippage and buckling of the fibres [70].

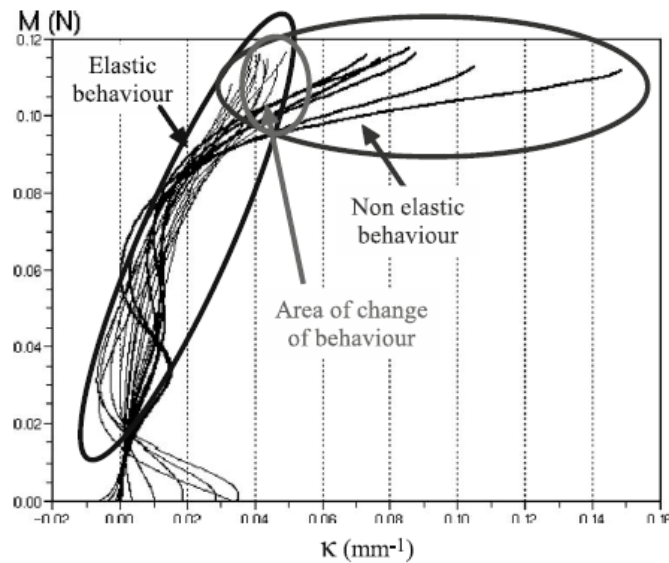


Figure 2.15. Bending moment per specimen width vs curvature along the sample profiles [70].

2.3.4 Friction

Friction plays a significant role during the composite forming process. The constraints imposed by the interaction between plies and ply-tool affect the deformation during the forming process [71]. The ply-tool friction influences the transfer of loads during the forming process [34]. Friction depends on parameters such as pressure or sliding velocity, as well as on the properties of the materials involved [71], [72].

In multi-layer forming, the friction between individual plies is also significant, especially when the plies present different orientations. As the stack undergoes forming, individual plies move relative to each other, as no deformation can occur parallel to the fibre deformation [73]. This relative movement can lead to defects such as wrinkling, fibre buckling and bridging [72]. Additionally, the friction

between the tool and the first ply of the stack can generate a wrinkle [74]. Therefore, understanding the friction behaviour is essential for achieving the desired quality of the formed component. One approach to improve the formability of plies over complex surfaces is to control inter-ply sliding by reducing the coefficient of friction [75].

Lawrence et al. [72] evaluated the inter-ply friction during DDF of biaxial NCFs. In this case, both fabrics present the same relative fibre angle, but the loading direction varies relative to the fibres. Figure 2.16 presents the effect of the slip direction on the static and dynamic inter-ply coefficients of friction.

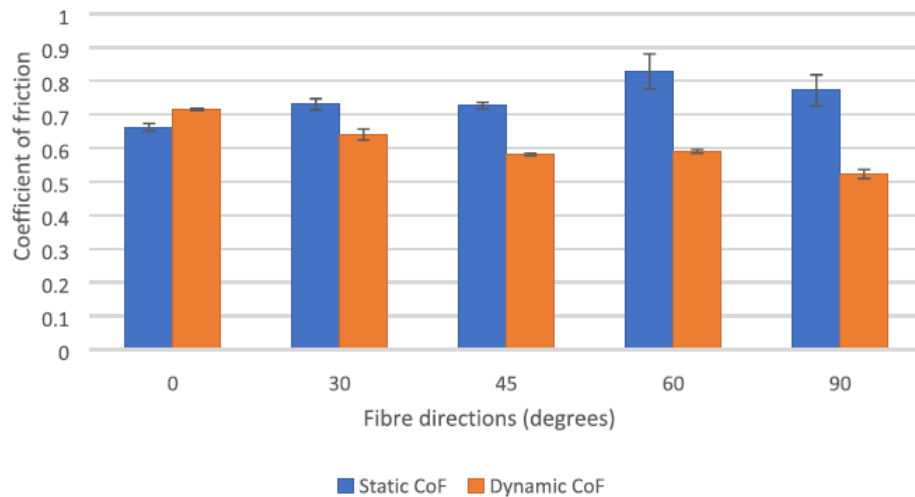


Figure 2.16. Static and dynamic coefficients of friction when varying the slip direction [72].

Increasing the angle between the fibre orientation and the slip direction decreases the dynamic coefficient of friction and increases the static coefficient of friction. For a fibre orientation perpendicular to the slip direction, the fibres must roll over each other. This creates a large initial resistance to motion, leading to a higher static coefficient of friction. For the parallel case, the fibres are not able to nest effectively, this reduces the contact area between plies reducing the dynamic coefficient of friction. These results indicate that the fabric-fabric friction behaviour is anisotropic, producing higher dynamic coefficients for parallel fibres, as the nesting is highly dependent on fibre orientation.

2.4 Forming related defects

The previous section detailed the different deformation mechanisms affecting biaxial non-crimp fabrics. Understanding the material behaviours is essential for achieving the desired quality of the formed components. This section describes the different defects that could affect the preform. Defects can arise as a result of the large deformations during forming due to constraints or the nature of the material [76].

The performance of the final component is affected by any defects introduced on the structure during the manufacturing process or in-service [36]. The strength of the fibres is located primarily along the longitudinal direction, and to effectively distribute the loads, the fibres need to be aligned with the applied load [19]. This makes the strength of the component highly dependent on the fibre direction.

The manufacturing defects commonly affecting textile structures are listed below and can be found in Figure 2.17 [77]. These defects can occur during the forming process if the preform is not reasonably constrained or if the forming deformation is beyond a certain limit [9].

- Through-thickness or out-of-plane defects: wrinkles, folds, thickness variations.
- In-plane defects: waves, tearing, bunching or spreading.

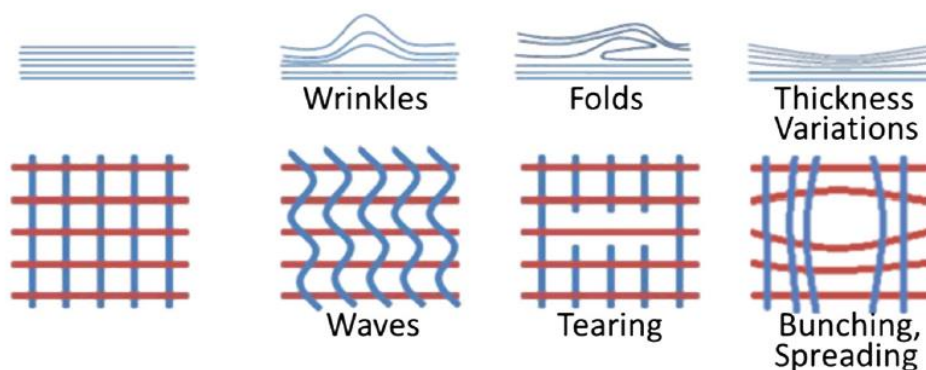


Figure 2.17. Out-of-plane and in-plane defects commonly affecting textile structures [77].

Yarn bunching or spreading is a type of fibre slippage, which leads to areas with no fibre reinforcement. These can cause resin-rich areas in the final component, creating initiation and propagation paths for internal crack propagation during matrix failure [78], [79]. Additionally, as composite materials rely on the fibres to withstand the load and on the matrix to efficiently transfer loads between the fibres, resin-rich areas weaken the structure by reducing the strength and stiffness of the component. Resin rich areas should be prevented as the flexural strength drops more than 25%, due to the fibre misalignment associated with the area [80].

From the defects mentioned above, fibre waviness is the most common defect affecting textile structures [81]. Fibre waviness is considered the most critical defect, as it dramatically affects the load carrying capacity, leading to a severe knockdown on the mechanical properties of the final component [82]. Fibre waviness can be described as a deformation that exhibits a wave-like pattern (see Figure 2.18) [83]. It can be classified into two categories [84]:

- Out-of-plane waviness (wrinkles), also known as out-of-plane wrinkling or wrinkling, where the plies in the laminate are misaligned in the thickness direction.
- In-plane waviness (waves), also known as in-plane buckling, where the fibres within a ply are misaligned.

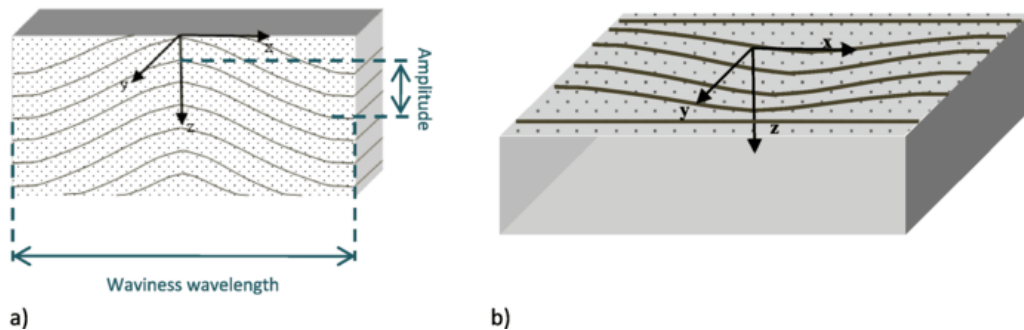


Figure 2.18. Schematic diagram of a) out-of-plane waviness and b) in-plane waviness [83].

Wrinkling occurs when less energy is required for an out-of-plane deformation than for an in-plane deformation [85]. When considering textile structures, it is important to understand that some inherent features of these structures contribute to the formation of fibre waviness. For NCFs, in-plane waviness is due to the effect of stitches or binder yarns [86], [87], whilst out-of-plane waviness is produced from a combination of the stitches and compaction during the forming process [87]. Additionally, biaxial NCFs are more likely to suffer from wrinkling on the positive shear area than on the negative [41]. Wrinkling could be mitigated by preventing the stitches to be parallel to the shear direction and by preventing sharp corners [58].

The geometry of the component affects the severity of the wrinkles; however, the wrinkling mechanisms depend on the particular fabric and not the geometry [58]. J. Krebs et al [88] explored the effect of the tool design on the drapability of the material. The behaviour of the material was investigated for male and female tooling. For a male tool, the diaphragm arrangement first contacts the highest tool point, this generates tension, stretching the diaphragms. This leads to compressive stress, leading to out-of-plane buckling or wrinkling. On the other hand, a female tool initially contacts the flat region around the cavity, creating a frictional force affecting the tension in the preform. This prevents the compressive stress but can lead to fabric bridging.

Thor et al. [86] found that the formation of waviness depends on the frictional behaviour between the plies. Therefore, in multi-layer forming the wrinkle severity is amplified as each layer tries to deform independently to accommodate the change in shape [89]. For example, Hallander et al. [90] were only able to prevent wrinkling by avoiding $[0^0/45^0]$ interfaces. Additionally, wrinkling is most likely to start in the ply with the least stiffness in the load direction.

Shear also affects wrinkling formation. Turk et al. [15] observed that excessive shearing frequently results in the formation of unwanted features such

as wrinkling. Additionally, the shear behaviour is an underlying mechanism behind fibre re-orientation, affecting the load carrying capacity of the final component. Similarly, Thor et al. [86] stated that wrinkling can occur when the shear needed to accommodate the material to the geometry is too high.

On the other hand, Viisainen et al. [58] stated that macroscale wrinkling cannot only be produced by excessive shear but also due to lateral fabric compression when the fabric is prevented from shearing due to the tow architecture or stitch pattern. The macroscale non-shear wrinkles for the NCF under study were shown to be severe and occurring in more critical locations. Additionally, the component geometry affects the severity of the wrinkles. However, the wrinkling mechanisms are dependent on the particular fabric and not the geometry

Similarly, Lee et al. [40] observed that most of the wrinkles are generated where large shear deformation occurs. However, some parts of the material present buckling even for small shear angles. Boisse et al. [91] also found regions with wrinkling where the shear angle was below the locking angle. This could only happen if more mechanisms are involved in wrinkling occurrence.

Boisse et al. [61] considered the effect of bending stiffness on the number and size of wrinkles in textile composites. The authors demonstrated that increasing the bending stiffness increases the size of wrinkles. Additionally, for double-curved shapes, the wrinkle onset does not only depend on the shear locking angle, but the strain energies also influence the process. Therefore, wrinkling could appear even for angles below the shear locking angle. This means that the appearance of wrinkles is driven by a coupling between shear, tension and bending behaviours [85]. Therefore, one property by itself is not enough to determine the deformation mechanism during preforming.

In-plane fibre buckling, and out-of-plane fibre wrinkling are the most common defects in NCFs, but fibre pull-out, stitch thread failure and inter-layer sliding have also been reported [33].

2.4.1 Defects specific to DDF

Defects caused during DDF are different to those appearing during matched tool forming, as the DDF constrains the material movement less than matched tool forming [92]. Wrinkling and bridging are more likely to occur due to this lack of out-of-plane constraint to the stack (see Figure 2.19) [55], [93]. Another defect affecting NCF structure is stitch damage, but it might not be critical if the primary yarns are not affected [94].

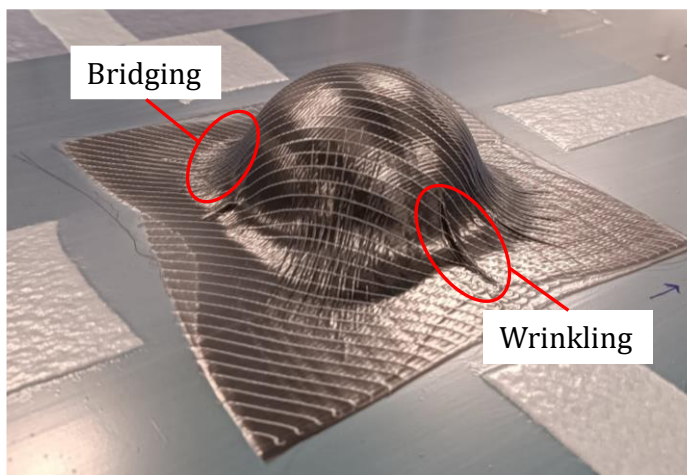


Figure 2.19. Example of bridging and wrinkling during the DDF process.

Wrinkling has been extensively described in section 2.4. Bridging can occur due to insufficient slippage between the diaphragm and the tool. Bridging is caused by excessive friction preventing the material to draw-in [94]. This defect depends on the tool geometry and can occur in areas with low shear deformation, especially at deep concave regions [41].

2.5 Material characterisation

The previous section described the different defects that could affect the quality of the preform. Characterising the formability of materials under

controlled circumstances is important to understand the mechanisms that influence the formation of defects during draping [95]. This accurate description can also be included in the material model to improve the accuracy of the predictions [34], [96].

This section focusses on describing the different tests that can be used to characterise the in-plane shear, in-plane tension, out-of-plane bending, and friction behaviours detailed in section 2.3. Non-standard tests methods are used to characterise the mechanical properties, and therefore, many researchers develop their own methodology [97].

2.5.1 In-plane shear tests

The objective of the in-plane shear tests is to characterise the non-linear mechanical response of the material during shear deformation. For dry biaxial fabrics, the bias extension test (BET) and picture frame test (PFT) are typically used to characterise this behaviour. For biaxial $\pm 45^\circ$ NCFs with pillar stitch, the results depend on the stitch pattern, therefore, tests must be performed with the stitches in tension and compression to fully characterise the asymmetric shear behaviour [39], [40], [98].

An important parameter related to the shear behaviour is the locking angle. This angle quantifies the shear angle limit after which wrinkling appears [99]. This behaviour arises from the rotating tows restricting further shear [100], so that the material has to wrinkle out-of-plane to accommodate the deformation. Even though both tests can be used to estimate the shear locking, BET is a quicker and reliable test [101].

During both tests, the axial forces required to deform the sample are recorded. The shear angle, defined as the angle variation between the fibres of two plies, can be calculated using the crosshead displacement [34]. In order to compare the results from both tests, the measurements must be normalised to

remove the effect of the sample size. This must be done using the side length instead of the area [101]. However, for the PFT, the shear angle calculations using the cross head displacement are only accurate until 30° - 35° , and optical methods should be used after this value [99].

The bias extension test consists of a rectangular piece of material clamped at 45° to the direction of the applied load (see Figure 2.20). To obtain a pure shear zone in the centre of the sample, zone A, the initial length of the sample needs to be more than twice the width of the sample [97]. The shear angle in zone A, which is free at both ends, is assumed to be twice that in zone B, whilst zone C remains undeformed assuming that the yarns are inextensible, and no slip occurs in the sample [38]. It is also assumed that the in-plane shear is constant in each zone. Another assumption is that the bending stiffness of the yarns is negligible [99].

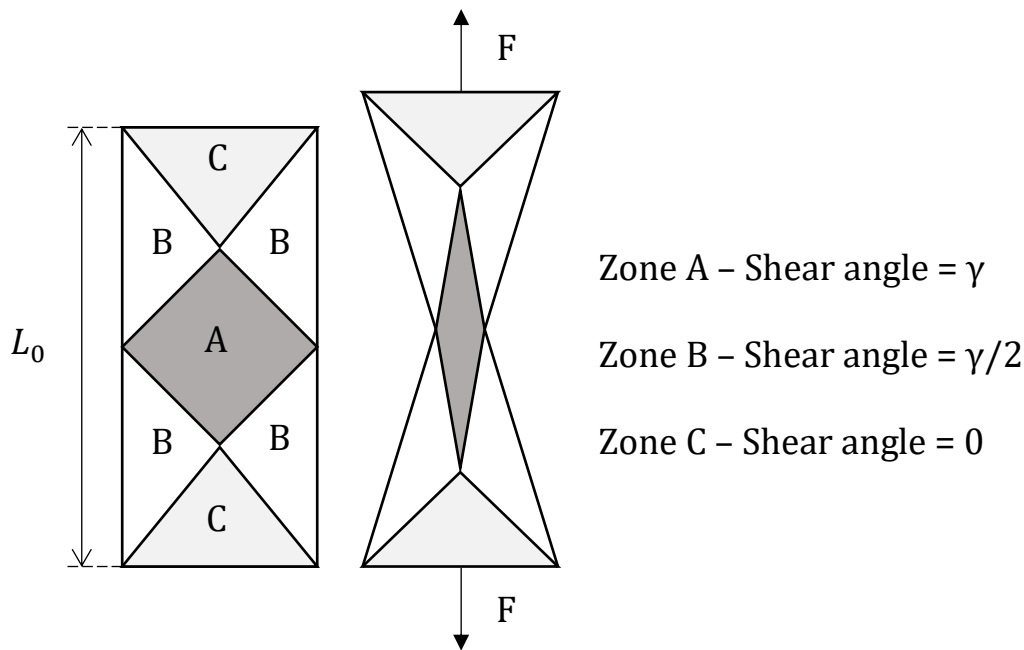


Figure 2.20. Schematic of the bias extension test and the different shear zones.

Alsayednoor et al. [102] investigated the two sources of error that can affect the accuracy of the BET: pre-shearing and out-of-plane wrinkling [102]. A few degrees of pre-shear are difficult to avoid when mounting the sample in the test machine, which depends on the care employed on mounting the sample. Useful

data is obtained for a pre-shear angle below 0.5° with a standard deviation of the initial pre-shearing below 2° . Out-of-plane wrinkling appears in the later stages of the test, with larger specimens wrinkling at lower shear angles and more severely. Wrinkling tends to appear at the centre of the specimen, where the shear measurements are performed. This can be mitigated by using a 3D digital image correlation equipment to measure the shear angle in-situ even in the presence of this defect.

Bel et al. [38] performed bias extension testing on NCF samples. The authors observed that the shear angle experimental values are lower than the theoretical ones, meaning that sliding occurs during the experiments. However, when using optical measurements, it was found that the assumption is acceptable in the central area, where the shear is constant, with sliding localised at the borders between the different shear areas. These results indicate that BET might not be ideal to characterise the shear behaviour of NCFs.

Similarly, Boisse et al. [99] observed sliding between the plies, concluding that the shear should be measured by two synchronised cameras, as the non-slippage assumption is not verified. These studies indicate that optical equipment might be necessary to assess the shear of NCFs. Bel et al. [62] suggested that this test can be used to characterise the sliding between layers using the difference between pure shear deformation and the deformation measured, as that difference arises from sliding.

The picture frame test consists of cruciform shaped fabric clamped to the frame with four rigid bars of equal length to prevent slippage (see Figure 2.21) [97]. One corner is pinned whilst the opposite corner is displaced, causing the frame to deform from a square to a rhombus. The specimen is subjected to pure and constant in-plane shear strain [99]. When mounting the samples, it must be ensured that the fibres are perfectly aligned with the edges of the frame [34]. Several runs of the test without a specimen loaded are required to obtain the

crosshead force to balance the weight and inertia of the frame during the test [62]. This force should be deducted from the crosshead forces recorded with samples loaded to calculate the shear force.

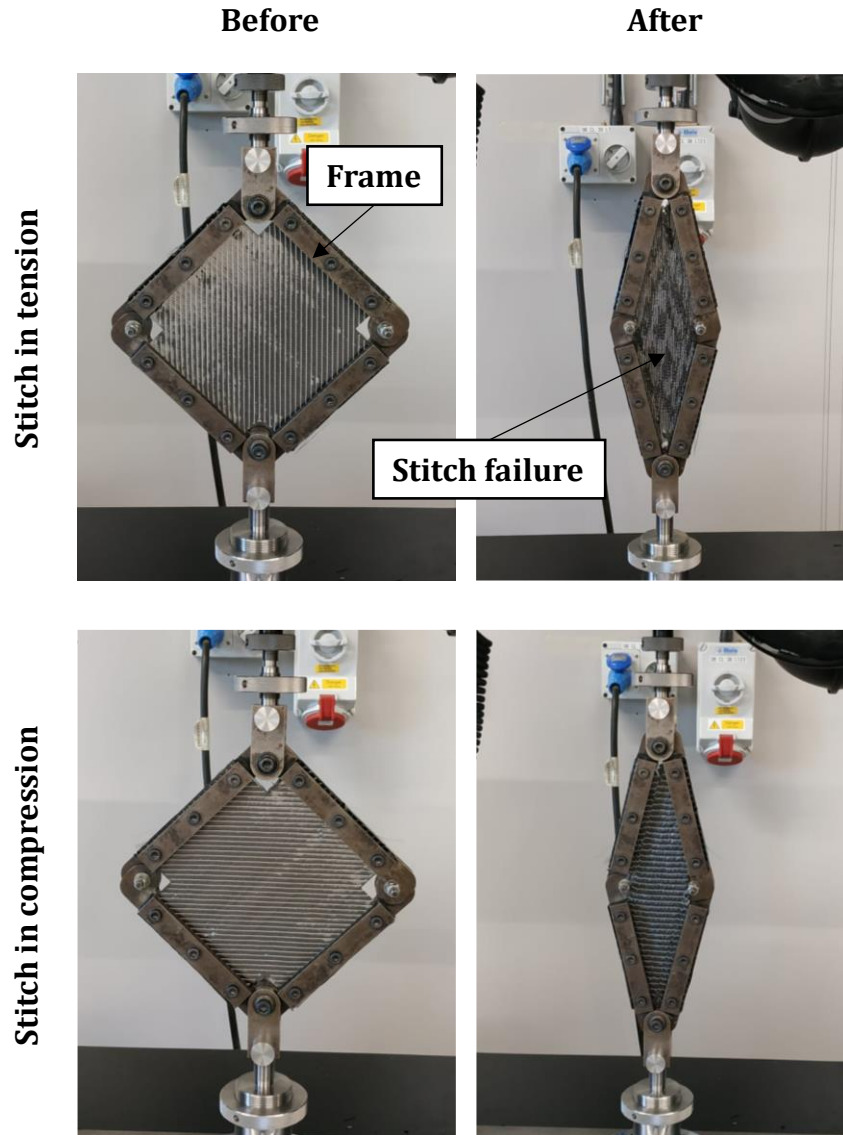


Figure 2.21. Picture frame test for a NCF sample with the stitches in tension and compression.

The PFT is simple, and the results are repeatable, as the deformation is homogeneous through the sample. The shear force and shear angle can be calculated following the equations in Cao et al. [97]. The shear angle, γ , is calculated from the geometry of the picture frame as:

$$\gamma = 90^\circ - 2\theta \quad (1)$$

Where θ is the angle of the frame (in degrees), calculated as:

$$\cos \theta = \frac{\sqrt{2}L_{frame} + d}{2 \cdot L_{frame}} \quad (2)$$

Where L_{frame} is the length of the frame and d is the extension/vertical displacement of the frame during the test. The shear force, F_s , can be calculated as:

$$F_s = \frac{F}{2 \cos \theta} = \frac{F'' - F'}{2 \cos \theta} \quad (3)$$

Where F is the load without the frame effect, θ is the angle of the frame, F'' is the load of the current experiment with the sample under study, and F' is the force of the experiment with an empty frame. The normalised force, F_{norm} , where the influence of the frame and fabric size is removed, can be calculated as:

$$F_{norm} = F_s \cdot \frac{L_{frame}}{L_{fabric}^2} \quad (4)$$

Where L_{frame} is the length of the frame and L_{fabric} is the length of the side of the cruciform fabric. This F_{norm} allows the results from different PFTs, where L_{frame} and L_{fabric} have different sizes, to be compared.

Two issues regarding PFT are identified by Krogh et al. [96], the sensitivity of the test to the boundary conditions and problems with the cruciform shape of the sample. The yarns near the gripping area are bent, so that the shear angle in the central area is different from the shear angle of the frame [103]. Reducing the bending resistance near the grips can lessen this effect. This can be minimised by removing the transverse tows parallel to the frame side [96], [103].

Li et al. [98] performed picture frame testing on NCF samples. The authors applied pre-tension to ensure that the fibres are parallel to each other. They also removed the transverse yarns to eliminate any potential contributions. The same sample was tested three times, revealing that the first test yields higher shear forces. However, this irregular behaviour was attributed to disturbance and tension of the fibres. After this test, the fibres are realigned parallel to the frame, reducing the variability of the measurements. Asymmetrical behaviour was observed, as expected. When the stitches are under tension, they apply a high fixation to the yarns. Initially the fibres are orthogonal, as the frame is pulled the fibres rotate around the cross point, until these rotations are restricted, leading to out-of-plane wrinkling. When the stitches are under compression, their contribution is much smaller, resulting in a low shear resistance.

The irregular behaviour was also observed by Endruweit et al. [104], who noted that the specimen history affects the fabric structure, a phenomenon sometimes referred to as 'mechanical fabric conditioning'. Shearing forces applied to the fabric result in a residual reduction in yarn width and an increase in inter-yarn gap width.

When comparing both tests, the BET is simpler and the yarns are free at least at one edge, therefore, there is no tension in the yarns [99]. However, sliding between the yarns can be observed [38]. For the PFT, the yarns are clamped, preventing slipping, but any misalignments with the frame could lead to an increase in the measured load, therefore, the test presents a higher sensitivity to fibre alignment with the frame.

2.5.2 In-plane tension tests

Tension tests are used to determine the tension deformability and breaking strength of material, several tests such as on-axis, biaxial or multi-axial can be performed [9]. NCFs present relatively linear behaviour, as the fibres remain parallel to the plane of the fabric [37]. However, they are linked by the stitching,

with the extent of the link depending on the fabric type and the direction of the test [66]. Biaxial tension tests are used to measure the behaviour (see Figure 2.22) [63]. The strain can be measured by optical methods or extensometers [37].

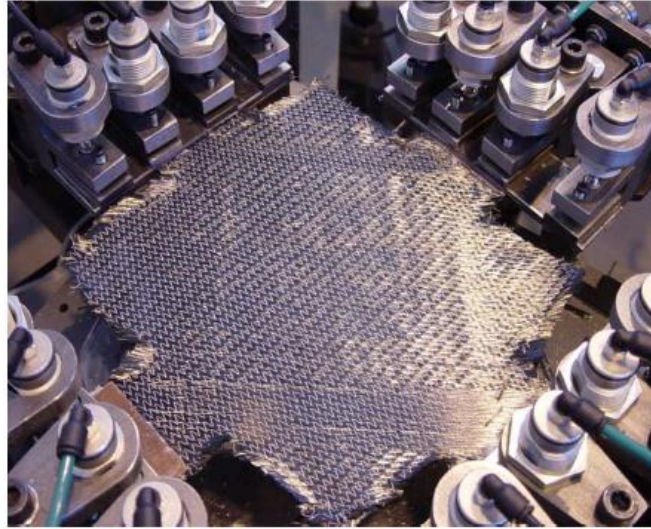


Figure 2.22. Biaxial tensile test for a NCF sample [63].

To generate useful data, a biaxial specimen should meet the following requirements [105]:

1. Wide homogeneous biaxially-stressed zone for strain measurements.
2. Failure must occur within this zone.
3. No spurious loads, other than tension or compression, should affect the specimen.
4. The specimen should accept arbitrary biaxial load ratios.

Several specimen designs can be used to test materials, but cruciform specimens are used for NCFs to obtain true biaxial stress, where only the central region is of interest. As with the in-plane shear test, the transverse yarns in the arms of the cruciform are removed to prevent any undesirable effects [37]. The biaxial tension is required to link the two strains to the two loads in each yarn direction of the material [9].

2.5.3 Out-of-plane bending tests

For biaxial NCFs, the bending stiffness is relatively low compared to the tension stiffness [9]. Therefore, this behaviour was initially overlooked, and less characterisation work was performed to understand this behaviour. Initially, a single value was used to define the bending stiffness of a fabric, however, these materials tend to have a non-linear behaviour which is a function of the curvature [106], [107]. Understanding the bending behaviour is important as it plays a critical role in determining the shape and location of wrinkles [9], [61].

The bending tests are performed to determine the relationship between the curvature and the bending moment [9]. The bending behaviour can be characterised using the cantilever bending test, the Kawabata test or the three-point bending test [34]. Although all the tests are commonly used, only the three-point bending test is standard test.

J. Xie et al [9] described two of the tests. The Kawabata test imposes a constant curvature on the textile by rotating one clamp. It allows to obtain a uniformly distributed bending curvature of the textile, directly determining the moment-curvature relationship. In the three-point bending test, the sample is supported at the ends and loaded in the middle, where the deflection is measured throughout the test. This test is only suitable for textiles with considerable bending stiffness, such as thick reinforcements.

In a cantilever bending test, the weight of the material defines the bending moment for a given length of the specimen (see Figure 2.23) [42], [61]. The measurements are performed for different lengths, providing the bending moment as a function of the curvature. The geometry of the sample and the free end contribute to an absence of spurious tension, which is important as the tensile stiffness is much larger than the bending stiffness [61].

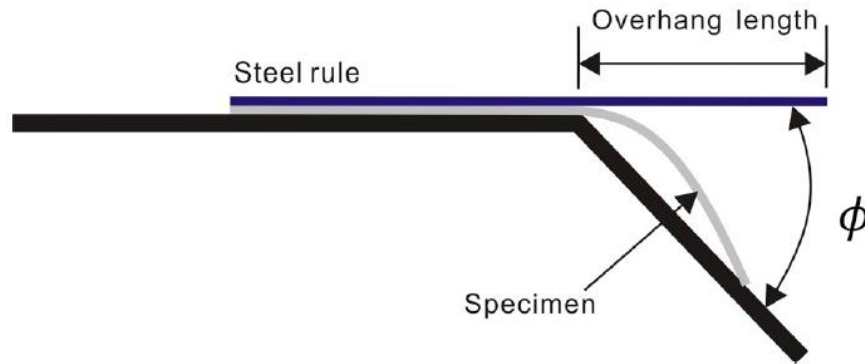


Figure 2.23. Schematic of a standard cantilever test [106].

A standard cantilever test produces a constant bending stiffness value, however, for NCFs non-linear behaviour has been observed [107]. Yu et al. [106], [107] characterised the bending behaviour by using a standard cantilever method to calculate a constant value. Then, a revised cantilever method to define the non-linear relationship. The revised cantilever method consists of a mechanical module and an optical module [70]. With the mechanical module the sample is placed in cantilever configuration under their own weight, with the possibility to add a mass at the free edge to reach larger curvatures. The optical module captures an image for each length. The images are processed to extract the characteristics of the bent shape.

2.5.4 Friction tests

Friction plays an important role in forming process. Fabrics might not exhibit a constant coefficient of friction, sled test or pull-out tests are used to characterise their friction behaviour [72].

The sled test is used to measure static and sliding friction forces between two surfaces, typically a sled and a table. Materials representing the surface pairings in the forming process are attached to the sled and the table [51], [108]. Common surface pairings include tool-diaphragm, diaphragm-fabric and fabric-fabric. A weight is placed on the sled to apply a normal force at the contact surface. The tangential force required to move the sled at a constant velocity is measured to

calculate the coefficient of friction. Some drawbacks of this test include the physical limit to the applied normal pressure and the occurrence of stick-slip motion, which can cause variations in the results [72].

The pull-out test overcomes some of the drawbacks of the sled test [72]. In the pull-out test the material is pulled from between two plates [109], [110], the pulling force and normal pressure are recorded during the test to characterise the friction behaviour (see Figure 2.24).

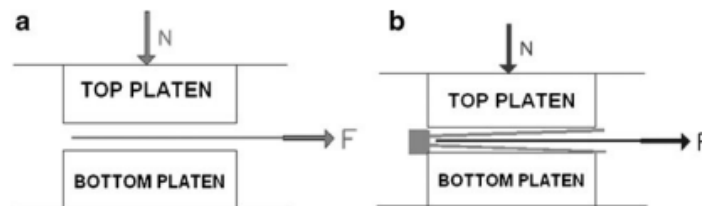


Figure 2.24. Schematic of the a) tool/fabric friction and b) fabric/fabric friction test setup [110].

2.6 Forming simulations

The previous section described the different testing methods that can be used to characterise the material behaviour. This data can be included in the simulations to improve the accuracy and reliability of the predictions. This section focusses on describing the different simulation approaches that can be used to model the forming processes.

2.6.1 Simulation approaches

Forming composite materials is a complex task due to their heterogeneous nature [24], arising from the different constituents with different mechanical properties. Additionally, composites are anisotropic as the properties depend on the direction, adding further complexity. Composite materials are expensive, so that the traditional development “trial and error” used for metals is not appropriate [10]. Therefore, numerical methods gained popularity. Mainly two approaches are used to simulate forming processes:

- Kinematic models, also known as fishing net algorithms [111], [112], [113], [114].
- Finite element analysis at different scales [42], [60], [62], [115].

Kinematic models use a geometrical approach, not considering the mechanical properties or process conditions. Whilst the finite element methods consider the physics of the forming, including contact and friction between components. Kinematic methods are faster although less accurate, therefore, the choice of method is a balanced between the required computational time and the expected accuracy of the model. Sections 2.6.1.1 and 2.6.1.2 describe both methods in more detail.

2.6.1.1 Kinematic models

The kinematic methods, also known as fishnet algorithm [111], appeared a few decades ago. These methods are used to find the best possible way to fit a fabric material on the mould surface, avoiding wrinkle formation and bridging [111]. The main assumptions are [62], [116], [117]:

1. Inextensibility of the fibres.
2. There is no slippage at the cross over of warp and weft yarns.
3. Relative rotation between warp and weft yarns at cross over are free.
4. No sliding between the fabric and the tool after coming into contact.
5. The yarns have no bending stiffness.

The procedure can be described as follows [111], [116], [118]. The first step is to analytically define the surface. This can be done fitting curved or straight patches, with straight patches simplifying the solution [112]. Additionally, smaller patches ensure fitting accuracy. The fabric is modelled using a pin-jointed net. To map the material onto the surface, the first node is positioned, and the draping directions are fixed. For symmetric parts, the start point is positioned in the plane of symmetry. A unique drape pattern is obtained, and the rest of the

tows are positioned using a mapping approach. Geometric equations are solved to determine the intersection of the surface with any possible crosspoints (see Figure 2.25). Geodesic or projected paths are used. The accuracy of the solution highly depends on the direction of the paths.

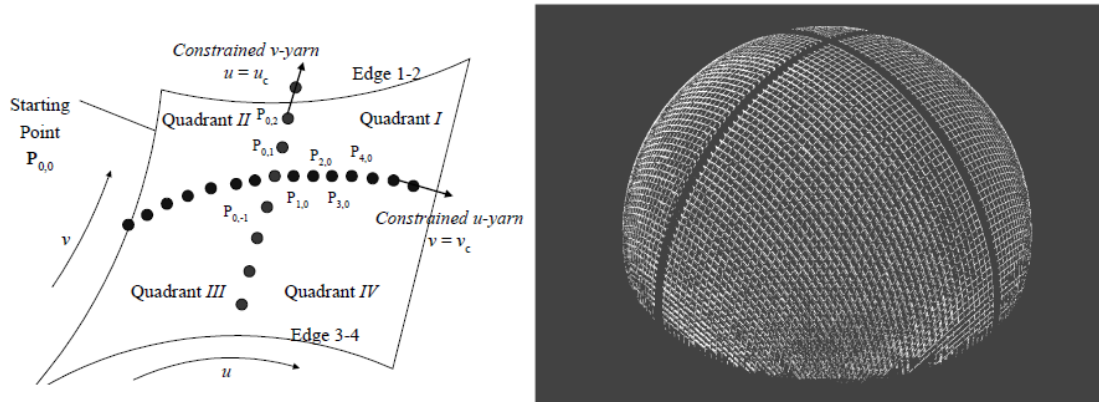


Figure 2.25. Draping algorithm with the initial constrained yarns and an example of draping on a hemispherical surface [111].

Kinematic methods indicate whether a geometry is drapeable [47], however they do not account for the mechanical behaviour of the reinforcement, the exterior loads, or the boundary conditions (sliding and friction on the tools) [10]. This method does not account for yarn slippage, which can occur in the real forming process [112]. In conclusion, kinematic methods are very fast but some effects, such as wrinkles and the effect of blank holders, cannot be predicted [24].

2.6.1.2 Finite element methods

Finite element (FE) methods provide a numerical solution to physical problems considering the governing equations, such as equilibrium, constitutive equations and boundary conditions [25]. These methods model the tools, contact and friction between the parts, and the mechanical behaviour of the composite during forming.

The simulation provides the conditions, such as loads, type of material or boundary conditions, which will make the forming process feasible, while describing the formation of defects such as wrinkles, porosity or fractures during

the process [60]. Additionally, FE methods provide the directions and density of the fibres of the formed component at any point, crucial to understand the performance of the final component [60]. Therefore, FE methods provide a more accurate prediction, at the expense of longer computational times. However, their accuracy depends on the description of the aspects involving the forming process and material behaviour [119].

The multiscale of the textile materials means that the macroscopic behaviour results from the interactions at lower scales [116]. Therefore, there are different approaches that could be used considering this hierarchy: continuous, discrete or mesoscopic and semi-discrete [24], [117].

Continuous approaches consider the reinforcement to be anisotropic continuum [120]. However, the material is not continuous at lower scales but can be considered continuous in average. In this case, the constitutive laws should specify the mechanical behaviour of the material, which mainly depends on the fibre directions that change during forming [120]. Capturing the effects of the fibre architecture and its evolution is complicated [62]. Additionally, this method assumes that there is no sliding between the yarns [25], and crimp or yarn compaction is generally not included in the model [60].

The discrete approach is the opposite to the continuous approach, modelling the reinforcement at a small scale [25]. This approach models the behaviour at a yarn level, considering also the stitches. Therefore, if some inter-ply sliding occurs, discrete models can simulate it. This approach usually involves beam, truss or spring elements [60], [62]. The approach does not require any assumptions with regards to the continuity of the material [116]. This approach is more realistic, but it involves an increased number of contacts between the yarns due to the number of fibres in the structure, considerably increasing the required computational time [116]. Therefore, this approach is limited to a small subdomain of the reinforcement to limit the computational time [62], [117].

Semi-discrete approaches are a compromise between continuous and discrete models. These methods associate a finite element description of the fabric with a mesoscopic analysis of the unit cell [60], [116]. To describe the fabric using finite element, the assumption that two points of each yarn which are initially superimposed, remain superimposed after forming is used [60]. This approach allows sliding between the layers whilst ensuring reasonable computational time [62]. This model allows to describe the non-linear tensile behaviour due to crimp of a NCF, and the behaviour before and after the shear locking angle [60].

Continuous approaches are the most popular method due to their high computational efficiency and accuracy [117]. Only continuous approaches are of interests in the current research process. Despite the amount of work on this field, there is no widely accepted model accurately describing all the aspects of the mechanical behaviour of fabrics [116]. To capture the material behaviour, two constitutive models are typically used: hyperelastic and hypoelastic approaches [121].

The hypoelastic model has been proposed for materials at large strains [122]. This method is used for geometrical non-linearities and elastic non-linear behaviours [123]. This method maps the strain rate using a tangent stiffness tensor to calculate the objective stress rate [115]. This means that the stress tensor at the current stress depends on the same tensor in the previous time increment. For fibrous materials, the objective derivative must be based on the direction of the fibre [117]. A drawback of this method is that an improper definition of the hypoelastic relations can lead to unphysical material behaviours [115].

The hyperelastic model can reproduce the non-linear behaviour of textile reinforcements [116]. Hyperelastic models typically require symmetry of the material at the initial stage [39]. Therefore, they are usually less used for fibrous materials [60]. This method calculates the stress response from the first derivative

of the strain energy function [115], [122]. This is done with respect to an objective quantity such as the right Cauchy-Green tensor, where the structural tensor invariants are defined using the fibre directions. For simplicity, it is assumed that the tensile and shear strain energies are not coupled. This coupling has an effect on the prediction of the maximum shear angle and the fibre orientations [117].

2.6.1.3 Implicit vs explicit algorithms

Most forming processes are quasi-static and can be simulated using implicit or explicit finite element methods. These techniques solve the governing equations during the analysis. The implicit method is typically more suited for static and quasi-static processes. However, the non-linear equations must be solved multiple times within each time increment, making the computational cost high [124].

Most forming processes are often solved using explicit dynamic approaches, especially when the forming leads to wrinkling [42], [125]. This approach obtains a solution to analyses that are difficult to solve using an implicit approach, particularly when there are convergence issues. Explicit methods do not require equilibrium correction after each loading step, allowing them to bypass difficult points where implicit methods might fail to converge. However, explicit methods are generally less precise. Although, the contact formulations are simpler and more robust.

To improve the numerical efficiency, the process can be simulated at a faster speed than in real life, provided that the dynamic effects remain small enough so that the predictions are not modified [62]. Quasi-static conditions are ensured when the kinetic energy of the deformable materials remains a small fraction (typically below 5-10%) of the internal energy of all parts throughout most of the analysis. This means that the deformation process is dominated by static forces,

and any acceleration or inertia effect in the material have a negligible effect on the results.

When using explicit methods, the time increment must be sufficiently small to ensure numerical stability. However, reducing the time increment increases the number of iterations required to cover an interval, which increases the computational cost as it requires more operations. The stable time increment can be expressed as [126]:

$$\Delta t = \frac{L^e}{c_d} = L^e \sqrt{\frac{\rho}{E}} \quad (5)$$

Where, Δt is the maximum size of the stable time increment, L^e the characteristic length of the element, ρ the density and E the Young's modulus of the material. To reduce the simulation run time, Δt should increase. Increasing L^e and/or decreasing c_d will increase the size of the stable time increment, therefore decreasing the computational time. This can be done by:

- Increasing element dimension increases L^e .
- Increasing the material density decreases c_d .
- Decreasing the modulus E decreases c_d .

Artificially increasing the density of the model, a technique known as mass scaling, can be applied to achieve larger stable time increment, reducing computational time.

2.6.2 Fabric forming modelling

Section 2.6.1 described the different simulation approaches available to model composite structures. This section focusses on modelling NCFs. Modelling this type of fibrous material is complex due to the fibre architecture and the presence of stitches.

When using the continuous approach on NCFs, it is essential to implement a non-orthogonal constitutive law due to the significant shearing required for the fabric to conform to the tool shape [33], [62], [121], [127]. Before deformation, the yarns in the NCF are typically orthogonal, but this alignment is lost after deformation (see Figure 2.26).

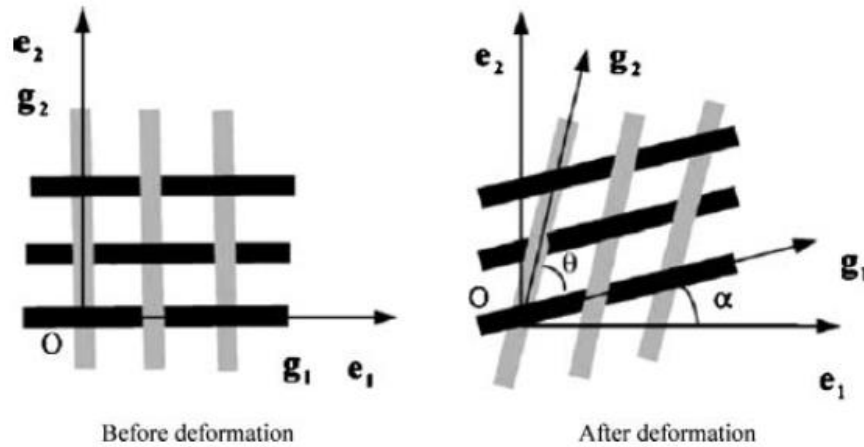


Figure 2.26 Schematic of the yarn directions before and after deformation [120].

The non-orthogonal constitutive law can capture the anisotropic behaviour of these materials under large shear deformation [25]. These deformations are originated due to the substantial variations in the angle between the warp and weft directions. By using a non-orthogonal frame aligned with the fibre directions, the stress and strain within the material can be determined. The constitutive equation consists of a contribution from the fibre direction properties and another from the shear properties [118].

The validity of this approach was demonstrated by [33], [121], [127]. The results presented on the articles present a good agreement between the simulations and the performing experiments. Therefore, the models are capable of accurately representing the mechanical responses of the different fabrics.

The non-orthogonal constitutive law can characterise the anisotropic behaviour of fabrics under large deformation. However, it is important to

understand what deformation modes should be implemented on the numerical model to accurately predict the behaviour of fabrics.

Initially, the bending behaviour was overlooked, since fabrics present a weak bending stiffness due to the relative slippage between fibres [61], [128]. The locking angle was usually used to determine wrinkling occurrence [117]. However, it was shown that the in-plane shear stiffness, even though it plays a role in wrinkling appearance, is not the only parameter determining wrinkling, with other strains and stiffnesses playing a role in their development [55], [117], [129].

In particular, it has been proved that the bending behaviour affects the number and size of defects [42]. Additionally, it has also been proved that the shear locking angle is insufficient to determine the onset of wrinkles [129].

Hamila et al. [42] investigated the draping on a cylinder considering different mechanical behaviours: tensile stiffness only, tensile and in-plane shear stiffness, and tensile, in-plane shear and bending stiffness (see Figure 2.27).

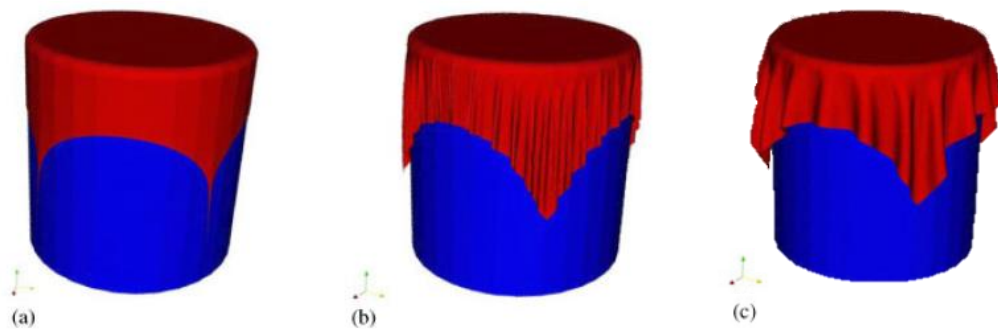


Figure 2.27. Draping on a cylinder considering a) tensile stiffness, b) tensile and in-plane shear stiffness, and c) tensile, in-plane shear and bending stiffness [42].

The results show that when considering only the tensile stiffness, the material presents very large shear angle in the corners of the fabric but not wrinkling. Adding the in-plane shear leads to wrinkling and the shear angles are limited. However, considering the three behaviours leads to increase wrinkle size and more realistic shape. These observations indicate that neglecting in-plane

shear leads to no wrinkling and that neglecting the bending behaviour affects the number and shape of the wrinkles, showcasing the importance of considering all three behaviours when modelling the fabric.

Similarly, P. Boisse et al. [129] simulated the compression in the fibre direction of a woven ply. The bending stiffness was set to 1 N/mm, 5 N/mm and 10 N/mm. The results, presented in Figure 2.28, show that the bending stiffness determines the number and size of wrinkles. Additionally, simulations from a thermoplastic prepreg forming showed that the wrinkles are smaller when the stiffness decreases and larger when the stiffness increases. Therefore, the bending stiffness affects wrinkling and should be accounted for.

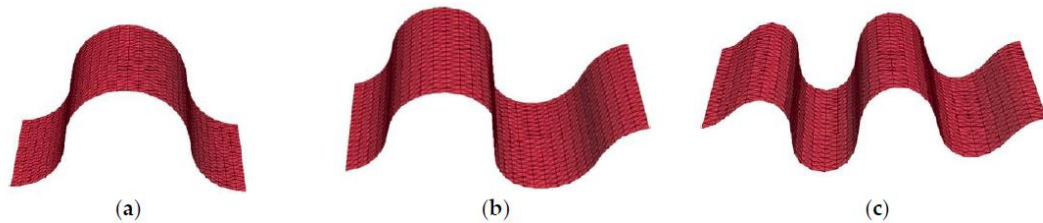


Figure 2.28. Compression in the fibre direction of a woven ply for a bending stiffness of a) 1 N/mm, b) 5 N/mm and c) 10 N/mm [129].

In order to determine wrinkling occurrence, different element types could be used. Forming simulations initially used membrane elements, since the tensile rigidities are large compared to the bending ones [91]. Membrane elements consider tension and in-plane shear; however, they neglect bending stiffness [61]. This is because membrane elements have no rotational degrees of freedom, meaning that they present no resistance to out-of-plane bending [89]. Membrane elements can predict wrinkles, but their predictions do not accurately reflect experimental observations, making them unsuitable for simulating wrinkling correctly [129].

A different approach involves using shell elements, which can be used for materials with low thickness [129]. Shell elements have a thickness that is small compared to their dimension in the plane [117]. These elements account for

transverse shear and bending stiffness, as they consider the stress gradient through the thickness [127]. Therefore, shell approaches can be used to predict wrinkling behaviour, but they require increased computational time as they consider more deformation modes. Shell structures exhibit coupling between membrane and bending [130].

When modelling fabrics using the shell approach, the relationship between bending and membrane stiffness is not verified when using the classical theory [117]. This is due to the possible slip between fibres, so that the bending is lower than that given by the classical shell theories. To improve the predictions, the bending behaviour can be decoupled from the membrane considering a moment-curvature relation independent of the membrane deformations [61]. This approach views the material as a laminate composed of layers with different Young's modulus (see Figure 2.29), so that both tensile and bending stiffness can be obtained [129]. This procedure means that the membrane and bending energies are no longer linked, so that the behaviours are considered decoupled.

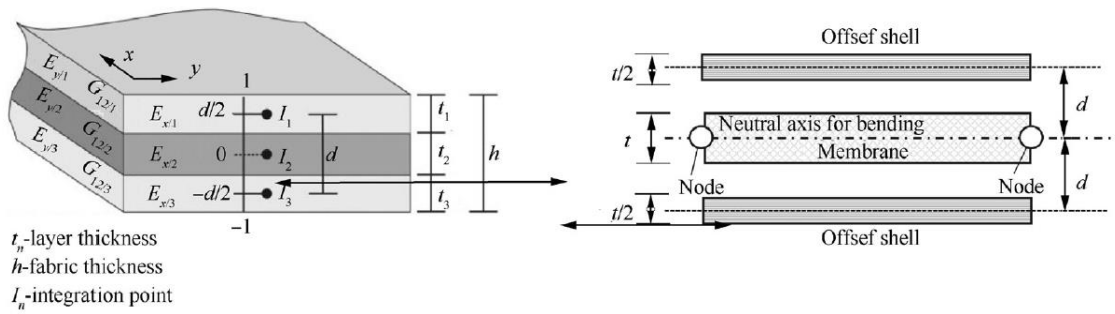


Figure 2.29. Decoupling the bending and tensile behaviour using the laminate technique [117].

A combined approach could also be used, as demonstrated by Yu et al. [131], where a 5 mm membrane element mesh is used in a full-scale simulation to locate the areas containing potential defects. Then, a high fidelity 1 mm shell element mesh is used in those areas of interest to explicitly predict the shape of forming induced defects, using boundary conditions derived from the full-scale simulation. This two-stage process reduces the computational time required to predict the size and location of defects from 120 h for the full-scale high fidelity

model to 15.7 h. This approach is capable of replicate macroscale wrinkling and bridging within 10%.

Accurate simulations of the forming process are crucial for understanding the impact of different parameters without the need for extensive experimentation. Wrinkling is a common defect that significantly reduces the mechanical properties of the final components. Therefore, the ability to accurately predict the onset and development of wrinkles is of outmost importance to improve the overall quality of the forming process.

In this research, the mechanical behaviour of the FCIM359 NCF was defined using a user-defined subroutine in Abaqus/Explicit. The subroutine was developed at the University of Nottingham by Chen [33]. The subroutine was based on a non-orthogonal constitutive material model, using a modified VFABRIC routine, which is valid for material exhibiting two structural directions which might not be orthogonal during deformation.

To describe the material behaviour, Chen characterised the in-plane shear behaviour, presented in Figure 2.30, using the picture frame test. The curve fitting was performed according to the following equations [33]:

$$F_{norm} = F_{norm}^{yarn\ rotation} + F_{norm}^{stitch} \quad (6)$$

where F_{norm} is the total normalised shear force, $F_{norm}^{yarn\ rotation}$ is the contribution from yarn rotation, and F_{norm}^{stitch} is the contribution from the stitches. The contribution of the yarn rotation was approximated by

$$F_{norm}^{yarn\ rotation} = (29.56\gamma_{12}^5 - 65.56\gamma_{12}^4 + 137.06\gamma_{12}^3 + 94.73\gamma_{12}^2 + 112.19\gamma_{12}) \text{ N/m} \quad (7)$$

where γ_{12} , in radians, is defined in the range of $\left(-\frac{\pi}{2}, \frac{\pi}{2}\right)^T$. And the contribution of the stitch tension, considering the progressive stitch failure, was described by:

$$F_{norm}^{stitch} = \begin{cases} (2000\gamma_{12} - 120) \text{ N/m}, & 0.006 \leq \gamma_{12} < 0.50; \\ (-3520\gamma_{12} + 2640) \text{ N/m}, & 0.50 \leq \gamma_{12} \leq 0.75; \\ 0 \text{ N/m}, & \text{else.} \end{cases} \quad (8)$$

The in-plane shear integration to the non-orthogonal constitutive model was validated on [33]. The results showed that the simulations based on the model could predict local shear angles within $\pm 5^\circ$ of the experimental values, as well as the wrinkling position and defect types presented on the experiments. Therefore, it could effectively capture the dominant forming mechanisms, including in-plane shear, fibre elongation and inter-tow slippage.

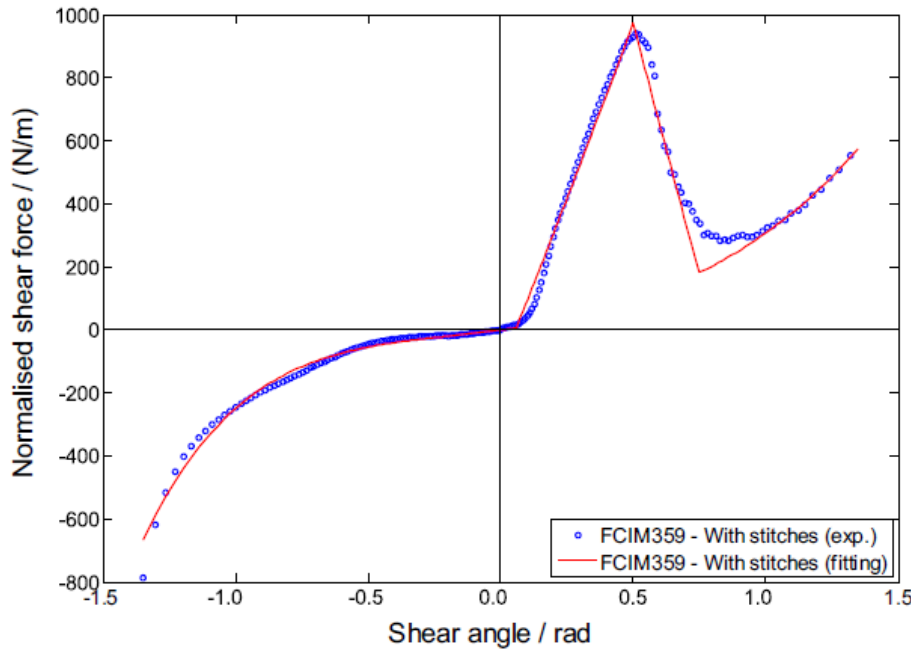


Figure 2.30. Shear resistance curve for FCIM359 biaxial non-crimp fabric [33].

Yu modified this subroutine to incorporate the bending behaviour to predict fabric wrinkling [106], [107], [131]. The bending behaviour, presented in Figure 2.31, was characterised using a revised cantilever test. It is important to note that

in Figure 2.31 the bending parameters are normalised by the width. Therefore, the bending moment M is given in N rather than N·m, and the bending stiffness B is given in N·m rather than N·m². The fitting was performed according to the following equations [106]:

- Linear bending model (LBM)

$$B_{init}^{NCF,pos} = 0.0080 \text{ Nm}; B_{init}^{NCF,neg} = 0.0057 \text{ Nm} \quad (9)$$

$$B_{41.5^\circ}^{NCF,pos} = 0.0038 \text{ Nm}; B_{41.5^\circ}^{NCF,neg} = 0.0032 \text{ Nm} \quad (10)$$

$$B_{inf}^{NCF,pos} = 0.0002 \text{ Nm}; B_{inf}^{NCF,neg} = 0.0001 \text{ Nm} \quad (11)$$

Where B_{init} is the bending stiffness at zero curvature, $B_{41.5^\circ}$ denotes the constant bending stiffness measured by the cantilever test at an angular deflection of 41.5° , and B_{inf} is the value taken from the asymptote of the non-linear bending curve as it approaches infinity.

- Non-linear bending model (NLBM)

$$M_{nonlinear}^{NCF,pos} = 0.19457 \cdot \kappa + 0.03139(1 - e^{-\kappa/0.0040}) \text{ N} \quad (12)$$

$$M_{nonlinear}^{NCF,neg} = 0.10279 \cdot \kappa + 0.036139(1 - e^{-\kappa/0.0065}) \text{ N} \quad (13)$$

Where κ is the curvature and $M_{nonlinear}$ denotes the non-linear bending moment measured by the revised cantilever test.

The bending stiffness was decoupled from the in-plane stiffness using the Abaqus built-in laminate shell layup, where the layer thickness and number of integration points within the layup can be tailored. Each fabric ply was represented by three artificial layers: the outer surface layers define the bending behaviour, while the central layer controls the membrane behaviour. The total

thickness of the element matches the fabric thickness, with identical thickness for both surface layers. All layers were assigned a single integration point to reduce computational time.

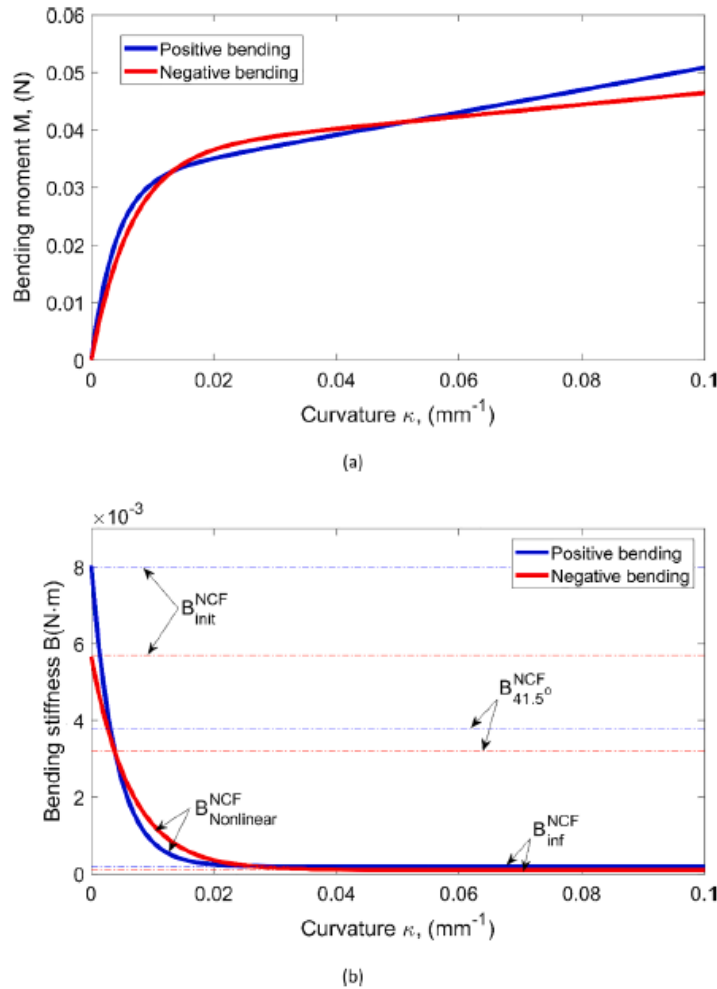


Figure 2.31. a) Bending moment vs. curvature and b) non-linear bending stiffness vs. curvature for the FCIM359 NCF [107].

The non-orthogonal constitutive material model was modified to update the bending moments and curvature at every time increment. This was implemented by defining the bending contribution of each primary yarn based on the current fibre orientation frame, which varies with the rotation of the yarns during in-plane shear. The bending properties were defined by updating the moduli values of three layers within the composite shell element for each fibre orientation.

The bending integration to the non-orthogonal constitutive model was validated on [106], [107]. The results showed that using a linear bending model underpredicted the tip deflection on a simple bending test. However, the response using a non-linear bending model was more representative, with an average relative error of only 0.6%, producing more realistic predictions of the formed shaped containing macroscale wrinkles.

2.6.3 DDF forming simulation

When modelling the double diaphragm forming process, the diaphragm material can be modelled using the Mooney-Rivlin model, plastic model, Ogden model or Marlow model [51], [55], [73], [131], [132]. Capturing the behaviour of the diaphragm is complex.

Sjolander et al. [73] modelled the diaphragm using an hyperelastic Mooney-Rivlin model. This model is used to model the large strain non-linear behaviour of incompressible materials such as rubber. The material's response is defined using the strain energy function based on the invariants of the deformation. The model relies on material empirical constants, which defined by fitting the experimental data from tensile or shear tests.

Sorrentino et al. [132] modelled the diaphragm using a plastic material based on an isotropic non-linear viscoelastic shell element. The stress and plastic strain are linked using a constitutive relation using the effective viscosity, which depends on the material consistency, the strain rate hardening exponent, the first and second straining hardening coefficient and the viscoelastic coefficient. These parameters can be determined as a function of temperature, but in this study, they were considered constant.

Chen et al. [51] modelled the diaphragm using the Ogden model [133], which describes the hyperelastic, non-linear stress-strain behaviour of silicone diaphragms. In this model, the behaviour can be described by a strain energy

density function expressed in terms of the principal stretches. The constitutive relations are obtained from the derivative of the strain energy with respect to stretch. The nominal stress-strain relations were obtained from the three load cases uniaxial tension, biaxial tension and pure shear.

Yu et al. [131] modelled the diaphragm using the Marlow model for hyperelastic material [134], which uses experimental stress-strain data. This is the procedure used in this thesis, Yu [131] characterised the in-plane behaviour of the diaphragm through the stress-strain response under various loading conditions (uniaxial tensile, equibiaxial tensile and planar shear test).

To implement the Marlow model in Abaqus, the stress-strain curved obtained from these experiments serve as direct inputs. The Marlow model does not require explicit characterisation of bending behaviour, as it captures the response of the material through the stress-strain data in these loading conditions. The stress-strain curves, presented in Figure 2.32, were generated using three specimens repeats for each deformation mode. The fitting was made according to the following equations, where σ and ε denote nominal stress and nominal strain respectively [131]:

- Uniaxial tension

$$\sigma = 6.364 \cdot (e^{0.004451\varepsilon} - e^{-0.07547\varepsilon}) \text{ MPa}, \quad 0 \leq \varepsilon \leq 500\% \quad (14)$$

- Equibiaxial tension

$$\sigma = 6.482 \cdot (e^{0.004871\varepsilon} - e^{-0.12040\varepsilon}) \text{ MPa}, \quad 0 \leq \varepsilon \leq 100\% \quad (15)$$

- Planar shear

$$\sigma = 7.238 \cdot (e^{0.003774\varepsilon} - e^{-0.083212\varepsilon}) \text{ MPa}, \quad 0 \leq \varepsilon \leq 200\% \quad (16)$$

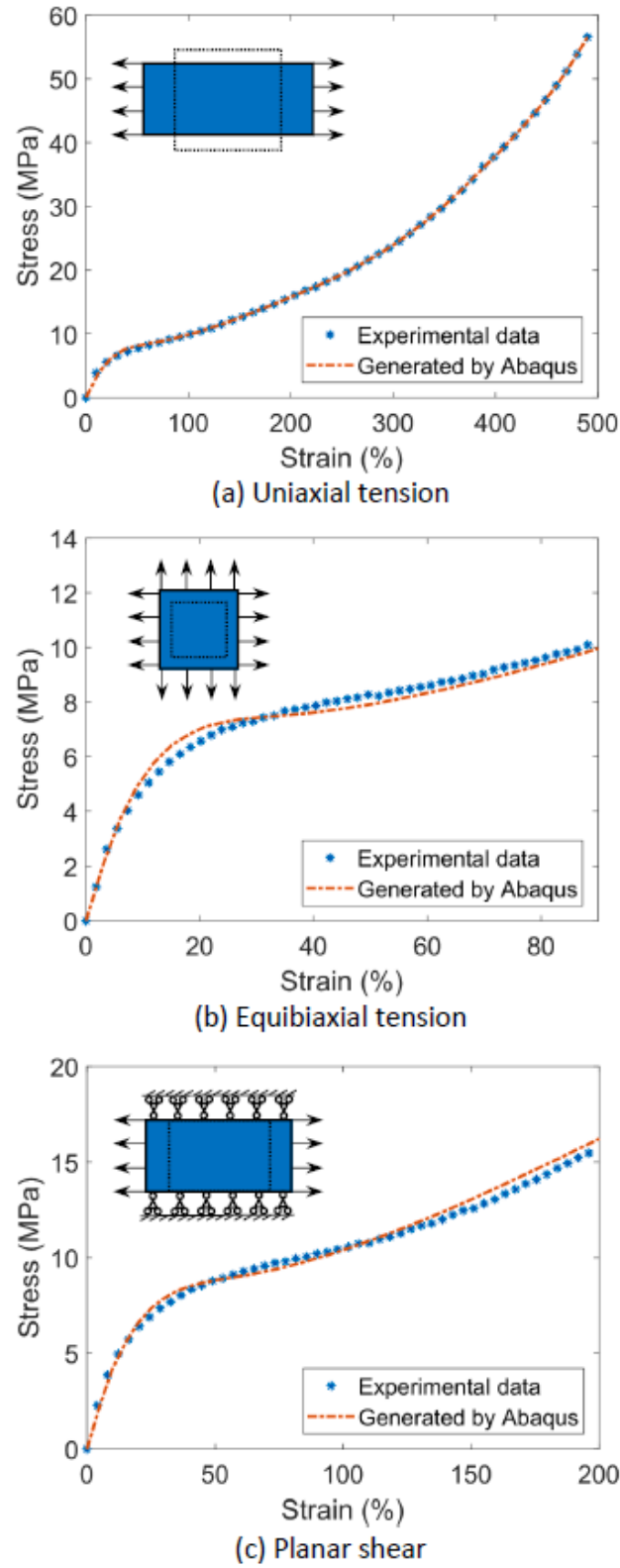


Figure 2.32. Characterisation of the diaphragm material using Marlow's hyperelastic model for a) uniaxial tension, b) equibiaxial tension and c) planar shear [131].

Section 2.6.2 discussed the various approaches to numerically model fabric behaviour, while this section focused on modelling the diaphragm material. However, the breather material, which is experimentally used to release trapped air during experimental forming, is omitted in these studies. Although its effect is critical in practice, it has not been numerically investigated or incorporated into existing models. None of the reviewed studies have addressed whether the breather must be included in simulations or if its influence can be neglected. This gap in the literature highlights the need for focussed research to determine the role of the breather in forming. This thesis will address this gap by examining the role of the breather in numerical models, assessing its impact on forming accuracy and defect prediction.

Chapter 3 Methodology

This chapter introduces the experimental and numerical methodologies used for the double diaphragm forming process. Section 3.1 describes the rig and equipment used in the experiments, along with the materials employed during forming. Section 3.2 details the modelling approach, listing the model set-up for future studies and establishing the mesh, mass scaling and fabric parameters for the thesis.

3.1 Experimental

3.1.1 Rig

The double diaphragm forming process is used to produce high-quality composite components. Vacuum is used to form complex 3D shapes from 2D materials before resin infusion. However, defects such as wrinkling or bridging can occur during preforming, affecting the performance of the final component.

The DDF process (see Figure 3.1) involves two elastic diaphragms that clamp the material to be formed in place using vacuum. This arrangement is then lowered to contact the tool surface. Subsequently, a second vacuum is applied between the tool and the lower diaphragm to conform the material to the desired shape. Once the material has conformed, the vacuum is released, allowing the preform to be retrieved.

The diaphragms transmit the pressure evenly across the material surface to ensure consistent forming. Their flexibility allows them to conform to complex geometries, enabling the material to adapt to intricate designs and reducing the likelihood of defects. Rubber, silicone and other elastomers are typically used to manufacture the diaphragm.

A powder binder can be used to hold the reinforcement together. If binder is used, the arrangement is heated to melt the binder, and the formed part is then allowed to cool to retain the desired shape. However, in this case, binder was not used as it can affect the reinforcement properties, stability and performance.

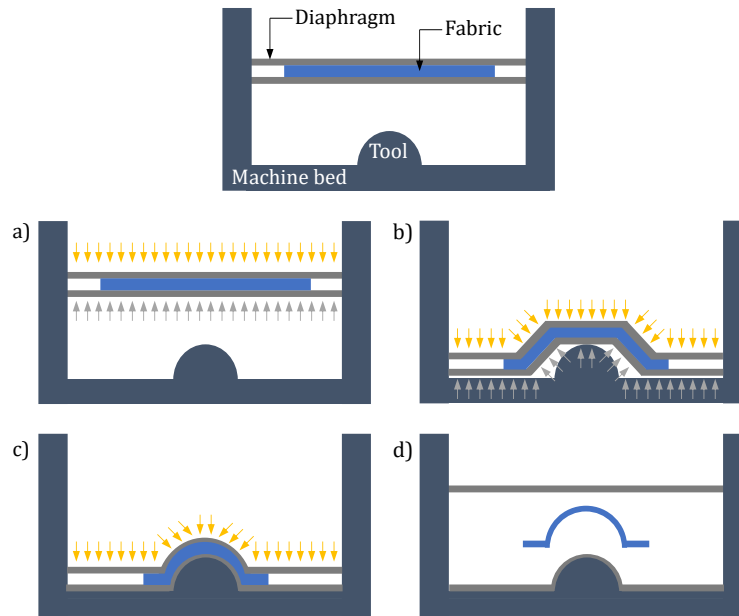


Figure 3.1. Schematic of the double diaphragm forming process.

A laboratory-scale double diaphragm forming machine, measuring 1600mm x 1240 mm and developed at the University of Nottingham, was used for the forming experiments (see Figure 3.2).

The lower diaphragm is clamped between a support frame and a rectangular picture frame, then the fabric stack is positioned on top of the lower diaphragm. The upper diaphragm is fixed to the frame using a vacuum-tight seal. A vacuum of 1 bar is applied between the diaphragms to clamp the material. This arrangement is attached to four pneumatic cylinders used to lower the set-up into contact with the tool. A second vacuum is drawn between the lower diaphragm and the tool, allowing the material to conform to the desired shape. The total cycle for this set-up is approximately 3 minutes. Since binder is not used, the material loses its shape once the vacuum is released.

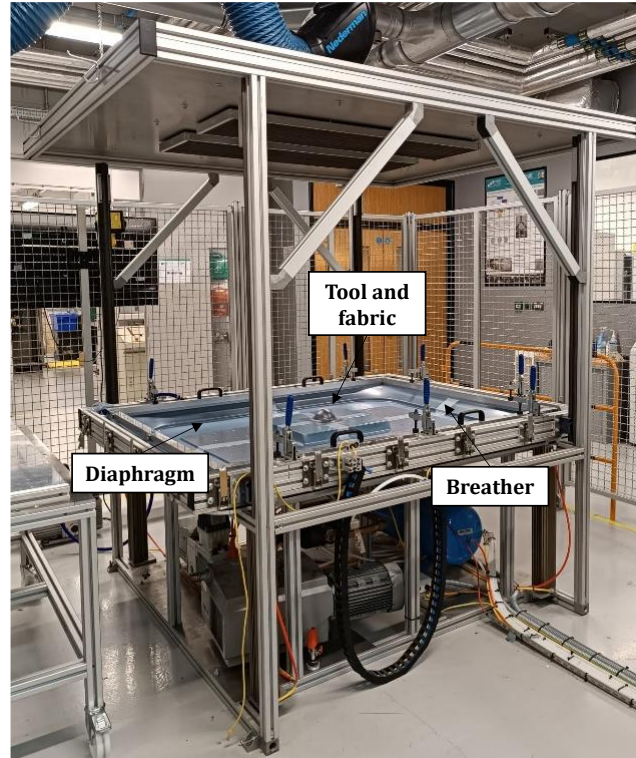


Figure 3.2. Laboratory-scale Double diaphragm forming machine.

Figure 3.3 a) presents the fabric stack between the diaphragms before any vacuum is applied between the lower diaphragm and the tool. The fabric is flat and unshaped at this stage. Figure 3.3 b) presents the fabric stack after vacuum has been applied between the lower diaphragm and the tool. The material has conformed to shape of the tool, exhibiting a 3D shape, in this case a hemisphere. This demonstrates how the double diaphragm forming process shapes the material to match the geometry of the tool.

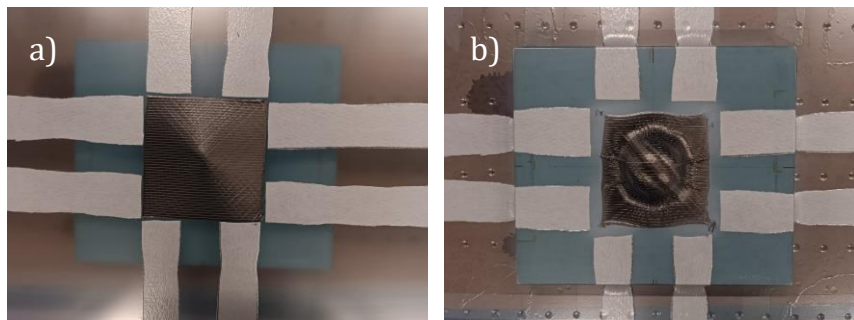


Figure 3.3. Fabric material a) before and b) after vacuum is applied between the lower diaphragm and the tool.

3.1.2 Tooling

In this thesis, three different hemispherical tools were used. The hemispherical tools are double curved surfaces, as the material curves in two directions simultaneously during forming, resulting in a more complicated shape. Highly curved shapes or with small radii generate additional stress in that specific area which forces the fabric to adapt to the geometry [135]. However, this adaptability is limited by the Poisson's effect: as a material stretches in one direction, it contracts perpendicularly, potentially leading to out-of-plane defects such as wrinkling or bridging.

Figure 3.4 presents schematics of the three tools. The fabric is centred on the tool, represented by the light blue square. The three tools are:

- A hemisphere with a 50 mm radius mounted on a platform, referred to as '50rplatf'.
- A hemisphere with a 50 mm of radius, referred to as '50r'.
- A hemisphere with a 100 mm of radius, referred to as '100r'.

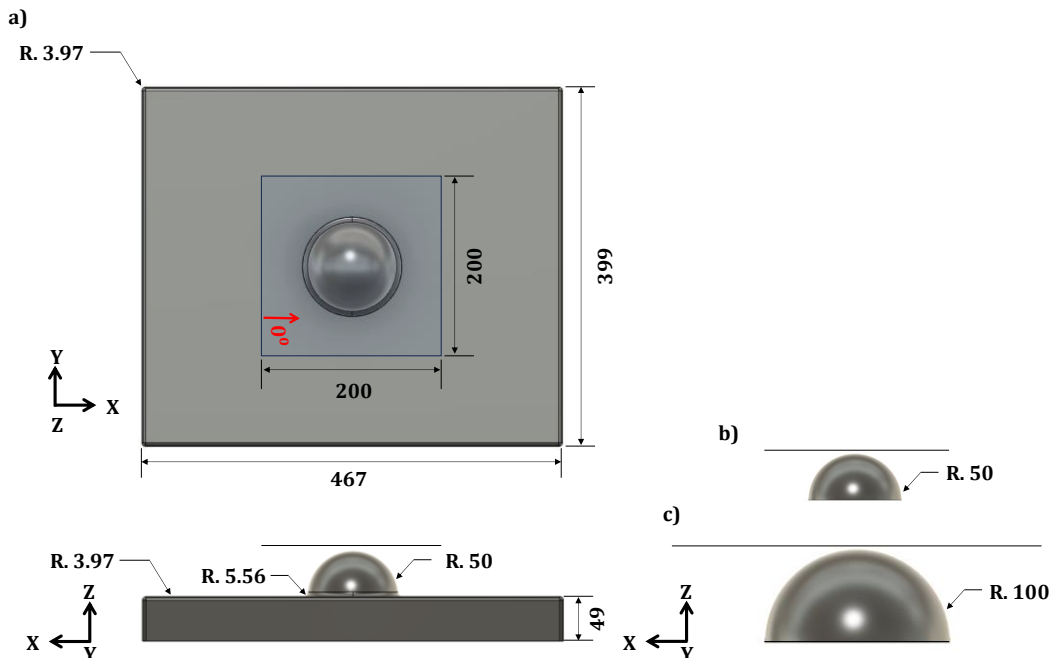


Figure 3.4. Schematic of a) the hemisphere with a 50 mm radius mounted on a platform, b) the hemisphere with a 50 mm radius and, c) the hemisphere with a 100 mm radius.

3.1.3 Equipment

3.1.3.1 *Sample preparation*

The first step in the forming process was sample preparation. To avoid fibre distortion and achieve more accurate cut to required size, the NCF samples were prepared using the X-CUT-TT automated ply cutter by Bullmer (see Figure 3.5). The equipment offers a cutting accuracy of 0.1 mm.



Figure 3.5. Automated cutting machine, X-CUT-TT, cutting the NCF samples to the required size.

A cutting plan was generated using a design software, in this case Autodesk Inventor. The material roll was carefully positioned on the machine bed, ensuring that the edge of the material was parallel to the edge of the machine bed to achieve a straight cut. Once satisfied with the alignment, the material was held in place using vacuum. When the cutting was finished, the vacuum was released so that the samples could be manually retrieved from the machine bed. The material was carefully removed by lifting the edges with a flat ruler to prevent pulling from the stitches and removing them locally. If the stitches were damaged during this procedure, the sample would no longer be suitable for forming.

3.1.3.2 Data acquisition

The acquisition of experimental data was performed using the HandySCAN 3D™ for in-situ scanning of the tooling and preforms. The preforms were scanned on the DDF machine bed whilst maintaining vacuum since no binder was used during forming (see Figure 3.6).

The scanner uses integrated photogrammetry algorithms to convert 2D images into 3D measurements, with part positioning determined by real-time triangulation. Therefore, no external positioning system is required. Positioning is related to the object by randomly fixing reference or target points, 6 mm retro-reflective target dots, to the surface. For accurate characterisation of the surface, at least 3 dots need to be visible at all times. The scanner produces real-time surface rendering as two cameras record the deformed laser projection on the shape and proceed to calculation.

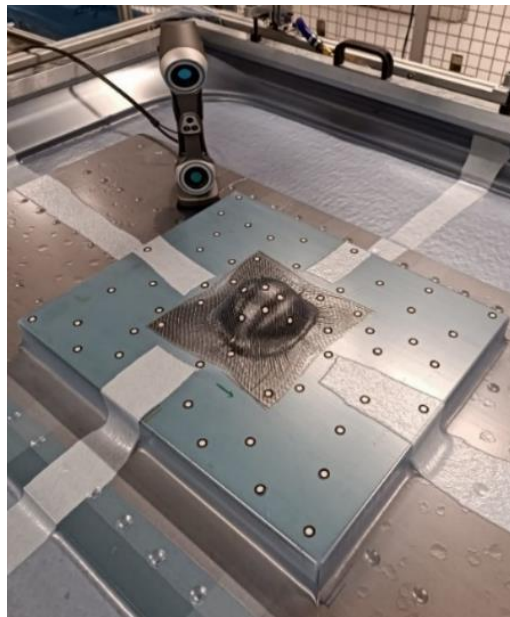


Figure 3.6. In-situ scanning of the preform with the HandySCAN 3D™.

The scanning distance is between 200 mm and 450 mm. During scanning, a meter display and the LEDs on top of the scanner indicate the distance from the object, with green indicators ensuring correct distancing. The scanner loses

tracking if too close or too far from the object. Additionally, to improve accuracy, the scanner must be as perpendicular as possible to the surface during scanning. This can be done visually, as the scanner captures more points when it is properly aligned.

The scanner has an accuracy of 0.025 mm, which is sufficient to detect macroscopic wrinkling. The mesh resolution was set to 0.5 mm to ensure the effective detection of macroscopic wrinkles. The automatic fill holes and isolated patches setting was set to 15, as this value worked well for the parts. These settings ensure minimal gapping in the mesh without compromising accuracy. If this setting is too high, the algorithm may overly smooth the surface by closing gaps excessively, leading to an unrealistic shape.

The measurements can be exported in several formats. In this case, the mesh was exported as a point cloud in .txt format for further data processing. For data processing purposes, it was assumed that there was no clearance between the diaphragms and the preform.

3.1.4 Materials

3.1.4.1 Biaxial non-crimp fabric (NCF)

A biaxial non-crimp fabric, Hexel FCIM359, consisting of two unidirectional carbon fibre layers oriented at $+45^{\circ}/-45^{\circ}$ bonded by a pillar stitch at 0° was used in this work. The material parameters can be found in Table 3.1. The uncompressed thickness of each ply is 0.4 mm.

Four NCF orientations are used in this work, $[0^{\circ}/90^{\circ}]$, $[90^{\circ}/0^{\circ}]$, $[+45^{\circ}/-45^{\circ}]$ and $[-45^{\circ}/+45^{\circ}]$. A schematic of the fibre and stitch directions is presented in Figure 3.7. The 0° direction (red arrow) is oriented with the X axis for all the tools. The NCF ply orientation is expressed from the lower (closest to tool) to the upper (farthest from tool). For each ply, the black line denotes the direction of the fibres and the yellow line denotes the direction of the stitches.

Table 3.1. Material parameters for the biaxial NCF, Hexcel FCIM359, under study.

Material designation	FCIM359
Supplier	Hexcel
Fibre material	Carbon fibre
Fibre type	Toray T620-50C
Fibre areal weight (gms)	440
Fibre orientation ($^{\circ}$)	± 45
Fibre tow size (K)	24
Stitch yarn	Polyester
Stitch pattern	Pillar
Stitch gauge (GG)	6
Stitch length (mm)	2.12
Stitch linear density (dtex)	78
Stitch areal weight (gsm)	9

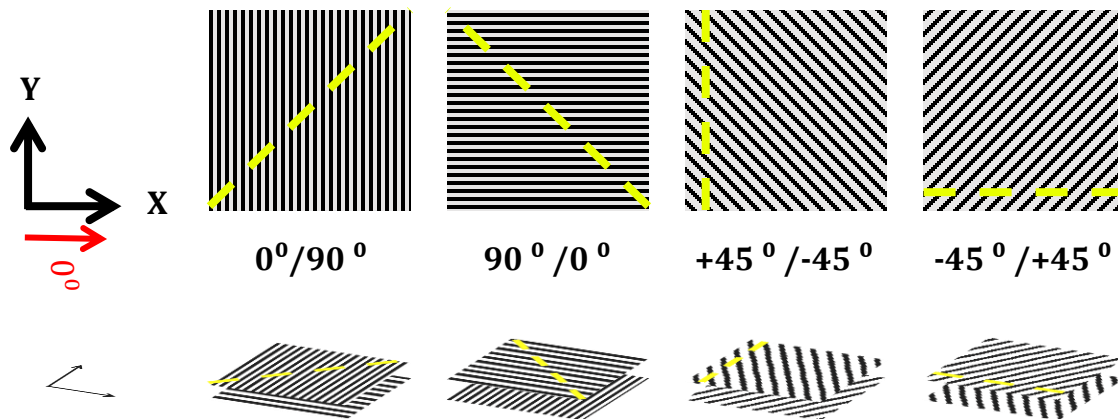
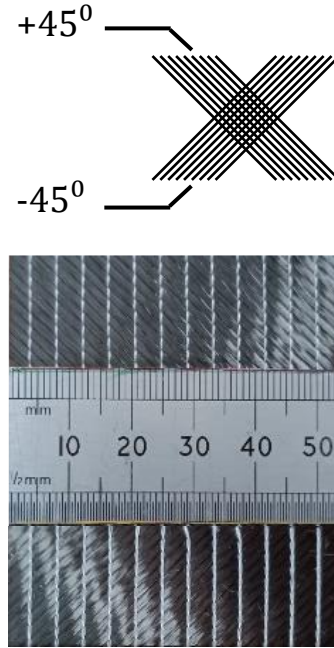


Figure 3.7. Relevant NCF ply orientations for the thesis.

As an example, for the $[0^{\circ}/90^{\circ}]$ ply, the lower unidirectional ply is oriented at 0° , whilst the upper unidirectional ply at 90° . The same rule applies to the other orientations. The chosen orientation affects the deformation, since NCFs present an anisotropic shear behaviour due to the presence of stitching.

3.1.4.2 Diaphragm

The diaphragm material plays a key role during double diaphragm forming, as it distributes pressure evenly across the material during forming. The diaphragm material must present high elasticity to stretch and conform to the desired shape without breaking. Additionally, if heat is used during the process, the diaphragm material must resist high temperatures without losing its mechanical properties.

Considering all these requirements, a thermoplastic high elongation vacuum bag film, Stretchlon HT-350 supplied by Airtech, was selected as the diaphragm material for this study. It is an excellent choice for ply compaction due to its very high elongation. This material is a higher temperature version of Stretchlon 200, with a maximum use temperature of 162 °C. However, the maximum use temperature is dependent on the duration of exposure and is process specific, so it should be tested before use. The thickness of each ply is 0.08 mm.

3.1.4.3 Breather

When forming experimentally, a breather cloth is essential to improve formability. Placed between the diaphragms without covering the fabric, the breather evenly distributes the pressure applied during forming. This ensures the fabric adapts more effectively to the desired shape. Additionally, the breather provides a pathway for releasing trapped air, enabling proper compaction of the fabric against the tool surface.

Experimental tests conducted without a breather cloth (see Figure 3.8) revealed issues, including air pockets, defects and poor conformity. These findings highlight the importance of using a breather cloth during the forming process.

The breather cloth used in this work was VACB4 lightweight polyester by Vac Innovation. The material parameters are listed in Table 3.2. This non-woven fabric is produced using the need punch manufacturing process, which converts

fibrous webs into self-locking structures using barbed needles. The needles mechanically align and reorient fibres from the surface, creating a complex three-dimensional structure [136].

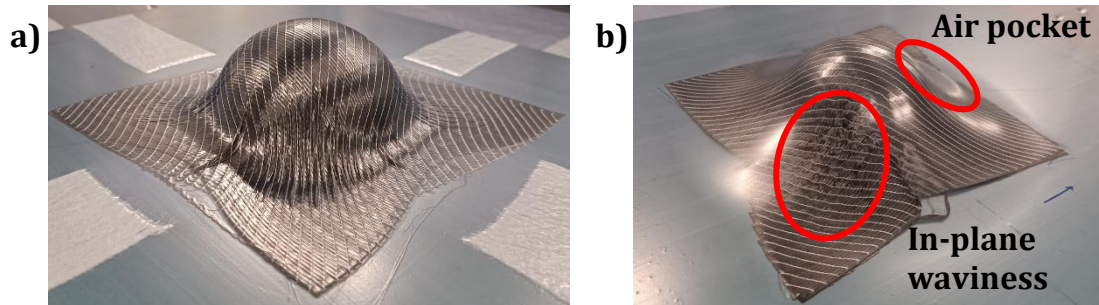


Figure 3.8. Double diaphragm hemispherical preform a) with breather and b) without breather.

Table 3.2. Material parameters for the breather material VACB4.

Material designation	VACB4
Supplier	Vac Innovation
Material colour	White
Material fibre	100% Polyester
Nominal weight (gsm)	150
Nominal thickness - uncompressed (mm)	2.5
Max usage temperature (°C)	200

Due to the nature of their manufacturing process, most non-woven materials are anisotropic. For some mechanically produced non-woven fabrics, fibres are often predominantly oriented in the machine direction, resulting in higher strength and stiffness in that direction. The machine direction corresponds to the direction in which the non-woven fabric is produced, running parallel to the production line along the length of the fabric.

The structural behaviour of VACB4 has not been previously characterised. The density was obtained by cutting two samples of known dimensions and measuring their mass. The density was determined to be approximately 50 kg/m³ (see Table 3.3).

Table 3.3. Breather dimensions, weight and density calculations.

Sample	Dimensions (mm)	Weight (g)	Density (kg/m ³)
1	70x70x2.5	0.6367	51.97
2	54x68x2.5	0.4566	49.74

To characterise the mechanical behaviour of the material, a tensile testing was performed using the Instron 5581 testing machine with a 1 kN load cell and a crosshead speed of 50 mm/min. (see Figure 3.9a). The sample size was 25 mm × 250 mm, with the grips separated by a distance of 150 mm (see Figure 3.9b). The test was finished when the applied force dropped to 50% of the peak force during the test. Figure 3.9c) presents the samples before (left) and after (right) the test, the breather samples deform significantly.

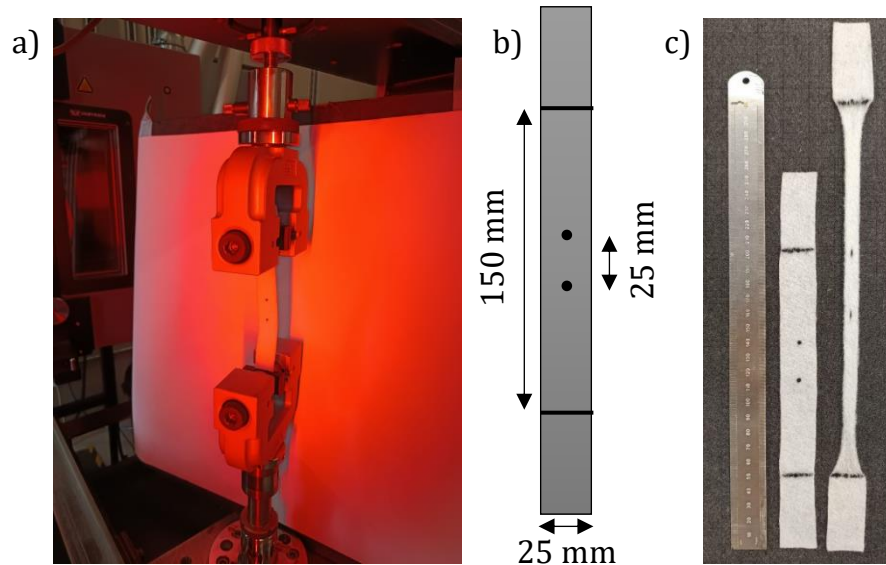


Figure 3.9. Breather tensile test a) set-up, b) sample size and c) samples before and after the test.

The samples were cut in three directions to determine the anisotropy of the material, the machine direction (parallel), the cross-machine direction (perpendicular) and at +45° from the machine direction (45°). 14 samples of each orientation were tested.

Figure 3.10 presents the force (N) vs displacement (mm) results for the three different directions. Since the breather was manufactured using needle punching, it is expected that the material presents higher strength in a particular direction.

As the direction of the samples gradually changes from perpendicular to parallel, the force required to cause displacement decreases. This means that the fabric stretches more easily under a given force. Weaker behaviour is observed because fewer fibres are aligned with the direction of the force, reducing resistance and increasing displacement. Therefore, this non-woven fabric is stronger in the perpendicular direction, which is the cross-machine direction. Additionally, when examining the samples oriented at 45° degrees, some behave more like the perpendicular samples, whilst others resemble the parallel samples, exhibiting mixed behaviour.

In this case, the material is stronger in the cross-machine direction. This could be due to fibre orientation and/or bonding process resulting in a denser and stronger structure in that direction.

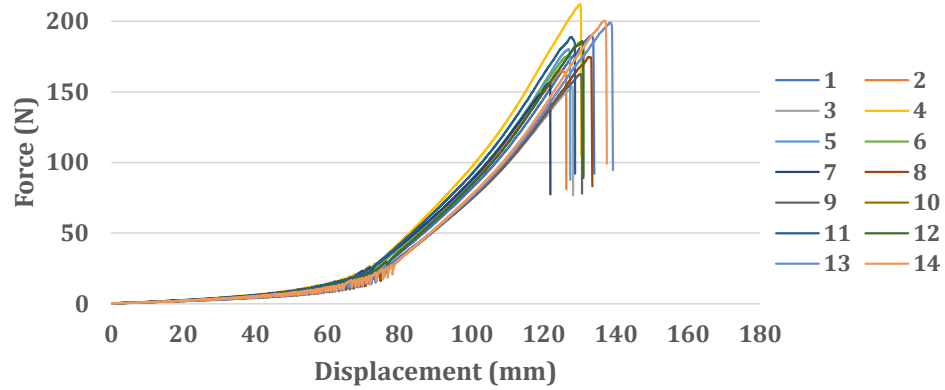
As all the samples deform considerably, it is important to understand the expected elongation during double diaphragm forming to further characterise the mechanical behaviour. This evaluation was performed by tracking three sets of points, spaced 25 mm apart, on four breather strips during forming.

The results showed that the strain levels were between 12% to 16% whilst the vacuum was on, and between 4% to 8% once the vacuum was removed. Since the initial length between grips for the tensile testing is of 150 mm, a strain of 16% is equivalent to a 24 mm displacement.

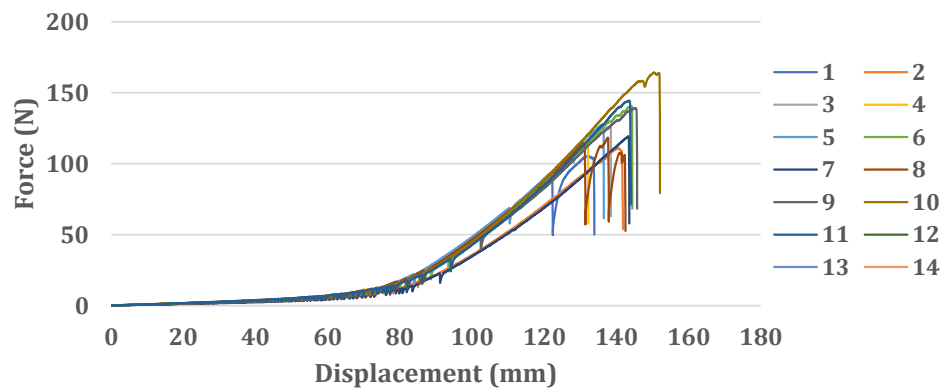
For that displacement, the force withstood by the samples was less than 4 N, being of 3.5 N for the perpendicular, 2.5 N for the 45° and 2.2 N for the parallel

samples. Since the samples deform considerably and withstand high force, the material properties depend on the stress-strain region of interest.

a) Perpendicular



b) 45°



c) Parallel

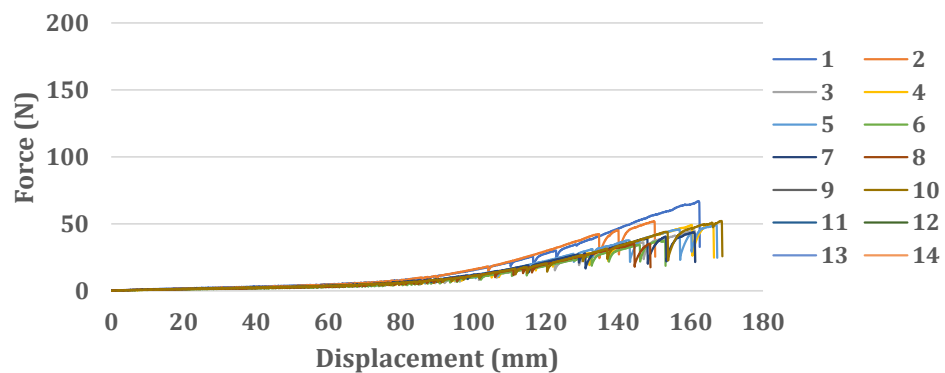


Figure 3.10. Force (N) vs crosshead displacement (mm) for samples cut in the a) perpendicular, b) 45° and c) parallel direction.

As the breather strips for all the experiments were always cut in the same direction, the perpendicular direction, the Young's modulus and Poisson's ratio will only be characterised in that direction and for a displacement of 6 mm, 12

mm, 18 mm and 24 mm, equivalent to the 4%, 8%, 12% and 16% strain experience during forming.

In general terms, the Young's modulus indicates how easily a material can stretch and deform. A higher Young's modulus corresponds to stiffer materials, whereas lower values indicate more flexible materials. The Poisson's ratio measures how much a material contracts when stretched. Most materials present a Poisson's ratio between 0 and 0.5, with materials like rubber with a ratio close to 0.5, and metals with a ratio around 0.3.

The Young's modulus, E , is the ratio of tensile stress, σ , to tensile strain, ε , and it is calculated as follows:

$$E = \frac{\sigma}{\varepsilon} = \frac{F \cdot L_0}{W \cdot t \cdot (L - L_0)} \quad (17)$$

Where σ , is calculated as the amount of applied force per unit area, and ε is calculated as the extension per unit length. Note that F is the applied force, $W \cdot t$ is the cross-sectional area after deformation, L_0 is the original length, and L is the length after deformation.

The Poisson's ratio, ν , is the ratio of the transverse strain, ε_t , to the longitudinal strain, ε_l , when the material is under tension or compression, and it can be calculated as follows:

$$\nu = -\frac{\varepsilon_t}{\varepsilon_l} = -\frac{\frac{W - W_0}{W_0}}{\frac{L - L_0}{L_0}} \quad (18)$$

Where ε_t , is calculated as the strain in the direction perpendicular to the applied load, and ε_l , is calculated as the strain in the direction of the applied load. Note that W_0 is the original width, and W is the width after deformation, L_0 is the original length, and L is the length after deformation.

To find the Young's modulus and Poisson's ratio of the perpendicular samples, a tensile test was performed using a crosshead speed of 50 mm/min. The sample size was 25 mm × 250 mm, with the grips at 150 mm.

Four samples were displaced a given distance of 6mm,12 mm,18 mm or 24 mm. For each specimen the force (F), original length (L_0), original width (W_0), final width (W) and final length (L) were recorded to calculate the Young's modulus and Poisson's ratio. Since the material is quite fluffy, its thickness was difficult to measure accurately and was therefore considered to be 2.5 mm throughout the experiment. Note that the force was extracted from the Instron readings, whilst the sample size was measured manually using a ruler; this can induce an error of ± 0.5 mm since the width variations were minimal.

The average Young's modulus and Poisson's ratio calculations for the four distances are presented in Table 3.4. The Young's modulus increases as the displacement increases, the same is observed for the Poisson's ratio, besides for the 18 mm displacement measurements, which seem to be a bit off. This is due to the difficult in measuring the width, which highly affects the Poisson's ratio calculation.

Table 3.4. Young's modulus and Poisson's ratio calculations for the different displacements

Displacement (mm)	E (MPa)	ν
6	0.165	0.49
12	0.210	0.52
18	0.209	0.38
24	0.238	0.59

Since the breather is mainly used to released trapped air and to prevent wrinkling by locally stiffening the diaphragm, the average values of 0.205 MPa for the Young's modulus and of 0.49 for the Poisson's ratio calculated are adequate.

3.2 Modelling

3.2.1 Modelling approach

The forming process is modelled in Abaqus/Explicit, as it is particularly effective to simulate complex contact interactions and large deformations involved in the forming process. This is due to its robust general contact algorithm, which can track dynamic contact regions and accommodate friction behaviour. The finite element model of the double diaphragm process consists of a machine bed with four frames, a tool, and a fabric positioned between two diaphragms (see Figure 3.11).

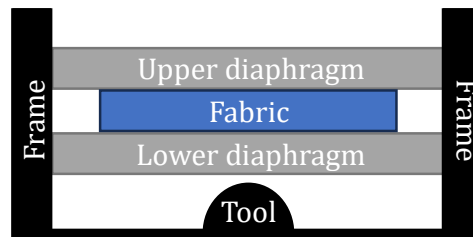


Figure 3.11. Schematic of the double diaphragm forming process with a hemispherical tool.

The tooling components – machine bed, frames, and tool – were modelled as rigid bodies using R3D4 elements. The deformable materials – fabric stack and diaphragms – were modelled as shell elements using S4R elements. The mesh and mass scaling configuration are discussed in section 3.2.3 and section 3.2.4.

The density of the fabric is 1200 kg/m^3 , and the density of the diaphragm is 1600 kg/m^3 [51]. The material properties for the fabric and diaphragm are detailed in section 2.6.2 and section 2.6.3, respectively. In general terms, the fabric properties are defined using a non-orthogonal constitutive model implemented through a user-defined subroutine, considering the in-plane shear and bending behaviours. The diaphragm properties are defined using the Marlow model for hyperelastic materials, which fits stress-strain response under different loading conditions [131].

The interactions between the parts were modelled using a penalty contact algorithm with Coulomb friction. The coefficients of friction for each contact pair were calculated by Yu et al. [131] using the methodology described in Chen et al. [51]: tool-diaphragm: 0.51, fabric-diaphragm: 0.40, fabric-fabric: 0.36, and diaphragm-diaphragm: 0.30. For the fabric-fabric and fabric-diaphragm couples, the coefficient of friction was obtained by averaging values at different fibre orientations.

Displacement boundary conditions were applied to the tooling components, restricting their translational and rotational degrees of freedom. Additionally, the diaphragms were constrained around their perimeter to replicate the constraints on the forming rig, similarly restricting their translational and rotational degrees of freedom. These constraints ensured that both the tooling components and diaphragms remained stationary in the specified directions, accurately modelling the physical set-up of the forming process.

The forming process was simulated using three dynamic analysis steps. Figure 3.12 shows the pressure variation for the upper and lower diaphragms throughout the simulation. The total simulation time was set to 1.6 seconds to ensure a reasonable computational time.

- In the first step, between times 0 s and 0.1 s, two pressures equal in magnitude (0.1 MPa) but opposite in direction were applied to model the in-bag vacuum between the diaphragms.
- In the second step, between times 0.1 s and 0.6 s, the pressure difference was maintained, and a displacement boundary condition was applied to the diaphragms to initiate contact with the machine bed.
- In the third step, between times 0.6 s and 1.6 s, the pressure of the lower diaphragm was reduced until it reached 0 MPa to generate vacuum between the lower diaphragm and the bed.

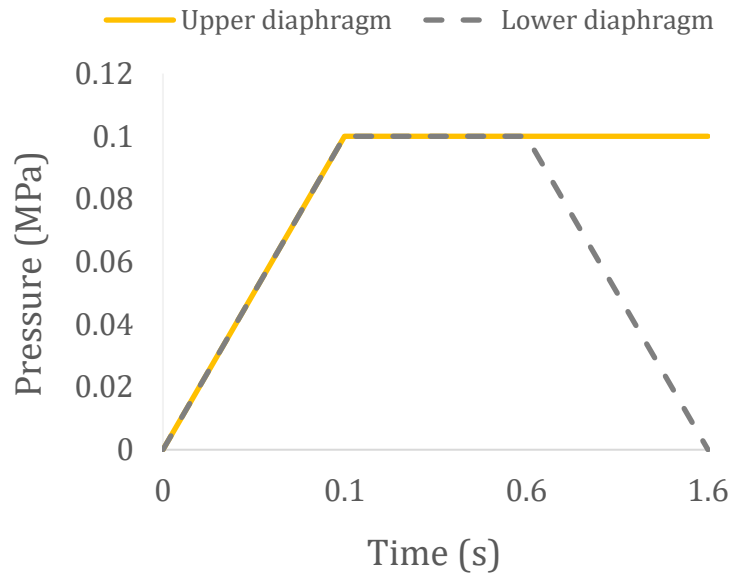


Figure 3.12. Pressure variation for the upper and lower diaphragms as a function of time.

3.2.2 Model set-up/ Parameters of simulations

Several numerical studies are introduced throughout this work. This section outlines the model parameters in Table 3.5 (mesh size, mass scaling, number of CPUs and PC specifications) and the process parameters in Table 3.6 (NCF orientation, fabric and diaphragm size and tool) for all the numerical studies. It is important to note that the number of CPUs used during the analysis impacts only the computational time, not the accuracy of the results. This was confirmed by running the same model with different number of CPUs and comparing the predictions, which showed no variation in the results.

Table 3.5. Model parameters for all the numerical studies.

Study	Mesh size (mm)	Mass scaling	Number of CPUs	PC Specifications
3.2.3.1 S4 vs S4R	2, 4 and 6	100	2	Intel® Core™ i3-8100 CPU @ 3.60GHz
3.2.3.2 Mesh size	1, 2, 3, 4, 5 and 6	100	2	Intel® Core™ i3-8100 CPU @ 3.60GHz
3.2.3.3 Mesh conf.	2	100	8	HPC facilities: Intel® Xeon® Gold 6138 CPU @ 2.0 GHz
3.2.4 MS effect	2	10, 50, 100-1,000	2	Intel® Core™ i3-8100 CPU @ 3.60GHz
3.2.5 Fabric par.	2	100	8 or 36	HPC facilities: Intel® Xeon® Gold 6138 CPU @ 2.0 GHz
5.1 Diap. size	2	100	2, 4 or 6	HPC facilities: Intel® Xeon® Gold 6138 CPU @ 2.0 GHz
5.2 Breather	2	100	36	HPC facilities: Intel® Xeon® Gold 6138 CPU @ 2.0 GHz
6.2 Hor. sep.	2	100	8	HPC facilities: Intel® Xeon® Gold 6138 CPU @ 2.0 GHz
6.3 Vert. sep.	2	100	8	HPC facilities: Intel® Xeon® Gold 6138 CPU @ 2.0 GHz

Table 3.6. Process parameters for all the numerical studies.

Study	NCF orientation	Fabric size (mm)	Diaphragm size (mm)	Tool
3.2.3.1 S4 vs S4R	$[0^0/90^0]$	200×200	500×500	50r
3.2.3.2 Mesh size	$[0^0/90^0]$	200×200	500×500	50r
3.2.3.3 Mesh conf.	$[90^0/0^0, 0^0/90^0]$	200×200	1600×1240	50rplatf
3.2.4 MS effect	$[0^0/90^0]$	200×200	500×500	50r
3.2.5 Fabric par.	$[90^0/0^0, 0^0/90^0]$	200×200	1600×1240	50rplatf
5.1 Diap. size	$[0^0/90^0]$ and $[+45^0/-45^0]$	400×400	412×412 to 2000×2000	100r
5.2 Breather	$[90^0/0^0, 0^0/90^0]$, $[90^0/0^0]$ and $[-45^0/+45^0, +45^0/-45^0]$	200×200	1600×1240	50rplatf
6.2 Hor. sep.	$[0^0/90^0]$	400×400	2000×2000	2x100r
6.3 Vert. sep.	$[0^0/90^0]$	400×400	2000×2000	2x100r

3.2.3 Mesh configuration

This section examines three different aspects of the mesh configuration, focusing on determining the appropriate mesh elements for the fabric and diaphragm, and conducting a mesh size sensitivity study to ensure the accuracy of the numerical predictions.

3.2.3.1 S4 vs S4R elements

The bending behaviour significantly influences wrinkling formation, as both the number and size of wrinkles are affected by the bending stiffness. While membrane elements only account for in-plane stiffness, shell elements also capture the bending and transverse shear stiffness. Therefore, shell elements provide an accurate representation of the mechanical behaviour of thin composite reinforcements.

Several shell element types are available in Abaqus/Explicit. This study was performed to evaluate the suitability of S4 and S4R shell elements for meshing the fabric.

A description of the S4 and S4R elements can be found in the Abaqus User's Manual [137]. The S4 element is a fully integrated finite-membrane-strain element designed for all purposes of the shell problem. However, this type of low-order quadratic element is prone to shear locking. Shear locking occurs when the element edges cannot bend, resulting in spurious shear stress. This phenomenon causes the element to deform less than expected, making it appear stiffer than it is. Shear locking can be overcome by reduced integration [130], as this method uses fewer integration points for the stiffness calculations, reducing the overestimated shear stiffness and allowing the element to deform more realistically in bending-dominated situations.

The S4R element is the reduced integrated quadrilateral finite-membrane-strain element. These elements exhibit reduced stiffness, and hourglass stabilisation can be applied to prevent mesh distortion. Additionally, reduced integration elements have less integration points, which significantly reduces computational time (see Figure 3.13). Therefore, S4R elements are preferred over S4 elements to simulate this forming process due to their ability to avoid shear locking and provide more consistent and realistic shear angle predictions.

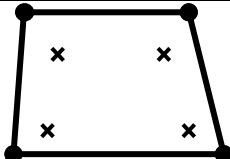
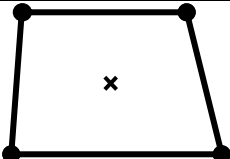
	S4 - Full integration	S4R - Reduced integration
First-Order interpolation		

Figure 3.13. Integration points for S4 and S4R elements for the first order-interpolation.

3.2.3.2 Mesh size sensitivity

When selecting an adequate mesh size, a mesh convergence study is essential to ensure that the numerical analysis provides accurate solutions to the desired level. Convergence is achieved when further refinement of the mesh produces negligible changes in the solution. It is advisable to begin with a coarse mesh that provides reasonable outputs and then gradually refining the mesh size until convergence is achieved.

The aim of this study is to understand the effect of mesh size on the accuracy of the model and to determine an appropriate mesh size that ensures convergence of results while reducing computational time.

For this study, the mesh size values range from 6 mm, representing the lowest mesh density, to 1 mm, representing the highest mesh density (see Figure 3.14). The fabric ply with a 6 mm mesh consists of 1,089 elements, whilst the fabric ply with a 1 mm mesh consists of 40,000 elements. This increase in number of elements considerably affects running time, since the solver needs to perform more calculations to solve the system of equations.

Figure 3.15 presents the shear angle contours for the S4R elements for different mesh sizes: 2 mm, 4 mm and 6 mm. As mentioned previously, NCFs exhibit an anisotropic shear behaviour due to stitching, displaying different performance in positive and negative shear [36]. The shear contours highlight the influence of the element size on the accuracy of the results, as wrinkling is barely visible with 4 mm and 6 mm meshes. Therefore, the mesh should be

sufficiently refined to accurately characterise the location, shape and size of defects.

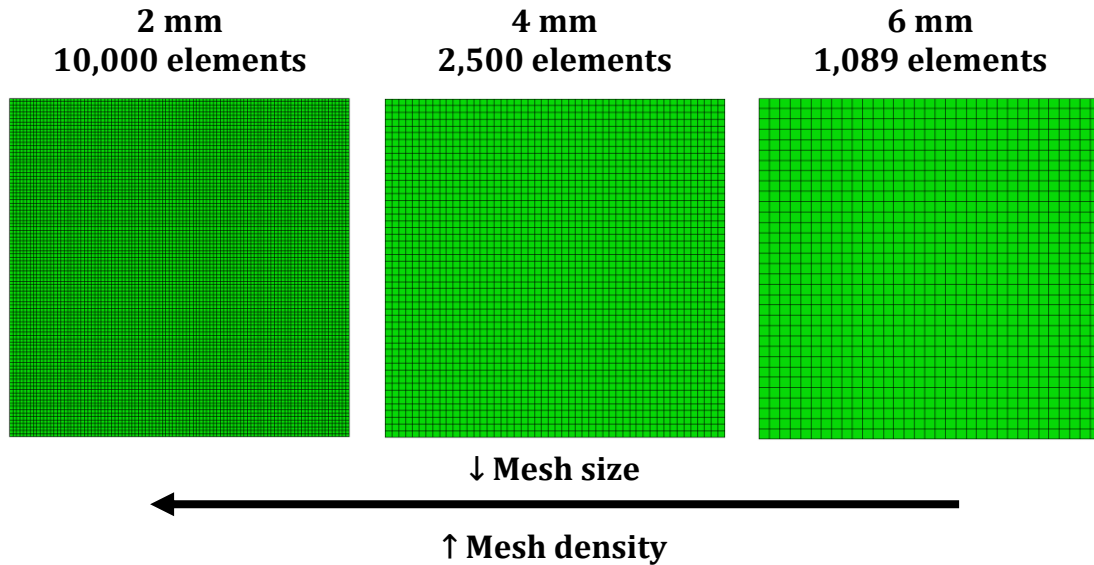


Figure 3.14. Mesh size vs mesh density for a mesh size of 2 mm, 4 mm and 6 mm.

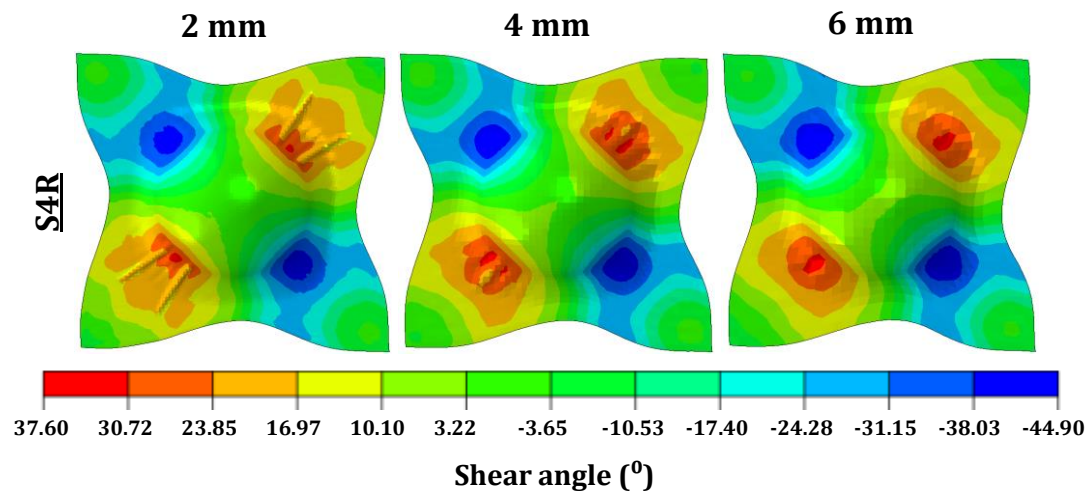


Figure 3.15. Shear angle ($^{\circ}$) contour for the fabric for S4R elements for the different mesh sizes.

While smaller mesh sizes capture details of meshed parts more accurately, they must be carefully considered. If the mesh size is too small relative to the dimensions and material properties of the part, shell elements can become overly rigid. Furthermore, decreasing the mesh size reduces the stable time increment

significantly increasing computational time. Therefore, selecting an appropriate mesh size is crucial for ensuring the accuracy of the results.

The parameters considered to assess mesh convergence were the CPU time and the maximum in-plane principal stress on the fabric. Initially, the energy balance was also considered. However, it exhibited only minor fluctuations, indicating that the mesh size presents a negligible dynamic effect, and thus only computational time and stress were considered.

Figure 3.16 presents the CPU time and maximum in-plane principal stress for the different mesh sizes under study. The CPU time decreases as the mesh size increases, as expected. Convergence for the maximum in-plane principal stress on the fabric is achieved for a mesh size of 2 mm. Based on these observations a mesh size of 2 mm was selected for this forming model.

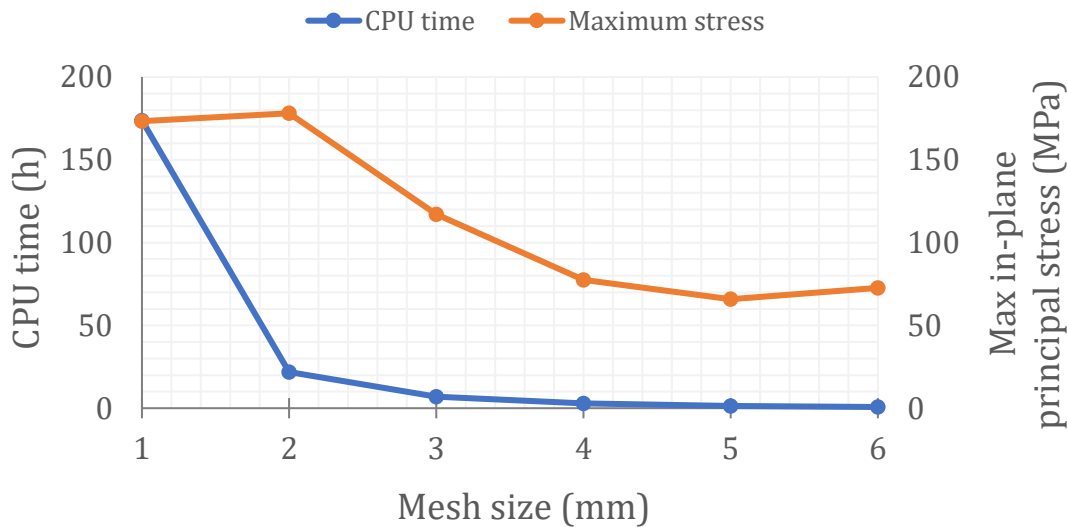


Figure 3.16. CPU time (h) and maximum in-plane principal stress on the fabric (MPa) for the different mesh sizes.

3.2.3.3 Diaphragm: membrane vs shell elements

The fabric material is modelled using shell elements due to the requirement to capture its bending behaviour. However, for the diaphragm material, either membrane or shell elements could be used, as its bending behaviour is not

explicitly defined when using the Marlow model, as explained in section 2.6.3. Since membrane elements are more computationally efficient than shell elements, incorporating bending behaviour in the simulation would likely increase the computational cost without significantly enhancing the accuracy of the numerical results. This section investigates which element type – membrane or shell – would be better suited for modelling the diaphragm.

The parameters considered to evaluate the element types were the shear angle distribution on the fabric, the von Mises stress distribution on the upper diaphragm and the computational time. Figure 3.17 presents the shear angle distribution on the fabric when using membrane and shell elements to mesh the diaphragm. The shear distribution is barely affected. The wrinkling patterns are quite similar for both element types, with wrinkles of similar size occurring in the same areas.

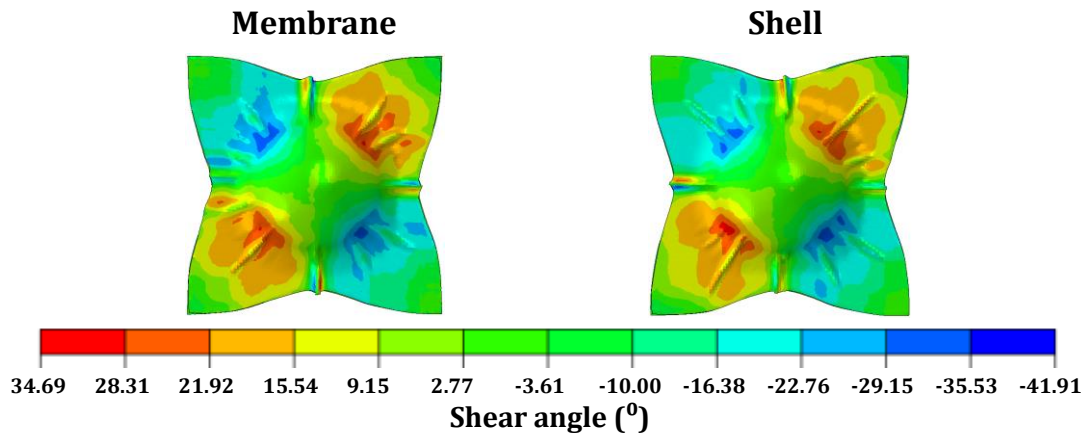


Figure 3.17. Shear angle ($^{\circ}$) contour for the fabric when using membrane and shell elements to mesh the diaphragm.

Table 3.7 presents the maximum and minimum shear values and the computational time when using membrane and shell elements for the diaphragm mesh. The predictions are 10^0 higher for the membrane elements. This indicates that membrane elements allow for higher deformation and, therefore, shear behaviour. In terms of computational time, the membrane diaphragm is only 2.35 hours quicker than the shell diaphragm. In this case, the computational

differences are not significant enough to outweigh the benefits of using shell elements for more accurate predictions.

Therefore, given the differences in predictions shown by both elements, shell elements were selected as the predictions are more accurate and reliable.

Table 3.7. Maximum and minimum shear angle values and computational time when using the membrane and shell elements to mesh the diaphragm.

Element type	Max shear (°)	Min shear (°)	CPU time
Membrane	44.55	-51.66	1d 13h 47m 55s
Shell	34.69	-41.91	1d 16h 7m

3.2.4 Effect of mass scaling

The mass scaling factor decreases the computational time by artificially increasing the density of the model, increasing the stable time increment. This should be done with caution, as higher mass scaling values can induce stability problems and result in incorrect solutions. Therefore, the aim of this study is to reduce computational time while ensuring the stability and accuracy of the forming predictions.

The aim of the study was to reduce the computational time while ensuring the energy levels indicate that the forming process was modelled as a quasi-static procedure. Quasi-static conditions are ensured when the kinetic energy of the deformable materials remains a small fraction (typically below 5% to 10%) of the internal energy of all parts throughout most of the analysis.

The parameters considered to evaluate the mass scaling factor were the CPU time, the energy levels and the shear angle distribution on the fabric. Figure 3.18 presents the CPU time and the ratio of all kinetic energy to all internal energy (%ALLKE/ALLIE) for the different mass scaling factor values under study. The CPU time decreases as the mass scaling factor increases, as expected. The

%ALLKE/ALLIE increases with the mass scaling factor, indicating that the process is becoming less quasi-static.

To ensure a quasi-static process, the energy ratio should be kept below 10%. Therefore, the mass scaling factor should ideally be below 500. When considering the CPU time, the mass scaling factor should ideally be above 50 to reduce running time. Considering both parameters, the mass scaling factor for this forming should ideally be between 50 and 500.

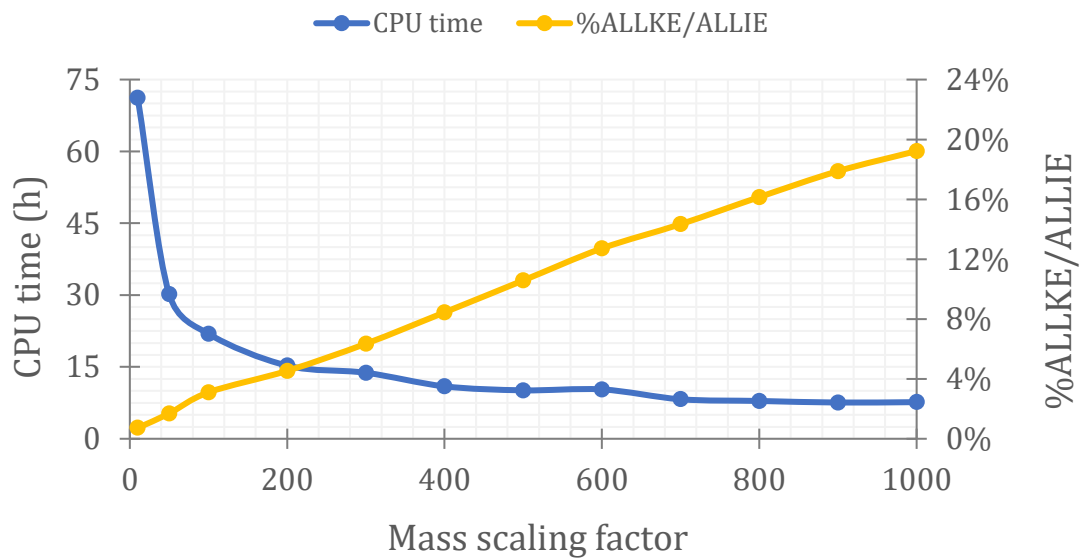


Figure 3.18. CPU time (h) and ratio of all kinetic energy versus all internal energy (%ALLKE/ALLIE) for the different mass scaling factor values ranging from 10-1000.

The dynamic effect is controlled by the energy balance of the model, which has been determined to be quasi-static for mass scaling values below 500. However, increasing the mass scaling value also increases the inertia of the elements, potentially affecting the initiation and growth of wrinkles.

Figure 3.19 presents the shear angle contours for mass scaling values of 10, 200, and 400. The shear distribution remains relatively consistent across the samples. The maximum shear values for all the samples have a standard deviation of 1.24, whilst the minimum shear values have a standard deviation of 0.79. These variations are not considered significant.

However, the wrinkling pattern, especially the size and number of wrinkles, varies with the mass scaling value. Therefore, validation against experimental data is needed to ensure that the mass scaling does not significantly affect the accuracy of wrinkling predictions.

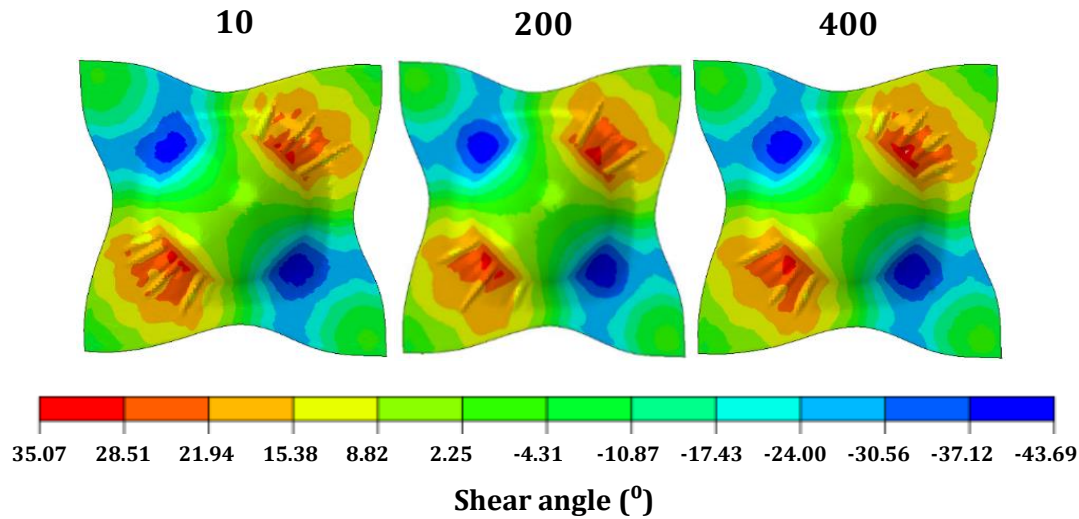


Figure 3.19. Shear angle ($^{\circ}$) contour for the fabric for a mass scaling of 10, 200 and 400.

3.2.5 Fabric parameters

Another approach to decrease computational time is to artificially reduce the tensile properties in each of the fibre directions. This reduction is allowed provided that the change in material properties has a negligible effect on the forming predictions [138].

Additionally, when modelling multiple NCF plies, the laminate can be represented either as a single part or as individual parts for each ply in the laminate (see Figure 3.20). In both cases, each ply has the same thickness, and the spacing between plies is identical to prevent any penetration issues. This choice affects the level of detail, computational resources, and results. However, it does not impact the material orientation definition, which is defined individually for each ply using the 'Composite Layup' module.

Modelling each ply individually can better represent the manufacturing process and capture the interaction between plies more accurately, but it also increases model complexity. Conversely, using a single part for the laminate assumes that the plies are bonded, which simplifies the model but might not fully capture the interactions between plies.

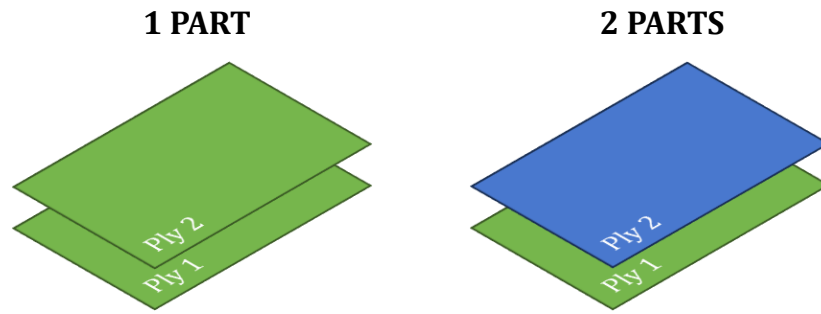


Figure 3.20. Schematic of the distribution of the plies per part.

The aim of this section is to investigate the impact of the selected Young's modulus for the fabric material, and the number of parts used to model the laminate on the model predictions.

Four different cases have been modelled to study the effect of the parameters, the parameter definition for each case can be found in Table 3.8. Note that the model with 2 parts and a Young's modulus of 3 GPa does not run to completion and therefore cannot be used for comparison. This is potentially due to contact issues that could not be resolved.

Table 3.8. Parameters for each case in the fabric parameter study.

Case	Number of parts	Young's modulus (GPa)
A	1 part	3
B	1 part	30
C	2 parts	30
D	2 parts	300

The shear angle distribution on the fabric and the von Mises stress distribution on the upper diaphragm were considered to evaluate the impact of the parameters on the forming predictions.

Figure 3.21 presents the shear angle contours for the different cases. The shear distribution is significantly affected by the number of parts used to model the laminate. The cases modelled with two parts (C and D) exhibit an uneven and distorted shear distribution, which is unrealistic. Additionally, the flat areas of the fabric present shakiness compared to cases A and B, indicating some instability or irregular behaviour in the simulation.

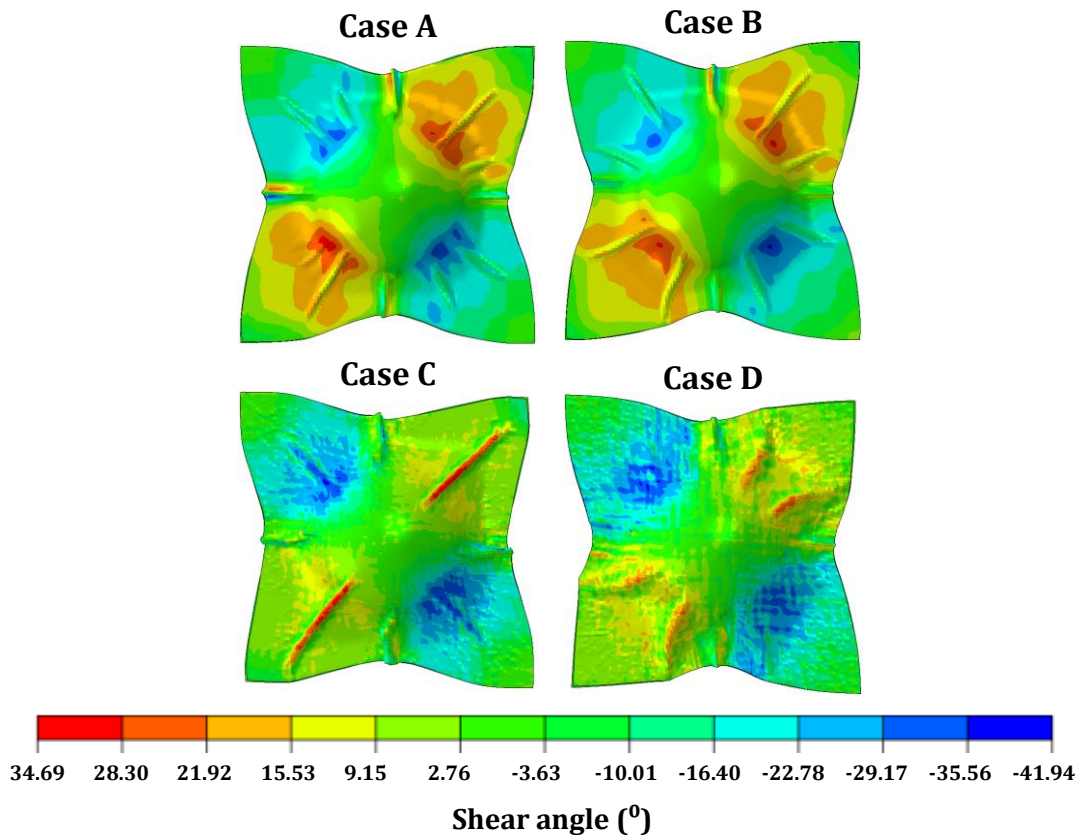


Figure 3.21. Shear angle (°) contour for the fabric for the different cases in the fabric parameter study.

The wrinkling pattern differs between cases C and D, suggesting that the Young's modulus influences the distribution of the defects and increases bridging around the tool. This can be explained by the increased rigidity of the material

with a higher modulus, which leads to shear concentration in specific areas. This behaviour is not observed for the 1 part cases (A and B), where the wrinkling pattern is more consistent and the preforms exhibit lower bridging around the hemisphere.

To investigate the possible causes of instability, the maximum and minimum shear angle values and the energy balance are analysed. Table 3.9 presents these values for the different cases under study. The maximum and minimum shear angles are generally close in value, except in Case C, which exhibits a considerably lower value. Regarding energy, Case A and B present similar energy levels for both fabrics. However, in Case C and D, fabric 1 exhibits significantly lower energy compared to fabric 2, with an energy balance 6 to 9 times higher than the other values.

In an ideal forming process, all the plies within a laminate should experience similar energy levels, assuming the same material properties, boundary conditions and applied loads. Variations in anisotropy, ply orientation, contact conditions, friction, boundary conditions, or process variability can result in differences in energy. In this case, all the models were identical except the modelling of the different plies within the laminate. This discrepancy suggests a potential issue with contact conditions, as one ply absorbs more energy than the other, indicating instability.

Table 3.9. Maximum and minimum shear, and energy balance for both plies for the different cases in the fabric parameter study.

Case	Max shear (°)	Min shear (°)	Ply1 %KE/ALLIE	Ply2 %KE/ALLIE
A	34.69	-41.94	0.300%	0.301%
B	35.30	-36.48	0.284%	0.283%
C	38.57	-57.63	0.191%	1.820%
D	30.16	-42.75	0.191%	1.810%

The von Mises stress distribution on the upper diaphragm was also assessed. When examining the distribution for Case A and B, there was minimal variation between the distributions. The same observation applied to Case C and D. Therefore, the preforms are subjected to the same stress distribution. This indicates that the forming differences observed between preforms with different Young's modulus arise from the increased rigidity with higher Young's modulus, and not from stress distribution on the diaphragm.

However, when comparing Case B and C, presented in Figure 3.22. some differences can be observed in the von Mises stress distribution. The outer stress distribution around the tool is similar for both cases, showing a gradual increase in stress towards the diaphragm edges.

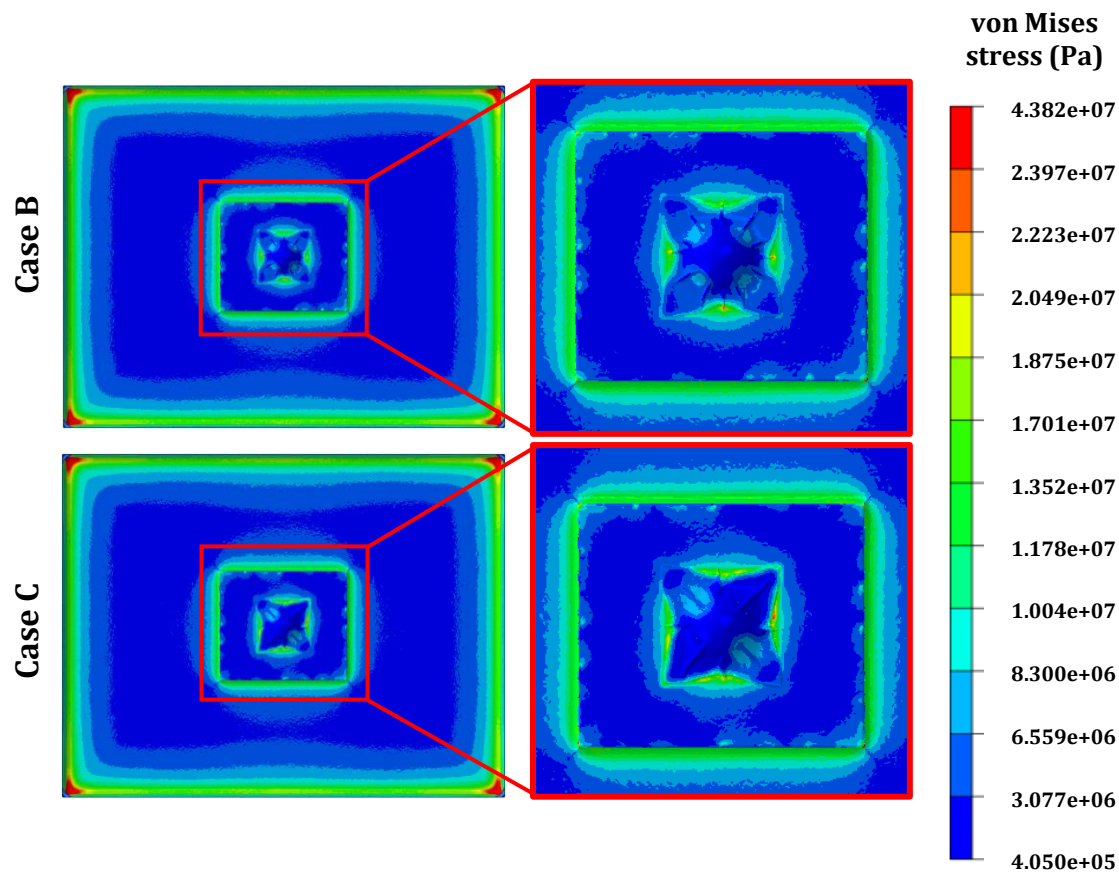


Figure 3.22. von Mises stress distribution in the upper diaphragm for case B and C in the fabric parameter study.

On the contrary, the stress distribution on the fabric is different. In Case B, the same pattern is observed in all the quadrants, with lower stress at the centre of the hemisphere and fabric edges, slightly increasing in the rest of the preform. In case C, two quadrants follow the same distribution, but the stress is reduced on the other two, corresponding to the wrinkling area in Figure 3.21. This clearly indicates that increased stress helps to reduce the occurrence of defects or the severity and length of wrinkles once the defect has formed.

Therefore, the results indicate that increasing the Young's modulus increases the rigidity of the material, leading to forming differences. Additionally, modelling the plies as separate parts or within a single part affects the shear stress and von Mises stress distribution. Hence, it is better to model all plies within one part and to use a Young's modulus below 30 GPa to minimise the impact of these parameters on defect predictions.

3.3 Chapter summary

This chapter introduced the experimental and numerical methodologies used in this work. The mechanical behaviour of the breather material was characterised. This information will be used in section 5.5 for the numerical simulations.

For the numerical model, reduced integration shell elements were found to offer more consistent and realistic predictions for both the fabric and diaphragm. A mesh size of 2 mm was determined to be sufficient, balancing result convergence and computational efficiency. To maintain quasi-static conditions while ensuring reasonable computational time, mass scaling should ideally be between 50 and 500, keeping the energy balance below 10%. However, the wrinkling pattern, particularly the size and number of wrinkles, was found to be influenced by the mass scaling.

Artificially increasing the Young's modulus of the fabric can reduce computational time, but it should remain below 30 GPa to avoid affecting the forming predictions. Additionally, modelling all plies within a layup as a single part was found to improve prediction accuracy, minimising the impact on predictions.

Chapter 4 Validating the numerical model

This chapter focuses on the validation of the numerical predictions. Section 4.1 outlines several approaches to evaluate the forming process. Section 4.2 presents the experimental and numerical data used in section 4.3 to compare the numerical predictions with the experimental results.

4.1 Characterisation/Evaluation of forming

Evaluating how the preform conforms to the tool is crucial, as this directly impacts the performance of the final component. Any defects in the preform before infusion will introduce weakness, such as reduced strength or durability, in the final component. This section explores several approaches to evaluate the forming process, each focusing on different parameters and techniques.

4.1.1 Shear angle

In fabrics, the shear angle represents the angle change between the yarns and can be used to monitor local deformation. This angle plays a crucial role in determining the performance of the final component, as the fibres are the principal load-carrying elements within the composite structure.

When the maximum shear angle is reached, the fabric can no longer deform in-plane, leading to out-of-plane deformation [64]. This angle is known as the shear locking angle. Maintaining the shear deformation below the locking angle should prevent the onset of wrinkles. Some forming simulation approaches use this concept to predict wrinkling if this angle is reached or exceeded [61]. However, it has been demonstrated that the locking shear angle is not the only parameter determining wrinkling behaviour. Bending stiffness also affects the number and size of wrinkles in textile composites [61].

When considering both shear and bending behaviour, the low bending stiffness of the biaxial NCF might make it easier to bend the material rather than shearing it at high shear angles. This could lead to localised buckling or wrinkling even if the shear locking angle has not been reached.

This effect can be observed in the results presented in section 3.2.3.1. In Figure 3.15, the shear contour for the 2 mm S4R sample presents wrinkling. The maximum and minimum shear values are both below the shear locking angle for the FCIM359 material, which is 43° for the positive shear and 50° for the negative shear [41]. Since the numerical model in this thesis considers bending behaviour, the material wrinkled before the shear locking angle was reached. These observations indicate that the shear angle alone is not sufficient to fully characterise the forming process.

4.1.2 Deformed shape

The outline of the preform is directly linked to the material draw-in, indicating changes in the material deformation during forming. The outline path and diagonal measurements can be compared between the simulation and the experiments to evaluate the predictions.

For a square preform, the outline shape is affected by the material orientation as the same deformation will affect how the fibres deform based on their alignment (see Figure 4.1).

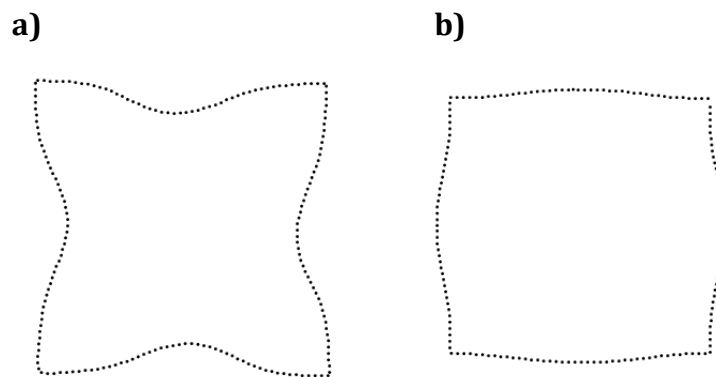


Figure 4.1. Deformed outline examples for the a) $[0^\circ/90^\circ]$ and b) $[+45^\circ/-45^\circ]$ NCF plies.

To assess the outline and the diagonal lengths throughout the thesis, the following nomenclature will be used (see Figure 4.2). The outline consists of four edges, labelled as top, bottom, right and left. The diagonals are labelled as diagonal 1 and diagonal 2.

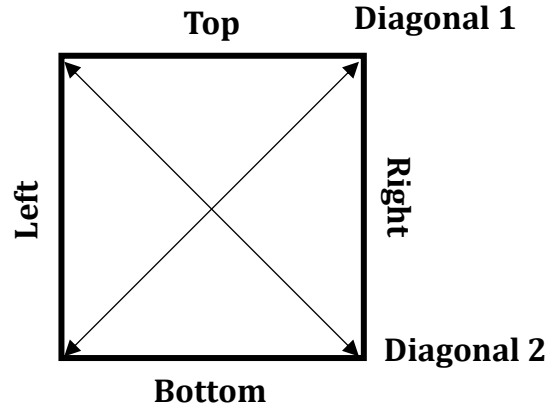


Figure 4.2. Outline and diagonal nomenclature for future assessment of the forming.

4.1.3 Preform-tool distance (Dist2Tool)

The preform-tool distance indicates the conformity of the preform to the desired shape, while also highlighting the location of out-of-plane defects such as wrinkling or bridging. The presence of these defects significantly reduces the performance of the final component.

The distribution of defects is established by calculating the Euclidean distance between the preform and the tool:

$$Dist2Tool = (x_P - x_T)^2 + (y_P - y_T)^2 + (z_P - z_T)^2 \quad (19)$$

where (x_P, y_P, z_P) are coordinates of a point on the preform and (x_T, y_T, z_T) coordinates of a point on the tool. This operation is performed by selecting the shortest distance between a preform point and all tool points. The shorter the distance, the closer the preform forms to the desired shape.

This calculation can be performed using 3D coordinates from experimental and numerical data. For the distance calculations to be accurate, both point

clouds should have the same origin. This is possible for numerical data, as all the parts are positioned using a global coordinate system. However, when using experimental data, each point cloud has a local coordinate system, as the position of the target dots varies with each scanner.

The experimental point cloud can be manually aligned using MATLAB before the *Dist2Tool* calculation. However, this manual alignment may introduce a variability of ± 0.5 mm, depending on the precision of the manual alignment. This alignment is done ensuring that the preform point cloud is centred with respect to the hemispherical tool point cloud, and that the preform cloud is positioned above the tool point cloud in the Z-axis, as there is no penetration during experimental forming.

4.1.3.1 Critical threshold

Out-of-plane defects are detected when the preform-tool distance, referred to as *Dist2Tool*, exceeds a critical threshold. Several threshold values – 1 mm, 1.5 mm, 1.75 mm and 2.5 mm – were selected for evaluation. Figure 4.3 presents the preform points where the distance exceeds the threshold and Table 4.1 presents the percentage of points above the critical distance.

As it can be observed, critical distances of 1 mm and 1.5 mm include points from the central hemispherical area, which typically does not present defects and conforms accurately to the tool. This suggests that these threshold values are too low, as they detect points which are known to conform to the tool. Critical distances of 1.75 mm and 2.5 mm provide a similar conformity percentage. However, when considering wrinkling length, the 2.5 mm threshold reduces their length. For example, a wrinkle measuring 79.93 mm for the 1.75 mm threshold is reduced to 71.55 mm when using the 2.5 mm threshold. This indicates that points which are part of the wrinkle are assumed to conform to the tool. Based on these observations, 1.75 mm was selected as the critical distance value for conformity.

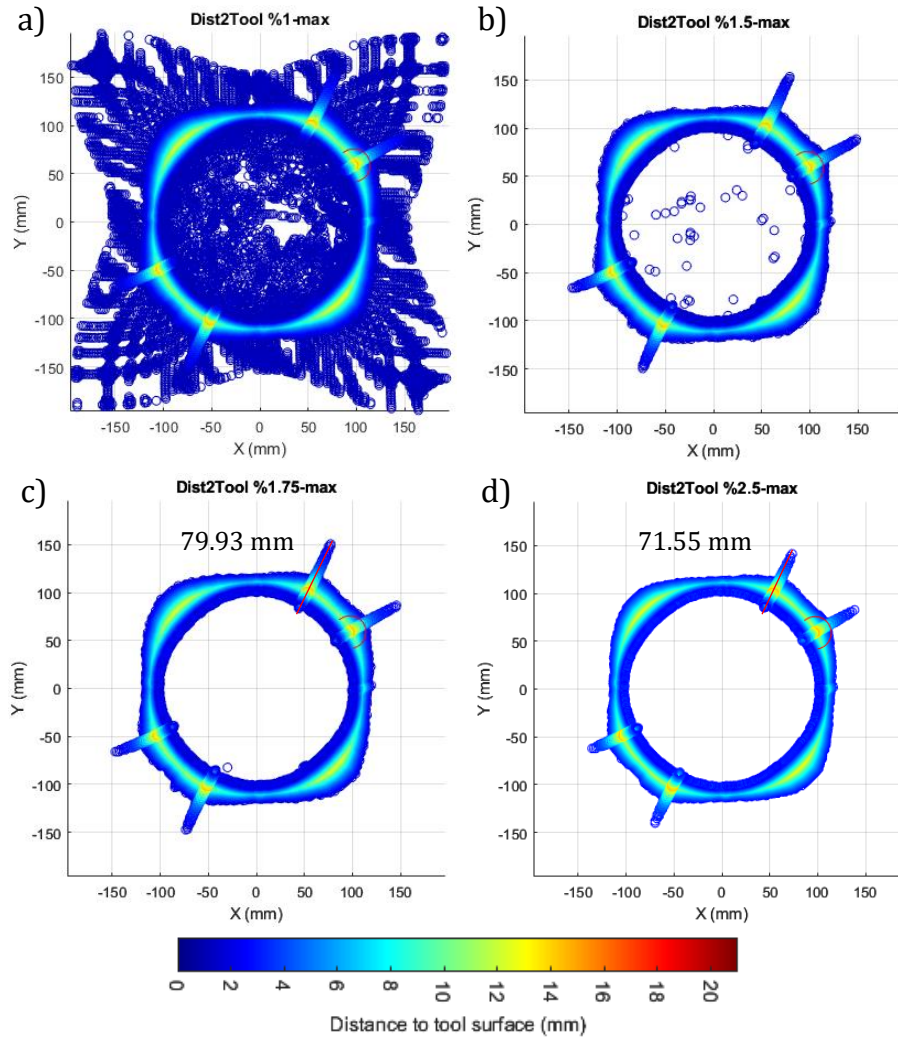


Figure 4.3. Preform points with a Dist2Tool above the threshold of a) 1 mm, b) 1.5 mm, c) 1.75 mm and 2.5 mm.

Table 4.1. Percentage of points above the threshold values of 1 mm, 1.5 mm, 1.75 mm and 2.5 mm.

Threshold (mm)	1	1.5	1.75	2.5
%threshold-20	44.68%	18.93%	17.56%	17.77%

The key information that can be extracted from the distance calculation to evaluate the preform conformity includes the preform-tool distance contour, the maximum distance value, and the percentage of points below the threshold, referred to as %0-1.75. This percentage represents the proportion of points that conform to the desired shape and will be referred to as ‘conformity’ when analysing the results.

In this thesis, wrinkle severity is defined by the size of the wrinkle, as measured by the preform-tool distance. A higher value indicates a more severe defect. For example, a wrinkle with a preform-tool distance of 13 mm is considered more severe than other with a distance of 7 mm, independent of the wrinkle length.

4.1.4 Evaluation of methods

Three approaches to evaluate the forming process have been presented. The information provided shows that relying on the shear angle might not be sufficient to fully characterise the forming process. Obtaining the shear angle distribution experimentally requires specialised equipment to detect fibre angles coupled with a grid method (see Figure 4.4) [33]. This methodology allows to directly compare the perimeter shape and local shear angles of the experimental samples against the numerical results. The grid method adds complexity to the evaluation, as it can be time consuming and intricate to draw accurately.

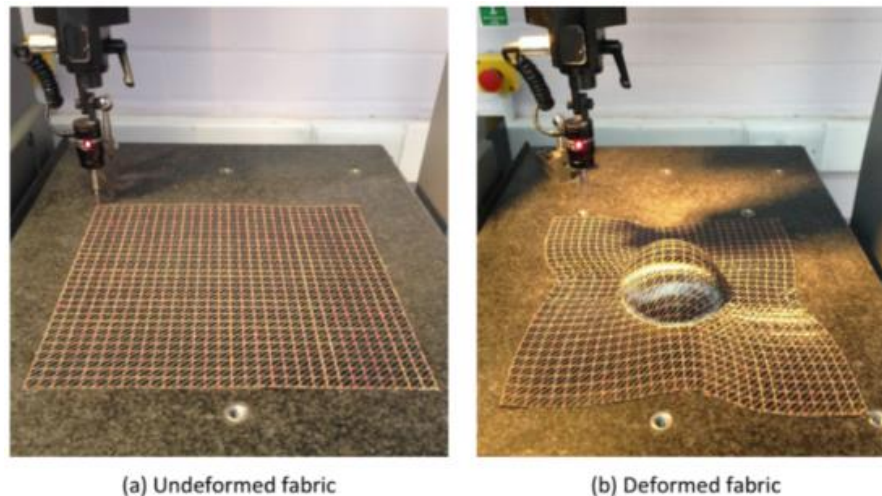


Figure 4.4. Grid measurement of the undeformed and deform fabric using a coordinate measuring machine [33].

In contrast, both the deformed shape and preform-tool distance can be extracted from 3D coordinates, simplifying the process. Experimentally, these coordinates are obtained using a scanner, whilst numerically, they are linked to the nodes of the part. The preform-tool distance provides insights into defect

distribution, whilst the deformed shape reveals information about the material draw-in during forming.

These parameters offer a comprehensive evaluation of the forming process, capturing essential information about the material behaviour and potential defects, making them sufficient to characterise the forming process without the added complexity of measuring shear angles.

4.1.5 Defect distribution chart

This section identifies and labels the areas of the preform that are most susceptible to defects. These labelled regions serve as reference areas for subsequent data analysis, simplifying the assessment of defect occurrence and distribution across the preforms.

These areas are labelled for the main material orientations used in this work, $[0^\circ/90^\circ]$ and $[+45^\circ/-45^\circ]$. Both orientations present different shear deformable areas, which depend on the stitch orientation. The shear deformable area is oriented at $\pm 45^\circ$ for the $[0^\circ/90^\circ]$ and at 0° and 90° for the $[+45^\circ/-45^\circ]$ orientation (see Figure 4.5). Opposing shear areas, denoted as A and B, present the same behaviour, either positive or negative.

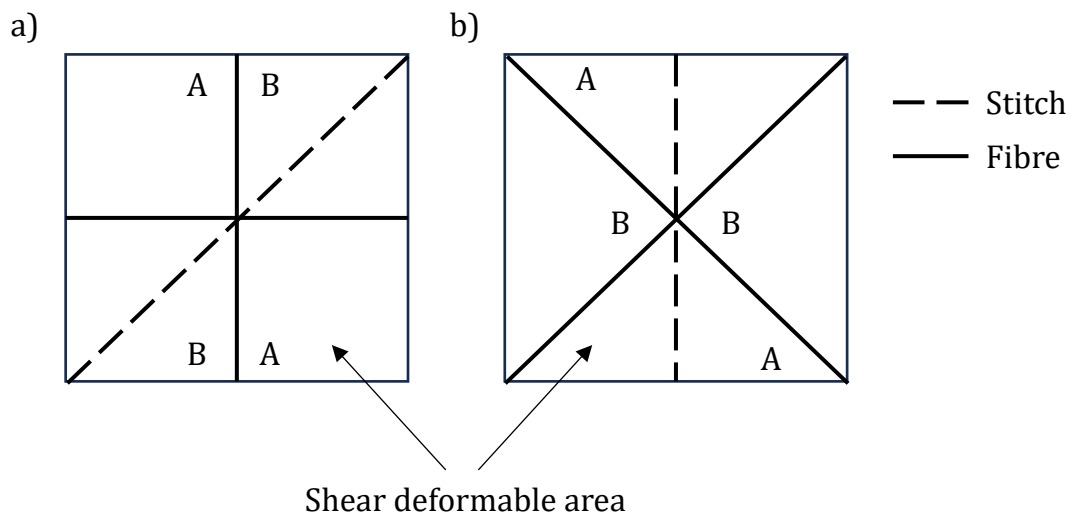


Figure 4.5. Shear deformable areas for the a) $[0^\circ/90^\circ]$ and b) $[+45^\circ/-45^\circ]$ NCF plies.

As it can be seen in Figure 4.6, the preforms were divided in four quadrants of interest, labelled Q1 to Q4 in a clockwise direction. Additionally, some samples present wrinkling along the horizontal (orange line in Figure 4.6a) and vertical (blue line in Figure 4.6a) directions or across the fabric diagonals (black lines in Figure 4.6b).

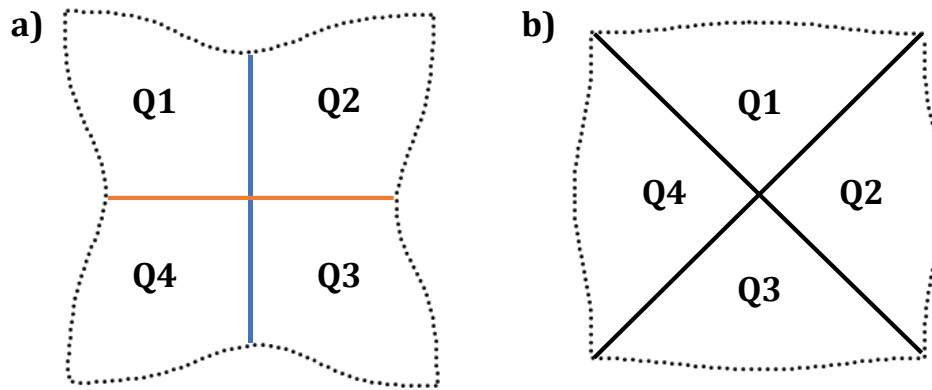


Figure 4.6. Preform areas more susceptible to defects for a) $[0^\circ/90^\circ]$ and b) $[+45^\circ/-45^\circ]$ NCF.

4.2 Validation results

This section presents the experimental and numerical results for the one and two NCF ply cases used in section 4.3 to validate the numerical predictions. The stacking sequence, breather configuration – for the experimental results – and tool used are detailed in Table 4.2.

Table 4.2. Parameters for the one and two ply studies to validate the numerical model.

	Stacking sequences	Breather configuration	Tool
One ply	$[90^\circ/0^\circ]$	Cross Square250x250	50r 100r 50rplatf
Two plies	$[90^\circ/0^\circ, 90^\circ/0^\circ]$ $[90^\circ/0^\circ, 0^\circ/90^\circ]$ $[90^\circ/0^\circ, -45^\circ/+45^\circ]$ $[-45^\circ/+45^\circ, -45^\circ/+45^\circ]$ $[-45^\circ/+45^\circ, +45^\circ/-45^\circ]$	Parallel8	50rplatf

Six scenarios are considered for the one ply cases varying both the breather configuration and tool. However, only three scenarios are considered for the numerical results as the model does not include the breather. On the other hand, five scenarios are considered for the two plies cases, as only the stacking sequence varies between scenarios.

4.2.1 Experimental data

This section presents and discusses the experimental data, starting with the one ply results. Figure 4.7 presents the preform-tool distance contour plots for the six scenarios. The 50r and 50rplatf samples show slight wrinkling in some of the quadrants. However, the 100r samples do not present wrinkling in any of the four quadrants. All the samples display wrinkling in the vertical direction, whilst only the 50r and 100r samples present wrinkling in the horizontal direction.

Table 4.3 presents the maximum Dist2Tool and %0-1.75 values for the six scenarios. The maximum Dist2Tool value is between 7.25 mm and 8.5 mm for the 50rplatf and 50r tools, and between around 12 mm and 13 mm for the 100r tool. Therefore, the maximum Dist2Tool value is higher for 100r samples. With regards to the %0-1.75, all the samples present a conformity percentage between 80%-85.5%.

Table 4.3. Maximum Dist2tool and %0-1.75 values for the six experimental one ply scenarios.

	Max Dist2Tool (mm)			%0-1.75		
	50rplatf	50r	100r	50rplatf	50r	100r
Cross	7.72	7.93	11.91	84.93%	82.43%	84.39%
Square 250x250	7.25	8.43	12.85	85.30%	80.23%	83.59%

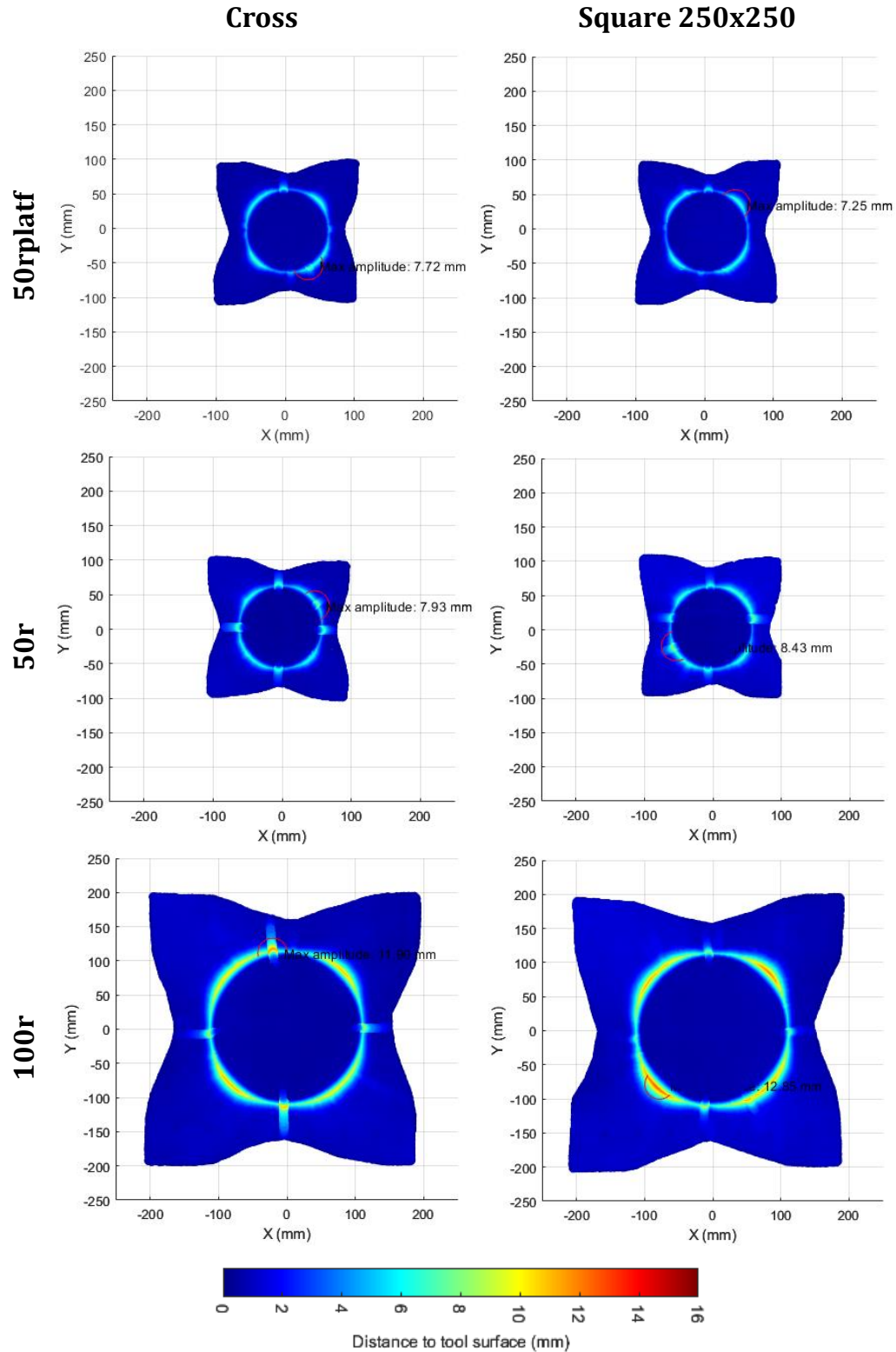


Figure 4.7. Preform-tool distance contour plot for the six experimental one ply scenarios.

The two ply results are presented and discussed below. Figure 4.8 presents the preform-tool distance contour plots for the five scenarios. All the samples present wrinkling, with the $[90^0/0^0, 0^0/90^0]$ case being the least severe case and the $[90^0/0^0, -45^0/+45^0]$ being the most severe case. The defect distribution analysis is performed individually:

- **$[90^0/0^0, 90^0/0^0]$** : Wrinkling is present in the Q1 and Q3 quadrants, which correspond to the positive shear area of both plies. Slight wrinkling is also presented in the vertical and horizontal directions.
- **$[90^0/0^0, 0^0/90^0]$** : Wrinkling is only present slightly in the vertical and horizontal directions. This indicates that the interaction between mirrored plies is beneficial to reduce defect occurrence, as no wrinkling is present in any of the quadrants. This could arise from the fact that in the same quadrant, fibres from one ply are in tension, whilst fibres from the other ply are in compression. This interaction in the material prevents wrinkling.
- **$[90^0/0^0, -45^0/+45^0]$** : Two wrinkles are present in all the quadrants. Slight wrinkling is observed in the fabric diagonal directions. The severity of the defects is higher than for the other cases.
- **$[-45^0/+45^0, -45^0/+45^0]$** : Wrinkling is only present in the Q2 and Q4 quadrants, which correspond to the positive shear area of both plies. The top wrinkles present increased severity compared to bottom ones for both quadrants.
- **$[-45^0/+45^0, +45^0/-45^0]$** : The wrinkling pattern is similar to the $[90^0/0^0, -45^0/+45^0]$ case. Wrinkling is present in all the quadrants but with reduced severity of the wrinkles compared to other cases.

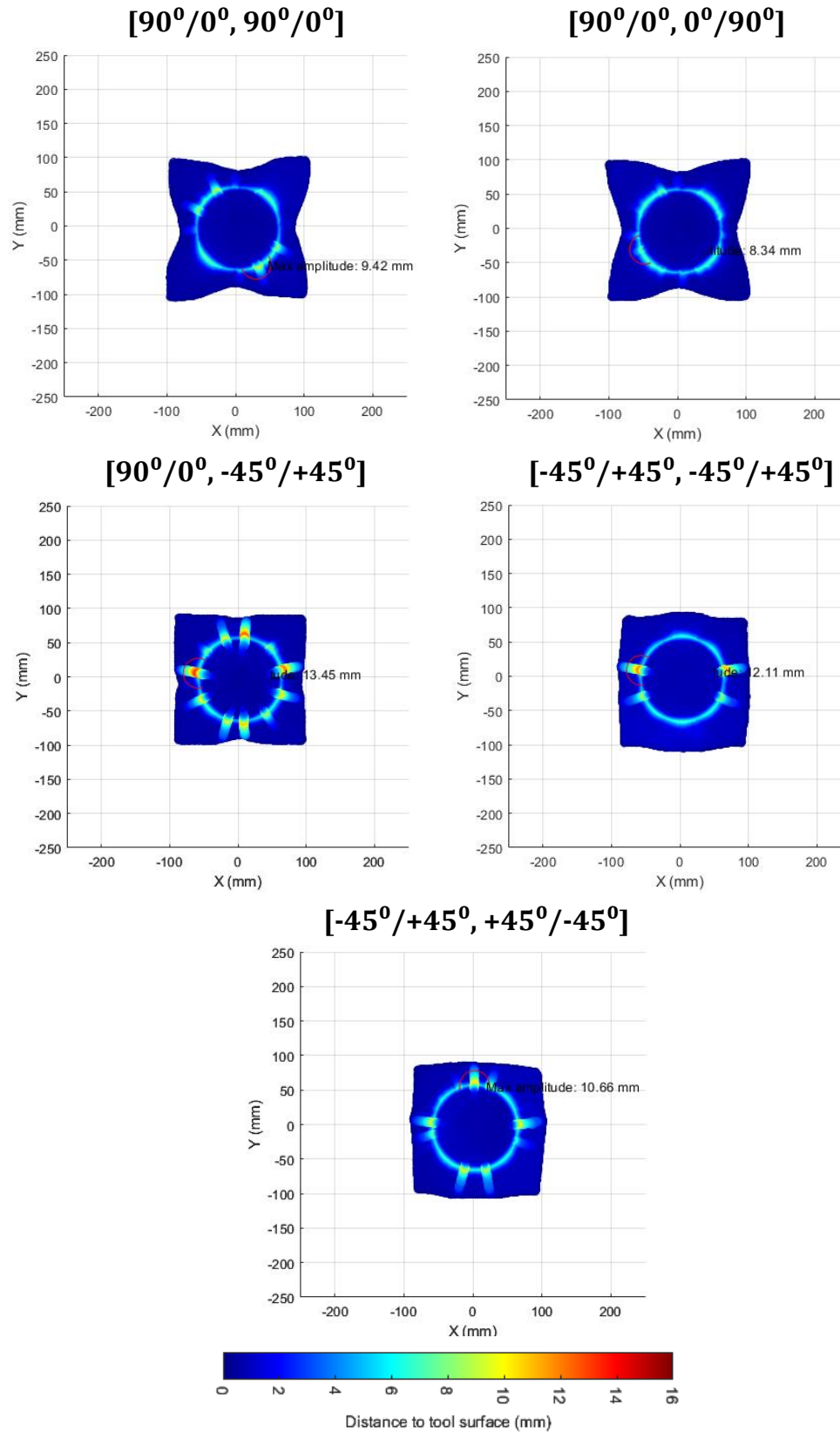


Figure 4.8. Preform-tool distance contour plot for the five experimental two ply scenarios.

Table 4.4 presents the maximum Dist2Tool and %0-1.75 values for the five scenarios. The maximum Dist2Tool value varies between 8.34 mm to 13.45 mm for all the samples, with the $[90^0/0^0, 0^0/90^0]$ stacking sequence presenting the lowest value and the $[90^0/0^0, -45^0/+45^0]$ the highest. The effect of stacking sequence on wrinkling occurrence is evaluated in chapter 5 (see section 5.4). With regards to the %0-1.75, all the samples present a conformity percentage between 77.22% and 80.70%, which is reduced compared to the one ply samples. This difference may result from the interaction between plies, as inter-ply sliding can influence defect occurrence, thus reducing the conformity of the stacking.

Table 4.4. Maximum Dist2tool and %0-1.75 values for the five experimental two ply scenarios.

	Max Dist2Tool (mm)	%0-1.75
$[90^0/0^0, 90^0/0^0]$	9.42	80.70%
$[90^0/0^0, 0^0/90^0]$	8.34	80.05%
$[90^0/0^0, -45^0/+45^0]$	13.45	75.25%
$[-45^0/+45^0, -45^0/+45^0]$	12.11	78.83%
$[-45^0/+45^0, +45^0/-45^0]$	10.66	77.22%

4.2.1.1 Repeatability

To evaluate the repeatability of the experimental method, three different stacking sequences were selected $[90^0/0^0, 90^0/0^0]$, $[90^0/0^0, 0^0/90^0]$ and $[90^0/0^0, -45^0/+45^0]$. The experiments were conducted using the 50rplatf tool and the parallel 8 breather configuration. By evaluating three stacking sequences the study captures a wide range of potential material behaviours. Therefore, two repetitions were deemed sufficient, provided that a consistent behaviour was observed across both repeats for each set-up.

Figure 4.9 presents the preform-tool distance contour plots for the different stacking sequences and all the repetitions. The contours present minimum variability since the wrinkling pattern is consistent between repeats.

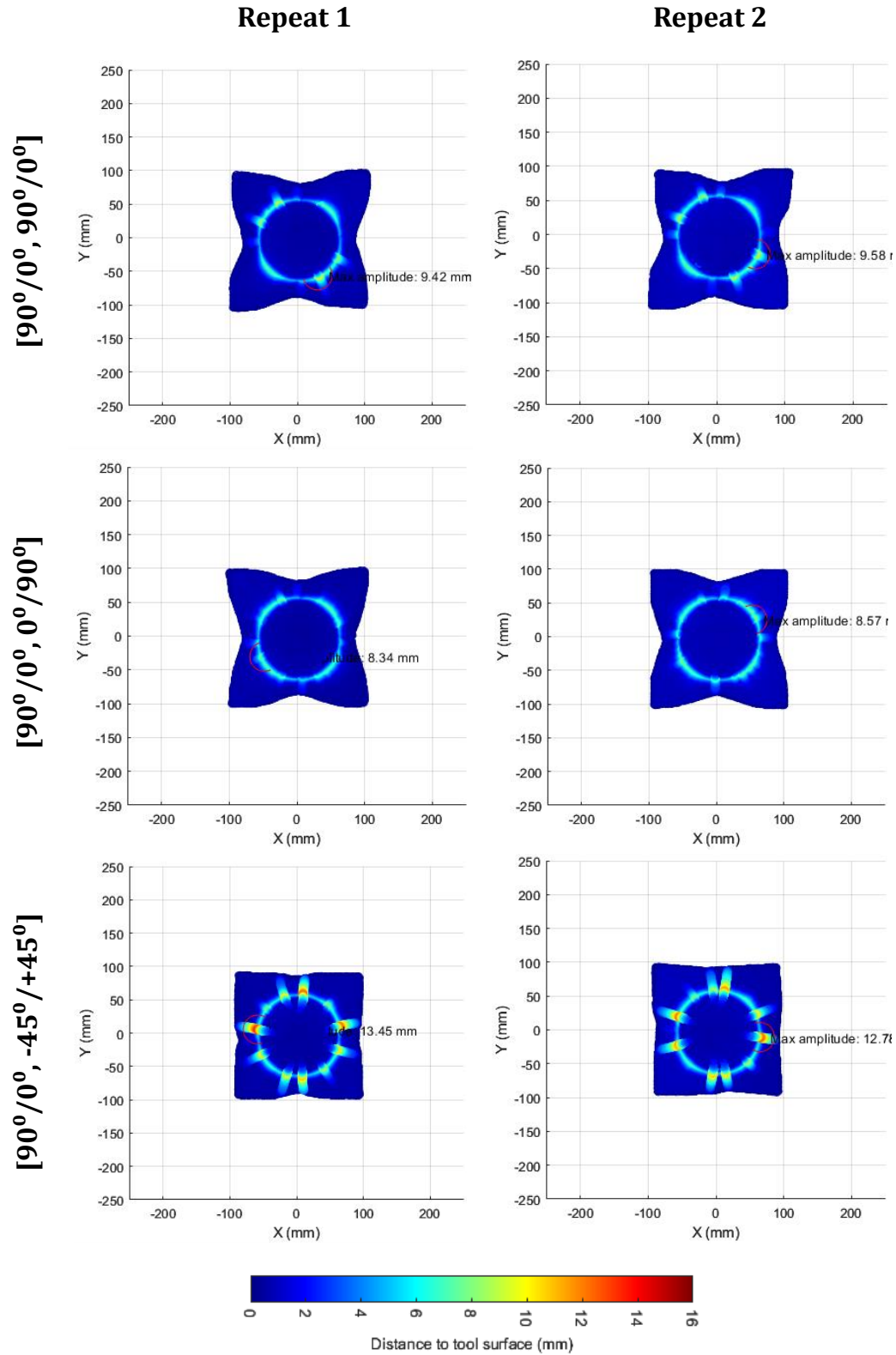


Figure 4.9. Preform-tool distance contour plot of the two repetitions for the three different stacking sequences to evaluate the repeatability of the experimental results.

Table 4.5 presents the maximum Dist2Tool and %0-1.75 values for the different stacking sequences and all the repetitions. For the Dist2Tool, the values fluctuate between 0.16 mm and 0.67 mm, which is acceptable given that the scanners are aligned manually, which can lead to discrepancies of ± 0.5 mm between scanners. For the conformity percentage, the values fluctuate around 2%, which is also acceptable. Therefore, it can be concluded that the experiments can be consistently reproduced. Each repetition produced similar results, showcasing the robustness of the experimental method.

Table 4.5. Parameters used to evaluate the repeatability of the experimental results.

	[90°/0°, 90°/0°]		[90°/0°, 0°/90°]		[90°/0°, -45°/+45°]	
	Rep 1	Rep 2	Rep 1	Rep 2	Rep 1	Rep 2
Max Dist2Tool (mm)	9.42	9.58	8.34	8.57	13.45	12.78
%0-1.75	80.70%	78.70%	80.05%	78.25%	75.25%	73.45%

4.2.2 Numerical data

This section presents and discusses the numerical data, starting with the one ply results. Figure 4.10 presents the preform-tool distance contour plots for the three scenarios. All the samples present wrinkling in the Q1 and Q3 quadrants, which in this case correspond to the positive shear area regions. The 50r and 100r samples also present vertical and horizontal wrinkling. This is not observed for the 50rplatf sample.

Table 4.6 presents the maximum Dist2Tool and %0-1.75 values for the three scenarios. The maximum Dist2Tool value is between 9.5 mm and 10 mm for the 50rplatf and 50r samples, and 14.56 mm for the 100r tools. Therefore, the maximum Dist2Tool value is higher for 100r samples. With regards to the %0-1.75, all the samples present a conformity percentage of around 81% and 82.5%.

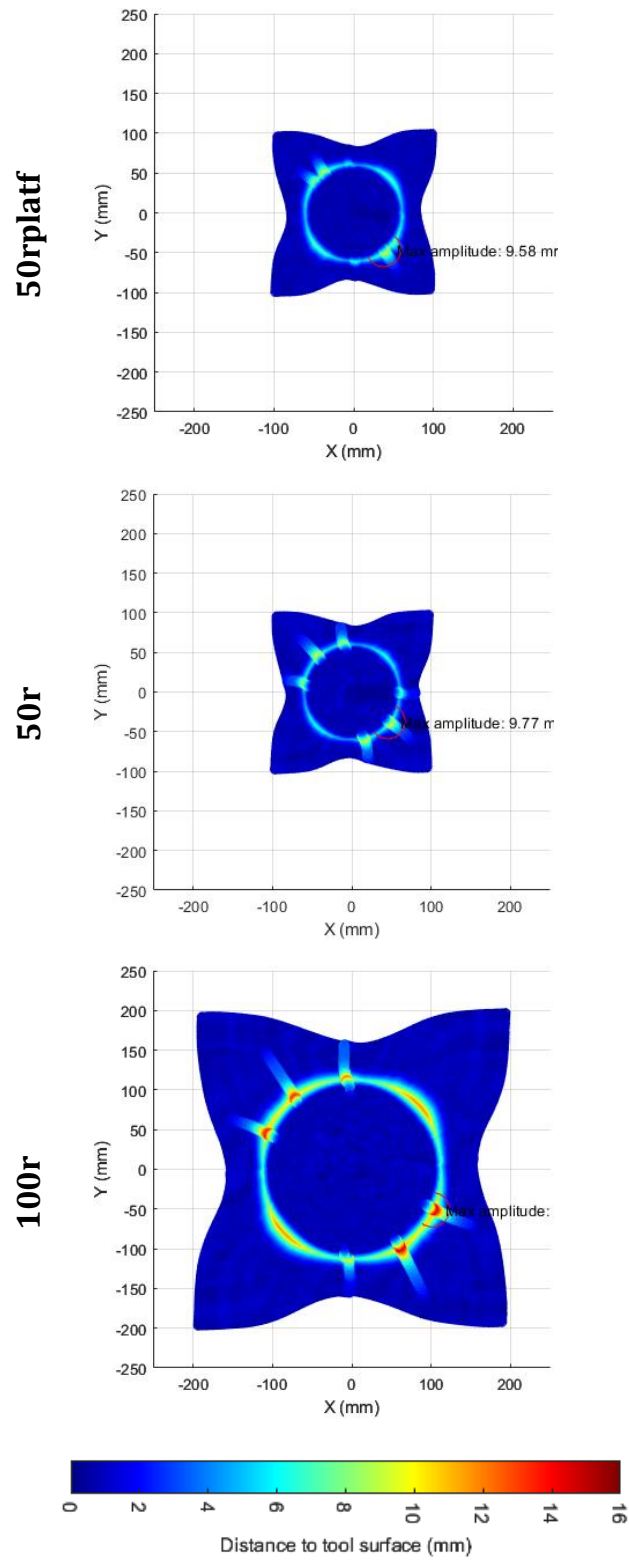


Figure 4.10. Preform-tool distance contour plot for the three numerical one ply scenarios.

Table 4.6. Maximum Dist2tool and %0-1.75 values for the three numerical one ply scenarios.

	Max Dist2Tool (mm)	%0-1.75
50rplatf	9.58	81.44%
50r	9.77	81.76%
100r	14.56	82.44%

The two ply results are presented and discussed below. Figure 4.11 presents the preform-tool distance contour plots for the five scenarios. All the samples present wrinkling, with the $[-45^0/+45^0, -45^0/+45^0]$ case being the least severe case and the $[90^0/0^0, -45^0/+45^0]$ being the most severe case, with less wrinkles than the $[90^0/0^0, 0^0/90^0]$ case but increased severity. The defect distribution analysis is done individually:

- **$[90^0/0^0, 90^0/0^0]$** : Wrinkling is present in the Q1 and Q3 quadrants, which correspond to the positive shear area of both plies. Slight wrinkling is also present in the vertical direction.
- **$[90^0/0^0, 0^0/90^0]$** : Wrinkling of similar severity is present in all the quadrants. Slight wrinkling is also present in the vertical direction.
- **$[90^0/0^0, -45^0/+45^0]$** : One wrinkle is present in the Q1, Q3 and Q4 quadrants, whilst two are presented in the Q2 quadrant. Wrinkling is also observed in the diagonal directions. The severity of the defects is higher than for the other cases.
- **$[-45^0/+45^0, -45^0/+45^0]$** : Wrinkling is only present in the Q2 and Q4 quadrants, which correspond to the positive shear area of both plies.
- **$[-45^0/+45^0, +45^0/-45^0]$** : Wrinkling is present in all the quadrants. However, the Q1 quadrant presents two wrinkles whilst the other quadrants present only one. One wrinkle is also observed in one of the fabric diagonals.

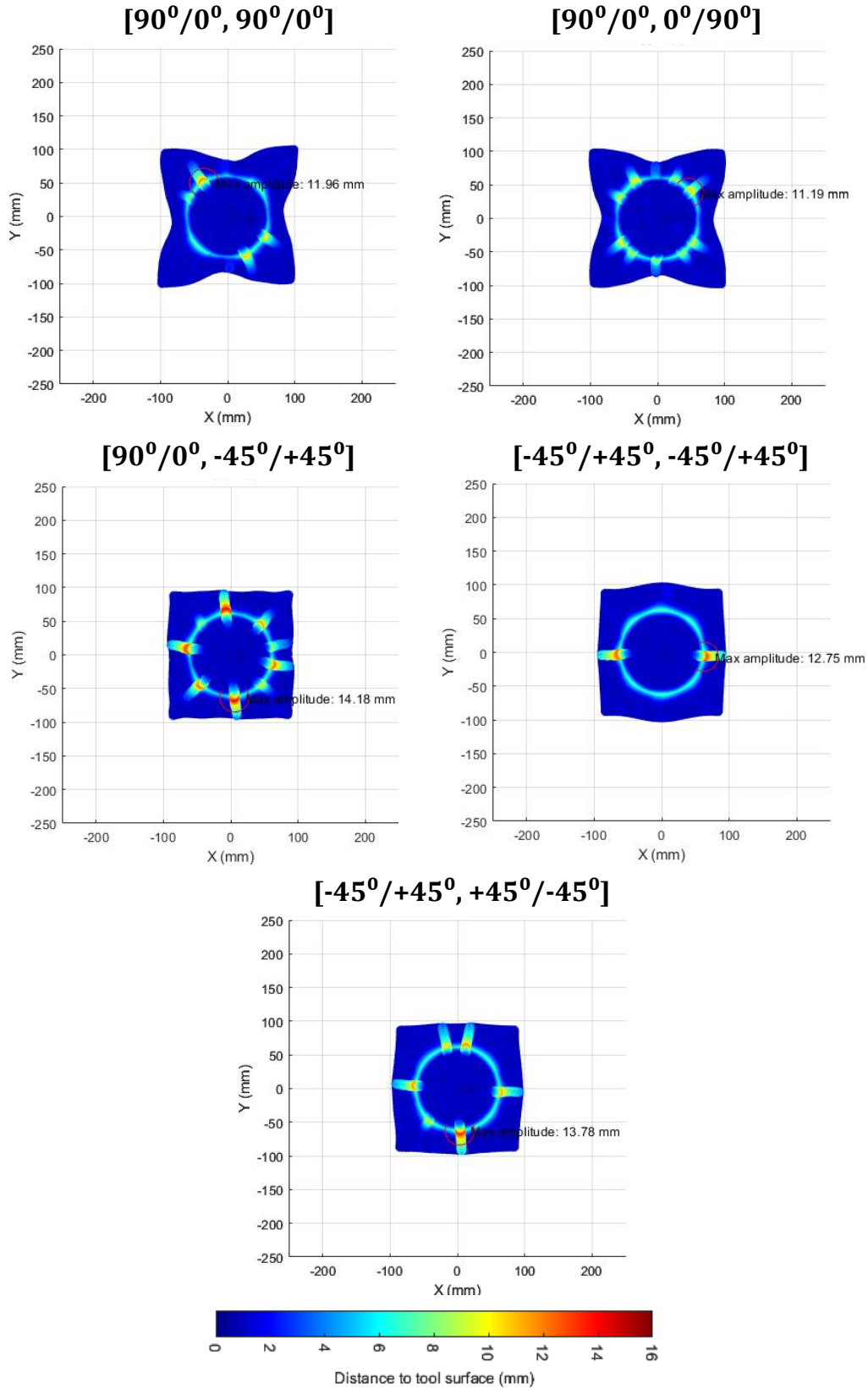


Figure 4.11. Preform-tool distance contour plot for the five numerical two ply scenarios.

Table 4.7 presents the maximum Dist2Tool and %0-1.75 values for the five scenarios. The maximum Dist2Tool value varies between 11.19 mm and 14.18 mm for all the samples, with the $[90^0/0^0, 0^0/90^0]$ stacking sequence presenting the lowest value and the $[90^0/0^0, -45^0/+45^0]$ the highest. With regards to the %0-1.75, all the samples present a conformity percentage between 70.69% and 78.40%, which is reduced compared to the one ply samples.

Table 4.7. Maximum Dist2tool and %0-1.75 values for the five numerical two ply scenarios.

	Max Dist2Tool (mm)	%0-1.75
$[90^0/0^0, 90^0/0^0]$	11.96	78.40%
$[90^0/0^0, 0^0/90^0]$	11.19	76.47%
$[90^0/0^0, -45^0/+45^0]$	14.18	70.69%
$[-45^0/+45^0, -45^0/+45^0]$	12.75	75.51%
$[-45^0/+45^0, +45^0/-45^0]$	13.78	72.66%

4.2.2.1 Repeatability

The repeatability of the numerical predictions was evaluated for a mesh of 2 mm and 6 mm, using the same model parameters as those used in the mesh study (see Table 3.2 and Table 3.5). This assessment aims to determine whether the use of multiple CPUs could induce variability due to differences in how the model is partitioned across processors or the order in which numerical operations are executed. Two repetitions were deemed sufficient to establish repeatability, provided that the same set-up presents consistent behaviour across both runs.

Table 4.8 presents several parameters used to evaluate the consistency of the predictions. No variability is presented for the predictions with the same mesh size. These observations indicate that the predictions can be consistently reproduced.

Table 4.8. Parameters used to evaluate the repeatability of the numerical predictions.

	2 mm		6 mm	
	Repeat 1	Repeat 2	Repeat 1	Repeat 2
%ALLKE/ALLIE	3.10%	3.10%	2.61%	2.61%
Max shear angle (°)	32.23	32.23	34.98	34.98
Min shear angle(°)	-41.70	-41.70	-44.86	-44.86
Max in-plane principal stress (MPa)	183.86	183.86	72.72	72.72

4.3 Comparison and validation of results

This section validates the numerical predictions presented in section 4.2.2, by comparing the results with the experimental data presented in section 4.2.1. This process ensures the validity and reliability of the predictions, identifies any necessary adjustments or improvements to the model, and acknowledges any limitations of the model and their impact on the results.

4.3.1 One-ply results

From Figure 4.7 and Figure 4.10, it can be observed that the experimental cases present no wrinkling on the positive shear area, whilst the numerical predictions do. Additionally, whilst the experimental samples exhibit both vertical and horizontal wrinkling, the numerical predictions present only vertical wrinkling.

When looking at the results in Table 4.3 and Table 4.6, it can be observed that the numerical predictions present a maximum distance value approximately 2 mm higher than the experimental data. The %0-1.75 value is lower for the 50rplatf and 100r numerical predictions, likely due to the increased wrinkling experienced by the numerical cases, resulting in worse conformity to the desired shape.

4.3.2 Two-ply results

From Figure 4.8 and Figure 4.11, it can be observed that both the experimental and numerical samples exhibit wrinkling in the same area. The wrinkling pattern predictions are similar for the $[90^0/0^0, 90^0/0^0]$ and $[90^0/0^0, -45^0/+45^0]$ cases. However, significant differences are observed for the other cases, especially in the $[90^0/0^0, 0^0/90^0]$ case, where wrinkling is predicted in all quadrants, even though the experimental results show no wrinkling in those areas. This suggests that a potential interaction between the mirrored plies, which experimentally reduces defect occurrence, is not captured in the numerical model. Additionally, the severity of the wrinkles is higher for the numerical predictions.

When looking at the results in Table 4.4 and Table 4.7, it can be observed that, in most cases, the numerical predictions present a maximum distance value approximately 2 mm higher than the experimental data. The %0-1.75 value is also 2% to 5% lower in the numerical predictions.

4.3.3 Evaluation of results

Experimentally, the one ply samples do not present any wrinkling, whilst the two ply samples do. This difference in behaviour can likely be attributed to two main factors:

- **Flexibility of a single ply:** A single ply is more flexible, allowing it to conform to the desired shape more easily without developing significant out-of-plane deformations.
- **Lack of inter-ply interactions:** In a single ply, there are no interactions with other fabric plies, meaning that there are no inter-ply sliding forces that could induce wrinkling.

The absence of wrinkling in a single ply can be attributed to its flexibility and the absence of inter-ply interactions, whilst the wrinkling observed in the multi-

ply configuration is likely due to interaction between plies. Wrinkling occurs when the friction between plies is high enough to prevent the surfaces from slipping. This behaviour is not observed for the one ply cases, as the material is only interacting with the diaphragms.

When comparing the experimental observations with the numerical predictions, the model predicts wrinkling for the one ply samples, which contradicts the experimental observations. For the two ply samples, the model can predict the general area where wrinkling occurs but does not accurately predict the wrinkling pattern. Additionally, the numerical predictions show a defect severity that is 2 mm higher than the experimental observations, and the conformity is reduced between 2 % to 5 %.

These discrepancies indicate that the model generally tends to overpredict the number and severity of defects, suggesting that the forming conditions might not be accurately replicated. The prediction of defects in the one ply case may result from simplification or assumptions in the material behaviour that apply to multi-ply cases but do not accurately reflect the behaviour of a single ply.

Therefore, the model could not be fully validated. It provides useful insights but requires further adjustments to better align with the experimental outcomes. Section 5.5 in Chapter 5 explores a potential adjustment to improve the predictions.

4.4 Chapter summary

This chapter aims to validate the numerical predictions against experimental results. A quantitative evaluation approach was developed using 3D coordinates to assess the forming process. Wrinkling amplitude is determined, allowing the detection of out-of-plane defects when a critical threshold of 1.75 mm was exceeded. Both experimental and numerical results were consistently reproduced, demonstrating the robustness of the methods.

Single ply and multi-ply experiments were carried out to validate the model. The absence of wrinkling in single ply experiments was attributed to the lack of inter-ply interactions, though the numerical model did not replicate this behaviour. In contrast, wrinkling was observed in multi-ply experiments, likely due to interaction between plies. While the model successfully predicted the general area of wrinkling, it did not accurately capture the wrinkling pattern. Defect severity was overestimated by 2 mm, and conformity predictions were 2% to 5% lower for the experimental results.

These discrepancies suggest that the model tends to overpredict both the number and severity of defects, indicating that the forming conditions may not be fully replicated.

Chapter 5 Process studies

This chapter investigates the effect of several parameters on the double diaphragm forming process. The studies in this chapter are listed in Table 5.1, indicating whether the study is experimental or numerical.

Table 5.1. Description of the studies in chapter 5.

Study	Type
Effect of diaphragm size	Numerical
Effect of breather arrangement	Experimental
Effect of two-step preforming	Experimental
Effect of stacking sequence	Experimental
Effect of modelling breather	Numerical

5.1 Effect of diaphragm size

When subjected to compression during forming, the material can experience localised buckling or folding, resulting in wrinkling. To address this issue, the double diaphragm forming process uses two diaphragms to support the material during preforming. As the material is pulled into shape, the diaphragms stretch, transmitting tension to the material and reducing the compressive forces. However, larger diaphragms tend to stretch less due to their size, deforming more easily. This can result in insufficient tension being applied to the material, which may lead to wrinkling. In contrast, smaller diaphragms provide stronger constraints to the material, preventing wrinkling.

When conducting numerical analysis, the size of the model significantly influences computational time, particularly for smaller element sizes as seen in section 3.2.3.2. Therefore, reducing the diaphragm size reduces the overall size of the model. Consequently, it is of interest to evaluate how much the diaphragm

size could be reduced without compromising the forming process and defect formation.

Therefore, the aim of this study is to improve the understanding of the impact of the diaphragm size on the forming process and to find an adequate diaphragm size for the forming process.

Since experimentally the diaphragm size mainly depends on the rig size, the study was performed numerically. The model and process parameters were presented in Table 3.5 and Table 3.6. The total number of elements ranges from 277,990 for the 412 mm diaphragm to 3,468,282 for the 2000 mm diaphragm, which is 12 times the smallest size.

Figure 5.1 presents the preform-tool distance contour plot for both orientations for the 412 mm, 700 mm, 1100 mm and 1300 mm cases. For both orientations, the edges of the fabric lift for a 412 mm size, indicating that the diaphragm is too small and is excessively pulling the material, preventing it from deforming.

For the $[0^0/90^0]$ orientation, the length of the wrinkles increases with the diaphragm size. Wrinkling is present in the Q2 and Q4 quadrants, which correspond to the positive shear angle area. Wrinkling in the vertical and horizontal directions appears from a 1300 mm size, indicating that the diaphragm is not adequately restricting the fabric, allowing out-of-plane deformation.

For the $[+45^0/-45^0]$ orientation, the length and severity of the wrinkles remain consistent, but more defects appear as the diaphragm size increases. Wrinkling is mainly located in the Q1 and Q3 quadrants, which correspond to the positive shear angle. Wrinkling on the Q2 and Q4 quadrants appears from a 1100 mm size. Wrinkling in the diagonal directions is noticeable from a 1000 mm size.

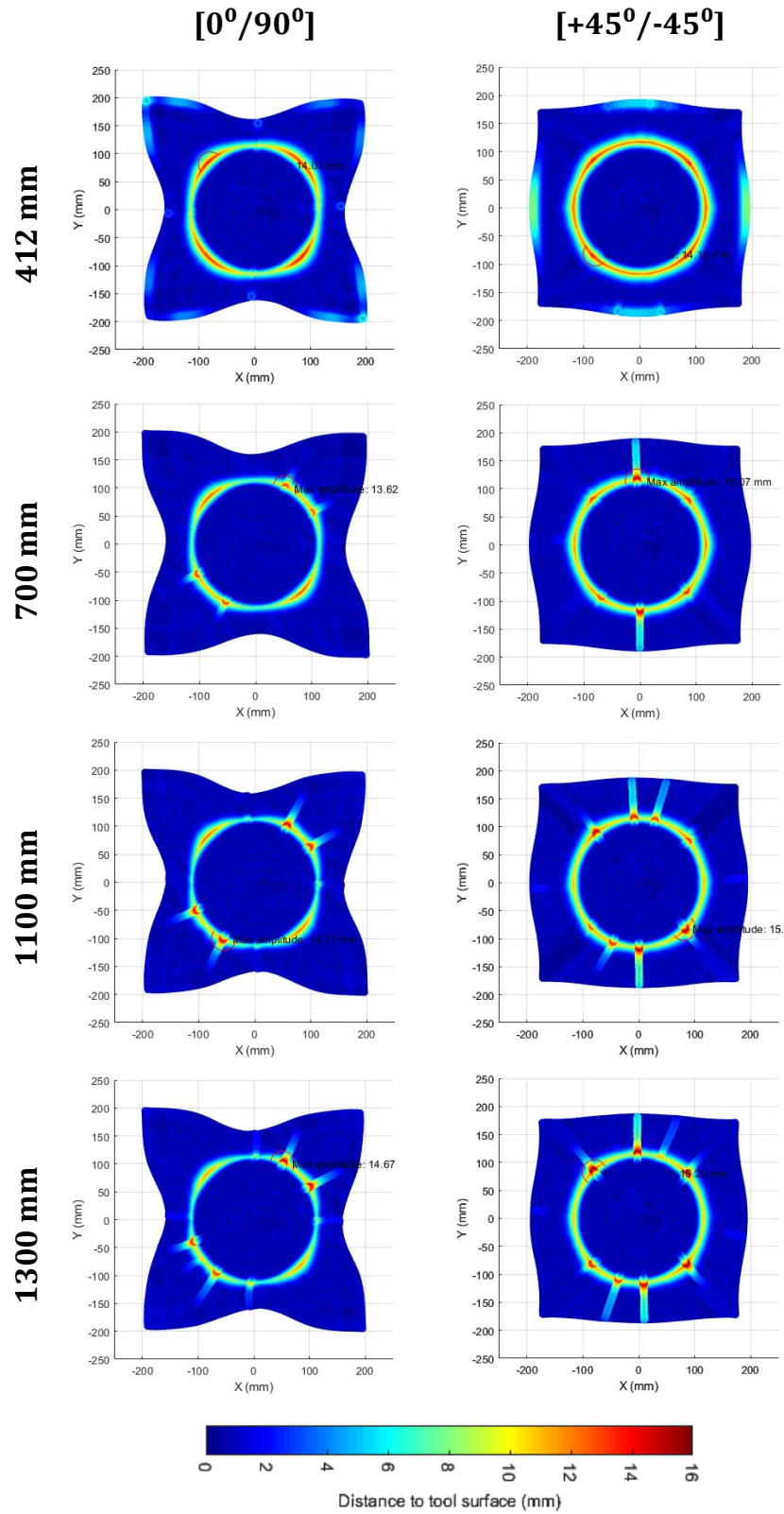


Figure 5.1. Preform-tool distance contour plot for the $[0^\circ/90^\circ]$ and $[+45^\circ/-45^\circ]$ orientations and 412 mm, 700 mm, 1100 mm and 1300 mm diaphragm sizes.

Figure 5.2 presents the maximum preform-tool distance for both orientations and all the diaphragm sizes under study. The maximum distance increases with the diaphragm size in both cases, but the values are higher for the $[+45/-45^0]$ orientation. The difference between the lowest and highest values is 1.15 mm for the $[+45/-45^0]$, whereas it is 2.15 mm for the $[0^0/90^0]$ orientation, suggesting greater variation in maximum Dist2Tool for the $[0^0/90^0]$ orientation.

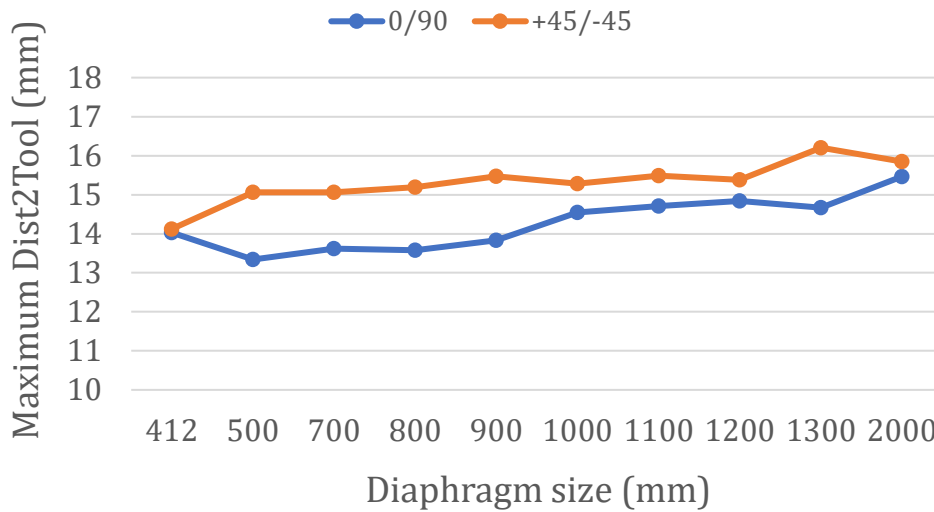


Figure 5.2. Maximum preform-tool distance for the $[0^0/90^0]$ and $[+45/-45^0]$ orientations and all the diaphragm sizes.

Figure 5.3 presents the %0-1.75 values for both orientations and all the diaphragm sizes under study. The conformity values converge for a 700 mm diaphragm size. This could be explained by the fact that as defects become more prominent, the material around them conforms better since there is less of it available to adapt to the shape, as most of the material contributes to the wrinkle.

The %0-1.75 values are between 4% to 5% higher for the $[0/90^0]$ orientation. This observation is consistent with the findings from Figure 5.1, where the $[+45/-45^0]$ orientation presents more wrinkling and bridging compared to the $[0/90^0]$ orientation. The difference between the lowest and highest value is 2% for the $[0/90^0]$ orientation, whereas it is 1.27% for the $[+45/-45^0]$ orientation. This again indicates a greater variation in results for the $[0^0/90^0]$ orientation.

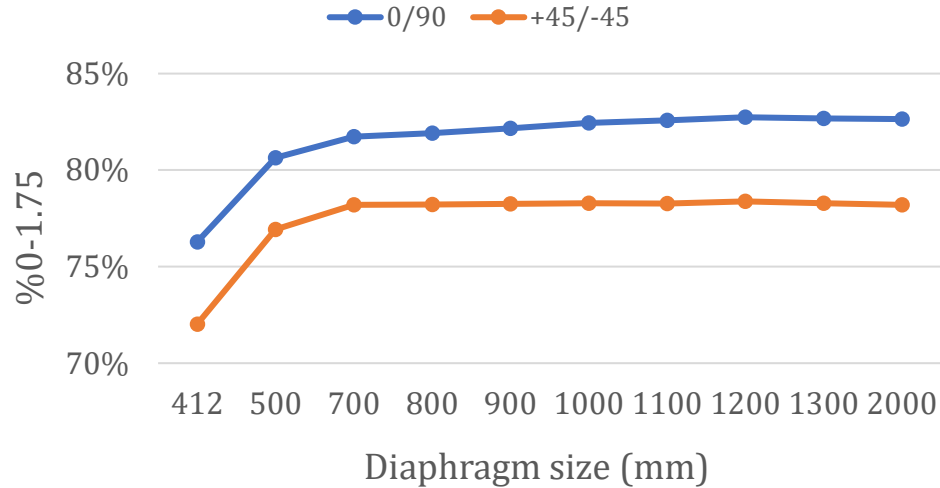


Figure 5.3. %0-1.75 conformity values for the $[0^0/90^0]$ and $[+45/-45^0]$ orientations and all the diaphragm sizes.

Figure 5.4 presents the diagonal and edge length for both orientations and all the diaphragm sizes under study. The length trends vary depending on the orientation.

Figure 5.4 a) presents the diagonal values for the $[0/90^0]$ orientation. The two diagonals converge for a diaphragm size of 500 mm but at different values. This difference in convergence lengths is due to the asymmetric behaviour of the fabric, which in this case deforms more along the negative shear direction, measured by diagonal 2. Diagonal 1, corresponding to the positive shear areas, has an average length of 540 mm, and diagonal 2, corresponding to the negative shear areas, has an average length of 555 mm.

Figure 5.4 b) presents the diagonal values for the $[+45/-45^0]$ orientation. The diagonals converge at a 500 mm diaphragm size, with the trend changing again from 1100 mm onwards. In this case both diagonals have the same length as they cross over a low shear area (below 10^0).

Figure 5.4 c) presents the edge values for the $[0/90^0]$ orientation. The edge lengths converge at a 500 mm diaphragm size for all edges, with the trend

decreasing from 1000 mm onwards. In this case, all the edges have the same length as they cross over both positive and negative shear areas.

Figure 5.4 d) presents the edge values for the $[+45^{\circ}/-45^{\circ}]$ orientation. The edge lengths converge at a 500 mm diaphragm size, with the trend changing from 1200 mm onwards. In this case, the top and bottom edges have the same length, which is greater than the length of the right and left edges. This is because the top and bottom edges cross over a positive shear area, whilst the right and left edges cross over a negative shear area.

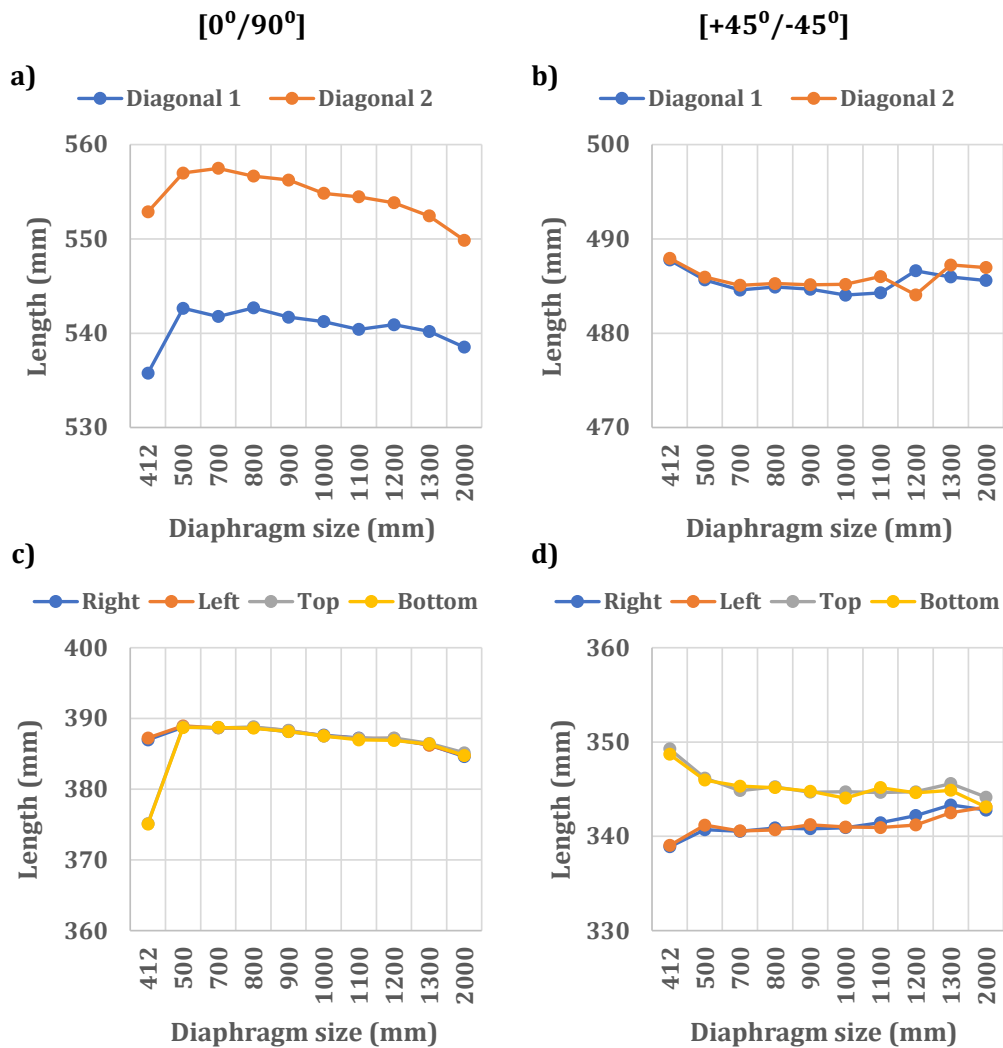


Figure 5.4. Diagonal and edge length for the $[0^{\circ}/90^{\circ}]$ and $[+45^{\circ}/-45^{\circ}]$ orientations and all diaphragm sizes.

Figure 5.5 presents the von Mises stress distribution in the upper diaphragm for both orientations and all the diaphragm sizes under study. The stress distribution where the fabric is located is similar for all the samples, indicating that the diaphragm is pinned to the fabric and no movement is experienced once they are in contact.

The stress distribution around the fabric decreases from 15 MPa to 0.1 MPa as the diaphragm size increases for both orientations. This reduction in stress explains the increase in wrinkling with larger diaphragm sizes, as the diaphragm stretches and becomes unable to adequately constrain the material as it adapts to shape, allowing for out-of-plane defects.

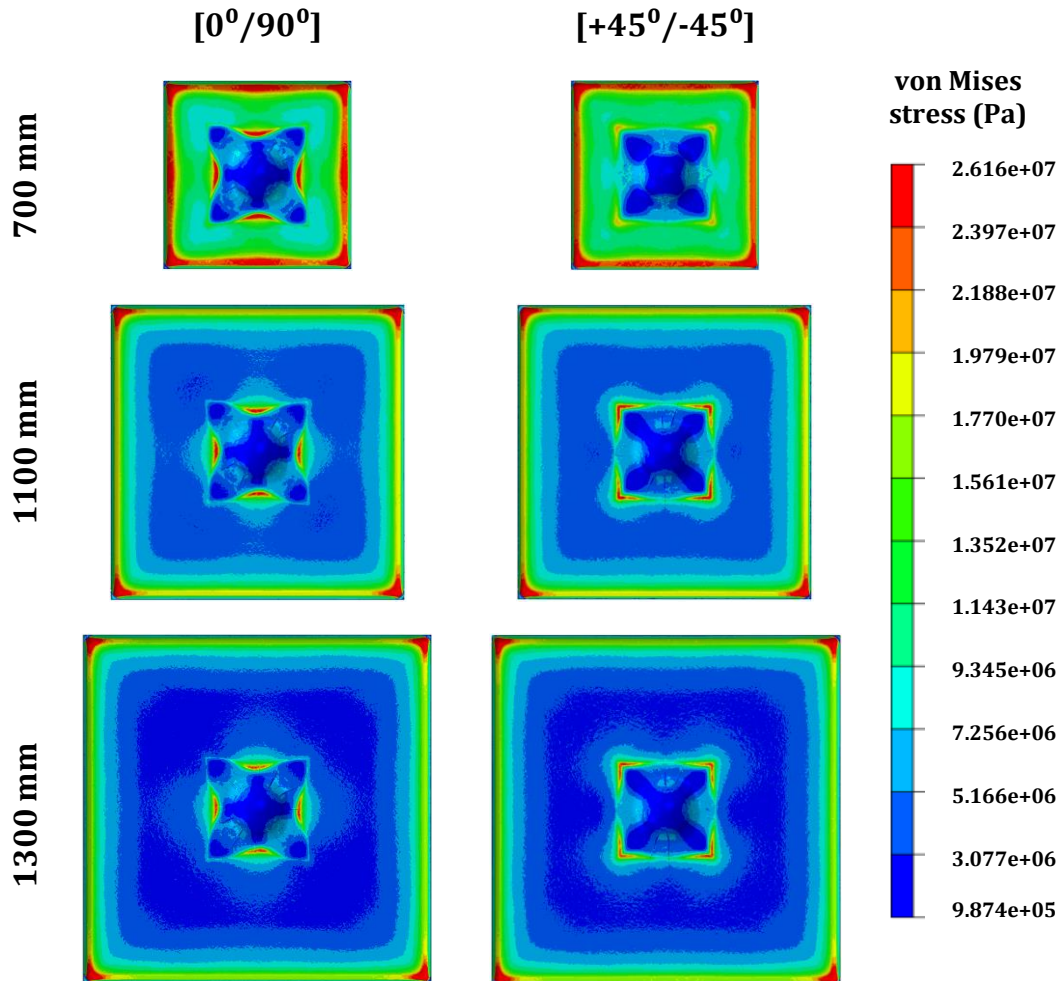


Figure 5.5. von Mises stress distribution in the upper diaphragm for the $[0^\circ/90^\circ]$ and $[+45^\circ/-45^\circ]$ orientations and 700 mm, 1100 mm and 1300 mm diaphragm sizes.

With regards to the distribution around the fabric outline, for the $[0^0/90^0]$ orientation, there is a high stress concentration on the outline areas where the fabric is draping. For the $[+45^0/-45^0]$ orientation, there is a high stress concentration on the corner of the fabric.

These observations highlight the effect of the diaphragm size on defect occurrence. The wrinkling pattern is influenced by the diaphragm size, with larger diaphragms providing insufficient tension on the fabric, leading to wrinkling, while smaller diaphragms can cause the fabric to lift at the edges.

The $[0^0/90^0]$ orientation presents lower maximum distance values and increased conformity, but also exhibits greater variation between results, indicating that this orientation is more susceptible to changes to the diaphragm size. For both orientations, all the diagonals and edge lengths converge for a diaphragm size of 500 mm, changing trend from 1000 mm and larger sizes.

For both orientations the diaphragm should be at least 500 mm, which is 1.25 times the size of the fabric. Defects outside the positive shear area start earlier for the $[+45^0/-45^0]$ orientation; in this case, the diaphragm should be below 1000 mm, which is 2.5 times the size of the fabric. For the $[0^0/90^0]$ orientation, the diaphragm should be below 1300 mm, which is 3.25 times the size of the fabric.

5.2 Effect of breather arrangement

When forming experimentally, a breather cloth is required. However, the distribution of the breather can influence defect formation and the draping of the fabric during the forming process. The aim of this study is to understand the effect of the breather arrangement on the forming process.

The study is performed experimentally with two different stacking sequences, and six different breather configurations for each sequence. Details of the stacking sequence, breather configuration and tool used are provided in Table 5.2. A schematic of the breather configurations is presented in Figure 5.6.

Table 5.2. Parameters for the breather arrangement study.

Stacking sequence	Breather configuration	Tool
$[90^0/0^0]$ $[-45^0/+45^0]$	Cross	50rplatf
	X shape	
	Cross & X shape	
	Square 250x250	
	Parallel 8	
	Full breather	

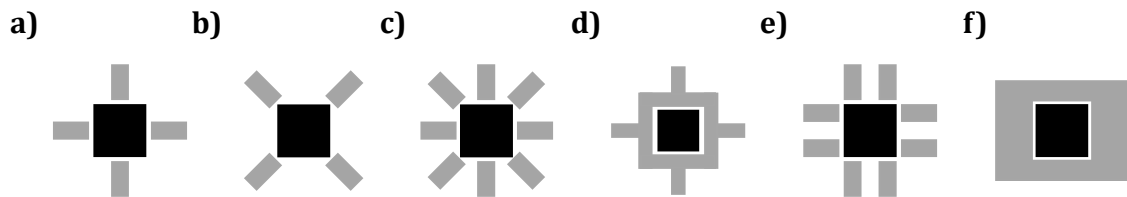


Figure 5.6. Schematic representation of the six breather arrangements: a) cross, b) X shape, c) cross and X shape, d) square 250x250, e) parallel 8, and f) full breather. The fabric is shown in black, and the breather in grey.

5.2.1 $[90^0/0^0]$ orientation

Figure 5.7 presents a picture of the forming for the six $[90^0/0^0]$ breather arrangement scenarios. Some inter-ply sliding between the NCF layers can be observed, especially on the draped areas.

A more detailed analysis can be performed using the preform-tool distance contour plots, presented in Figure 5.8. The predominant defect mode is bridging around the hemisphere, with the maximum distance occurring in that area for all configurations except the cross and the X shape. The defect distribution analysis is performed individually:

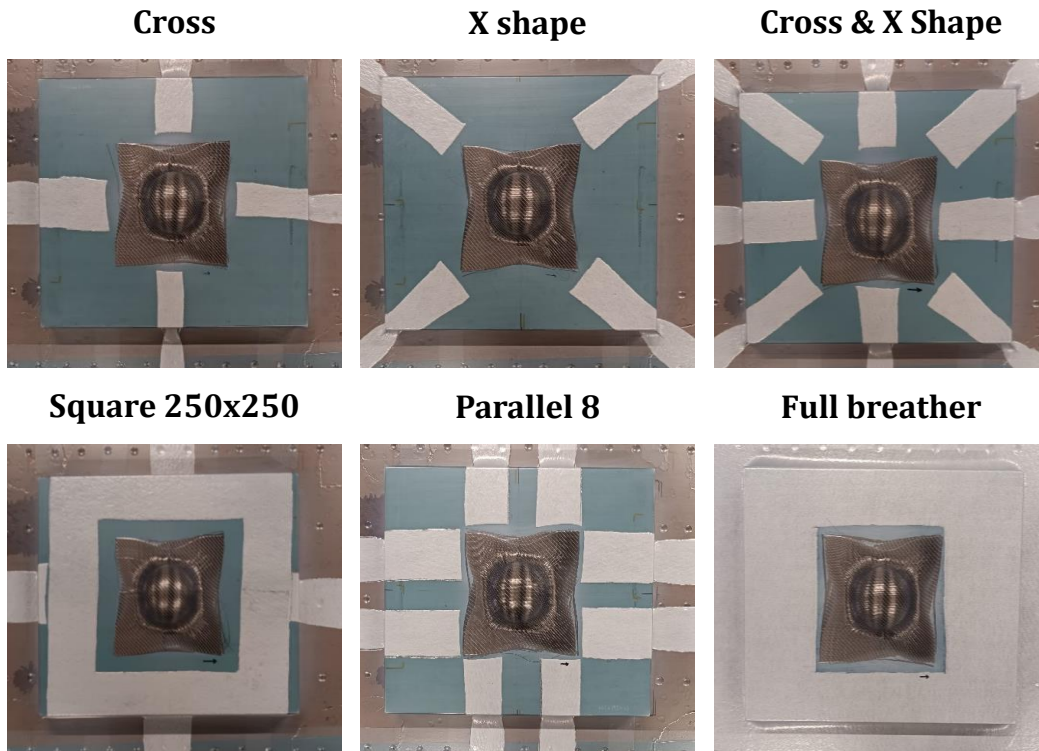


Figure 5.7. Picture of the forming for the six $[90^\circ/0^\circ]$ breather arrangement scenarios.

- **Cross:** Wrinkling is present in the vertical and horizontal directions. One small wrinkle is present in the Q3 quadrant.
- **X shape:** Wrinkling is mainly present in the Q1 and Q3 quadrants. Slight wrinkling can be observed in the upper vertical direction.
- **Cross & X shape:** Slight wrinkling is present in the Q1 quadrant and the lower vertical direction. This combination provides better formability compared to the individual cases, as the horizontal and vertical wrinkling has been mitigated and the wrinkling in the Q1 and Q3 quadrants has been considerably reduced.
- **Square 250x250:** Wrinkling is present in the vertical and slightly in the horizontal directions.
- **Parallel 8:** No wrinkling is present in any of the quadrants. The main defect is bridging around the hemisphere.
- **Full breather:** No wrinkling is present in any of the quadrants. The main defect is bridging around the hemisphere.

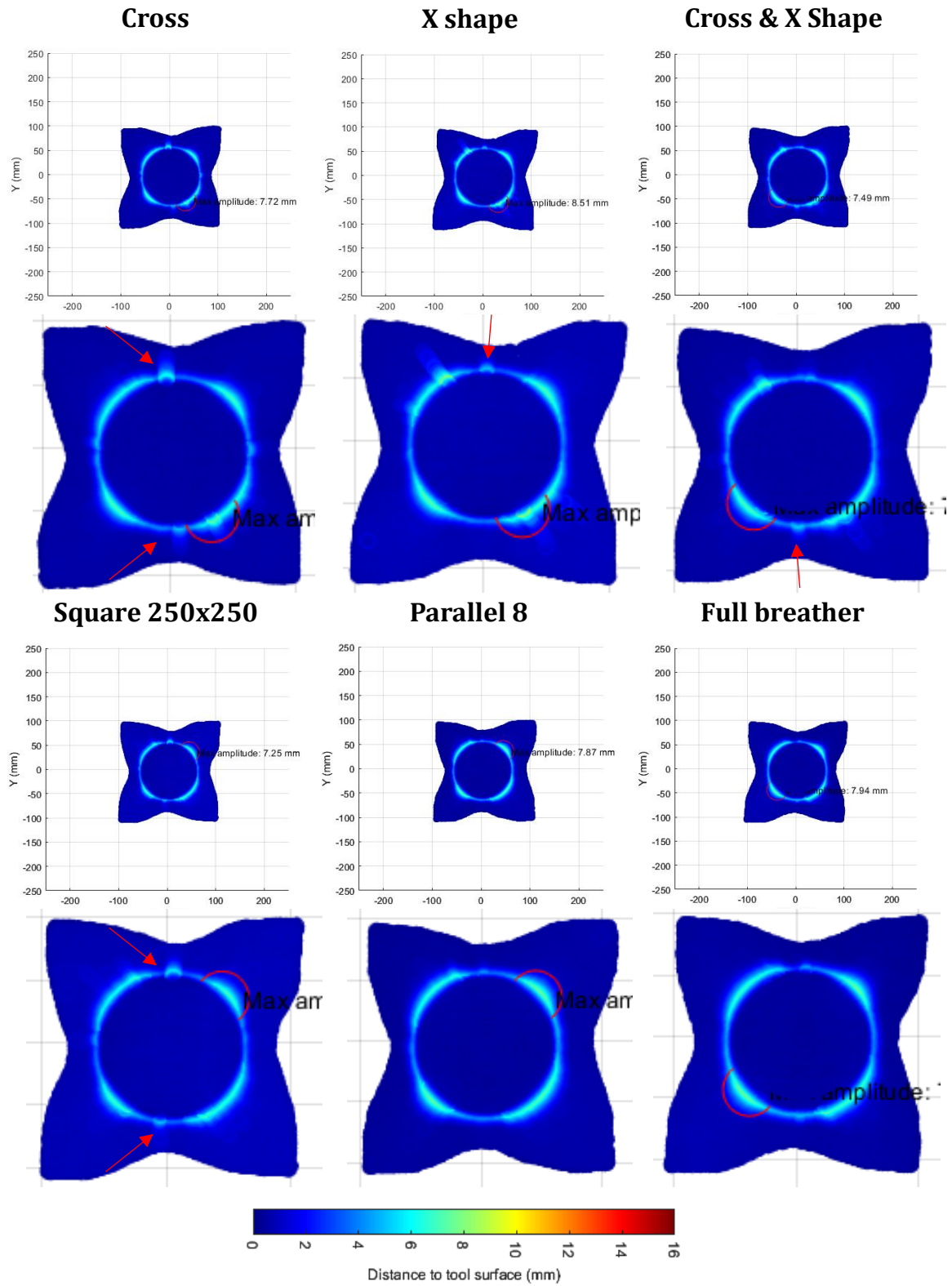


Figure 5.8. Preform-tool distance contour plot for the six $[90^0/0^0]$ breather arrangement scenarios.

These observations indicate that the difference between the configurations is not major. However, parallel 8 or full breather provide better conformity for this orientation.

Table 5.3 presents the maximum Dist2Tool and %0-1.75 values for the six scenarios. The maximum distance values range from 7.25 mm to 8.5 mm, while the conformity values range from 83.5% to 86.2%. These observations suggest that the variability of these parameters is minimal.

Table 5.3. Maximum Dist2Tool and %0-1.75 values for the six $[90^0/0^0]$ scenarios.

	Max Dist2Tool (mm)	%0-1.75
Cross	7.72	84.93%
X shape	8.51	86.19%
Cross & X shape	7.49	85.30%
Square 250x250	7.25	85.30%
Parallel 8	7.87	86.67%
Full breather	7.94	83.69%

Comparing the parallel 8 and full breather configurations, parallel 8 presents slightly lower maximum distance and 3% higher conformity. Therefore, parallel 8 would be slightly better than the full breather configuration for this orientation.

5.2.2 $[-45^0/+45^0]$ orientation

Figure 5.9 presents a picture of the forming for the six $[-45^0/+45^0]$ scenarios. In this case, no inter-ply sliding between the NCF layers can be observed.

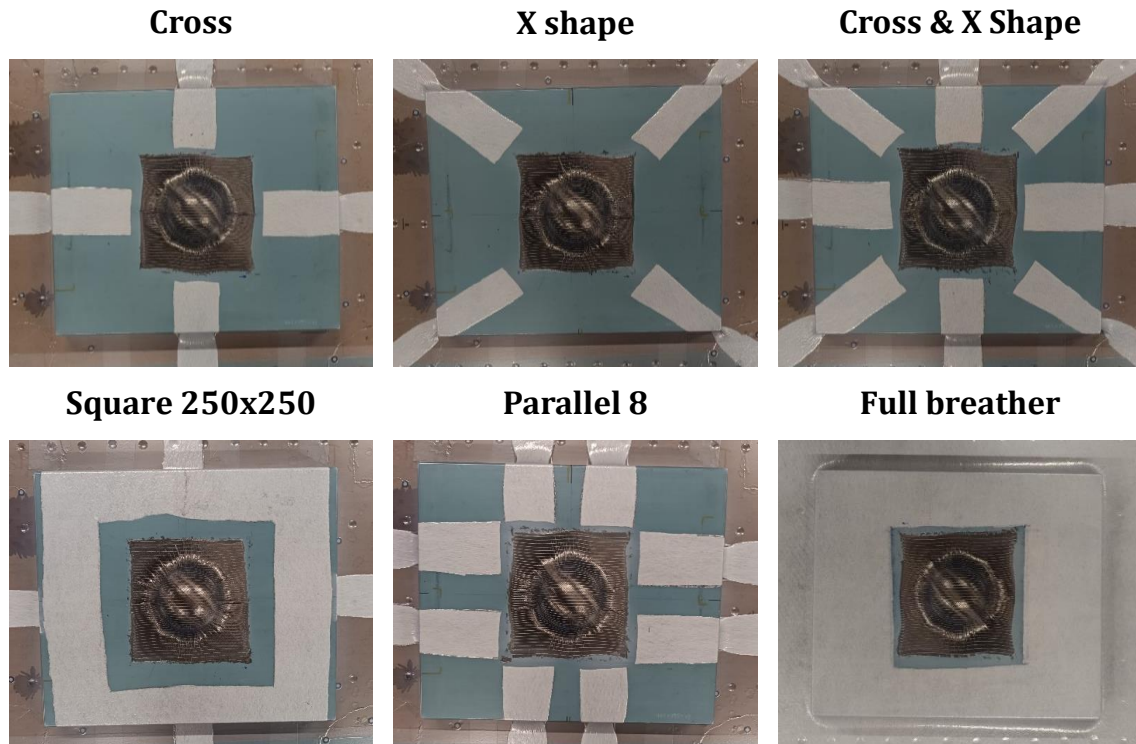


Figure 5.9. Picture of the forming for the six $[-45^0/+45^0]$ breather arrangement scenarios.

A more detailed analysis can be performed using the preform-tool distance contour plots, presented in Figure 5.10. All the configurations exhibit wrinkling in the Q2 and Q4 quadrants. Bridging is also noticeable, but the maximum distance is observed only in that area for the full breather configuration. In this case, no inter-ply sliding between the NCF layers is observed. The defect distribution analysis is performed individually:

- **Cross:** One wrinkle is observed in both Q2 and Q4 quadrants. The defects are of similar length and severity.
- **X shape:** Several wrinkles are observed in both Q2 and Q4 quadrants. The severity and length vary among the defects, being the central ones more severe, similar to the previous configuration.
- **Cross & X shape:** One wrinkle is observed in both Q2 and Q4 quadrants. The defects are of similar length and severity. This combination provides slightly better formability compared to the individual cases, since it presents less wrinkles than the X shape

configuration and the maximum distance is lower than for the cross configuration.

- **Square 250x250:** One wrinkle is observed in the Q2 quadrant, whilst two are present in the Q4 quadrant. The severity and length of the middle defects is similar for both quadrants.
- **Parallel 8:** Two wrinkles are observed in the Q2 quadrant, whilst one is present in the Q4 quadrant. The severity of the defects is reduced compared to the other cases.
- **Full breather:** Minimal wrinkling is present, with only a very small wrinkle in the Q4 quadrant. The maximum distance value is located on a bridging area.

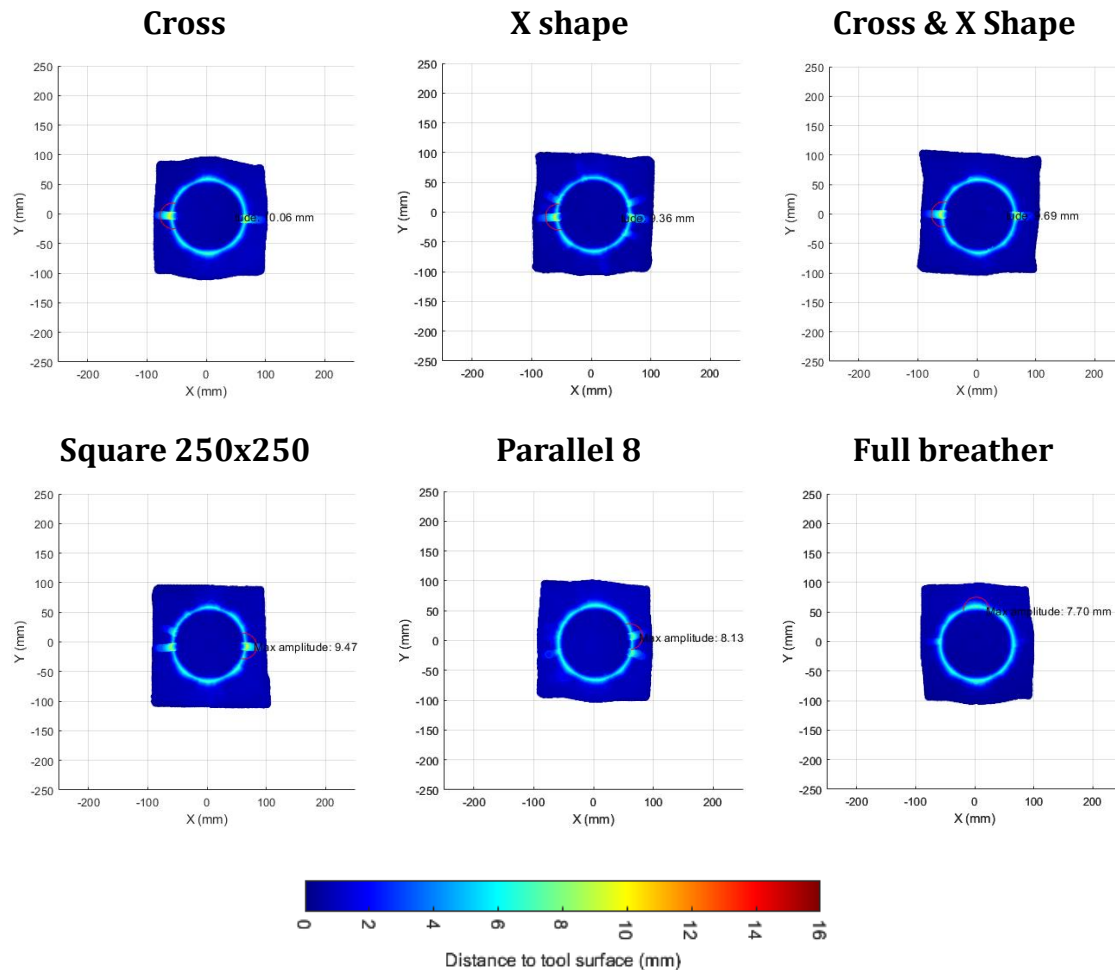


Figure 5.10. Preform-tool distance contour plot for the six $[-45^0/+45^0]$ scenarios.

In this case, the difference between configurations is greater, leading to different number and severity of defects. The full breather configuration presents minimal wrinkling when compared to the other scenarios. Therefore, this would be the best breather arrangement for this orientation.

Table 5.4 presents the maximum Dist2Tool and %0-1.75 values for the six scenarios. The maximum distance values range from 7.70 mm to 10.06 mm, which are 2 mm higher than those for the $[90^0/0^0]$ orientation. The conformity values range between 79.50%-83%, which is 3% to 6% lower than for the $[90^0/0^0]$ orientation. These observations suggest increased variability of this parameters with the different breather arrangements and indicate that this orientation conforms less effectively than the $[90^0/0^0]$ orientation.

The full breather configuration presents the lowest maximum distance; however, its conformity percentage is amongst the lowest. Since the other samples experience more wrinkling but their conformity is higher, these observations suggest that the full breather configuration suffers more from bridging, which aligns with the observations in Figure 5.10.

Table 5.4. Maximum Dist2Tool and %0-1.75 values for the six $[-45^0/+45^0]$ scenarios.

	Max Dist2Tool (mm)	%0-1.75
Cross	10.06	80.35%
X shape	9.36	82.10%
Cross & X shape	9.69	82.80%
Square 250x250	9.47	81.50%
Parallel 8	8.13	79.47%
Full breather	7.70	80.70%

5.2.3 Strain distribution on the diaphragm

From the previous observations it is evident that the breather configuration affects both the location and severity of defects. This section aims to investigate

the effect of the breather location on strain distribution in the diaphragm. The strain was tracked on the upper diaphragm using a 10 mm × 10 mm grid. The grid was drawn manually using a dotted stencil, the dots were then connected using a ruler. Details of the stacking sequence, breather configuration and tool used are provided in Table 5.5.

The grid drawing process is time consuming, therefore, the diaphragm material was reused up to four times. To control for any effects on deformation, two repetitions were performed for the cross configuration. Since the pattern appeared undisturbed, reusing the diaphragm did not affect the strain pattern. The fabric material was also reused for the same diaphragm, as the focus was on the strain pattern. For the first diaphragm, the grid covered the entire diaphragm and was used for the cross and parallel 8 configurations. As the grid remained undeformed across most of the diaphragm area, the grid for the second diaphragm was limited to the area around the tool. This grid was used for the X shape, cross & X shape, square 250x250 and full breather configurations.

Table 5.5. Parameters for the strain tracking study.

Diaphragm set-up	Stacking sequence	Breather configuration	Tool
1	[90°/0°, 0°/90°]	Cross Parallel 8	50rplatf
2	[90°/0°, 0°/90°]	X shape Cross & X shape Square 250x250 Full breather	50rplatf

Figure 5.11 presents the strain pattern around the tool for the different breather arrangements. No deformation occurs around the tool corners for all the breather configuration, however, deformation occurs in the fabric and breather areas. The following observations were made:

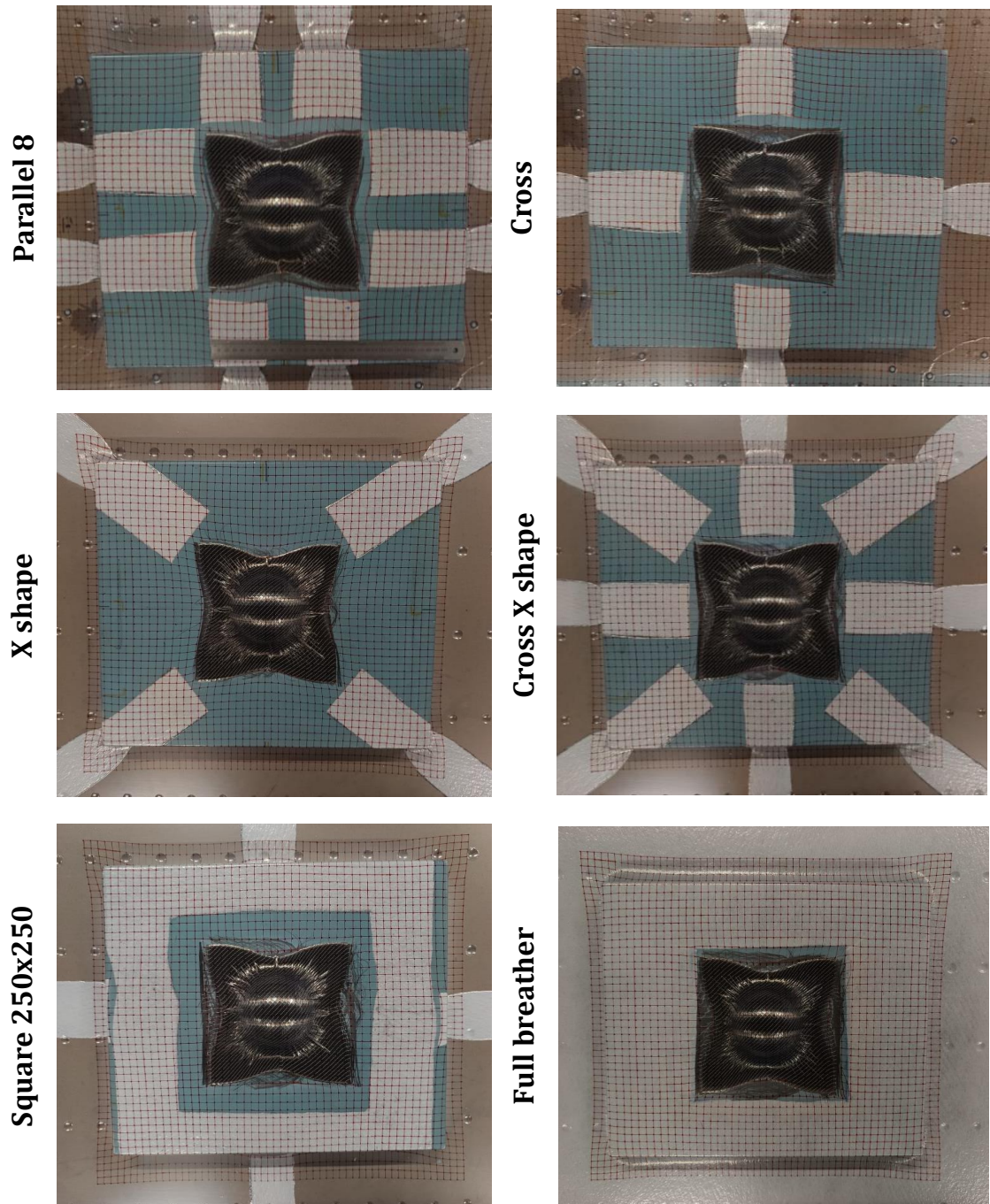


Figure 5.11. Distortion of regular grid around the tool for the different breather arrangements.

- **Parallel 8:** The strain pattern follows the fabric deformation, straining at the corners and allowing for draping in the middle, so that the material can move freely where is needed. High strain is presented between the fabric and breather, this strain distributes uniformly in the fabric outline.

- **Cross:** The strain pattern within the fabric is the same, however, high strain is only present in the middle of the fabric outline, as the breather is pinning the diaphragm, preventing draping where it should be happening, which is detrimental for the forming.
- **X shape:** The strain pattern is quite similar to parallel 8, however, it strains less around the preform. In this case, the breather only pulls from the corner of the preform, allowing draping on the middle, but to a lesser extent than parallel 8.
- **Cross & X shape:** The cross strips prevent draping, however, to a lesser extent than for the cross configuration. This is because, the X shape strips also hinder the diaphragm movement, producing a more constant deformation around the fabric outline than for the cross configuration.
- **Square 250x250:** The deformation around the fabric outline is fully prevented in all areas, since the diaphragm is pinned around the fabric outline.
- **Full breather:** Similar observations to the previous configuration, however, given that the space between the breather and the preform is smaller, the strain between the fabric and the breather is higher, allowing the preform to adapt better to shape.

Figure 5.12 presents the strain pattern on the edge of the upper diaphragm for the parallel 8 and cross breather arrangements. The diaphragm strain is reduced where the breather is located, therefore stiffening the diaphragm. This means that the straining mentioned previously is due to the breather stiffening the diaphragm and pinning it down, which pulls from the fabric, preventing its deformation.

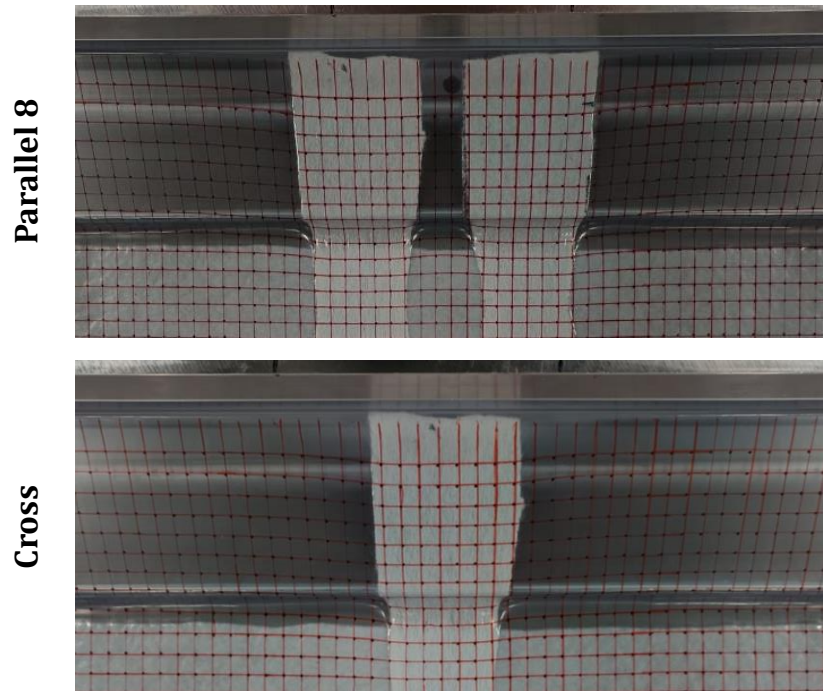


Figure 5.12. Strain pattern on the edge of the upper diaphragm for the parallel 8 and cross breather arrangements.

5.2.4 Evaluation of results

In conclusion, the study highlights the impact of different breather configurations on diaphragm stiffness and fabric deformation, influencing wrinkling formation for the different NCF orientations. The strain patterns observed support these findings, showing how some breather configurations allow for fabric deformation, whilst others restrict draping, hindering the forming process. Despite the time-consuming nature of hand-drawing the grid, reusing the diaphragm material did not alter the strain pattern, validating this experimental approach.

Therefore, optimising the breather configuration is essential, as the breather pulls from the fabric. The breather should be placed in areas where the material does not drape, allowing it to adapt to the desired shape and preventing wrinkling.

5.3 Effect of two-step preforming

Observations from the DDF experiments revealed that multi-ply forming led to more defects compared to single-ply forming. This prompted the question: Would individually performing the plies before multi-ply forming reduce defects or result in a defect free preform?

The initial idea was to manufacture hemispheres with slightly different radii. This variation in radii would allow for stacking the plies while accounting for the differences in deformation caused by the thickness of the laminate. However, since two hemisphere tools with identical radii were already available, the study was conducted using the existing tools. As a result, the radii difference between plies was not accounted for.

The aim of this study is to investigate the impact of a two-step preforming process on defects and assess its potential benefits, considering that implementing this method increases manual labour and material usage. Details of the stacking sequence, breather configuration and tool used are provided in Table 5.6. The stacking sequence was selected due to its susceptibility to wrinkling.

Table 5.6. Parameters for the two-step preforming study.

Stacking sequence	Breather configuration	Tool
[90°/0°, -45°/+45°]	Parallel 8	50rplatf

Figure 5.13 presents the preform-tool distance contour plots for the two configurations. When comparing both scenarios, it can be seen that the two-step preforming does not reduce the number of wrinkles, but it reduces their severity. Since the plies present reduced number of wrinkles when formed individually, as shown in Figure 5.8 and Figure 5.10, the defects observed are generated by the

interaction between the two plies. Additionally, the outline of the fabric undergoing two-step preforming is wider. This behaviour can be attributed to the pre-stretch undergone by the plies during the individual preforming, which makes the plies less compacted, allowing for the same draping with less displacement of the material when compared to the traditional one-step preforming process.

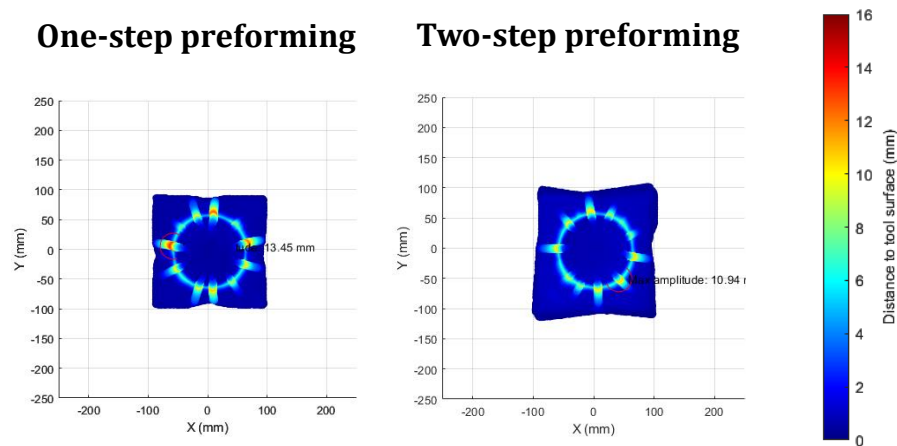


Figure 5.13. Preform-tool distance contour plot for a conventional one-step forming and a two-step forming for a stack sequence of $[90^0/0^0, -45^0/+45^0]$.

Table 5.7 presents the maximum Dist2Tool and %0-1.75 values for the two scenarios. The maximum distance is reduced by 3 mm and the conformity is increased by 2% for the two-step preforming process.

Table 5.7. Maximum Dist2Tool and %0-1.75 values for a conventional one-step forming and a two-step forming for a stacking sequence of $[90^0/0^0, -45^0/+45^0]$.

	Max Dist2Tool (mm)	%0-1.75
One-step preforming	13.45	75.25%
Two-step preforming	10.94	77.35%

These observations suggest that the improvement presented by the two-step preforming is not considered sufficient, as the process requires increased manual labour and material usage compared to the traditional method. However, further investigation using tooling of different radii could be beneficial to improve the stacking efficiency of the plies by considering the thickness of the laminate.

5.4 Effect of stacking sequence

When forming multiple plies with different orientations over complex shapes, the likelihood of defect occurrence increases compared to forming single plies due to relative inter-ply movement between plies. These defects can significantly reduce the mechanical performance of the final component. Therefore, understanding the mechanisms that cause these defects is critical to improve the quality of the final component.

Since the results for one ply show very minimal wrinkling, it can be concluded that the tool geometry has a negligible effect on wrinkle formation. Therefore, any wrinkles observed in this study are likely caused by relative inter-ply movement between the plies.

The aim of this study is to investigate the effect of the stacking sequence on the forming. Two sets of experiments were conducted with the $[90^0/0^0]$ and a $[-45^0/+45^0]$ orientation as base ply. The second ply has been tailored to ensure a relative fibre angle of 0^0 , 45^0 and 90^0 between the plies. Details of the stacking sequence, breather configuration and tool used are provided in Table 5.8.

Table 5.8. Parameters for the stacking study.

Relative fibre angle	Stacking sequence	Breather configuration	Tool
0^0	$[90^0/0^0, 0^0/90^0]$ $[-45^0/+45^0, +45^0/-45^0]$	Parallel 8	50rplatf
45^0	$[90^0/0^0, -45^0/+45^0]$ $[-45^0/+45^0, 90^0/0^0]$	Parallel 8	50rplatf
90^0	$[90^0/0^0, 90^0/0^0]$ $[-45^0/+45^0, -45^0/+45^0]$	Parallel 8	50rplatf

Figure 5.14 presents the preform-tool distance contour plots for the two configurations. The stacking sequence influences the distribution and severity of

defects. Since one of the cases for the $[90^0/0^0]$ base presents no wrinkling, whilst all the cases do for the $[-45^0/45^0]$ base, this indicates, as pointed out previously, that the parallel 8 configuration is not ideal for a 45^0 NCF orientation. The following observations were made:

- **Relative fibre angle 0^0**

- $[90^0/0^0]$ base: Slight wrinkling is present in the vertical and horizontal directions. Since NCFs tend to wrinkle in the positive shear area, the lack of wrinkling could be due to the interaction between plies. One ply effectively pins the other, thus hindering out-of-plane deformation and allowing both plies to conform to the desired shape.
- $[-45^0/+45^0]$ base: Two wrinkles are present in all the quadrants. In this case, both plies do not interact as effectively, as wrinkling appears in the positive shear area of each ply. The length and severity of all the defects is similar.

- **Relative fibre angle 45^0**

- $[90^0/0^0]$ base: Two wrinkles are present in all the quadrants. Some wrinkles are also present in one of the diagonal directions.
- $[-45^0/+45^0]$ base: Two wrinkles are present in all the quadrants.

- **Relative fibre angle 90^0 :**

- $[90^0/0^0]$ base: Wrinkling is present in the Q1 and Q3 quadrants. The length and severity of these wrinkles is similar. Slight wrinkling is also present in the vertical and horizontal directions.
- $[-45^0/+45^0]$ base: Wrinkling is present in the Q2 and Q4 quadrants, with the top wrinkle presenting increased severity for both quadrants.

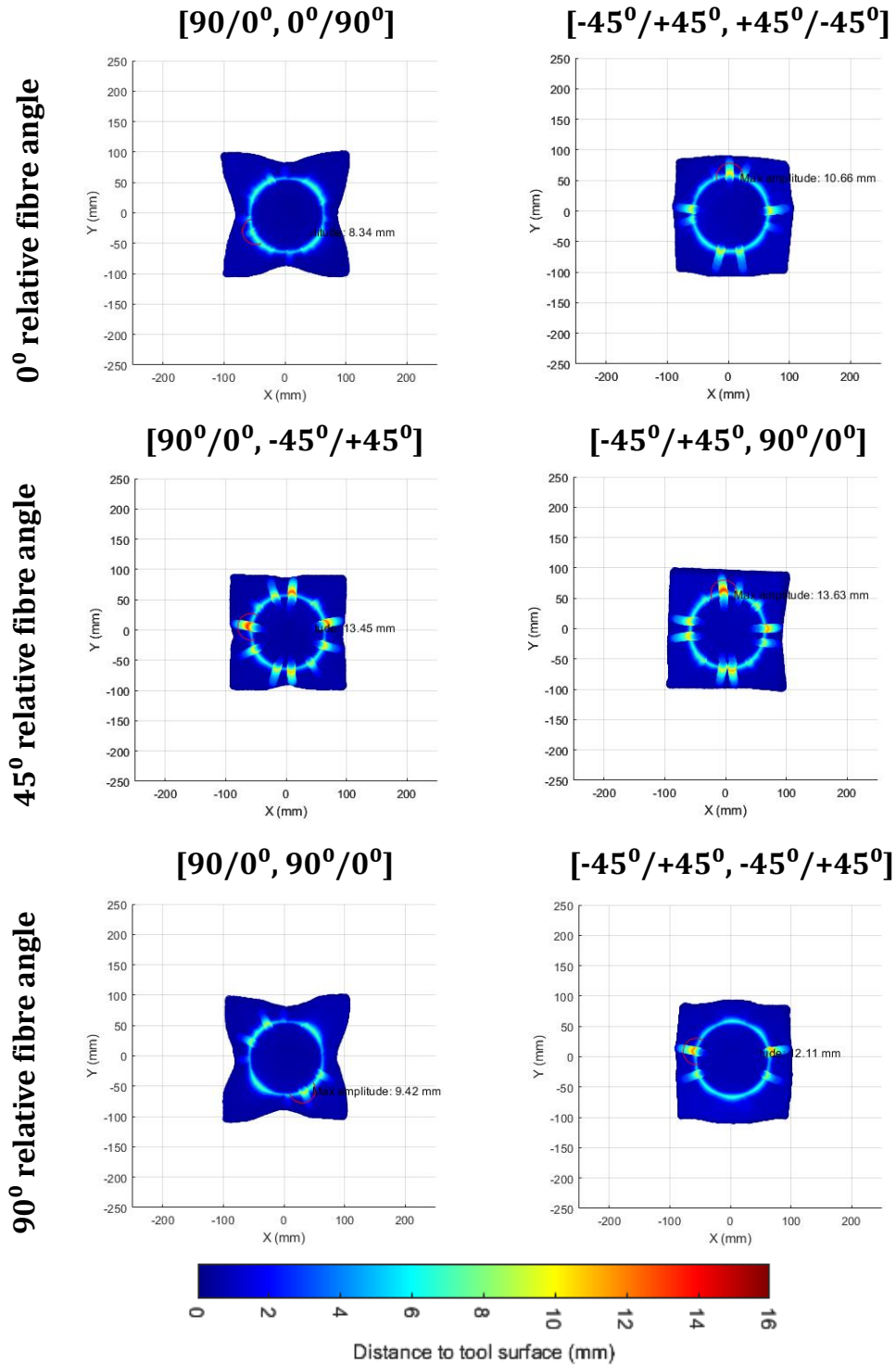


Figure 5.14. Preform-tool distance contour plot for the different stacking sequence cases by relative fibre angle.

These observations indicate that the choice of base ply significantly influences defect occurrence during forming. For both base plies, a relative fibre

angle of 45^0 is detrimental, leading to an increased number of wrinkles across all quadrants. The best results are achieved with a relative fibre angle 0^0 for the $[90^0/0^0]$ base, whilst for the $[-45^0/+45^0]$ base, the best results occur with a relative fibre angle of 90^0 , even though the latter still presents some wrinkling.

Table 5.9 presents the maximum Dist2Tool and %0-1.75 values for the different cases. The highest distance is obtained for a relative fibre angle of 45^0 . Therefore, this configuration not only leads to increased wrinkling but also to increased severity of defects. Both cases present the lowest distance with a relative fibre angle of 0^0 , although the maximum distance for the $[90^0/0^0]$ base is 2.3 mm lower. Additionally, even though the $[-45^0/+45^0]$ base presents reduced wrinkling at a relative fibre angle of 90^0 , the defect severity is not the lowest.

With regards to the conformity, the $[90^0/0^0]$ base exhibits 2% to 3% higher conformity for the same relative fibre angle compared to the $[-45^0/+45^0]$ base. For both cases the relative fibre angles of 0^0 and 90^0 yield a similar conformity, which is reduced around 5% for the 45^0 case.

Table 5.9. Maximum Dist2Tool and %0-1.75 value for different stacking sequence cases by relative fibre angle between plies.

Relative fibre angle	$[90^0/0^0]$ base		$[-45^0/+45^0]$ base	
	Maximum Dist2Tool (mm)	%0-1.75	Maximum Dist2Tool (mm)	%0-1.75
0^0	8.34	80.05%	10.66	77.22%
45^0	13.45	75.25%	13.63	73.71%
90^0	9.42	80.70%	12.11	78.83%

These observations indicate that the orientation of the base ply affects the number of wrinkles, the maximum distance and conformity but does not influence the wrinkling amplitude trend. A fibre angle of 0^0 was found to reduce the severity of wrinkles and, in some cases, decrease the number of defects,

whilst a relative fibre angle of 45^0 was found to be detrimental, as Figure 5.14 it is more likely to induce severe wrinkling in the preform.

5.5 Effect of modelling breather

To simplify the numerical model, it was initially assumed that the breather material does not have a noticeable effect on the forming predictions. This assumption was established as the numerical results did not exhibit air pockets, unlike the experimental results do when not using breather.

Section 5.2 demonstrates that the breather affects the stress and strain distribution on the diaphragm, significantly impacting fabric draping, therefore, influencing wrinkling formation. The previous chapter highlighted that the model requires further adjustments to better align with the experimental outcomes. Therefore, the aim of this section is to model the breather and evaluate whether its inclusion improves the accuracy of the predictions.

The evaluation is done for three stacking sequences, the model and process parameters are presented in Table 3.5 and Table 3.6. The breather has been modelled as a deformable part using M3D4R membrane elements. The density of the material was determined to be 50 kg/m^3 , as calculated in section 3.1.4.3. For simplification, the material was treated as elastic with isotropic properties, requiring only the Young's modulus and Poisson's ratio values. The breather was positioned between the diaphragms, with a 2 mm gap from the fabric, using the same breather configuration as in the experimental tests, in this case the parallel 8 configuration (see Figure 5.15).

The study starts by comparing the effect of the breather parameters, Young's modulus and Poisson's ratio, on the predictions. This is done for a stacking sequence of $[90^0/0^0, 0^0/90^0]$. Once these parameters are established, the predictions are further validated for two additional stacking sequences, $[90^0/0^0]$ and $[-45^0/+45^0, +45^0/-45^0]$. It is important to validate both one and two ply

predictions, as chapter 4 demonstrates that the one ply model predicts wrinkling contradicting the experimental observations, whilst the two ply model accurately predicts the affected area but not the wrinkling pattern.

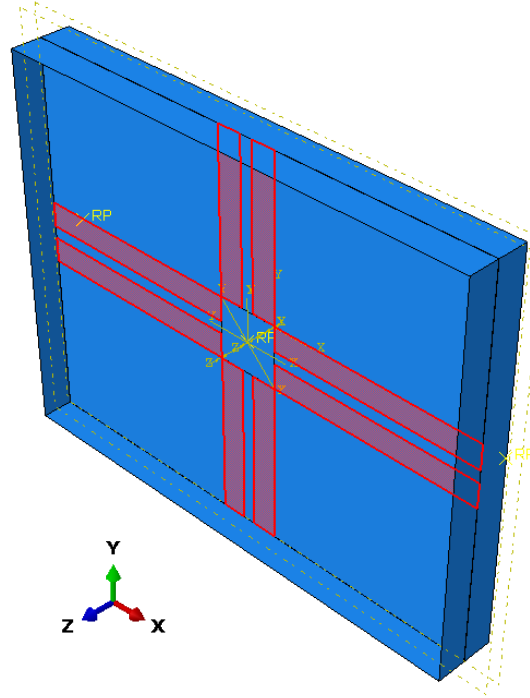


Figure 5.15. Schematic of the breather positioning for the parallel 8 configuration. The breather strips are highlighted in red.

For the first stacking sequence, $[90^0/0^0, 0^0/90^0]$, the breather was modelled using a Young's modulus of 0.25 MPa and a Poisson's ratio of 0.49, as calculated in section 3.1.4.3. However, the values did not seem appropriate, as the material is quite stiff and showed minimal deformation at lower strains. Therefore, a second set of properties was proposed, a higher Young's modulus of 25 MPa and a lower Poisson's ratio of 0.25. The 25 MPa Young's modulus suggests that the material is soft and flexible, deforming significantly under stress compared to metals or ceramics. The Poisson's ratio of 0.25 suggests moderate transverse contraction under tension or compression, which aligns with the expected behaviour of this material.

These cases are compared with the experimental and numerical with no breather results to evaluate the effect of the breather on the predictions. A summary of where to find the results and the observations is provided in Table 5.10.

Table 5.10. Summary of the experimental and numerical no breather results previously presented for the $[90^\circ/0^\circ, 0^\circ/90^\circ]$ stacking sequence.

Data	Figure	Observations
Experimental	Figure 4.8	No wrinkling in any quadrant
Numerical no breather	Figure 4.11	Two wrinkles in all the quadrants, slight wrinkling in vertical direction

Figure 5.16 presents the preform-tool distance contour plot for the numerical cases with breather for the $[90^\circ/0^\circ, 0^\circ/90^\circ]$ stacking sequences. The deformation pattern for the E 0.25 case is similar to the no breather case, presenting wrinkling in all the quadrants. On the other hand, the E 25 case presents no wrinkling. Therefore, the defect predictions for these new properties are much closer to the experimental results.

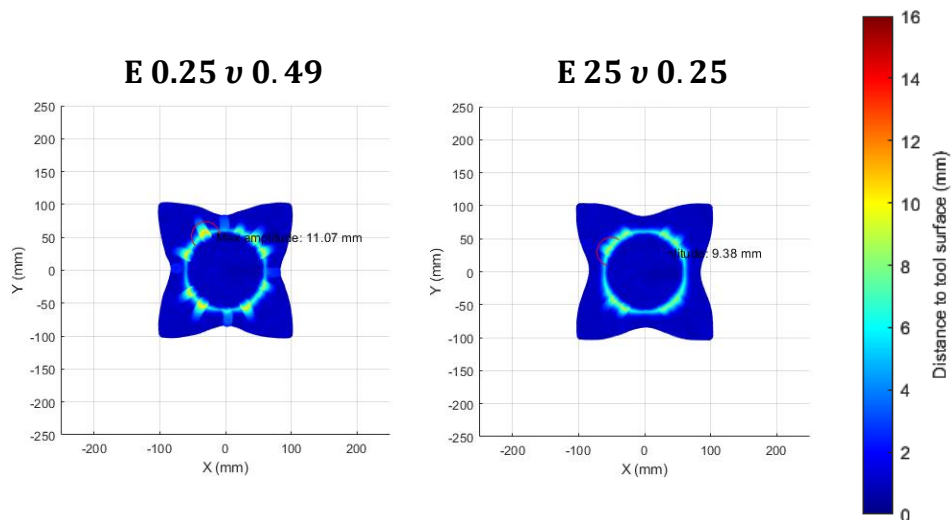


Figure 5.16. Preform-tool distance contour plot for the numerical cases with breather for the $[90^\circ/0^\circ, 0^\circ/90^\circ]$ stacking sequence.

Table 5.11 presents the maximum Dist2Tool and %0-1.75 values for the different cases. The maximum distance is similar for the no breather case and for the E 0.25 case, whilst the E 25 case is only 1.03 mm higher than the experimental case. This indicates that when using the proposed properties, the maximum distance is still overpredicted, but to a lesser extent. With regards to the conformity, all the numerical results present a reduced conformity of around 4%. This indicates that the conformity is still underpredicted.

Table 5.11. Maximum Dist2Tool value for different breather modelling cases.

	Maximum Dist2Tool (mm)	%0-1.75
Exp	8.34	80.05%
Num - no breather	11.19	76.47%
Num - E 0.25 v 0.49	11.06	76.16%
Num - E 25 v 0.25	9.37	76.44%

Therefore, the proposed breather properties, $E = 25$ MPa and $\nu = 0.25$, provide better predictions, with the wrinkling pattern and maximum distance presenting an improvement, although the conformity is still underpredicted.

Once the breather parameters are established, the predictions are further validated for two additional stacking sequences. These cases are again compared with the experimental and numerical with no breather results. Table 5.12 provides a summary of the numerical with no breather and experimental results and observations for both stacking sequences.

Figure 5.17 presents the preform-tool distance contour plot for the numerical cases for those stacking sequences. Both predictions have been improved compared to the no breather predictions, as the $[90^0/0^0]$ case presents no wrinkling and the $[-45^0/+45^0, +45^0/-45^0]$ case presents 2 wrinkles in all the quadrants. However, in the latter case, the wrinkling length and severity is higher than observed experimentally.

Table 5.12. Summary of the experimental and numerical no breather results previously presented for the $[90^\circ/0^\circ]$ and $[-45^\circ/+45^\circ, +45^\circ/-45^\circ]$ stacking sequences.

	Data	Figure	Observations
$[90^\circ/0^\circ]$	Experimental	Figure 5.8	No wrinkling in any quadrant
	Numerical no breather	Figure 4.10	Slightly wrinkling in the Q1 and Q3 quadrants
$[-45^\circ/+45^\circ, +45^\circ/-45^\circ]$	Experimental	Figure 4.8	Two wrinkles in all the quadrants
	Numerical no breather	Figure 4.11	Two wrinkles in Q1 and only one wrinkle in the other quadrants

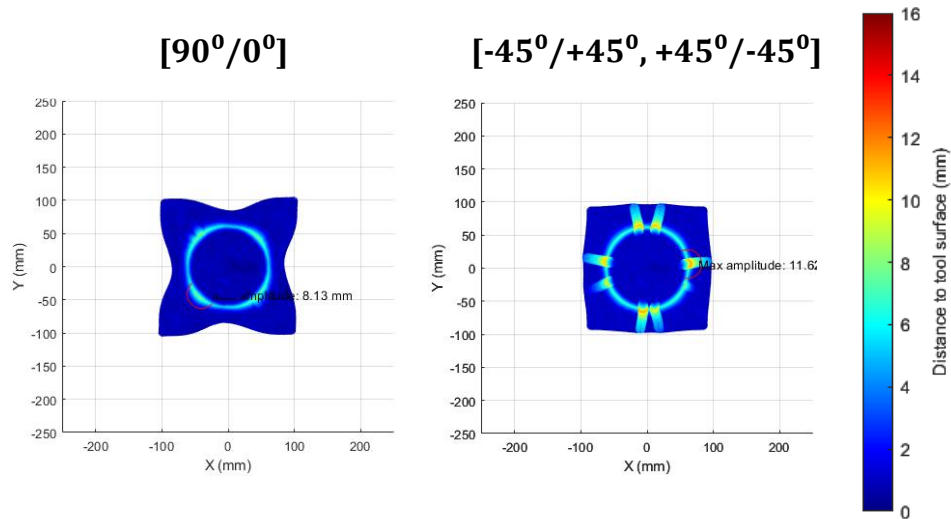


Figure 5.17. Preform-tool distance contour plot for the numerical cases with breather for the $[90^\circ/0^\circ]$ and $[-45^\circ/+45^\circ, +45^\circ/-45^\circ]$ stacking sequences.

Table 5.13 presents the maximum Dist2Tool and %0-1.75 values for the different cases. The predictions considering the breather are closer to the experimental observations. For the $[90^\circ/0^\circ]$ case, the maximum distance is only

0.26 mm higher, and for the $[-45^0/+45^0, +45^0/-45^0]$ is only 0.96 mm higher. This indicates that, when modelling the breather, the maximum distance is still overpredicted by 3.3% and 9.01%, but to a lesser extent compared to the predictions without a breather, which are overpredicted by 21.73% and 29.27%. With regards to the conformity, all the numerical results present a reduced conformity between 3% to 5%. This indicates that the conformity is still underpredicted even when considering the breather.

When looking at the three stacking sequences in this study, the results indicate that the defect predictions are improved when modelling the breather. The wrinkling pattern matches the pattern observed experimentally, and the maximum distance is less than 1.25 mm higher than that observed experimentally. However, the conformity is still underpredicted, as it is reduced by approximately 5% for all the numerical predictions.

Table 5.13. Maximum Dist2Tool value for different breather modelling cases.

	$[90^0/0^0]$		$[-45^0/+45^0, +45^0/-45^0]$	
	Maximum Dist2Tool (mm)	%0-1.75	Maximum Dist2Tool (mm)	%0-1.75
Experimental	7.87	83.67%	10.66	77.22%
Numerical no breather	9.58	81.44%	13.78	72.66%
Numerical breather	8.13	80.14%	11.62	72.14%

5.6 Chapter summary

This chapter investigates the effect of several parameters on the forming process. The wrinkling pattern is influenced by the diaphragm size, with larger diaphragms providing insufficient tension and smaller diaphragms over-

constraint the material. For the conditions studied, an optimal diaphragm size ranges between 1.25 to 2.5 or 3.25 times the size of the fabric.

The breather arrangement affects defect formation depending on the stacking sequence. For a $[90^0/0^0]$ orientation, defect formation is not significantly influenced, and the parallel 8 or full breather provided better results. In contrast, for a $[-45^0/+45^0]$ orientation, different arrangements lead to variations in defect number and severity, with the full breather providing the most favourable results. Additionally, the presence of breather reduces the strain in the diaphragm, preventing the deformation of the fabric. These observations highlight the importance of optimising the breather configuration, ensuring it is positioned in areas where the fabric does not require draping, which improves the adaptability of the fabric and minimises wrinkling occurrence.

When evaluating two-step preforming, performing plies individually before stacking them was found to reduce wrinkle severity, though not necessarily the number of defects. Regarding stacking sequence, the base ply orientation affects the number of wrinkles but not amplitude trends. A relative angle of 0^0 reduces wrinkling severity and, in some cases, the number of defects, whereas a 45^0 angle is more likely to induce severe wrinkling.

Incorporating the breather into the numerical model improved defect predictions by better replicating the experimental wrinkling pattern. However, conformity remains underpredicted.

Chapter 6 Investigating multi-component forming

The previous chapter provided insights into how certain parameters affect the forming process, improving the understanding of material behaviour during forming as process parameters are altered. This knowledge can now be applied to understand how fabrics interact during multi-component forming and assess the feasibility of this approach. Multi-component forming consists of simultaneously producing multiple preforms in the same machine bed and using the same consumables within one forming cycle. This process has the potential to increase efficiency, reduce material waste and operational time, increasing the overall productivity and sustainability of the process.

This chapter evaluates the feasibility of multi-component forming by examining the effects of fabric-fabric and fabric-diaphragm spacing on the forming process. The studies discussed in this chapter are listed in Table 6.1, indicating the number of tools used and whether the study was experimental, numerical or both.

Table 6.1. Description of the studies presented in this chapter.

Study	Tools	Type
Horizontal separation	Two	Both
Vertical separation	Two	Numerical
Three tool forming	Three	Experimental

6.1 Numerical considerations and benchmark results

For the numerical studies, when selecting the distance between fabrics, it was important to ensure that the fabric and diaphragm meshes were aligned. These means that the edge of the fabric aligns with the mesh, and it does not sit in between elements. This alignment ensures smoother load transfer between the

parts, reducing the likelihood of convergence issues and improving the accuracy of the results. The model and process parameters for the numerical studies were presented in Table 3.5 and Table 3.6.

In the previous chapter, particularly in section 5.1, the numerical predictions when forming a $[0^0/90^0]$ established that diagonal 2 measures 555 mm, which is longer than diagonal 1, measuring 540 mm. Furthermore, it was determined that all the edges should exhibit the same length after forming, approximately 390 mm. These findings provide a reference when analysing the numerical predictions in this chapter, as they set the expected benchmarks for both diagonal and edge measurements. Note that the numerical values apply only to the 100r hemisphere.

6.2 Horizontal separation

This section investigates the effect of horizontal separation (in x-direction) of the fabrics during a two tool forming. Both fabrics were centred at $y = 0$, with displacement occurring along the x-direction. Several distances were evaluated numerically and experimentally.

6.2.1 Numerical study

For this numerical study, fabric 1 was located at $x < 0$ and fabric 2 at $x > 0$, ensuring no overlapping between the fabrics. The x-distance between fabrics, $d_{x_{fabrics}}$, was measured between facing fabric edges. The fabric-diaphragm edge distance, d_{edge} , was measured between facing fabric and diaphragm edges. A schematic of the positioning and distances is presented in Figure 6.1. The $d_{x_{fabrics}}$ and d_{edge} distances evaluated are presented in Table 6.2.

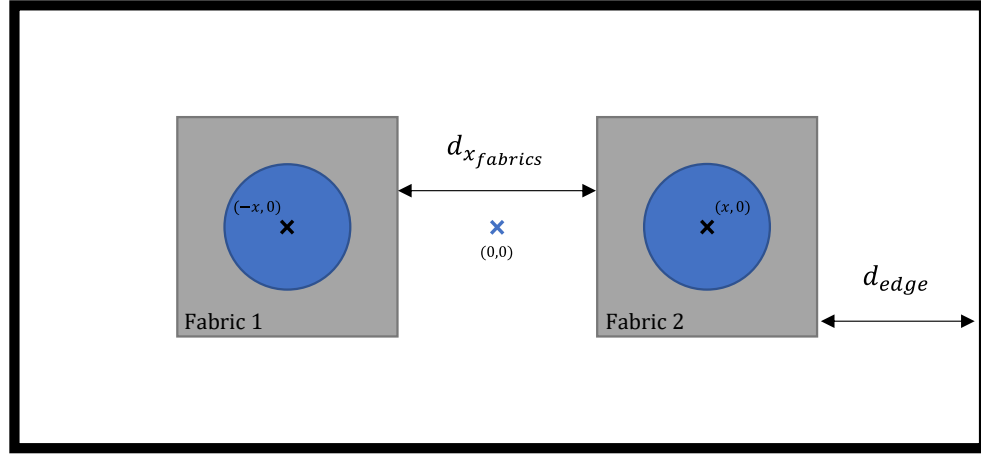


Figure 6.1. Schematic of the fabric positions for the numerical two tool study.

Table 6.2. Distances between fabrics evaluated for the numerical two tool study, and their fabric-diaphragm edge distances. All the distances are in millimetres.

$d_{x_{fabrics}}$	d_{edge}	$d_{x_{fabrics}}$	d_{edge}
12	594	500	350
52	574	600	300
76	562	700	250
100	550	800	200
200	500	900	150
300	450	1000	100
400	400		

Figure 6.2 presents the diagonal and edge lengths for both fabrics and all the $d_{x_{fabrics}}$ distances. Figure 6.2 a) and b) present the diagonal values for fabric 1 and 2, respectively. In both cases, diagonal 2 is longer than diagonal 1. For both fabrics, the diagonal values increase with the fabric distance, with the values converging at a 100 mm distance, and the trend increasing from 700 mm onwards. Both diagonal values in that region are around 5 mm below the benchmark values.

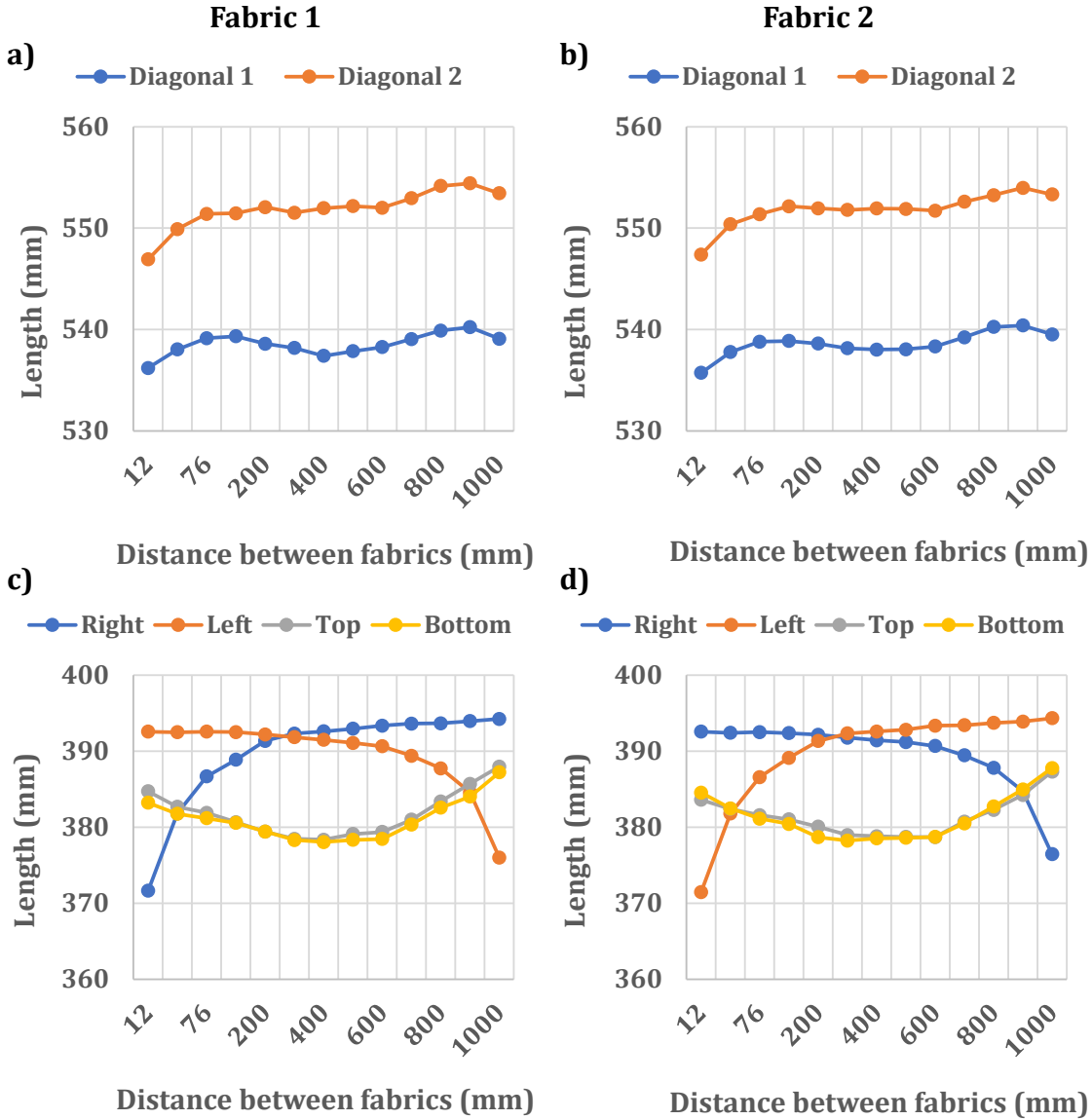


Figure 6.2. Diagonals and edge length for fabric 1 and 2 and all the $d_{x_{fabrics}}$ distances for the numerical two tool study.

Figure 6.2 c) and d) present the edge values for fabric 1 and 2, respectively. In both cases, all edges are not the same length. The length of the top and bottom decreases until a 400 mm distance, at which point it starts to increase. The values converge 12 mm below the benchmark for a distance between 300 mm and 600 mm. When examining the lengths of the left and right edges, the same trend but inverted is observed for the two fabrics. The length values converge for a distance between 200 mm and 600 mm, aligning with the benchmark results. This trend

suggests that the fabrics are too close to each other until a distance of 200 mm, whilst at a distance of 600 mm the fabrics become too close to the diaphragm. The edge values in that interval match the benchmark results.

These results indicate that the optimal distancing varies depending on which diagonal or edge is under consideration. The diagonals converge at distances between 100 and 700 mm, although their lengths are 5 mm shorter than the benchmark. The top and bottom edges converge at distances between 300 mm and 600 mm, although their lengths are 12 mm shorter than the benchmark. Only the right and left edges achieved the expected benchmark length at distances between 200 mm and 600 mm.

These observations suggest that forming two fabrics simultaneously slightly reduces the draping of the material, as the diagonals and the top and bottom edges exhibit less deformation compared to when the fabrics are formed individually. Based on all the observations, the ideal spacing is likely between 200 and 600 mm.

Figure 6.3 presents the preform-tool distance contour plot for both fabrics at distances of 12 mm, 400 mm and 1000 mm between the fabrics. The wrinkling pattern occurs in all samples within the Q2 and Q4 quadrants, with the wrinkling pattern slightly changing based on the distance. Horizontal and vertical wrinkling is also observed for some of the cases.

For a 12 mm distance between fabrics, the fabrics are too close, resulting in horizontal wrinkling on the fabric edges facing each other. When the distance is increased to 400 mm, this horizontal wrinkling disappears. At a 1000 mm distance, the fabrics are too close to the diaphragm edge, leading to horizontal wrinkling on the fabric edges facing the diaphragm. This horizontal wrinkling accounts for the variations observed in the length of the right and left edges, which decreases when horizontal wrinkling is presented.

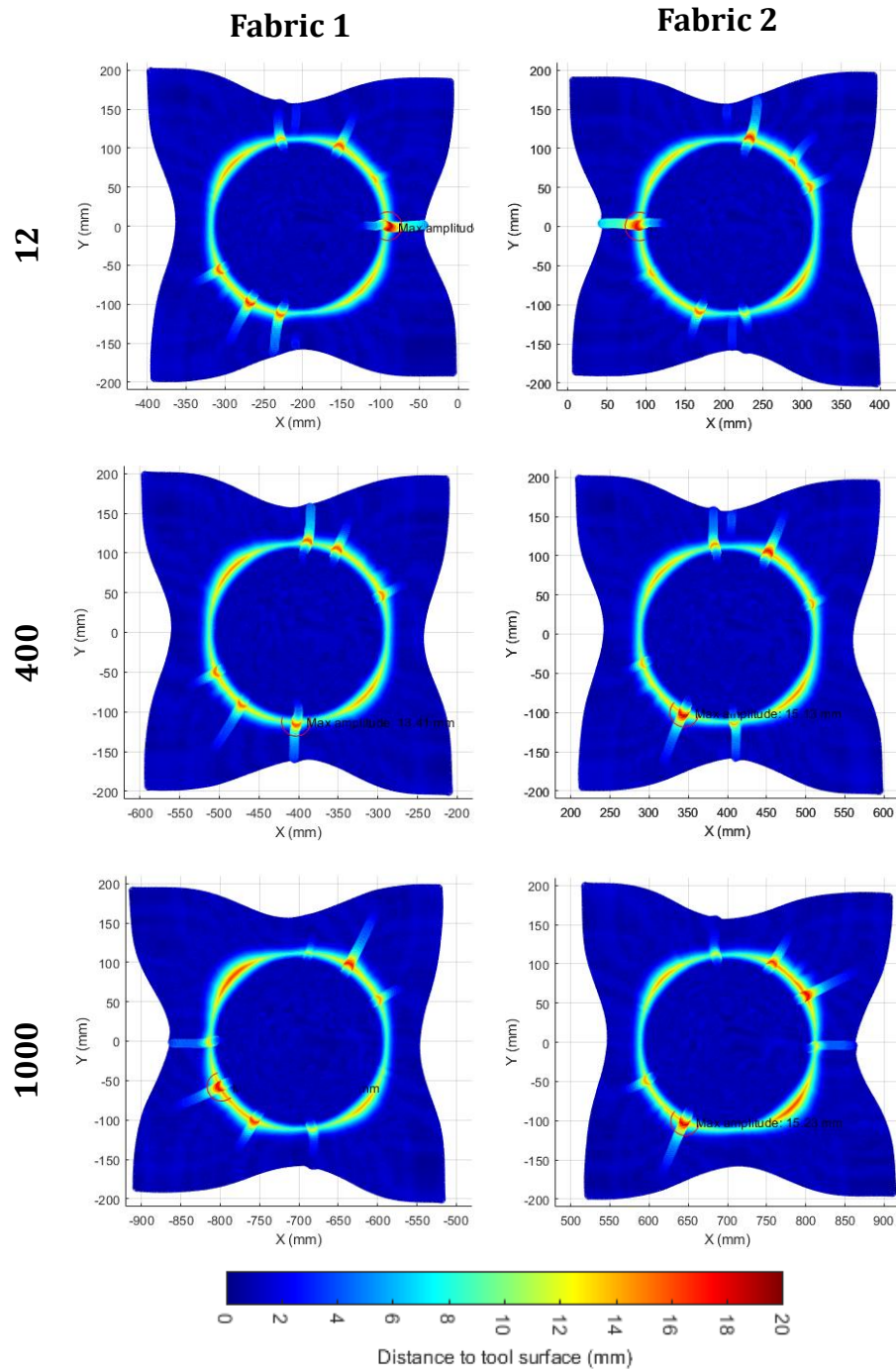


Figure 6.3. Preform-tool distance contour plot for both fabrics and a distance between fabrics of 12, 400 and 100 mm for the numerical two tool study.

When the fabrics are too close, vertical wrinkling occurs, but its severity is reduced. As the distance between fabrics increases, the vertical wrinkling becomes more noticeable. However, if the fabrics are spaced too far apart, this wrinkling disappears. This vertical wrinkling explains the variations observed in

the length of the top and bottom edges, which initially decrease and then start to increase at a distance of 600 mm.

Additionally, the outline variations are well represented in this contour. The outline is relatively symmetric for a 400 mm fabric distancing. However, in the other two cases, one side of the fabric is restricted from moving, causing the fabric corners to no longer align. This reduced mobility leads to wrinkling, as the same amount of material is forced to form within a smaller space. This outline variations account for the behaviour observed in the length of the diagonals.

6.2.2 Experimental study

For this experimental study, fabric 1 was located at $x < 0$ and fabric 2 at $x > 0$, ensuring no overlapping between the fabrics. A schematic of the positioning and distances is presented in Figure 6.4.

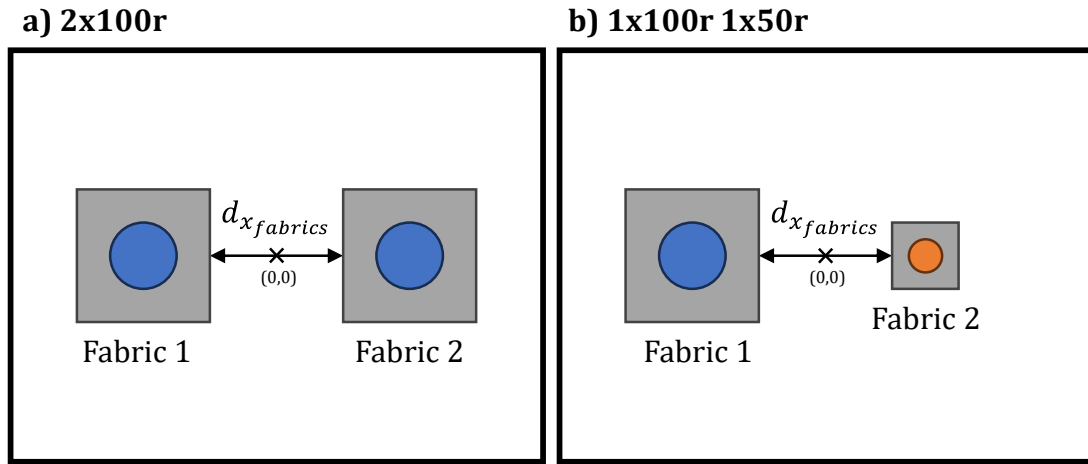


Figure 6.4. Schematic of the fabric positions for the experimental lateral study for the two tool arrangements. The $d_{x_{fabrics}}$ is the x-distance between fabrics for the experimental two tool study.

In this case, two different sets of hemispherical tools were used. Details of the breather configuration, tools, $d_{x_{fabrics}}$, and d_{edge} are provided in Table 6.3. The distances are provided in millimetres. The fabric size for the 100r hemisphere is 400 mm \times 400 mm, whilst for the 50r hemisphere is 200 mm \times 200 mm. The d_{edge} distance depends on the fabric size.

Table 6.3. Parameters for the experimental two tool study.

Breather arrangement	Tools	$d_{x_{fabrics}}$	Fabric size	d_{edge}
Modified Parallel 8	2x100r	100	200	550
				400
	1x100r 1x50r	400	400	350
				200

Two different stacking sequences, either A, $[0^0/90^0, 0^0/90^0]$, or B, $[90^0/0^0, 90^0/0^0]$, were used for the different scenarios, as shown in Table 6.4. As the positive and negative shear areas depend on the material orientation, the defects will be located in different quadrants. Additionally, for some of the scenarios the hemispheres were not perfectly centred, however, this does not affect the wrinkling pattern, as shown by Codolini et al [59].

Table 6.4. Stacking sequence for both fabrics for the experimental two tool study, where A is $[0^0/90^0, 0^0/90^0]$ and B is $[90^0/0^0, 90^0/0^0]$.

Tool	$d_{x_{fabrics}}$	Fabric 1	Fabric 2
2x100r	100	B	B
	400	B	B
1x100r 1x50r	100	B	A
	400	A	A

Figure 6.5 presents the diagonal and edge lengths for both fabrics for the 2x100r configuration and all the $d_{x_{fabrics}}$ distances. In this case, the stacking sequence both fabrics and both distances is B.

Figure 6.5 a) presents the diagonal values for fabric 1. Diagonal 1 is longer than diagonal 2. Both diagonal values are quite similar for both distances. Figure 6.5 b) presents the diagonal values for fabric 2. Diagonal 1 is longer than diagonal

2. In this case, diagonal 2 values are quite similar for both distances, but the length of diagonal 1 is reduced 7 mm when increasing the distance to 400 mm.

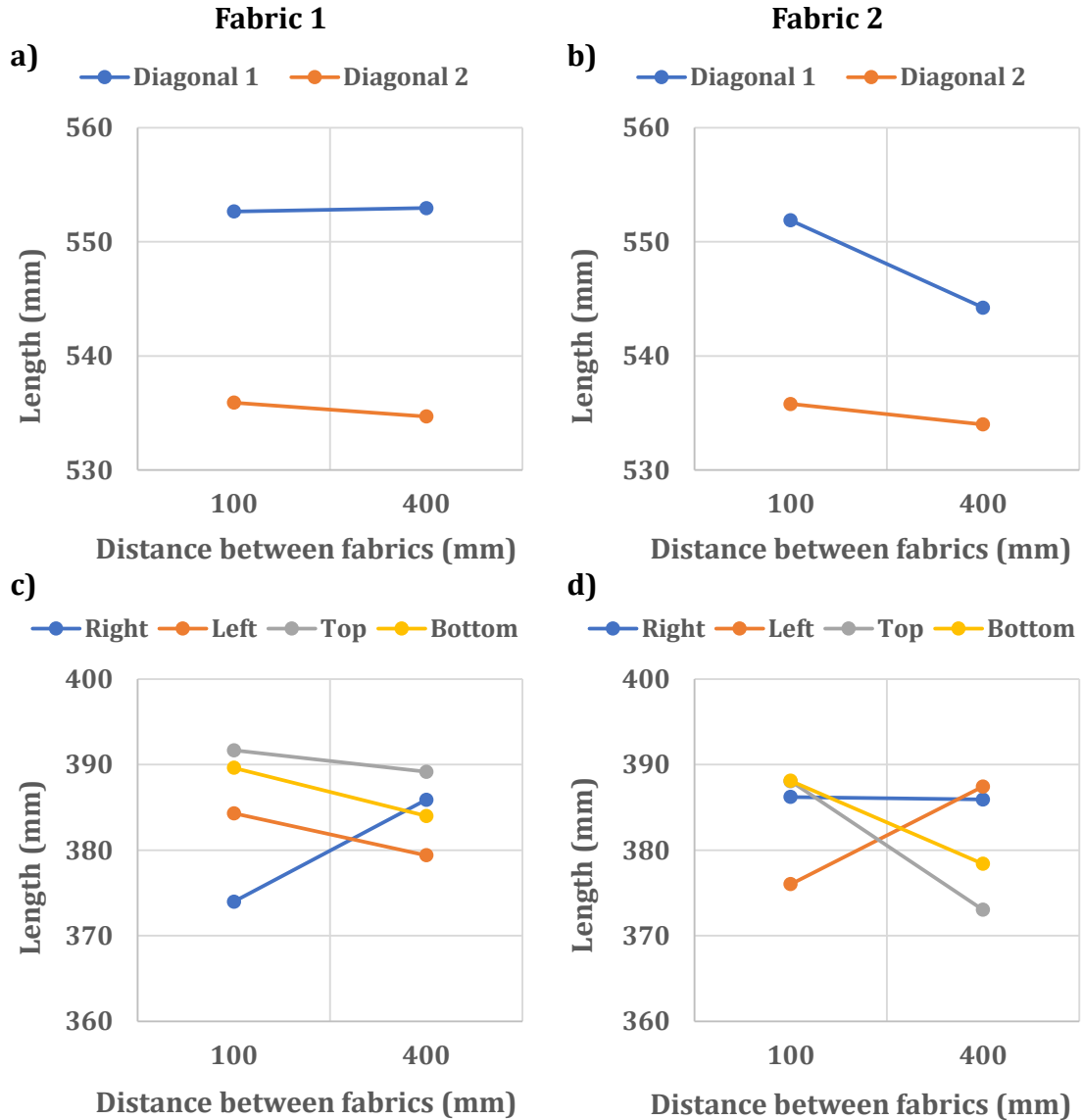


Figure 6.5. Diagonals and edge length for fabric 1 and 2, for the 2x100r configuration and all the $d_{xfabrics}$ distances for the experimental two tool study.

Figure 6.5 c) presents the edge values for fabric 1. The left, top and bottom edges reduced their length as the distance increases to 400 mm. This change is more pronounced for the left and bottom edges, which reduced their length by 5 mm to 6 mm, compared to the 2 mm reduction for the top edge. The right edge increased by 12 mm in length as the distance increases to 400 mm. Since the right

side faces fabric 2, increasing the distance between the fabrics improves the drape of this edge.

Figure 6.5 d) present the edge values for fabric 2. The length of the right edge is quite similar for both distances. The left edge increased by 11 mm in length as the distance increased to 400 mm. Since this side faces fabric 1, increasing the distance between the fabrics improves the drape of this edge. The top and bottom edges reduced their length as the distance increased to 400 mm. This change is more pronounced for the top edge, reducing its length by 15 mm, compared to the 10 mm reduction for the bottom edge.

Figure 6.6 presents the diagonal and edge lengths for both fabrics for the 1x100r 1x50r configuration and all the $d_{x_{fabrics}}$ distances. In this case, the stacking sequence for fabric 1 is different for both distances, this is important to consider when comparing results.

Figure 6.6 a) presents the diagonal values for fabric 1. The diagonal values are inverted with the distance. This is due to fabric 1 having the B orientation for a 100 mm and the A orientation for a 400 mm distance between fabrics.

Figure 6.6 b) presents the diagonal values for fabric 2. The diagonal values are lower since the fabric measures 200 mm × 200 mm. Diagonal 2 is longer than diagonal 1. The diagonal 2 values are quite similar for both distances, whilst diagonal 1 decreases 8 mm in length as the distance increases to 400 mm.

Figure 6.6 c) presents the edge values for fabric 1. All the edges are similar in length. The left and bottom edges decrease in length as the distance increases to 400 mm, consistent with the observations in Figure 6.5 c). The right and top edges increase their length as the distance increases to 400 mm. In this case, the trend of the top edge is inverted when compared to Figure 6.5 c). Since the right

side faces fabric 2, increasing the distance between the fabrics improves the drape of this edge.

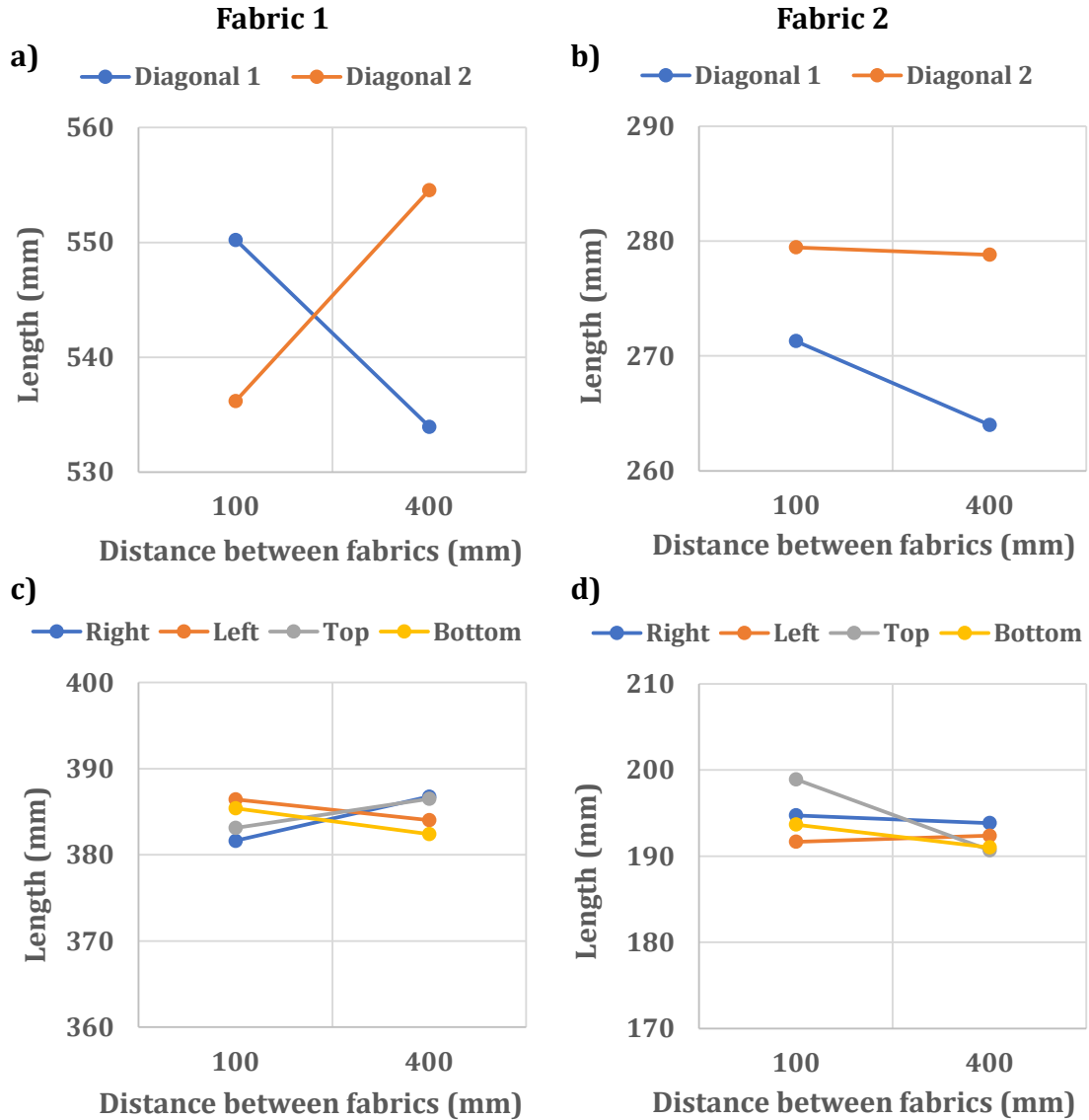


Figure 6.6. Diagonals and edge length for fabric 1 and 2, for the 1x100r 1x50r configuration and all the $d_{xfabrics}$ distances for the experimental two tool study.

Figure 6.6 d) present the edge values for fabric 2. The right edge length remains similar for both distances, as does the left edge. However, the top and bottom edges decrease in length as the distance increases to 400 mm. This change is more pronounced for the top edge, reducing its length by 8 mm,

compared to the 2 mm reduction for the bottom edge. This behaviour is similar to that observed in Figure 6.5 d), although, the length values are closer in the current cases.

Figure 6.5 and Figure 6.6 show that increasing the distance between fabrics is beneficial for the facing fabric edges, as their length increase. When comparing the edge length between the different tool cases, the lengths are more similar for the 1x100r 1x50r cases, which show the best results at a distance of 400 mm. This effect is not observed for the 2x100r cases. This could suggest that forming two hemispheres of different sizes is advantageous to the forming process, or that forming two fabrics with AA or AB orientation is better than with BB orientation.

Figure 6.7 and Figure 6.8 present the preform-tool distance contour plot for both fabrics and both tool configurations at distances of 100 mm and 400 mm between the fabrics. The fabrics present the same wrinkling pattern observed when forming one tool experimentally in Figure 4.7, with wrinkles mainly appearing in the positive shear areas, Q1 and Q3 for the orientation B and Q2 and Q4 for the orientation A, and slightly in both vertical and horizontal directions.

For all the fabrics, horizontal wrinkling improves as the distance between the fabrics increases. This can be explained by the fact that when the fabrics are close together, the deformation of the diaphragm is constrained. This reduced mobility leads to wrinkling, as the fabrics are forced to form within a smaller space.

When looking at wrinkling in the positive area, the number of wrinkles decreases when increasing the distance, but their severity increases. This can be explained by the fact that as the distance increases, the fabrics have more freedom to deform. Therefore, the material can better adapt to the shape, resulting in fewer wrinkles, but those that form are more severe due to the greater amount of material that deforms out-of-plane.

For the 2x100r cases, it can be observed that increasing the distance between fabrics reduced bridging. However, for the 1x100r 1x50r cases, the bridging is of similar severity. This indicates that forming the BA or AA configurations is less effective at reducing bridging than forming the BB configuration.

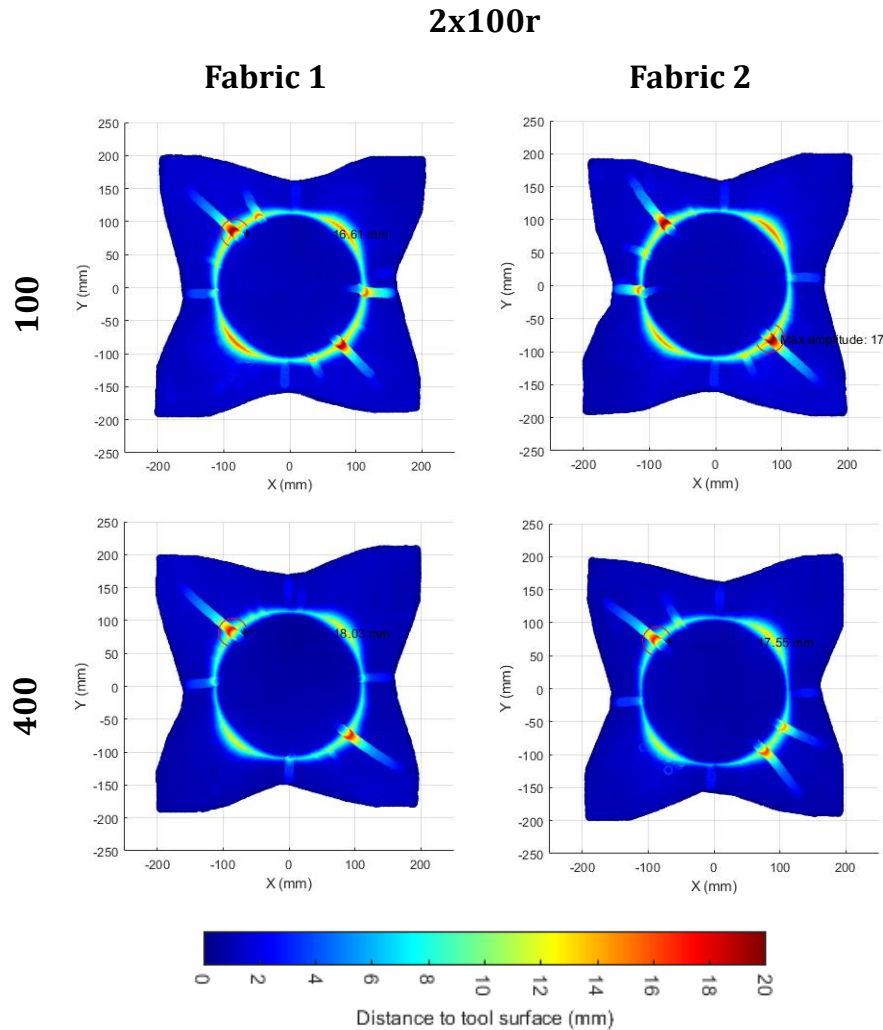


Figure 6.7. Preform-tool distance contour plot for both fabrics, 2x100r configuration and a x-distance between fabrics of 100 mm and 400 mm for the experimental two tool study.

Table 6.5 presents the maximum Dist2Tool and %0-1.75 values for the different configurations. The maximum distance is highly affected by the distance between fabrics, whilst the %0-1.75 is similar across all cases.

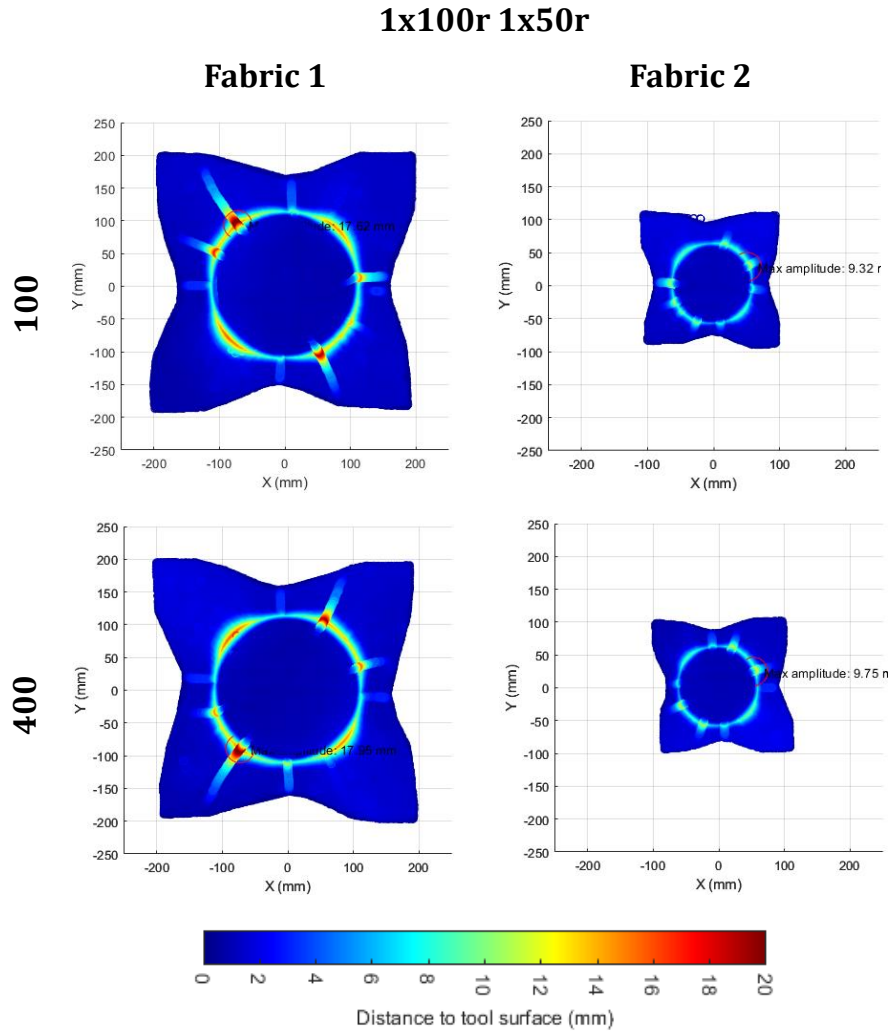


Figure 6.8. Preform-tool distance contour plot for both fabrics, 1x100r 1x50r configuration and a x-distance between fabrics of 100 mm and 400 mm for the experimental two tool study.

For the 2x100r cases, as the spacing between fabrics increases, the maximum distance increases by 1.42 mm for fabric 1 and 0.54 mm for fabric 2, whilst the conformity increases 1.3% for fabric 1 and only 0.31% for fabric 2. For the 1x100r 1x50r cases, the maximum distance increases 0.34 mm for fabric 1 and 0.43 mm for fabric 2, whilst the conformity increases 0.19% for fabric 1 and decreases 0.31% for fabric 2. These observations align with those from Figure 6.7 and Figure 6.8: when the fabrics are too close, the deformation of the diaphragm is constrained, leading to wrinkling. As the distance between fabrics increases, the material can better adapt to shape, resulting in few wrinkles, but of increased severity.

Table 6.5. Maximum Dist2Tool and %0-1.75 value for both fabrics, both tool configurations and a x-distance between fabrics of 100 mm and 400 mm for the experimental two tool study.

	Distance (mm)	Fabric 1		Fabric 2	
		Maximum Dist2Tool (mm)	%0-1.75	Maximum Dist2Tool (mm)	%0-1.75
2x100r	100	16.61	80.10%	17.01	81.18%
	400	18.03	81.40%	17.55	81.49%
1x100r	100	17.62	80.76%	9.32	78.07%
1x50r	400	17.96	80.95%	9.75	77.76%

Based on these observations, it can be concluded that increasing the distance between fabrics improves conformity and reduces the number of defects, even though the maximum distance increases. Therefore, increasing the separation between fabrics is beneficial for the forming process.

6.2.3 Evaluation of results

When comparing experimental and numerical results, it is important to note that both rigs used were of different sizes, the numerical rig measured 2000x800 mm, whilst the experimental rig was 1600x1240 mm. Additionally, the stacking sequence differed between samples. Despite these differences, the main observations from both studies are consistent. Both suggesting that forming two fabrics simultaneously slightly reduces the draping of the material and separating the fabrics in the x-direction is beneficial.

The numerical results suggested that a spacing of 200-600 mm is optimal, which aligns with the experimental findings that show a 400 mm distancing providing better results. Furthermore, the experimental results suggest that forming two hemispheres of different sizes or using AA or AB orientation instead of BB could be advantageous for the forming process.

6.3 Vertical separation

This numerical study investigates the effect of vertical movement of the fabrics during a two tool forming. The x-distance between fabrics ($d_{x_{fabrics}}$) was set to 12 mm. Fabric 1 was fixed at $y = 0$, whilst fabric 2 moved along the positive y-axis. The y-distance between fabrics, $d_{y_{fabrics}}$, was measured from the centre of fabric 2 to the centre of fabric 1. A schematic of the positioning is presented in Figure 6.9. The $d_{y_{fabrics}}$ distances evaluated were 6, 12, 52, 100, 152 and 176 mm.

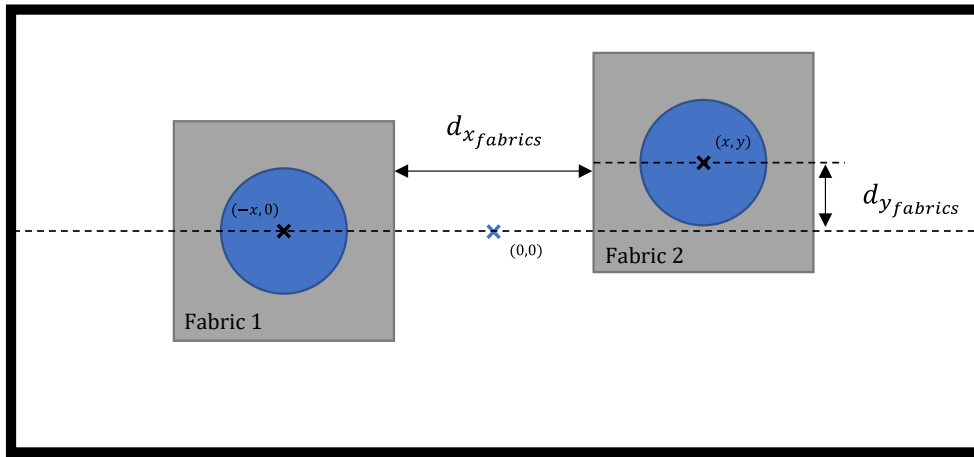


Figure 6.9. Schematic of the fabric positions for the numerical two tool vertical separation study. The $d_{x_{fabrics}}$ is the x-distance between fabrics, and the $d_{y_{fabrics}}$ is the y-distance between fabrics.

Figure 6.10 presents the diagonal and edge length for both fabrics and all the $d_{y_{fabrics}}$ distances. Figure 6.10 a) presents the diagonal values for fabric 1. Diagonal 1 increases in length as the distance between fabrics increases, exceeding 540 mm for distances greater than 100 mm. In contrast, diagonal 2 decreases in length as the distance between fabrics increases, remaining at least 10 mm below the benchmark length.

Figure 6.10 b) presents the diagonal values for fabric 2. Diagonal 1 increases in length up to a distance of 100 mm, after which it begins to decrease, reaching the benchmark length only at distances of 100 mm and 152 mm. In contrast, diagonal 2 decreases in length as the distance between the fabrics increases,

remaining at least 10 mm below the benchmark length. The reduction for this diagonal in fabric 2 is more pronounced than for fabric 1, with the lowest length being 20 mm below the benchmark. This indicates that fabric 2 is too close to the diaphragm edge for distances greater than 100 mm.

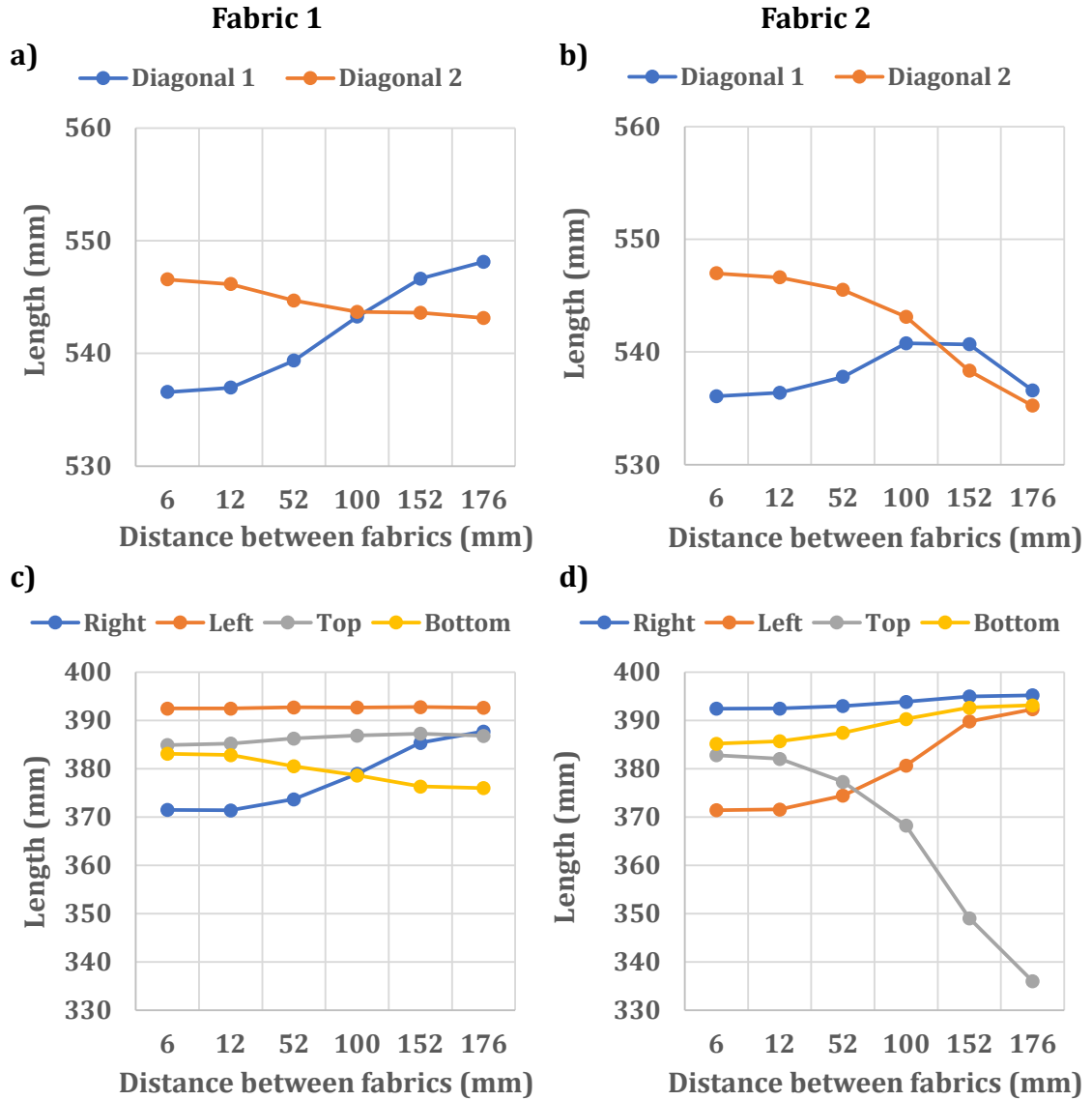


Figure 6.10. Diagonals and edge length for fabric 1 and 2 and all the $d_{y_{fabrics}}$ distances the numerical two tool vertical separation study.

Figure 6.10 c) presents the edge values for fabric 1. The left and top edges are close to the benchmark length. The right edge increases in length as the distance between fabrics increases, suggesting that this distancing could be beneficial for

this edge, reaching the benchmark length at distance of 152 mm and 176 mm. However, the bottom edge decreases in length as the distance between fabrics increases. In this case, the length is closer to the benchmark at distances below 52 mm.

Figure 6.10 d) present the edge values for fabric 2. The right and bottom edges are close to the benchmark length. The left edge increases in length as the distance between fabrics increases, reaching the benchmark length for distances greater than 152 mm. However, the top edge decreases considerably in length as the distance between fabrics increases, with the lowest value being 54 mm below the benchmark, suggesting that increasing the distance between fabrics is detrimental for this edge. This indicates that fabric 2 is too close to the diaphragm edge for distances greater than 100 mm.

Figure 6.11 presents the preform-tool distance contour plot for both fabrics at distances of 6 mm, 12 mm, 52 mm, 100 mm, 152 mm and 176 mm between the fabrics. The outline is affected by the distance between fabrics. The fabrics wrinkle mainly in the Q2 and Q4 quadrants, which correspond to the positive shear area.

Horizontal wrinkling occurs only in the facing edges, as the x-distance between fabrics is only 6 mm. This horizontal wrinkle shifts angle as the distance between fabrics increases.

Vertical wrinkling is present in both fabrics, suggesting that the diaphragm may be too small in that direction or that it should be square rather than rectangular. For fabric 2, the vertical wrinkle on the top edge increases severity and amplitude as the distance between fabrics increases, becoming critical for a distance of 100 mm, indicating that the fabric is too close to the diaphragm edge.

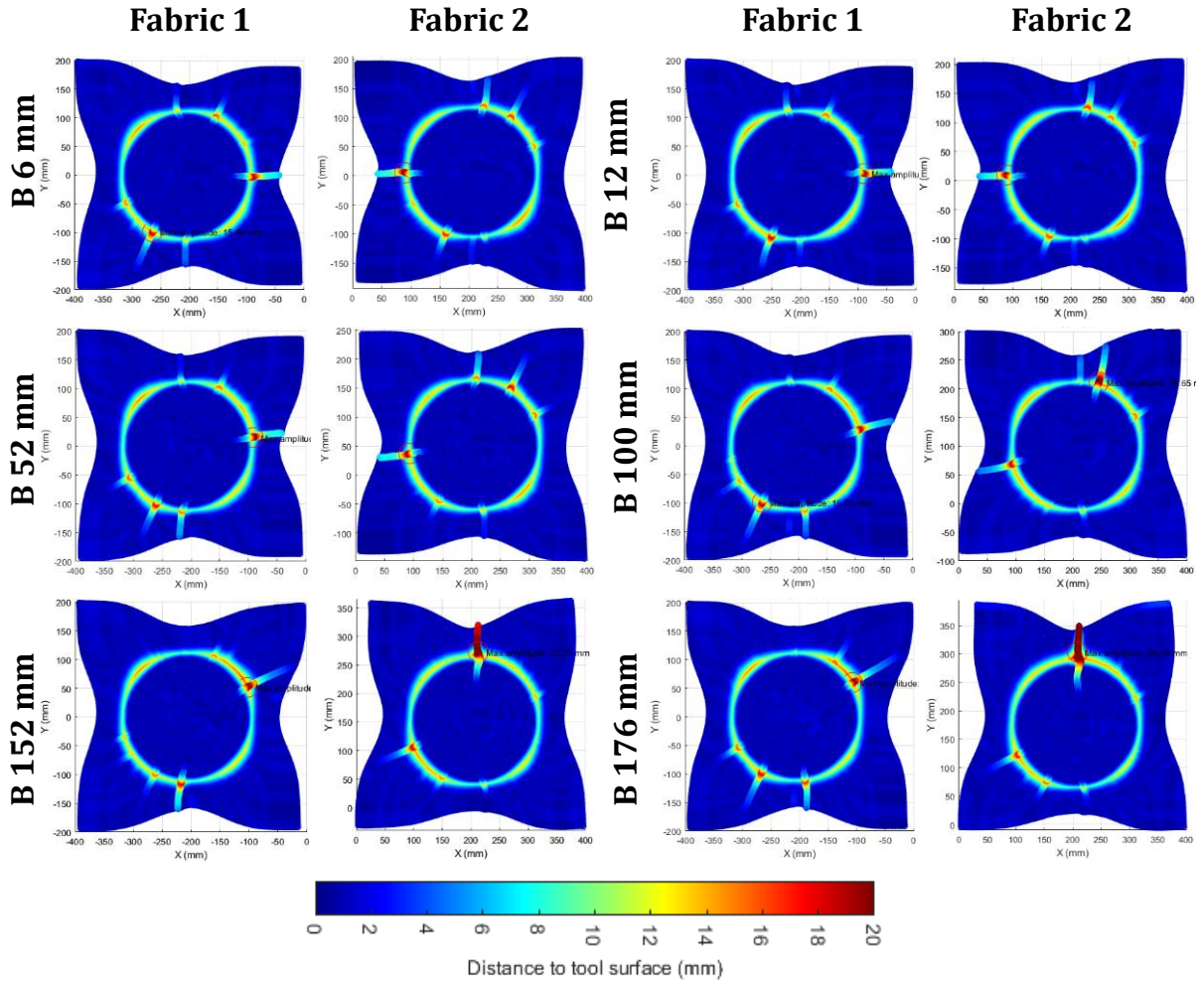


Figure 6.11. Preform-tool distance contour plot for both fabrics and the different y-distances for the numerical two tool vertical separation study.

Figure 6.12 presents the maximum Dist2Tool and %0-1.75 values for the six scenarios. Both parameters are highly affected by the y-distance between fabrics.

Figure 6.12 a) presents the maximum distance value for both fabrics. The values for fabric 1 show minimal variation. However, for fabric 2, the maximum distance values increase significantly for distances greater than 100 mm. The total difference between values is of 13.28 mm.

Figure 6.12 b) presents the %0-1.75 values for both fabrics. For fabric 1, the values peak at a distance of 52 mm, and then increase again, with a total variability of 0.24%, which is not significant. In contrast, for fabric 2, the values decrease for distances greater than 100 mm, with a total difference of 1.86%.

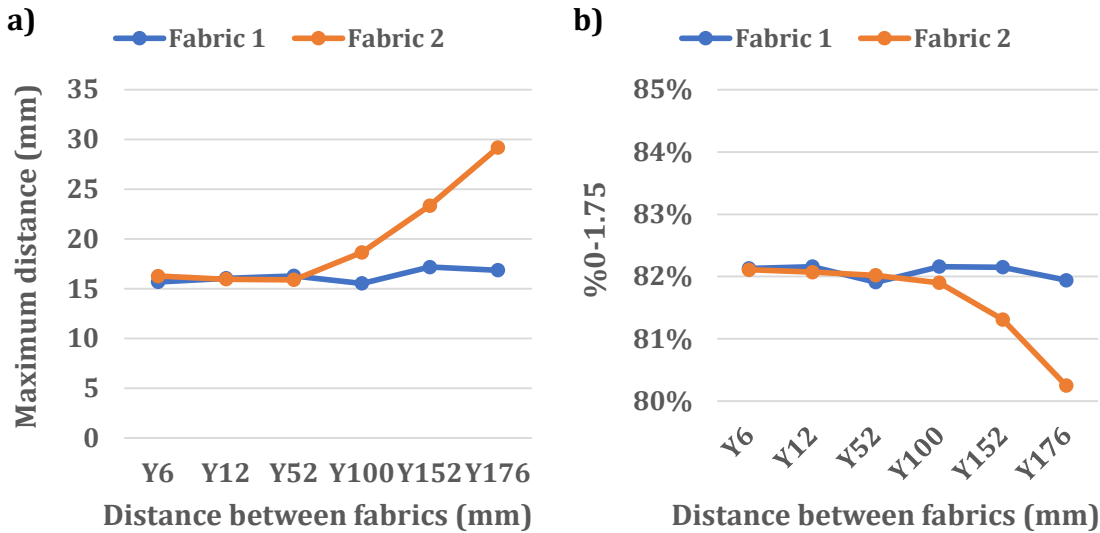


Figure 6.12. Maximum Dist2Tool and %0-1.75 value for both fabrics and the different y-distances for the numerical two tool vertical separation study.

From these observations it can be concluded that when the fabrics are considerably close in the x-direction, they conform better for y-distances below 100 mm. The results indicate that, especially for fabric 2, distances greater than 100 mm are detrimental to the draping of the material, reducing its conformity and increasing the severity of defects.

6.4 Three tool forming

This experimental study investigates the effect of horizontal and vertical separation of the fabrics during a three tool forming. Three configurations varying the x- and y-distance between fabrics were investigated. For this study fabric 1 was located at $x < 0$, fabric 2 at $x = 0$, and fabric 3 at $x > 0$, ensuring no overlapping between the fabrics. The tools used are one 50r hemisphere, located between two 100r hemispheres. The stacking sequence for the fabrics was $[90^\circ/0^\circ, 90^\circ/0^\circ]$.

A schematic of the positioning and distances is presented in Figure 6.13. The x-distance between fabric 1 and fabric 3, $d_{x_{fab1-3}}$, was measured between facing

edges. The fabric-diaphragm distance, d_{edge} , was measured between facing fabric and diaphragm edges. The y-distance to fabric 2, d_{yfab2} , was measured between the centre of fabrics 1 and 3 and the edge of fabric 2.

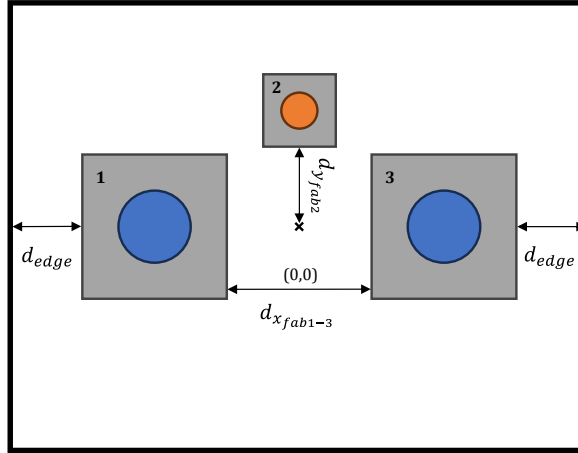


Figure 6.13. Schematic of the fabric positions for the experimental three tool study.

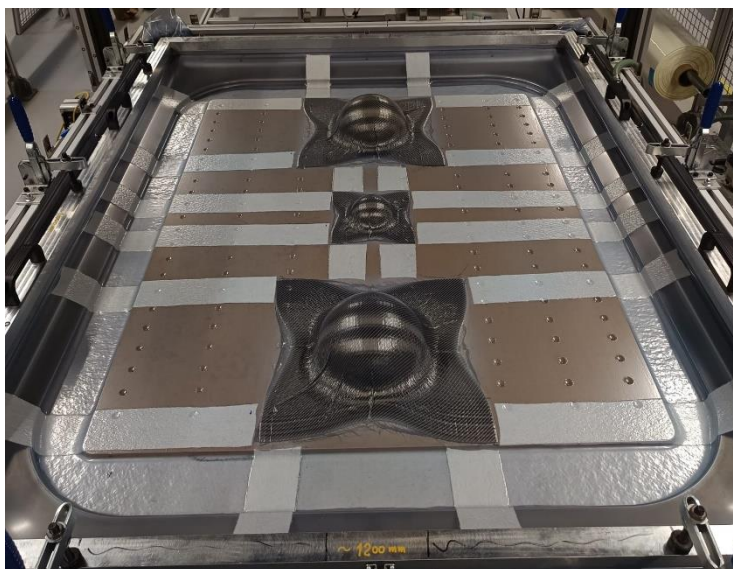
The stacking sequence for the experiments is $[90^0/0^0, 90^0/0^0]$. Details of the breather configuration, $d_{x_{fab1-3}}$, d_{edge} , and $d_{y_{fab2}}$ are provided in Table 6.6. Three different configurations are assessed. The nomenclature used to name the configurations is as follows: X $d_{x_{fab1-3}}$ Y $d_{y_{fab2}}$.

Table 6.6. Coordinates of the fabric centres in mm for the experimental three tool study.

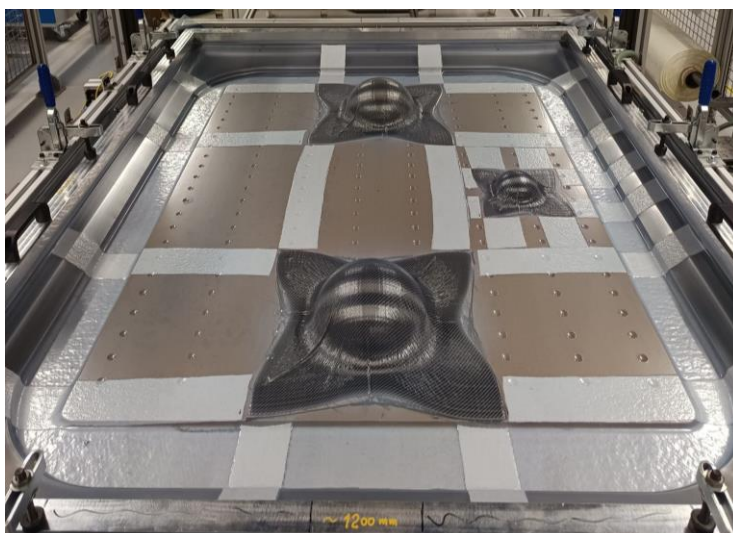
	Breather configuration	$d_{x_{fab1-3}}$	d_{edge}	$d_{y_{fab2}}$
X400 Y0	Modified Parallel8	400	200	0
X400 Y220		400	200	220
X200 Y220		200	300	220

Figure 6.14 presents the experimental distribution for the three tool cases under study. The fabrics, from top to bottom, are identified as fabric 1, fabric 2 and fabric 3. The breather configuration was modified for each case, aiming to maintain parallel 8 for each fabric as close as possible, considering the spacing between fabrics.

X400 Y0



X400 Y220



X200 Y220

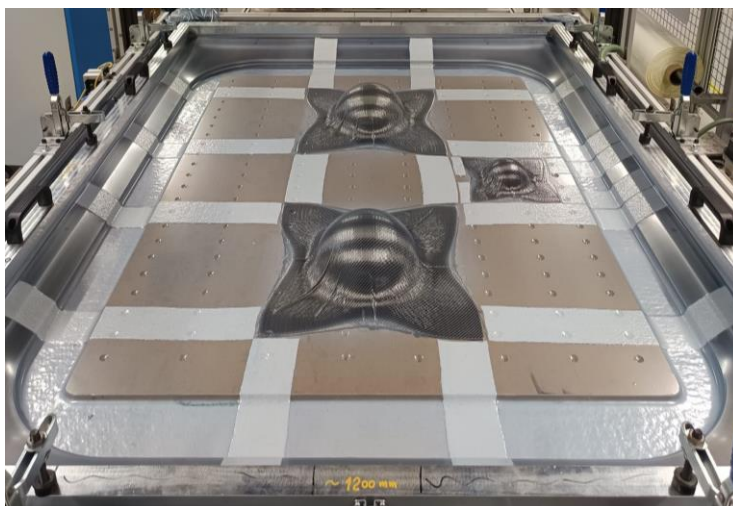


Figure 6.14. Pictures of the experimental distribution for the three tool study.

Figure 6.15 presents the diagonal and edge lengths for fabric 1 for the three forming cases. Figure 6.15 a) presents the diagonal values for fabric 1. Diagonal 1 is longer than diagonal 2. Diagonal 1 presents the lowest value for the X400 Y220 case, whilst the diagonal 2 presents the highest value for that case. The difference is 8 mm for diagonal 1, and 5 mm for diagonal 2.

Figure 6.15 b) presents the edge values for fabric 1. The lengths of the top and left edges increase when the y-distance between fabrics increases and the x-distance decreases. The bottom edge behaves similarly to diagonal 1, presenting the lowest value for the X400 Y220 case. The right edge behaves like diagonal 2, presenting the highest value for the X400 Y220 case. For the X400 Y0 case all the edges present similar length. Therefore, increasing the x-distance while reducing the y-distance is beneficial for forming.

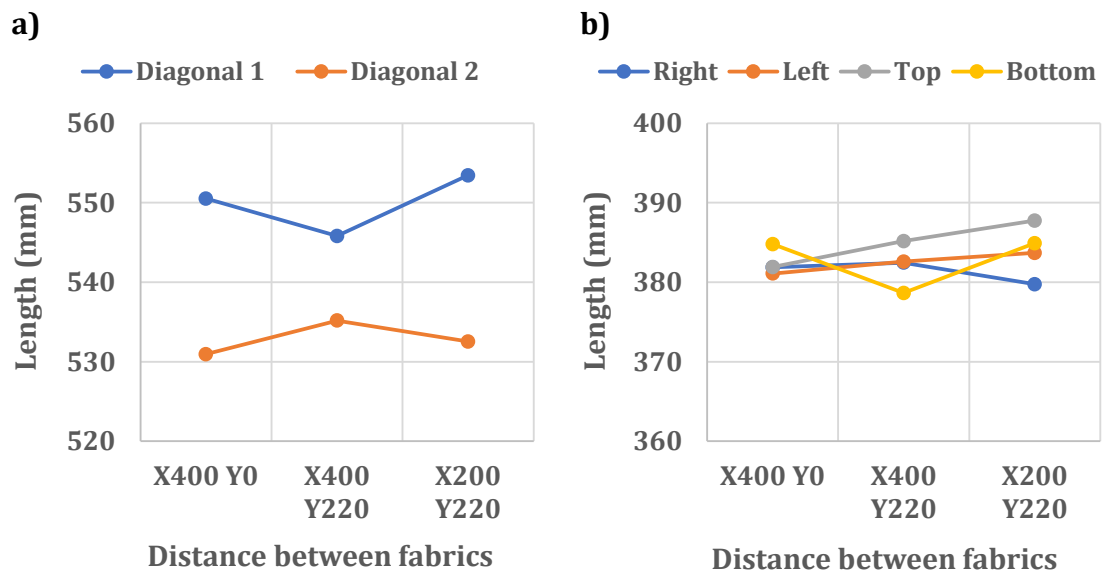


Figure 6.15. Diagonals and edge length for fabric 1 for the experimental three tool study.

Figure 6.16 presents the diagonal and edge lengths for fabric 2 for the three forming cases. Figure 6.16 a) presents the diagonal values for fabric 2. Diagonal 1 is longer than diagonal 2. The length of diagonal 1 barely varies with the distances. Diagonal 2 increases in length as the y-distance increases and the x-

distance decreases. The variability is 1 mm for diagonal 1, and 4 mm for diagonal 2.

Figure 6.16 b) presents the edge values for fabric 2. The lengths of the top and bottom edges decrease when the y-distance between fabrics increases and the x-distance decreases, whilst the length of the left edge increases. The length of the right edge increases when the y-distance between fabrics increases. For the X400 Y220 case all the edges present similar length. Therefore, increasing the y-distance while maintaining the x-distance is beneficial for forming.

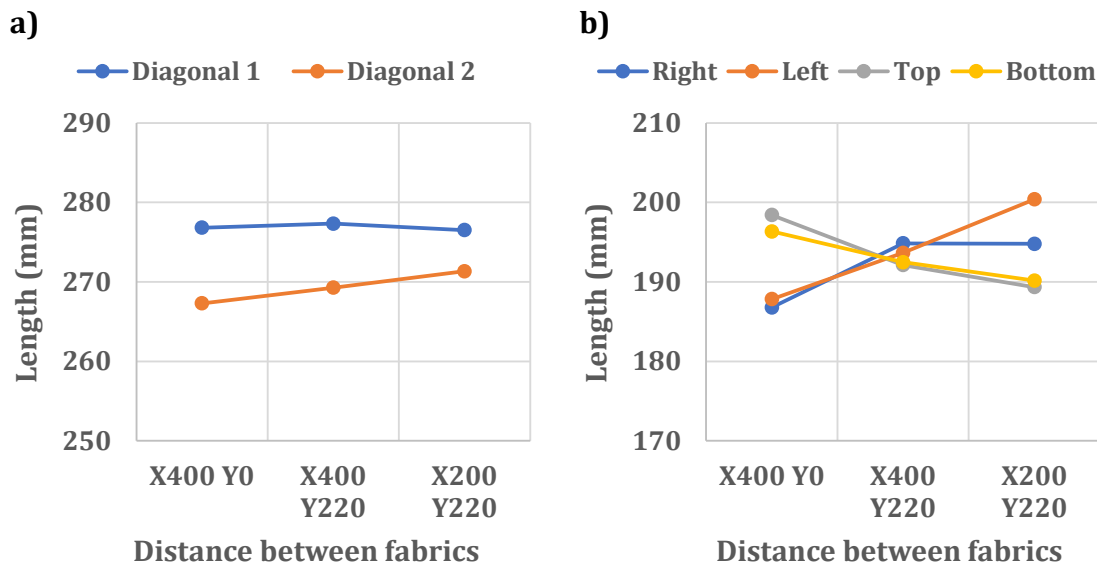


Figure 6.16. Diagonals and edge length for fabric 2 for the experimental three tool study.

Figure 6.17 presents the diagonal and edge lengths for fabric 3 for the three forming cases. Figure 6.17 a) presents the diagonal values for fabric 3. Diagonal 1 is longer than diagonal 2. The length of diagonal 1 increases in length as the y-distance increases and the x-distance decreases. The length of diagonal 2 increases when increasing the y-distance between fabrics. The variability is 4 mm for diagonal 1, and 6 mm for diagonal 2.

Figure 6.17 b) presents the edge values for fabric 3. The lengths of the top and bottom edges increases when the y-distance between fabrics increases and

the x-distance decreases. The length of the left edge increases when the y-distance between fabrics increases, whilst the length of the right edge decreases. For the X200 Y220 case all the edges present similar length. Therefore, for this fabric increasing the y-distance while decreasing the x-distance is beneficial for forming.

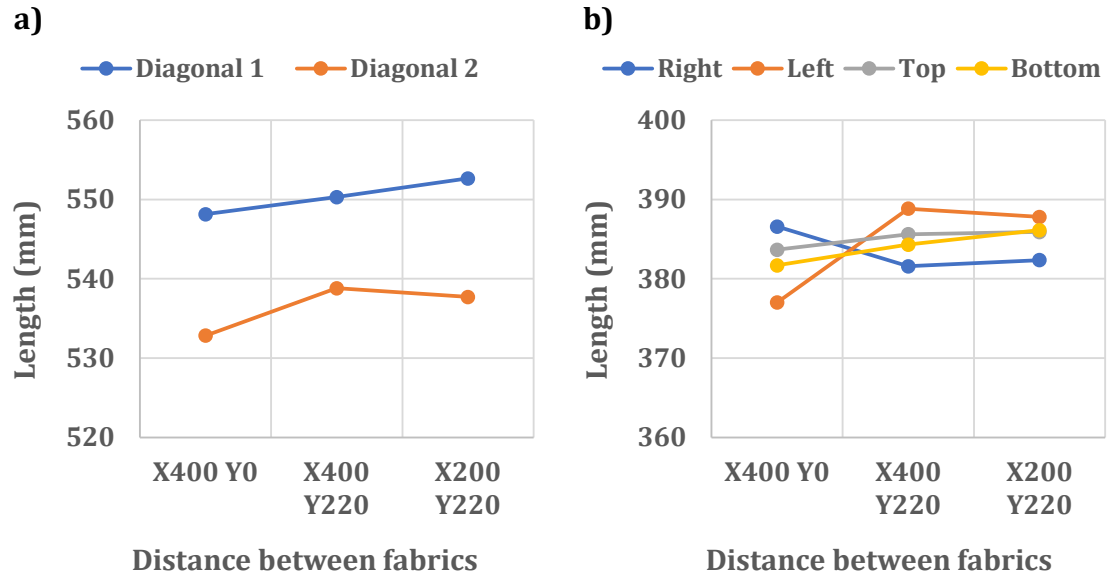


Figure 6.17. Diagonals and edge length for fabric 3 for the experimental three tool study.

These observations indicate that the X400 Y0 case is more beneficial for fabric 1, whilst the X400 Y220 case for fabric 2 and the X200 Y220 case for fabric 3. This suggests that increasing the x-distance between fabrics is beneficial for fabrics 1 and 2, while increasing the y-distance is beneficial for fabrics 2 and 3.

The lack of symmetry in the results can be attributed to the location of the shear areas in the fabrics. Due to the chosen material orientation, the shear areas are located as shown in Figure 6.18, with symmetry occurring along the $\pm 45^\circ$. However, the spacing between fabrics is symmetric in the 0° direction. This means that when folding fabric 2 along that direction, the shear areas are not mirrored, resulting in a positive shear area being opposite a negative one, rather

than another positive. Consequently, despite the symmetric spacing, the asymmetry of the shear areas leads to non-symmetric results.

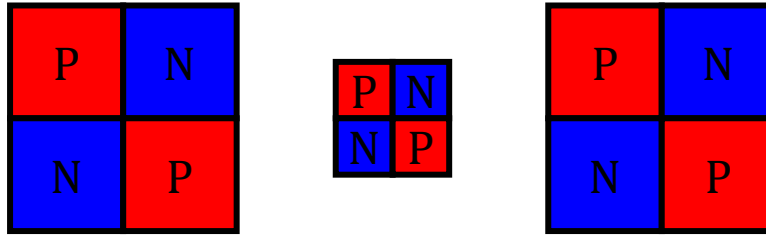


Figure 6.18. Location of the shear areas for the three tool experiments.

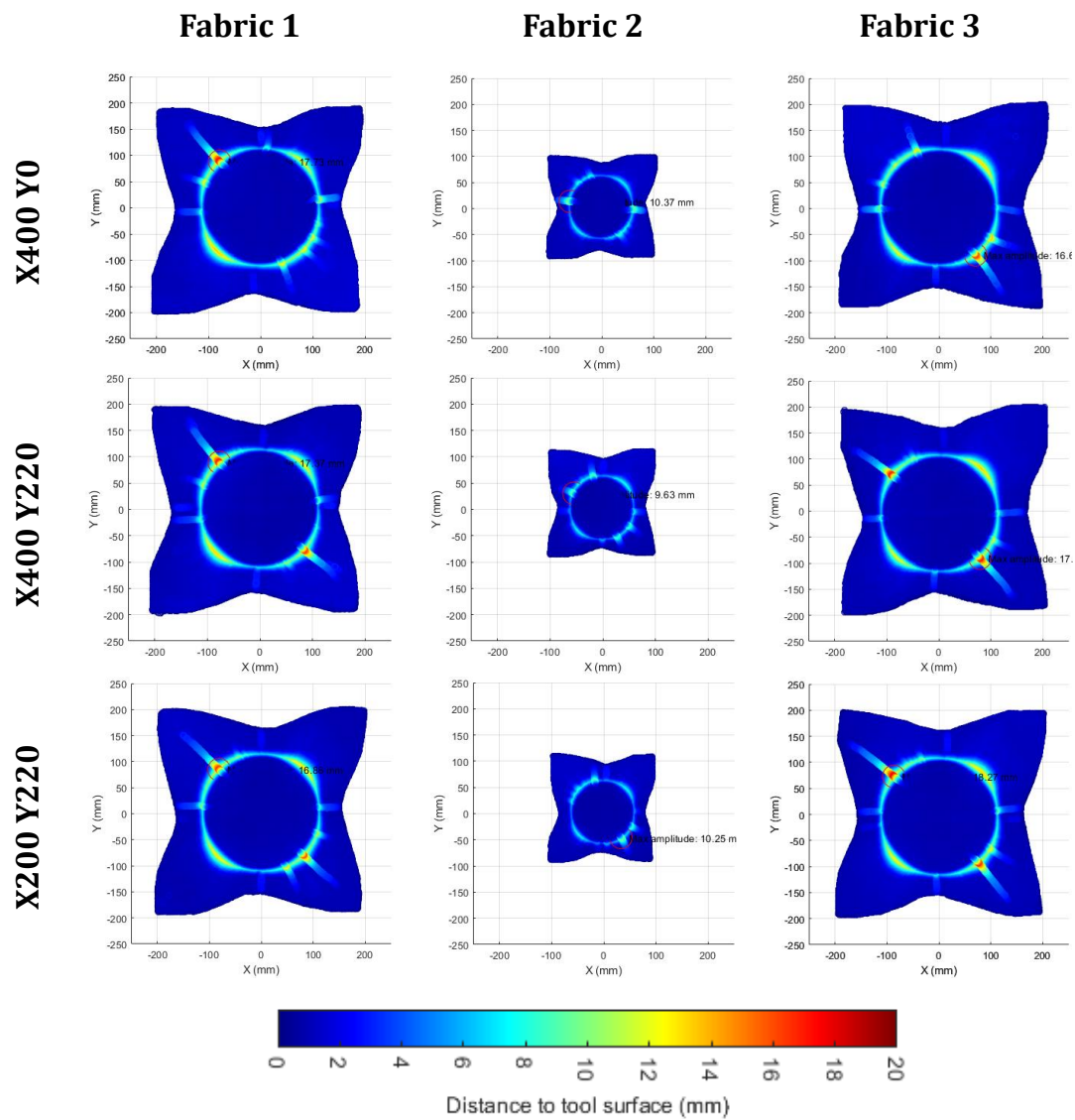


Figure 6.19. Preform-tool distance contour plot for both fabrics for the experimental three tool study.

Figure 6.19 presents the preform-tool distance contour plot for both fabrics for the three tool forming cases. The fabrics present the same wrinkling pattern observed when forming one tool experimentally in Figure 4.7, with wrinkles appearing only in the positive shear areas, Q1 and Q3 quadrants, and slightly in both vertical and horizontal directions.

For fabric 1, the Q1 quadrant presents a severe wrinkle in all the cases, whilst the Q3 quadrant exhibits severe wrinkling only for the Y220 cases. In the Y0 case, there are several small wrinkling, but they are less severe. The severity of both horizontal and vertical wrinkling decreases as the y-distance between fabrics increases.

For fabric 2, wrinkling mainly occurs in the Q1 and Q3. The Y0 sample presents horizontal wrinkling, which disappears for the Y220 samples, indicating that this distancing is beneficial. However, increasing the y-distance also increases the severity of the wrinkles in the Q1 and Q3 quadrants.

For fabric 3, the Q3 quadrant presents a severe wrinkle in all the cases, whilst the Q1 quadrant only in the Y220 cases. The Y0 case has only slight wrinkling. Horizontal wrinkling slightly improves when increasing the y-distance between fabrics, whereas the vertical wrinkling is not affected by the fabric distancing.

The absence of severe wrinkling in some quadrants for fabric 1 and 2 for Y0 suggests that this positioning could be beneficial for draping. However, fabric 2 presents severe horizontal wrinkling, indicating that it does not drape properly. This wrinkling disappears when y-distancing is applied.

Table 6.7 presents the maximum Dist2Tool and %0-1.75 values for both fabrics for the three tool forming cases. The maximum distance and %0-1.75 values vary slightly with the distance between fabrics.

Fabric 1 presents the lowest distance value for the X200 Y220 case, with a variability is of 0.87 mm between cases. The conformity is best for the X400 Y220 case, with a variability of 1.97% between cases.

Table 6.7. Maximum Dist2Tool and %0-1.75 value for both fabrics for the experimental three tool study.

		X400 Y0	X400 Y220	X200 Y220
Fabric 1	Maximum Dist2Tool (mm)	17.73	17.37	16.86
	%0-1.75	78.90%	80.87%	79.82%
Fabric 2	Maximum Dist2Tool (mm)	10.37	9.63	10.25
	%0-1.75	77.13%	77.08%	78.62%
Fabric 3	Maximum Dist2Tool (mm)	16.65	17.51	18.27
	%0-1.75	82.24%	83.18%	80.44%

Fabric 2 presents the lowest distance value for the X400 Y220 case, with a variability of 0.74 mm between cases. The conformity is best for the X200 Y220 case, with a variability of 1.54% between cases.

Fabric 3 presents the lowest distance value for the X400 Y0 case, with a variability of 1.62 mm. The conformity is best for the X400 Y220 case, with a variability of 2.74% between cases.

Therefore, distancing fabric 2 in the y-direction is beneficial for fabrics 1 and 2. However, for fabric 3 the best results are obtained for the X400 cases. The highest variability is presented by fabric 3, indicating that this fabric is more susceptible to fabric distancing.

In terms of wrinkling pattern, the Y0 positioning is beneficial for fabrics 1 and 3 but not for fabric 2, which exhibits severe horizontal wrinkling in this case.

Considering the other parameters, y-distancing is generally more beneficial for fabric 1 and 2, whilst x-distancing proves more advantageous for fabric 3. Therefore, when forming three tools, applying a y-displacement typically improves conformity. However, determining the optimal x-distance is more complex, as fabric 3 is more sensitive to changes in x-distancing compared to fabrics 1 and 2.

6.5 Chapter summary

This chapter builds on the findings from chapter 5 to investigate fabric interactions during multi-component forming and assess the feasibility of this approach.

From the two tool studies, it was observed that forming two fabrics simultaneously reduces the draping of the material. Separating the fabrics in the x-direction proved beneficial, with numerical results suggesting an optimal spacing between 200 mm and 600 mm. Experimental observations further supported this, with a 400 mm separation providing best results. Additionally, the experimental results suggests that forming two hemispheres of different sizes or using AA or AB fabric orientations could be advantageous to the forming.

When separating the fabrics in the y-direction, results showed that if fabrics are positioned considerably close in the x-direction, conformity is improved for y-distances below 100 mm. However, increasing the y-distancing beyond 100 mm led to more severe defects, due to the proximity of fabric 2 to the diaphragm edge.

In the three tool experiments, increasing the y-distance for fabric 2 improved conformity for fabrics 1 and 2. However, fabric 3 presented the best results when spaced in the x-direction with no y-separation. Fabric 3 presented the highest variability, suggesting that this fabric is more sensitive to fabric distancing. While a y-separation typically improves conformity, determining an optimal x-distance

is more complex, due to the sensitivity of fabric 3 to this parameter compared to the other fabrics.

Chapter 7 Conclusions and outlook

This chapter summarises the key findings, highlighting the primary contributions, discussing any limitations, and providing an outlook for future research.

7.1 Contributions and reflections

The thesis aimed to improve the understanding of the DDF process and evaluate the feasibility of multi-component forming. Numerical and experimental methodologies were established to examine the key process parameters affecting defect formation. The following conclusions have been drawn:

Chapter 3 – Methodology

- Shell elements are preferred over membrane elements for modelling the deformable materials, as they represent shear behaviour and stress distribution better.
- A mesh size of 2 mm and a mass scaling factor between 50 and 500 were found to be adequate.
- When artificially modifying the Young's modulus of the fabric, it should be kept below 30 GPa.
- Plies within a layup should be modelled as a single part.

Chapter 4 – Validating the numerical model

- Discrepancies between predicted and experimental wrinkling patterns were identified, with the model generally overpredicting defect severity and number of defects.
- While the model provided useful insights, further refinement is needed to improve alignment with experimental observations.

Chapter 5 – Process studies

- The diaphragm size significantly influences wrinkling patterns. For the conditions studied, an optimal diaphragm size ranges between 1.25 to 2.5 or 3.25 times the size of the fabric.
- The breather arrangement affects material draping, as the strain in the diaphragm is reduced where the breather is located. The breather should be located where fabric draping is not needed.
- Preforming the plies individually reduces the severity of wrinkles but not their number.
- The stacking sequence and relative angles between plies impact defect severity. A 0^0 relative angle reduces wrinkling severity and, in some cases, the number of defects, whereas a 45^0 angle increases the likelihood of severe wrinkling.
- Including the breather in the numerical model improves defect predictions, as the wrinkling patterns align more closely with the experimental observations. However, conformity remains underpredicted.

Chapter 6 – Investigating multi-component forming

- Simultaneously forming two fabrics reduces draping and requires specific spacing in both horizontal and vertical directions to optimise results. A horizontal spacing of 200 mm to 600 mm was beneficial, while a vertical spacing below 100 mm improved conformity due to the proximity to the diaphragm edge. The conformity is reduced when the fabric is too close to the diaphragm edge.
- Experimental results suggest that forming two hemispheres of different sizes or using AA or AB orientations, instead of BB, could benefit the forming process. Note that the orientation A is $[0^0/90^0, 0^0/90^0]$ and B is $[90^0/0^0, 90^0/0^0]$.

- Fabric positioning critically influences defect patterns in three tool forming experiments. Increasing vertical spacing for the middle fabric generally improved the conformity for fabrics 1 and 2, while increasing horizontal spacing was more beneficial for fabric 3. The fabrics are numbered sequentially from left to right.

7.2 Key outcomes

The primary contributions of the thesis are:

- Development of an experimental and numerical methodology, particularly in understanding the effects of mesh configuration, mass scaling, and material parameters.
- Identification of the influence of key parameters on the process, providing guidelines to optimise the diaphragm size, breather arrangement and stacking sequence to reduce defect formation.
- Evaluation of multi-component forming, providing insights into fabric and diaphragm spacing requirements, setting a foundation for more complex forming processes.

7.3 Limitations

Some limitations were identified:

- Further refinement of the numerical model is required to improve its ability to predict wrinkling patterns and defect severity.
- The studies were limited to two fabric orientations and hemispherical tooling, which might not be representative of all industrial applications.

7.4 Outlook and future work

Future work could be focused on:

- Refining the numerical model to improve its accuracy in predicting wrinkling.
- Exploring a broader range of experimental conditions, such as different fabric orientations or tool geometries.
- Investigating two-step forming using tooling of varying radii to improve the conformity of the preform, considering the thickness of the plies.
- Expanding multi-component forming studies to include different tool geometries.
- Investigating more complex forming sequences to fully explore the potential of multi-component approach.

References

- [1] D. D. L. Chung, 'Composite material structure and processing', in *Composite materials*, 2nd ed., Springer, 2010, ch. 1, pp. 1–34.
- [2] Hannah Mason, 'Composites end markets: Automotive (2024)', [https://www.compositesworld.com/articles/composites-end-markets-automotive-\(2024\)](https://www.compositesworld.com/articles/composites-end-markets-automotive-(2024)).
- [3] Grace Nehls, 'Autocomposites market is expected to double revenue by 2032', <https://www.compositesworld.com/news/autocomposites-market-report-expected-to-double-revenue-by-2032>.
- [4] Hannah Mason, 'Composites end markets: Energy (2024)', [https://www.compositesworld.com/articles/composites-end-markets-energy-\(2024\)](https://www.compositesworld.com/articles/composites-end-markets-energy-(2024)).
- [5] Hannah Mason, 'Composites end markets: Sports and recreation (2025)', [https://www.compositesworld.com/articles/composites-end-markets-sports-and-recreation-\(2025\)](https://www.compositesworld.com/articles/composites-end-markets-sports-and-recreation-(2025)).
- [6] Lucintel, 'Composites in sporting goods market: Trends, opportunities and competitive analysis [2024-2030]', <https://www.lucintel.com/composites-in-sporting-goods-market.aspx>.
- [7] 'Aerospace composites market: Key trends and technological advancements', <https://industry europe.com/sectors/aerospace-defence/aerospace-composites-market-key-trends-and-technological-adv/>.
- [8] K. Balasubramanian, M. T. H. Sultan, and N. Rajeswari, 'Manufacturing techniques of composites for aerospace applications', in *Sustainable*

- composites for aerospace applications*, Woodhead Publishing, 2018, ch. 4, pp. 55–68.
- [9] J. Xie *et al.*, ‘Mechanics of textiles used as composite preforms: a review’, *Compos Struct*, vol. 304, no. 116401, pp. 1–13, Jan. 2023, doi: 10.1016/j.compstruct.2022.116401.
- [10] P. Boisse, N. Naouar, and A. Charmetant, ‘Finite element analysis of composite forming at macroscopic and mesoscopic scale’, in *Advances in composites manufacturing and process design*, London: Elsevier, 2015, ch. 14, pp. 297–315.
- [11] W. Tan, B. G. Falzon, and M. Price, ‘Predicting the crushing behaviour of composite material using high-fidelity finite element modelling’, *International Journal of Crashworthiness*, vol. 20, no. 1, pp. 60–77, Jan. 2015, doi: 10.1080/13588265.2014.972122.
- [12] V. Lunetto, M. Galati, L. Settineri, and L. Iuliano, ‘Sustainability in the manufacturing of composite materials: A literature review and directions for future research’, *J Manuf Process*, vol. 85, pp. 858–874, Jan. 2023, doi: 10.1016/j.jmapro.2022.12.020.
- [13] S. S. Bhattacharya and S. A. Agrawal, ‘Textile reinforced structure: A review’, *Int J Eng Res Appl*, vol. 07, no. 07, pp. 84–86, Jul. 2017, doi: 10.9790/9622-0707088486.
- [14] R. Rolfes, G. Ernst, D. Hartung, and J. Teßmer, ‘Strength of textile composites - A voxel based continuum damage mechanics approach’, in *III European Conference on Computational Mechanics*, Lisbon, 2006.
- [15] M. A. Turk, B. Vermes, A. J. Thompson, J. P. H. Belnoue, S. R. Hallett, and D. S. Ivanov, ‘Mitigating forming defects by local modification of dry preforms’, *Compos Part A Appl Sci Manuf*, vol. 128, pp. 1–12, Jan. 2020, doi: 10.1016/j.compositesa.2019.105643.

- [16] S. Korkiakoski, E. Sarlin, R. Suihkonen, and O. Saarela, 'Internal structure and fatigue performance of quasi-unidirectional non-crimp fabric reinforced laminates', *J Compos Mater*, vol. 51, no. 24, pp. 3405–3423, Oct. 2017, doi: 10.1177/0021998316683783.
- [17] T.-D. Ngo, 'Introduction to composite materials', in *Composite and nanocomposite materials - From knowledge to industrial applications*, IntechOpen, 2020, ch. 1. [Online]. Available: www.intechopen.com
- [18] H. Towsyfyan, A. Biguri, R. Boardman, and T. Blumensath, 'Successes and challenges in non-destructive testing of aircraft composite structures', *Chinese Journal of Aeronautics*, vol. 33, no. 3, pp. 771–791, Mar. 2020, doi: 10.1016/j.cja.2019.09.017.
- [19] J. Summerscales, 'Manufacturing defects in fibre-reinforced plastics composites', *Insight*, vol. 36, no. 12, pp. 936–942, 1994.
- [20] S. Bagherpour, 'Fibre reinforcement polyester composites', in *Polyester*, IntechOpen, 2012, ch. 6, pp. 135–166.
- [21] A. C. Long, 'Introduction', in *Design and manufacture of textile composites*, Boca Raton: CRC, 2005, ch. 1, pp. xiii–xvi.
- [22] S. Lomov, I. Verpoest, and F. Robitaille, 'Manufacturing and internal geometry of textiles', in *Design and manufacture of textile composites*, Boca Raton: CRC, 2005, ch. 1, pp. 1–61.
- [23] A. C. Long and L. P. Brown, 'Modelling the geometry of textile reinforcements for composites: TexGen', in *Composite reinforcement for optimum performance*, Oxford: Woodhead Publishing, 2011, ch. 8, pp. 239–264.

- [24] P. Bussetta and N. Correia, 'Numerical forming of continuous fibre reinforced composite material: A review', Oct. 01, 2018, *Elsevier Ltd.* doi: 10.1016/j.compositesa.2018.07.010.
- [25] P. Boisse, 'Finite element analysis of composite forming', in *Composites forming technologies*, Boca Raton: Woodhead Publishing Limited, 2007, ch. 3, pp. 46–79.
- [26] J. W. S. Hearle, 'Mechanical properties of textile reinforcements for composites', in *Advanced in composites manufacturing and process design*, Cambridge: Elsevier, 2015, ch. 11, pp. 231–251.
- [27] L. Maragoni, G. Modenato, N. De Rossi, L. Vescovi, and M. Quaresimin, 'Effect of fibre waviness on the compressive fatigue behavior of woven carbon/epoxy laminates', *Compos B Eng*, vol. 199, pp. 1–10, Oct. 2020, doi: 10.1016/j.compositesb.2020.108282.
- [28] K. Potter, B. Khan, M. Wisnom, T. Bell, and J. Stevens, 'Variability, fibre waviness and misalignment in the determination of the properties of composite materials and structures', *Compos Part A Appl Sci Manuf*, vol. 39, no. 9, pp. 1343–1354, Sep. 2008, doi: 10.1016/j.compositesa.2008.04.016.
- [29] S. Bel, 'Mechanical behaviour of non-crimp fabric (NCF) preforms in composite materials manufacturing', in *Advanced in composites manufacturing and process design*, Cambridge: Elsevier, 2015, ch. 12, pp. 253–268.
- [30] A. Schnabel and T. Gries, 'Production of non-crimp fabrics for composites', in *Non-crimp fabric composites: Manufacturing, properties and applications*, Cambridge: Woodhead Publishing, 2011, ch. 1, pp. 3–41.
- [31] A. Margossian, S. Bel, J. M. Balvers, D. Leutz, R. Freitas, and R. Hinterhoelzl, 'Finite element forming simulation of locally stitched non-crimp fabrics',

- Compos Part A Appl Sci Manuf*, vol. 61, pp. 152–162, 2014, doi: 10.1016/j.compositesa.2014.02.020.
- [32] D. S. Ivanov, S. L. Lomov, and I. Verpoest, ‘Predicting the effect of stitching on the mechanical properties and damage of non-crimp fabric composites: Finite element analysis’, in *Non-crimp fabric composites: Manufacturing, properties and applications*, Cambridge: Woodhead Publishing, 2011, ch. 15, pp. 360–385.
- [33] S. Chen, O. P. L. McGregor, L. T. Harper, A. Endruweit, and N. A. Warrior, ‘Defect formation during preforming of a bi-axial non-crimp fabric with a pillar stitch pattern’, *Compos Part A Appl Sci Manuf*, vol. 91, pp. 156–167, Dec. 2016, doi: 10.1016/j.compositesa.2016.09.016.
- [34] A. C. Long and M. J. Clifford, ‘Composite forming mechanisms and materials characterisation’, in *Composites forming technologies*, Cambridge: Woodhead Publishing Limited, 2007, ch. 1, pp. 1–21.
- [35] M. Y. Matveev, A. Endruweit, D. S. A. De Focatiis, A. C. Long, and N. A. Warrior, ‘A novel criterion for the prediction of meso-scale defects in textile preforming’, *Compos Struct*, vol. 226, no. 111263, pp. 1–8, Oct. 2019, doi: 10.1016/j.compstruct.2019.111263.
- [36] H. Krieger, T. Gries, and S. E. Stapleton, ‘Shear and drape behavior of non-crimp fabrics based on stitching geometry’, *International Journal of Material Forming*, vol. 11, no. 5, pp. 593–605, Sep. 2018, doi: 10.1007/s12289-017-1368-1.
- [37] A. C. Long, P. Boisse, and F. Robitaille, ‘Mechanical analysis of textiles’, in *Design and manufacture of textile composites*, Cambridge: Woodhead Publishing, 2005, ch. 2, pp. 62–109.
- [38] S. Bel, P. Boisse, and F. Dumont, ‘Analyses of the deformation mechanisms of non-crimp fabric composite reinforcements during preforming’, *Applied*

- Composite Materials*, vol. 19, no. 3–4, pp. 513–528, Jun. 2012, doi: 10.1007/s10443-011-9207-x.
- [39] E. Guzman-Maldonado, S. Bel, D. Bloom, P. Fideu, and P. Boisse, ‘Experimental and numerical analyses of the mechanical behavior during draping of non-orthogonal bi-axial non-crimp fabric composite reinforcements’, *Mater Des*, vol. 218, no. 110682, pp. 1–13, Jun. 2022, doi: 10.1016/j.matdes.2022.110682.
- [40] J. S. Lee, S. J. Hong, W. R. Yu, and T. J. Kang, ‘The effect of blank holder force on the stamp forming behavior of non-crimp fabric with a chain stitch’, *Compos Sci Technol*, vol. 67, no. 3–4, pp. 357–366, Mar. 2007, doi: 10.1016/j.compscitech.2006.09.009.
- [41] S. Chen, A. M. Joesbury, F. Yu, L. T. Harper, and N. A. Warrior, ‘Optimisation of intra-ply stitch removal for improved formability of biaxial non-crimp fabrics’, *Compos B Eng*, vol. 229, pp. 1–5, Jan. 2022, doi: 10.1016/j.compositesb.2021.109464.
- [42] N. Hamila, P. Boisse, F. Sabourin, and M. Brunet, ‘A semi-discrete shell finite element for textile composite reinforcement forming simulation’, *Int J Numer Methods Eng*, vol. 79, no. 12, pp. 1443–1466, 2009, doi: 10.1002/nme.2625.
- [43] R. Reddy Nagavally, ‘Composite materials - history, types, fabrication techniques, advantages and applications’, in *Proceedings of 29th IRF International Conference*, Bengaluru, 2016, pp. 25–30.
- [44] P. Paton, ‘Forming technology for thermoset composites’, in *Composites forming technologies*, Cambridge: Woodhead Publishing Limited, 2007, ch. 10, pp. 239–255.

- [45] S. K. Mazumdar, 'Manufacturing techniques', in *Composites manufacturing. Materials, product, and process engineering*, Boca Raton: CRC Press, 2002, ch. 6, pp. 99–234.
- [46] B. Middleton, 'Composites: Manufacture and application', in *Design and manufacture of plastic components for multifunctionality - structural composites, injection molding, and 3D printing*, Elsevier, 2016, ch. 3, pp. 53–102.
- [47] K. Potter and C. Ward, 'Draping process for composites manufacture', in *Advances in composite manufacturing and process design*, Amsterdam: Woodhead Publishing, 2015, ch. 5, pp. 93–110.
- [48] M. Elkington, D. Bloom, C. Ward, A. Chatzimichali, and K. Potter, 'Hand layup: understanding the manual process', *Advanced Manufacturing: Polymer and Composites Science*, vol. 1, no. 3, pp. 138–151, Jul. 2015, doi: 10.1080/20550340.2015.1114801.
- [49] F. C. Campbell, 'Commercial Processes', in *Manufacturing processes for advanced composites*, Oxford: Elsevier, 2004, ch. 11, pp. 400–439.
- [50] H. E. N. Bersee, 'Diaphragm forming of continuous fibre reinforced thermoplastics', Delft University, Delft, 1996.
- [51] S. Chen *et al.*, 'Double diaphragm forming simulation for complex composite structures', *Compos Part A Appl Sci Manuf*, vol. 95, pp. 346–358, Apr. 2017, doi: 10.1016/j.compositesa.2017.01.017.
- [52] M. G. Bader, 'Composites fabrication processes', in *Handbook of materials selection*, New York: John Wiley and Sons, Inc, 2002, ch. 34, pp. 1037–1112.
- [53] O. P. L. McGregor, S. Chen, L. T. Harper, A. Endruweit, and N. A. Warrior, 'Defect reduction in the double diaphragm forming process', in *21st International Conference on Composite Materials*, Aug. 2017.

- [54] C. M. O'Brádaigh, R. B. Pipes, and P. J. Mallon, 'Issues in diaphragm forming of continuous fiber reinforced thermoplastic composites', *Polym Compos*, vol. 12, no. 4, pp. 246–256, 1991, doi: 10.1002/pc.750120406.
- [55] H. Alshahrani and M. Hojjati, 'Experimental and numerical investigations on formability of out-of-autoclave thermoset prepreg using a double diaphragm process', *Compos Part A Appl Sci Manuf*, vol. 101, pp. 199–214, Oct. 2017, doi: 10.1016/j.compositesa.2017.06.021.
- [56] I. G. Crouch, J. Sandlin, and S. Thomas, 'Polymers and fibre-reinforced plastics', in *The science of armour materials*, Amsterdam: Woodhead Publishing, 2017, ch. 5, pp. 203–268.
- [57] C. Jimenez Martin *et al.*, 'Observations of wrinkling in Non-Crimp Fabrics during multi-ply stack forming using in situ XCT scanning', *Compos Part A Appl Sci Manuf*, vol. 176, Jan. 2024, doi: 10.1016/j.compositesa.2023.107880.
- [58] J. V. Viisainen, A. Hosseini, and M. P. F. Sutcliffe, 'Experimental investigation, using 3D digital image correlation, into the effect of component geometry on the wrinkling behaviour and the wrinkling mechanisms of a biaxial NCF during preforming', *Compos Part A Appl Sci Manuf*, vol. 142, no. 106248, pp. 1–14, Mar. 2021, doi: 10.1016/j.compositesa.2020.106248.
- [59] A. Codolini, S. Chen, G. D. Lawrence, L. T. Harper, and M. P. F. Sutcliffe, 'Characterisation of process-induced variability in wrinkle defects during double diaphragm forming of non-crimp fabric', *Compos B Eng*, vol. 281, no. 111549, pp. 1–10, Jul. 2024, doi: 10.1016/j.compositesb.2024.111549.
- [60] P. Boisse, N. Hamila, F. Hélénon, Y. Aimene, and T. Mabrouki, 'Draping of textile composite reinforcements: continuous and discrete approaches',

- Advanced Composites Letters*, vol. 16, no. 4, pp. 125–132, 2007, doi: 10.1177/096369350701600401.
- [61] P. Boisse, J. Colmars, N. Hamila, N. Naouar, and Q. Steer, 'Bending and wrinkling of composite fiber preforms and prepregs. A review and new developments in the draping simulations', *Compos B Eng*, vol. 141, pp. 234–249, May 2018, doi: 10.1016/j.compositesb.2017.12.061.
- [62] S. Bel, N. Hamila, P. Boisse, and F. Dumont, 'Finite element model for NCF composite reinforcement preforming: importance of inter-ply sliding', *Compos Part A Appl Sci Manuf*, vol. 43, no. 12, pp. 2269–2277, Dec. 2012, doi: 10.1016/j.compositesa.2012.08.005.
- [63] S. V. Lomov *et al.*, 'Carbon composites based on multiaxial multiply stitched preforms. Part 3: biaxial tension, picture frame and compression tests of the preforms', *Compos Part A Appl Sci Manuf*, vol. 36, no. 9, pp. 1188–1206, Sep. 2005, doi: 10.1016/j.compositesa.2005.01.015.
- [64] A. G. Prodromou and J. Chen, 'On the relationship between shear angle and wrinkling of textile composite preforms', *Composites Part A*, vol. 28, no. A, pp. 491–503, 1997.
- [65] P. Boisse, M. Borr, K. Buet, and A. Cherouat, 'Finite element simulations of textile composite forming including the biaxial fabric behaviour', *Compos B Eng*, vol. 28, no. B, pp. 453–464, 1997.
- [66] S. V. Lomov, 'Deformability of textile preforms in the manufacture of non-crimp fabric composites', in *Non-crimp fabric composites*, Oxford: Woodhead Publishing, 2011, ch. 6, pp. 117–143.
- [67] R. Akkerman and S. P. Haanappel, 'Thermoplastic composites manufacturing by thermoforming', in *Advances in composite manufacturing and process design*, Amsterdam: Woodhead Publishing, 2015, ch. 6, pp. 111–129.

- [68] P. Harrison, 'Modelling the forming mechanics of engineering fabrics using a mutually constrained pantographic beam and membrane mesh', *Compos Part A Appl Sci Manuf*, vol. 81, pp. 145–157, Feb. 2016, doi: 10.1016/j.compositesa.2015.11.005.
- [69] O. Döbrich, T. Gereke, O. Diestel, S. Krzywinski, and C. Cherif, 'Decoupling the bending behavior and the membrane properties of finite shell elements for a correct description of the mechanical behavior of textiles with a laminate formulation', *Journal of Industrial Textiles*, vol. 44, no. 1, pp. 70–84, 2014, doi: 10.1177/1528083713477442.
- [70] E. de Bilbao, D. Soulat, G. Hivet, and A. Gasser, 'Experimental study of bending behaviour of reinforcements', *Exp Mech*, vol. 50, no. 3, pp. 333–351, 2010, doi: 10.1007/s11340-009-9234-9.
- [71] R. Akkerman, M. P. Ubbink, M. B. De Rooij, and R. H. W. Ten Thijs, 'Tool-ply friction in composite forming', in *10th ESAFORM Conference on Material Forming*, American Institute of Physics Inc., 2007, pp. 1080–1085. doi: 10.1063/1.2729658.
- [72] G. D. Lawrence, S. Chen, N. A. Warrior, and L. T. Harper, 'The influence of inter-ply friction during double-diaphragm forming of biaxial NCFs', *Compos Part A Appl Sci Manuf*, vol. 167, pp. 1–14, Apr. 2023, doi: 10.1016/j.compositesa.2023.107426.
- [73] J. Sjölander, P. Hallander, and M. Åkermo, 'Forming induced wrinkling of composite laminates: a numerical study on wrinkling mechanisms', *Compos Part A Appl Sci Manuf*, vol. 81, pp. 41–51, Feb. 2016, doi: 10.1016/j.compositesa.2015.10.012.
- [74] J. S. Lightfoot, M. R. Wisnom, and K. Potter, 'A new mechanism for the formation of ply wrinkles due to shear between plies', *Compos Part A Appl*

References

- Sci Manuf*, vol. 49, pp. 139–147, 2013, doi: 10.1016/j.compositesa.2013.03.002.
- [75] F. Yu, S. Chen, L. T. Harper, and N. A. Warrior, ‘Investigation into the effects of inter-ply sliding during double diaphragm forming for multi-layered biaxial non-crimp fabrics’, *Compos Part A Appl Sci Manuf*, vol. 150, pp. 1–15, Nov. 2021, doi: 10.1016/j.compositesa.2021.106611.
- [76] X. Sun, J. P. H. Belnoue, A. Thompson, B. El Said, and S. R. Hallett, ‘Dry textile forming simulations: a benchmarking exercise’, *Front Mater*, vol. 9, pp. 1–20, Mar. 2022, doi: 10.3389/fmats.2022.831820.
- [77] L. M. Dangora, C. J. Mitchell, and J. A. Sherwood, ‘Predictive model for the detection of out-of-plane defects formed during textile-composite manufacture’, *Compos Part A Appl Sci Manuf*, vol. 78, pp. 102–112, Nov. 2015, doi: 10.1016/j.compositesa.2015.07.011.
- [78] X. Li, S. Shonkwiler, and S. McMains, ‘Detection of resin-rich areas for statistical analysis of fiber-reinforced polymer composites’, *Compos B Eng*, vol. 225, no. 109252, pp. 1–10, Nov. 2021, doi: 10.1016/j.compositesb.2021.109252.
- [79] A. Iwata, T. Inoue, N. Naouar, P. Boisse, and S. V. Lomov, ‘Coupled meso-macro simulation of woven fabric local deformation during draping’, *Compos Part A Appl Sci Manuf*, vol. 118, pp. 267–280, Mar. 2019, doi: 10.1016/j.compositesa.2019.01.004.
- [80] K. D. Potter, ‘Understanding the origins of defects and variability in composites manufacture’, in *Proceedings of ICCM-17 Conference*, Edinburgh: International Conference on Composites Materials, 2009, pp. 1–19.
- [81] J. S. Lightfoot, M. R. Wisnom, and K. Potter, ‘Defects in woven preforms: Formation mechanisms and the effects of laminate design and layup

- protocol', *Compos Part A Appl Sci Manuf*, vol. 51, pp. 99–107, 2013, doi: 10.1016/j.compositesa.2013.04.004.
- [82] M. Thor *et al.*, 'Numerical and experimental investigation of out-of-plane fiber waviness on the mechanical properties of composite materials', *International Journal of Material Forming*, vol. 14, no. 1, pp. 19–37, Jan. 2021, doi: 10.1007/s12289-020-01540-5.
- [83] D. Pain and B. W. Drinkwater, 'Detection of fibre waviness using ultrasonic array scattering data', *J Nondestr Eval*, vol. 32, no. 3, pp. 215–227, Sep. 2013, doi: 10.1007/s10921-013-0174-z.
- [84] W. J. R. Christian, F. A. Diazdelao, K. Atherton, and E. A. Patterson, 'An experimental study on the manufacture and characterization of in-plane fibre-waviness defects in composites', *R Soc Open Sci*, vol. 5, no. 5, pp. 1–16, May 2018, doi: 10.1098/rsos.180082.
- [85] S. Allaoui, C. Cellard, and G. Hivet, 'Effect of inter-ply sliding on the quality of multilayer interlock dry fabric preforms', *Compos Part A Appl Sci Manuf*, vol. 68, pp. 336–345, 2015, doi: 10.1016/j.compositesa.2014.10.017.
- [86] M. Thor, M. G. R. Sause, and R. M. Hinterhölzl, 'Mechanisms of origin and classification of out-of-plane fiber waviness in composite materials — a review', 2020, *MDPI AG*. doi: 10.3390/jcs4030130.
- [87] A. Shipsha, S. Hallström, and M. Burman, 'Effect of stacking sequence and bundle waviness in quasi-isotropic NCF composites subjected to compression', *Compos B Eng*, vol. 178, no. 107423, pp. 1–12, Dec. 2019, doi: 10.1016/j.compositesb.2019.107423.
- [88] J. Krebs, D. Bhattacharyya, and K. Friedrich, 'Production and evaluation of secondary composite aircraft components - a comprehensive case study', *Compos Part A Appl Sci Manuf*, vol. 28, no. A, pp. 481–489, 1997.

-
- [89] A. J. Thompson, J. P. H. Belnoue, and S. R. Hallett, 'Modelling defect formation in textiles during the double diaphragm forming process', *Compos B Eng*, vol. 202, no. 108357, pp. 1–13, Dec. 2020, doi: 10.1016/j.compositesb.2020.108357.
- [90] P. Hallander, J. Sjölander, and M. Åkermo, 'Forming induced wrinkling of composite laminates with mixed ply material properties; an experimental study', *Compos Part A Appl Sci Manuf*, vol. 78, pp. 234–245, Nov. 2015, doi: 10.1016/j.compositesa.2015.08.025.
- [91] P. Boisse, N. Hamila, E. Vidal-Sallé, and F. Dumont, 'Simulation of wrinkling during textile composite reinforcement forming. Influence of tensile, in-plane shear and bending stiffnesses', *Compos Sci Technol*, vol. 71, no. 5, pp. 683–692, 2011, doi: 10.1016/j.compscitech.2011.01.011.
- [92] J. Krebs, K. Friedricha, and D. Bhattacharyyab, 'A direct comparison of matched-die versus diaphragm forming', *Compos Part A Appl Sci Manuf*, vol. 29, no. A, pp. 183–188, 1998.
- [93] S. Chen, O. P. L. McGregor, L. T. Harper, A. Endruweit, and N. A. Warrior, 'Optimisation of local in-plane constraining forces in double diaphragm forming', *Compos Struct*, vol. 201, pp. 570–581, Oct. 2018, doi: 10.1016/j.compstruct.2018.06.062.
- [94] S. Chen and L. Harper, 'Two-dimensional to three-dimensional dry fibre preforming', in *Design and manufacture of structural composites*, Cambridge: Elsevier, 2023, ch. 5, pp. 101–124.
- [95] M. Ghazimoradi, E. A. Trejo, V. Carvelli, C. Butcher, and J. Montesano, 'Deformation characteristics and formability of a tricot-stitched carbon fiber unidirectional non-crimp fabric', *Compos Part A Appl Sci Manuf*, vol. 145, no. 106366, pp. 1–16, Jun. 2021, doi: 10.1016/j.compositesa.2021.106366.

- [96] C. Krogh, K. D. White, A. Sabato, and J. A. Sherwood, 'Picture-frame testing of woven prepreg fabric: an investigation of sample geometry and shear angle acquisition', *International Journal of Material Forming*, vol. 13, no. 3, pp. 341–353, May 2020, doi: 10.1007/s12289-019-01499-y.
- [97] J. Cao *et al.*, 'Characterization of mechanical behavior of woven fabrics: Experimental methods and benchmark results', *Compos Part A Appl Sci Manuf*, vol. 39, no. 6, pp. 1037–1053, Jun. 2008, doi: 10.1016/j.compositesa.2008.02.016.
- [98] L. Li, Y. Zhao, H. gia nam Vuong, Y. Chen, J. Yang, and Y. Duan, 'In-plane shear investigation of biaxial carbon non-crimp fabrics with experimental tests and finite element modeling', *Mater Des*, vol. 63, pp. 757–765, Nov. 2014, doi: 10.1016/j.matdes.2014.07.007.
- [99] P. Boisse, N. Hamila, E. Guzman-Maldonado, A. Madeo, G. Hivet, and F. dell'Isola, 'The bias-extension test for the analysis of in-plane shear properties of textile composite reinforcements and preregs: a review', Aug. 01, 2017, *Springer-Verlag France*. doi: 10.1007/s12289-016-1294-7.
- [100] S. B. Sharma, M. P. F. Sutcliffe, and S. H. Chang, 'Characterisation of material properties for draping of dry woven composite material', *Compos Part A Appl Sci Manuf*, vol. 34, no. 12, pp. 1167–1175, Dec. 2003, doi: 10.1016/j.compositesa.2003.09.001.
- [101] P. Harrison, M. J. Clifford, and A. C. Long, 'Shear characterisation of viscous woven textile composites: a comparison between picture frame and bias extension experiments', *Compos Sci Technol*, vol. 64, no. 10–11, pp. 1453–1465, Aug. 2004, doi: 10.1016/j.compscitech.2003.10.015.
- [102] J. Alsayednoor, P. Harrison, and W. R. Yu, 'Influence of specimen pre-shear and wrinkling on the accuracy of uniaxial bias extension test results',

- Compos Part A Appl Sci Manuf*, vol. 101, pp. 81–97, Oct. 2017, doi: 10.1016/j.compositesa.2017.06.006.
- [103] S. V. Lomov, A. Willems, I. Verpoest, Y. Zhu, M. Barburski, and T. Stoilova, ‘Picture frame test of woven composite reinforcements with a full-field strain registration’, *Textile Research Journal*, vol. 76, no. 3, pp. 243–252, 2006, doi: 10.1177/0040517506061032.
- [104] A. Endruweit, X. Zeng, and A. C. Long, ‘Effect of specimen history on structure and in-plane permeability of woven fabrics’, *J Compos Mater*, vol. 49, no. 13, pp. 1563–1578, Jun. 2015, doi: 10.1177/0021998314536070.
- [105] D. A. Arellano Escrpita, D. Crdenas, H. Elizalde, R. Ramirez, and O. Probst, ‘Biaxial tensile strength characterization of textile composite materials’, in *Composites and Their Properties*, InTech, 2012, ch. 5, pp. 83–106. doi: 10.5772/48105.
- [106] F. Yu, S. Chen, J. V. Viisainen, M. P. F. Sutcliffe, L. T. Harper, and N. A. Warrior, ‘A macroscale finite element approach for simulating the bending behaviour of biaxial fabrics’, *Compos Sci Technol*, vol. 191, pp. 1–11, May 2020, doi: 10.1016/j.compscitech.2020.108078.
- [107] F. Yu, S. Chen, L. T. Harper, and N. A. Warrior, ‘Simulating the effect of fabric bending stiffness on the wrinkling behaviour of biaxial fabrics during preforming’, *Compos Part A Appl Sci Manuf*, vol. 143, pp. 1–19, Apr. 2021, doi: 10.1016/j.compositesa.2021.106308.
- [108] E. I. Avgoulas *et al.*, ‘Frictional behaviour of non-crimp fabrics (NCFs) in contact with a forming tool’, *Tribol Int*, vol. 121, pp. 71–77, May 2018, doi: 10.1016/j.triboint.2018.01.026.
- [109] R. H. W. ten Thije and R. Akkerman, ‘Design of an experimental setup to measure tool-ply and ply-ply friction in thermoplastic laminates’,

- International Journal of Material Forming*, vol. 2, no. 1, pp. 197–200, Dec. 2009, doi: 10.1007/s12289-009-0638-y.
- [110] K. A. Fetfatsidis, D. Jauffrès, J. A. Sherwood, and J. Chen, ‘Characterization of the tool/fabric and fabric/fabric friction for woven-fabric composites during the thermostamping process’, *International Journal of Material Forming*, vol. 6, no. 2, pp. 209–221, Jun. 2013, doi: 10.1007/s12289-011-1072-5.
- [111] P. Potluri, S. Sharma, and R. Ramgulam, ‘Comprehensive drape modelling for moulding 3D textile preforms’, *Compos Part A Appl Sci Manuf*, vol. 32, pp. 1415–1424, 2001, [Online]. Available: www.elsevier.com/locate/compositesa
- [112] J. Wang, R. Paton, and J. R. Page, ‘The draping of woven fabric preforms and prepregs for production of polymer composite components’, *Compos Part A Appl Sci Manuf*, vol. 30, pp. 757–765, 1999.
- [113] F. Van Der Weeën, ‘Algorithms for draping fabrics on doubly-curved surfaces’, *Int J Numer Methods Eng*, vol. 31, no. 7, pp. 1415–1426, 1991, doi: 10.1002/nme.1620310712.
- [114] Y. Baillargeon and T. Vu-Khanh, ‘Prediction of fiber orientation and microstructure of woven fabric composites after forming’, *Compos Struct*, vol. 52, pp. 475–481, 2001, [Online]. Available: www.elsevier.com/locate/compstruct
- [115] V. N. Khiêm, H. Krieger, M. Itskov, T. Gries, and S. E. Stapleton, ‘An averaging based hyperelastic modeling and experimental analysis of non-crimp fabrics’, *Int J Solids Struct*, vol. 154, pp. 43–54, Dec. 2018, doi: 10.1016/j.ijsolstr.2016.12.018.

- [116] P. Boisse, 'Simulations of woven composite reinforcement forming', in *Woven fabric engineering*, IntechOpen Access Publisher, 2010, ch. 20, pp. 1–28.
- [117] B. Liang and P. Boisse, 'A review of numerical analyses and experimental characterization methods for forming of textile reinforcements', Aug. 01, 2021, *Elsevier B.V.* doi: 10.1016/j.cja.2020.09.027.
- [118] W. R. Yu and A. C. Long, 'Forming textile composites', in *Design and manufacture of textile composites*, Boca Raton: CRC, 2005, ch. 4, pp. 149–180.
- [119] H. Lin, J. Wang, A. C. Long, M. J. Clifford, and P. Harrison, 'Predictive modelling for optimization of textile composite forming', *Compos Sci Technol*, vol. 67, no. 15–16, pp. 3242–3252, Dec. 2007, doi: 10.1016/j.compscitech.2007.03.040.
- [120] P. Boisse, N. Hamila, F. Helenon, B. Hagege, and J. Cao, 'Different approaches for woven composite reinforcement forming simulation', *International Journal of Material Forming*, vol. 1, no. 1, pp. 21–29, Mar. 2008, doi: 10.1007/s12289-008-0002-7.
- [121] F. J. Schirmaier, D. Dörr, F. Henning, and L. Kärger, 'A macroscopic approach to simulate the forming behaviour of stitched unidirectional non-crimp fabrics (UD-NCF)', *Compos Part A Appl Sci Manuf*, vol. 102, pp. 322–335, Nov. 2017, doi: 10.1016/j.compositesa.2017.08.009.
- [122] P. Boisse *et al.*, 'Hypoelastic, hyperelastic, discrete and semi-discrete approaches for textile composite reinforcement forming', *International Journal of Material Forming*, vol. 3, pp. 1229–1240, 2010, doi: 10.1007/s12289-009-0664-9.

- [123] A. Aridhi *et al.*, ‘Textile composite structural analysis taking into account the forming process’, *Compos B Eng*, vol. 166, pp. 773–784, Jun. 2019, doi: 10.1016/j.compositesb.2019.02.047.
- [124] S. Chen and F. Yu, ‘Process simulation: Fabric forming’, in *Design and manufacture of structural composites*, Cambridge: Elsevier, 2023, ch. 15, pp. 373–400.
- [125] E. Guzman-Maldonado, P. Wang, N. Hamila, and P. Boisse, ‘Experimental and numerical analysis of wrinkling during forming of multi-layered textile composites’, *Compos Struct*, vol. 208, pp. 213–223, Jan. 2019, doi: 10.1016/j.compstruct.2018.10.018.
- [126] M. Smith, ‘Getting started with ABAQUS/Explicit: Keywords version’, 2006.
- [127] W. R. Yu, P. Harrison, and A. Long, ‘Finite element forming simulation for non-crimp fabrics using a non-orthogonal constitutive equation’, *Compos Part A Appl Sci Manuf*, vol. 36, no. 8, pp. 1079–1093, Aug. 2005, doi: 10.1016/j.compositesa.2005.01.007.
- [128] E. Syerko, S. Comas-Cardona, and C. Binetruy, ‘Models of mechanical properties/behavior of dry fibrous materials at various scales in bending and tension: a review’, *Compos Part A Appl Sci Manuf*, vol. 43, no. 8, pp. 1365–1388, Aug. 2012, doi: 10.1016/j.compositesa.2012.03.012.
- [129] P. Boisse, J. Huang, and E. Guzman-Maldonado, ‘Analysis and modeling of wrinkling in composite forming’, *Journal of Composites Science*, vol. 5, no. 3, pp. 1–16, 2021, doi: 10.3390/jcs5030081.
- [130] A. Laulusa, O. A. Bauchau, J. Y. Choi, V. B. C. Tan, and L. Li, ‘Evaluation of some shear deformable shell elements’, *Int J Solids Struct*, vol. 43, no. 17, pp. 5033–5054, Aug. 2006, doi: 10.1016/j.ijsolstr.2005.08.006.

- [131] F. Yu, S. Chen, L. T. Harper, and N. A. Warrior, 'Double diaphragm forming simulation using a global-to-local modelling strategy for detailed defect detection in large structures', *Compos Part A Appl Sci Manuf*, vol. 147, pp. 1–12, Aug. 2021, doi: 10.1016/j.compositesa.2021.106457.
- [132] L. Sorrentino and C. Bellini, 'Potentiality of hot drape forming to produce complex shape parts in composite material', *International Journal of Advanced Manufacturing Technology*, vol. 85, no. 5–8, pp. 945–954, Jul. 2016, doi: 10.1007/s00170-015-7998-x.
- [133] R. W. Ogden, 'Large deformation isotropic elasticity-on the correlation of theory and experiment for incompressible rubberlike solids', vol. 326, pp. 565–584, 1972, [Online]. Available: <https://royalsocietypublishing.org/>
- [134] R. S. Marlow, J. Busfield, and A. Muhr, 'A general first-invariant hyperelastic constitutive model', in *Constitutive models for rubber*, London: Balkema, Jan. 2003, pp. 157–160.
- [135] R. Azzouz, S. Allaoui, and R. Moulart, 'Composite preforming defects: a review and a classification', *International Journal of Material Forming*, vol. 14, pp. 1259–1278, 2021, doi: 10.1007/s12289-021-01643-7/Published.
- [136] A. Rawal, A. Majumdar, S. Anand, and T. Shah, 'Predicting the properties of needlepunched nonwovens using artificial neural network', *J Appl Polym Sci*, vol. 112, no. 6, pp. 3575–3581, Jun. 2009, doi: 10.1002/app.29687.
- [137] M. Smith, 'ABAQUS/CAE User's Manual (v6.6)', 2006.
- [138] P. Harrison, M. F. Alvarez, and D. Anderson, 'Towards comprehensive characterisation and modelling of the forming and wrinkling mechanics of engineering fabrics', *Int J Solids Struct*, vol. 154, pp. 2–18, Dec. 2018, doi: 10.1016/j.ijsolstr.2016.11.008.